

---

# Towards high resolution spectroscopy on trapped helium ions

Fabian Dominik Schmid

---



München 2022



---

# Towards high resolution spectroscopy on trapped helium ions

Fabian Dominik Schmid

---

Dissertation  
an der Fakultät für Physik  
der Ludwig-Maximilians-Universität  
München

vorgelegt von  
Fabian Dominik Schmid  
aus München

München, den 06.09.2022

Erstgutachter: Prof. Dr. Thomas Udem  
Zweitgutachter: Prof. Dr. Randolph Pohl  
Tag der mündlichen Prüfung: 19.10.2022



## Zusammenfassung

Um eine physikalische Theorie präzise zu testen, muss sie in einem System untersucht werden, das einfach genug ist, um eine präzise theoretische Beschreibung zu erlauben, und dessen Eigenschaften mit hoher Genauigkeit gemessen werden können. Seit vielen Jahrzehnten dient das Wasserstoffatom als ein solches System zum Testen der Quantenelektrodynamik (QED) gebundener Systeme. Wegen seiner Einfachheit lassen sich die Energieniveaus des Wasserstoffs mit Hilfe der QED präzise berechnen. Experimentell wurden Übergangsfrequenzen in Wasserstoff mittels Laserspektroskopie genau vermessen. Durch den Vergleich der experimentellen Daten mit dem theoretischen Ausdruck können zwei physikalische Konstanten, die Rydberg-Konstante und der Ladungsradius des Atomkerns, bestimmt und die Gültigkeit der Theorie selbst getestet werden.

In dieser Arbeit wird über Fortschritte auf dem Weg zur Spektroskopie des 1S-2S-Zwei-Photonen-Übergangs in dem wasserstoffartigen Ion  $\text{He}^+$  berichtet. Da  $\text{He}^+$  die selbe Struktur wie Wasserstoff hat, wird es im wesentlichen durch die selbe Theorie beschrieben. Allerdings tragen QED-Terme höherer Ordnung einen größeren Anteil zu den Energieniveaus bei, da sie mit großen Potenzen der Kernladung skalieren. Durch Kombination der 1S-2S-Übergangsfrequenz mit dem genau bekannten Ladungsradius des Heliumkerns könnte die Rydberg-Konstante zum ersten Mal in einem anderen System als Wasserstoff genau gemessen werden. Der Vergleich dieses Wertes mit dem aus der Wasserstoffspektroskopie gewonnenen Wert wird dann einen strengen Test der Universalität der QED liefern.

Die Genauigkeit der Wasserstoffspektroskopie wird derzeit durch Effekte aufgrund der Atombewegung limitiert. Wegen ihrer Ladung können  $\text{He}^+$ -Ionen nahezu bewegungslos in einer Paul-Falle gefangen werden, was diese Effekte stark reduziert. Der erste Teil dieser Arbeit befasst sich mit dem Ionenfallenaufbau. Etwa 50  $\text{He}^+$ -Ionen sind zusammen mit einigen tausend lasergekühlten  $\text{Be}^+$ -Ionen gefangen, die zur sympathetischen Kühlung dienen. Die Anregung des 1S-2S-Übergangs in einem  $\text{He}^+$ -Ion kann zur Drei-Photonen-Ionisierung zu  $\text{He}^{2+}$  führen. Es wird eine Technik demonstriert, mit der diese Ionen in Echtzeit und mit Einzelteilchenauflösung nachgewiesen werden können. Dies wird als empfindliches und hintergrundfreies Detektionsverfahren für die Spektroskopie dienen.

Während Wasserstoffspektroskopie mit ausgereiften Lasersystemen im tiefen Ultraviolett durchgeführt werden kann, ist zur Anregung des 1S-2S-Übergangs in  $\text{He}^+$  schmalbandige Strahlung mit einer Wellenlänge von 60,8 nm erforderlich. Dies liegt im extremen Ultraviolett (XUV), wo keine Dauerstrichlaser verfügbar sind. Stattdessen werden die hochintensiven Pulse eines infraroten Frequenzkamms mittels der Erzeugung hoher Harmonischer in einem Überhöhungsresonator kohärent in das XUV umgewandelt. Die diskreten Moden des resultierenden XUV-Frequenzkamms können dann den Übergang effizient anregen und ermöglichen eine hohe spektrale Auflösung. Der Frequenzkamm, aus dem die hohen Harmonischen erzeugt werden, benötigt eine außergewöhnliche spektrale Reinheit, damit schmale Moden im XUV erreicht werden können. Im zweiten Teil dieser Arbeit wird der Aufbau eines stabilisierten Frequenzkamm-Systems beschrieben, das diese Anforderung erfüllt. Im Rahmen dieser Arbeit wird eine neue Technik zur Messung des Phasenrauschens von resonatorstabilisierten Lasersystemen demonstriert.

## Abstract

For a precision test of a physical theory, it has to be studied in a system that is simple enough to allow a precise theoretical description and whose properties can be measured with high accuracy. For many decades, the hydrogen atom has served as such a system for testing bound-state quantum electrodynamics (QED). Due to its simplicity, the energy levels of hydrogen can be precisely calculated using QED. On the experimental side, transition frequencies in hydrogen have been accurately measured using laser spectroscopy. By comparing the experimental data to the theory expression, two physical constants, the Rydberg constant and the nuclear charge radius, can be determined, and the validity of the theory itself is tested.

This thesis reports on progress towards spectroscopy on the 1S-2S two-photon transition in the hydrogen-like ion  $\text{He}^+$ . Since  $\text{He}^+$  has the same structure as hydrogen, it is described by essentially the same theory. However, higher-order QED terms contribute a larger fraction of the energy levels since they scale with large powers of the nuclear charge. By combining the 1S-2S transition frequency with the accurately known helium nuclear charge radius, the Rydberg constant could for the first time be accurately measured in a system other than hydrogen. Comparing this value to the one obtained from hydrogen spectroscopy will then provide a stringent test of the universality of QED.

The accuracy of hydrogen spectroscopy is currently limited by effects due to atomic motion. Due to their charge,  $\text{He}^+$  ions can be held near-motionless in a Paul trap which greatly reduces these effects. The first part of this thesis describes the ion trap system. Around 50  $\text{He}^+$  ions are trapped together with a few thousand laser cooled  $\text{Be}^+$  ions that provide sympathetic cooling. Exciting the 1S-2S transition in a  $\text{He}^+$  ion can result in three-photon ionization to  $\text{He}^{2+}$ . A technique is demonstrated that allows detecting these ions in real time with single-particle resolution. This will serve as a sensitive and background-free detection scheme for the spectroscopy.

While hydrogen spectroscopy can be performed with mature deep ultraviolet laser systems, driving the 1S-2S transition in  $\text{He}^+$  requires narrow-band radiation at a wavelength of 60.8 nm. This lies in the extreme ultraviolet (XUV) where no continuous-wave laser sources are available. Instead, intracavity high harmonic generation is used to coherently convert the high intensity pulses of an infrared frequency comb to the XUV. The discrete spectral modes of the resulting XUV frequency comb can then efficiently excite the transition and enable high spectral resolution. The frequency comb that drives the high harmonic generation requires exceptional spectral purity such that narrow mode linewidths in the XUV can be achieved. The second part of this thesis reports on a stabilized frequency comb system that was set up and fulfills this requirement. As part of this work, a new technique for characterizing the phase noise of cavity-stabilized laser systems is demonstrated.

# Contents

<b>1</b>	<b>Introduction</b>	<b>1</b>
1.1	Testing QED with laser spectroscopy . . . . .	3
1.2	From hydrogen to helium ions . . . . .	6
<b>2</b>	<b>Ion trapping and cooling</b>	<b>11</b>
2.1	Paul traps . . . . .	12
2.1.1	Working principle . . . . .	13
2.1.2	Pseudopotential approximation . . . . .	15
2.1.3	Linear Paul traps . . . . .	17
2.1.4	Trapping different species . . . . .	20
2.1.5	Trapping many ions . . . . .	21
2.2	Laser cooling . . . . .	22
2.3	Ion Coulomb crystals . . . . .	25
2.4	Sympathetic cooling and mixed ion crystals . . . . .	25
2.5	The Be <sup>+</sup> ion . . . . .	27
<b>3</b>	<b>Two-photon direct frequency comb spectroscopy on trapped ions</b>	<b>31</b>
3.1	Optical frequency combs . . . . .	31
3.2	Two-photon transitions . . . . .	33
3.2.1	Frequency comb excitation . . . . .	37
3.3	Excitation dynamics . . . . .	42
3.4	Motional dynamics . . . . .	44
3.4.1	Multiple ions . . . . .	47
3.4.2	Comparison of excitation geometries . . . . .	50
<b>4</b>	<b>Ion trap setup</b>	<b>61</b>
4.1	Ion trap . . . . .	61
4.1.1	Trap electrodes . . . . .	61
4.1.2	Trap potential . . . . .	62
4.1.3	RF resonator . . . . .	64
4.1.4	Electrode connections . . . . .	70
4.1.5	Magnetic field coils . . . . .	71
4.2	Fluorescence detection . . . . .	72

4.2.1	Objectives . . . . .	72
4.2.2	Detectors . . . . .	77
4.3	Be <sup>+</sup> cooling laser . . . . .	79
4.3.1	Frequency stabilization . . . . .	81
4.3.2	Switch and frequency shifter . . . . .	85
4.4	Vacuum system . . . . .	86
4.4.1	Differential pumping . . . . .	87
4.4.2	Laser beam lines . . . . .	91
4.5	Experiment control system . . . . .	93
4.6	Ion loading . . . . .	94
4.6.1	Be <sup>+</sup> loading . . . . .	95
4.6.2	He <sup>+</sup> /H <sub>2</sub> <sup>+</sup> loading . . . . .	102
4.7	Trap characterization . . . . .	104
4.7.1	Radial secular frequencies . . . . .	104
4.7.2	Axial secular frequencies . . . . .	107
4.7.3	Excess micromotion . . . . .	109
<b>5</b>	<b>Detecting individual dark ions</b>	<b>119</b>
5.1	Introduction . . . . .	119
5.2	Experimental setup . . . . .	121
5.3	Secular scans . . . . .	121
5.4	Detecting individual H <sub>2</sub> <sup>+</sup> and H <sub>3</sub> <sup>+</sup> ions . . . . .	123
5.5	Molecular dynamics simulations . . . . .	124
5.6	Theoretical description . . . . .	128
<b>6</b>	<b>A low-noise driving laser for high harmonic generation</b>	<b>131</b>
6.1	Laser noise in spectroscopy experiments . . . . .	131
6.1.1	Amplitude and phase noise basics . . . . .	133
6.2	Cavity-stabilized continuous-wave laser . . . . .	141
6.2.1	Interference-filter stabilized ECDL . . . . .	142
6.2.2	Reference cavity and feedback system . . . . .	144
6.2.3	Linewidth and stability . . . . .	147
6.2.4	Phase noise characterization . . . . .	152
6.3	Stabilized driving laser system . . . . .	156
6.3.1	Laser oscillator and amplifiers . . . . .	156
6.3.2	Low-noise beat detection . . . . .	159
6.3.3	Frequency stabilization . . . . .	165
6.3.4	Path length stabilization . . . . .	172
<b>7</b>	<b>Conclusion and outlook</b>	<b>175</b>
7.1	Two-photon excitation of Be <sup>+</sup> . . . . .	175
<b>A</b>	<b>Objective design data</b>	<b>183</b>

B Micromotion fluorescence fit function

187

Bibliography

189



# Chapter 1

## Introduction

The basic principle of the scientific method is to make theories that describe the behavior of nature and to challenge these theories by comparison with experimental observations. One particularly fruitful example has been the analysis of the spectrum of atomic hydrogen. Due to its enormous impact, it has been described as the “Rosetta stone of modern physics” [1].

In the late 19th century, it became clear that the wavelengths of the spectral lines emitted by excited atoms follow regular patterns. The simplest pattern is that of the hydrogen lines whose wavelengths are given by the Rydberg formula:

$$\frac{1}{\lambda_{nm}} = R_\infty \left( \frac{1}{m^2} - \frac{1}{n^2} \right), \quad (1.1)$$

where  $R_\infty \approx 1.097 \times 10^7 \text{ m}^{-1}$  is the Rydberg constant, and  $m$  and  $n$  are positive integers. Initially, the Rydberg constant was just an empirical parameter that had to be determined from experiments. This changed in 1913 when N. Bohr introduced his famous model of the hydrogen atom [2]. By introducing several ad hoc hypotheses, such as the quantization of the electron orbits, he obtained an expression that relates the Rydberg constant to other physical constants:

$$R_\infty = \frac{m_e e^4}{8\varepsilon_0^2 h^3 c}, \quad (1.2)$$

where  $m_e$  and  $e$  are the mass and charge of the electron, respectively,  $\varepsilon_0$  is the vacuum electric permittivity,<sup>1</sup>  $h$  is the Planck constant, and  $c$  is the speed of light. The Bohr model was clearly incompatible with classical physics, and an entirely new kind of theory was required to consistently describe the behavior of atoms. This was achieved by E. Schrödinger who in 1926 wrote down what is now known as the *time-independent Schrödinger equation* for the hydrogen atom [3]:

$$\nabla^2 \psi(\mathbf{r}) + \frac{2m_e}{\hbar^2} \left( E + \frac{e^2}{4\pi\varepsilon_0 |\mathbf{r}|} \right) \psi(\mathbf{r}) = 0, \quad (1.3)$$

---

<sup>1</sup>Like most physicists in the early 20th century, Bohr used cgs units where  $4\pi\varepsilon_0 = 1$ . All formulas in this thesis are given in SI units.

where  $\psi(\mathbf{r})$  is the time-independent part of the *wave function*,<sup>2</sup>  $\hbar = h/(2\pi)$  is the reduced Planck constant, and  $E$  is the energy of the system. Schrödinger was able to show that Equation 1.3 has solutions for any  $E > 0$ . However, for  $E < 0$  the equation can only be fulfilled at certain discrete energy levels which are given by

$$E_n = -\frac{hcR_\infty}{n^2}, \quad (1.4)$$

where  $n = 1, 2, 3, \dots$  is the *principal quantum number*. These energy levels turn out to be identical to the energies of the quantized electron orbits that Bohr had to introduce in his model. The postulate that the transition between states with energies  $E_n$  and  $E_m$  is accompanied by the emission or absorption of a photon with wavelength  $1/\lambda_{nm} = |E_n - E_m|/(hc)$  then leads to the Rydberg formula.

Already in 1887, A. Michelson and E. Morley used their famous interferometer to demonstrate that the red ( $n = 2, m = 3$ ) hydrogen line actually consists of a pair of lines [4]. Since this *fine structure splitting* is a relativistic effect, Schrödinger's non-relativistic theory cannot explain it. A. Sommerfeld extended the Bohr model by using relativistic electron orbits and was able to calculate the fine structure in agreement with the observations [5]. However, his model suffered from the same conceptual problems as the Bohr model. By the late 1920s, P. Dirac and others had managed to formulate a relativistic version of quantum mechanics. According to the Dirac equation, the energy levels of a hydrogen-like atom are [6]

$$E_D = m_e c^2 \left[ 1 + \frac{(Z\alpha)^2}{(n - \delta)^2} \right]^{-1/2}, \quad (1.5)$$

where  $Z$  is the nuclear charge number,  $\alpha = e^2/(4\pi\epsilon_0\hbar c)$  is the fine-structure constant, and

$$\delta = j + \frac{1}{2} - \left[ \left( j + \frac{1}{2} \right)^2 - (Z\alpha)^2 \right]^{1/2}, \quad (1.6)$$

where  $j$  is the *total angular momentum quantum number*. Possible values of  $j$  are  $|l \pm s|$ , where  $l = 0, 1, \dots, n - 1$  is the *orbital angular momentum quantum number*, and  $s = 1/2$  is the *electron spin quantum number*. In the relativistic theory, the electron in a hydrogen atom generates a magnetic moment which is due to a combination of its spin and its orbital angular momentum. The interaction between this magnetic moment and the nuclear magnetic moment gives rise to the *hyperfine structure*.

In Dirac's theory, states with the same  $n$  and  $j$  have the same energy. However, in 1947, W. Lamb and R. Retherford showed that the  $2S_{1/2}$  and  $2P_{1/2}$  states<sup>3</sup> are split by around 1 GHz [7]. This difference was later called the *Lamb shift*. One effect that is not taken into account in the Dirac equation is a level shift due to the finite size of the nucleus. Only the wave functions of S states have significant overlap with the nucleus, while

<sup>2</sup>The interpretation of what the wave function represents has been hotly debated ever since.

<sup>3</sup>We label the states with the usual notation  $nl_j$  where the angular momentum quantum number is given as a letter (S, P, D, ... for  $l = 0, 1, 2, \dots$ ).



wave functions with larger angular momentum quantum numbers vanish at the origin. However, the resulting energy shift is too small to explain the observed effect [8]. The mystery could be solved after the theory of quantum electrodynamics (QED) was developed by S. Tomonaga, J. Schwinger, and R. Feynman. In this theory, light and matter are described by quantum fields which leads to a variety of new effects that influence the energy levels of bound electrons [6]. Since then, QED has withstood experimental tests with ever increasing sensitivity and today is one of the most accurately tested theories in all of physics. Figure 1.1 shows a detailed level scheme of the first two principal quantum numbers in atomic hydrogen.

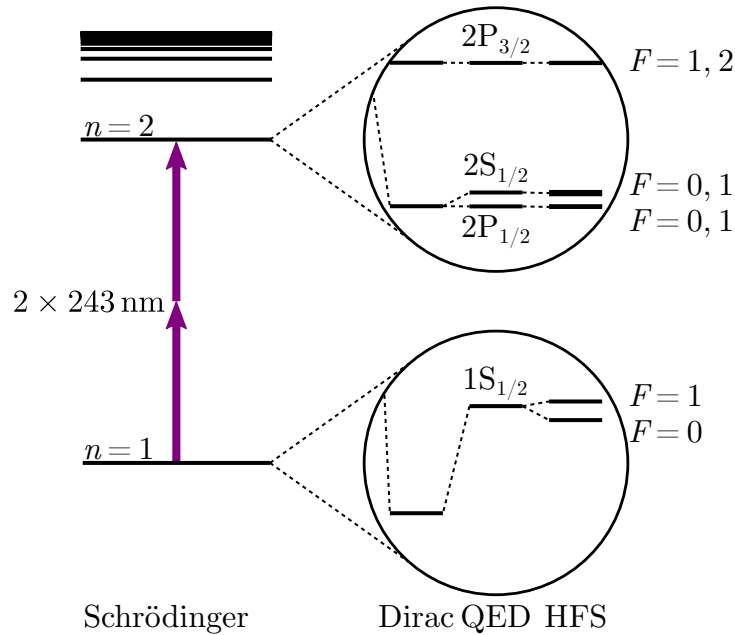


Figure 1.1: Level scheme of atomic hydrogen (adapted from [9]). The insets are magnified by a factor of 100 000. At this scale the excited state hyperfine structure (HFS) is not resolved. The quest to calculate the levels with increasing accuracy has been a major driving force in the development of modern physics. The narrow 1S-2S two-photon transition can be driven with ultraviolet light at 243 nm and has been measured most accurately [10, 11].

## 1.1 Testing QED with laser spectroscopy

The QED expression for the energy levels of a hydrogen-like atom is usually grouped into three parts:

$$E_{nj} = E_D + E_M + E_L, \quad (1.7)$$

where  $E_D$  are the Dirac energy levels given by Equation 1.5,  $E_M$  are recoil corrections due to the finite nuclear mass, and  $E_L$  is the Lamb shift which includes a variety of QED effects, as well as corrections due to the finite nuclear size. The full expressions for the

latter two terms are quite lengthy and can be found in the literature [6, 12]. The energy levels depend on a number of physical constants at different levels of precision. To quantify this statement,  $E_D$  is expanded into powers of  $Z\alpha$ . Equation 1.7 can then be recast into the form<sup>4</sup> [13]

$$E_{nlj} = hcR_\infty \left[ -\frac{Z^2}{n^2} + f_{nlj}(Z, \alpha, \frac{m_e}{m_N}, \dots) + \delta_{l0} \frac{C_{NS}}{n^3} r_N^2 \right]. \quad (1.8)$$

We can identify the first term inside the brackets as the non-relativistic approximation of the energy levels which was obtained by Bohr and Schrödinger. It is on the order of 1 for low-lying states in light hydrogen-like atoms, while the other two terms are much smaller than 1. The second term  $f_{nlj}(Z, \alpha, \frac{m_e}{m_N}, \dots)$  contains relativistic corrections, recoil corrections, QED effects, and higher-order nuclear charge distribution contributions. It depends on the fine structure constant  $\alpha$ , the mass ratio between the electron and the nucleus  $m_e/m_N$ , and on several other physical constants. It can be calculated with sufficient accuracy for analyzing spectroscopy results using values for these constants that have been measured in other experiments [6]. The last term is the leading-order finite nuclear size correction which depends on the mean square nuclear charge radius  $r_N^2$  and only affects S states. The coefficient  $C_{NS}$  depends on  $\alpha$ ,  $m_e/m_N$ , and on the Compton wavelength of the electron which are known much more precisely than  $r_N^2$  from independent measurements [6].

From these considerations we can see that spectroscopy on hydrogen-like atoms is most sensitive to the Rydberg constant  $R_\infty$  and to the nuclear charge radius  $r_N$ . A value pair  $\{R_\infty, r_N\}$  can be extracted by combining the measured frequencies of two different transitions. If more than two measurements are available, the constants can be determined using different combinations. The agreement between the results then serves as a consistency check of the expression for the energy levels (Equation 1.8). In atomic hydrogen the frequency of the 1S-2S two-photon transition is known with by far the highest accuracy [10, 11]. This is due to the narrow linewidth of only 1.3 Hz [14] and due to the possibility of driving the transition with two counter-propagating laser beams which cancels the Doppler effect to first order. The results of other measurements are therefore usually combined with the 1S-2S result to extract  $R_\infty$  and the proton charge radius  $r_p$ .

Figure 1.2 shows the current status of this comparison. The ‘‘H-world’’ data point is the combination of 15 different measurements that were performed before 2010 and are compiled in the CODATA<sup>5</sup>-2014 report [15]. In 2010, the CREMA<sup>6</sup> collaboration published a value of the proton charge radius that was obtained by measuring the frequency of the 2S-2P transition (Lamb shift) in muonic hydrogen [21]. Muonic hydrogen is an exotic version of the hydrogen atom where the electron is replaced by a muon. Since the muon is around 200 times heavier than the electron, the atomic orbitals are smaller by the same factor. This dramatically enhances the overlap of the S state wave function with the

<sup>4</sup>The rest mass term  $m_e c^2$  is dropped since it is the same for all energy levels and therefore has no influence on the transition frequencies.

<sup>5</sup>Committee on Data for Science and Technology.

<sup>6</sup>Charge Radius Experiments with Muonic Atoms.

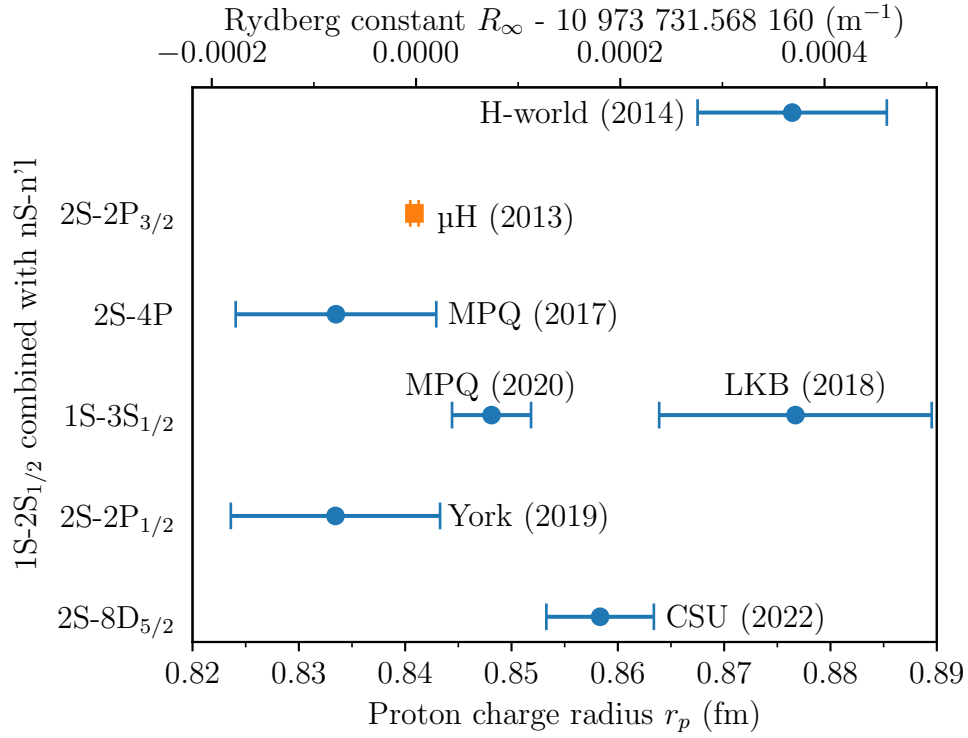


Figure 1.2: Values of the proton charge radius  $r_p$  and the Rydberg constant  $R_\infty$  obtained by hydrogen spectroscopy (blue dots) and by muonic hydrogen spectroscopy (orange square). The “H-world” point is obtained by combining 15 different measurements that were performed before 2010 (Adj. 8 in Table XXIX in [15]). Since then, new measurements were performed at the Max Planck Institute of Quantum Optics, Garching, Germany (MPQ) [13, 16], the Laboratoire Kastler Brossel, Paris, France (LKB) [17], York University, Toronto, Canada (York) [18], and Colorado State University, Fort Collins, United States (CSU) [19]. The muonic hydrogen data point is a reanalysis [20] of the original measurement [21] which makes use of improved theory and additional data from a second hyperfine component. The values for  $r_p$  and  $R_\infty$  are highly correlated such that they can be shown in a single graph (top and bottom axes).

nucleus. The finite size of the proton therefore contributes around 2% to the Lamb shift. A measurement with moderate accuracy was thus sufficient to extract the proton charge radius with an order of magnitude higher precision than was previously achieved. However, the result was discrepant by 5.0 standard deviations from the previously accepted value obtained from hydrogen spectroscopy and electron-proton scattering. This *proton radius puzzle* has spurred a number of new measurements (see Figure 1.2). While there is some tension between the data points, most of the new results are compatible with the muonic hydrogen value, but disagree with the “H-world” value. This suggests that experimental issues, such as underestimated systematic errors, may be responsible for the discrepancy.

## 1.2 From hydrogen to helium ions

Figure 1.3 shows a timeline of the accuracy achieved in measurements of the 1S-2S transition frequency in hydrogen. Until the late 1990s, the uncertainty was limited by the optical frequency metrology, i.e. by how well the frequency of the spectroscopy laser could be determined [24]. This problem was solved with the invention of the optical frequency comb which allows counting the frequency of a laser with the accuracy of the best atomic

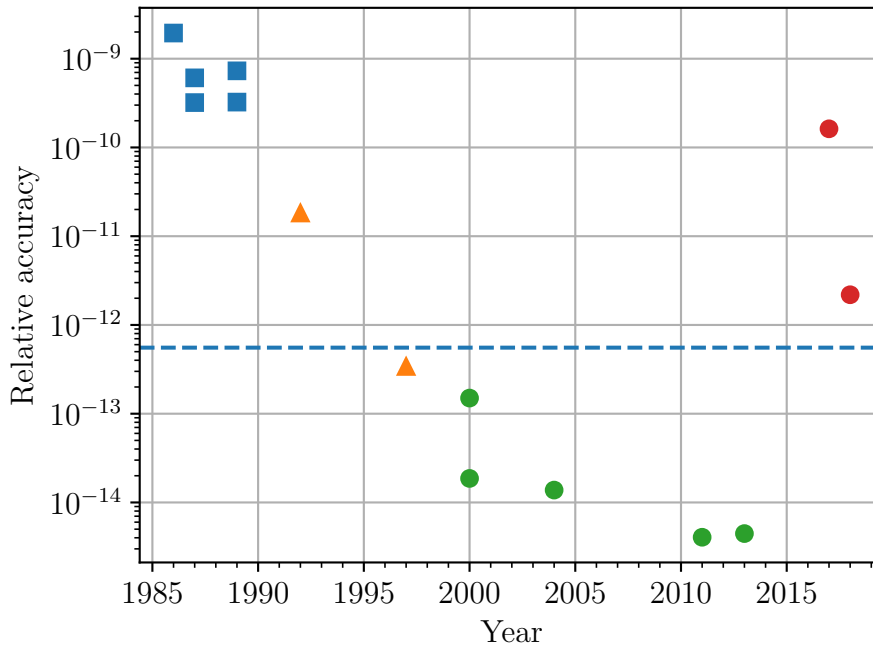


Figure 1.3: Timeline of hydrogen 1S-2S spectroscopy. The optical frequency metrology evolved from molecular vapor cells (blue squares) over optical frequency chains (orange triangles) to optical frequency combs (green circles). The blue dashed line shows the second-order Doppler shift for atomic hydrogen at 4 K. The red circles are measurements in antihydrogen [22, 23].

clocks [25, 26].

The uncertainty of the best 1S-2S measurements [10, 11] is now limited by motional effects, such as the relativistic second-order Doppler effect and time-of-flight broadening. To give a sense for the scale of the issue, the relative second-order Doppler shift of transitions in atomic hydrogen at liquid helium temperature ( $\approx 4$  K) is  $-6 \times 10^{-13}$  [27, p. 238]. This is two orders of magnitude larger than the achieved measurement uncertainty (see Figure 1.3).

In many atoms motional effects can be minimized by trapping and laser cooling. However, hydrogen is notoriously difficult to laser cool due to the very short wavelength of the 1S-2P transition of 121.6 nm [28]. Trapping of hydrogen under conditions suitable for highly accurate spectroscopy has not yet been achieved, and the best measurements were performed on cryogenic atomic beams.

We have therefore set out to perform spectroscopy on the 1S-2S transition in the hydrogen-like ion  $\text{He}^+$ . Due to their charge,  $\text{He}^+$  ions can be suspended near-motionless in vacuum using the oscillating electric fields of a *Paul trap*. This provides an ideal environment for high precision spectroscopy. The charge radius of the  $^4\text{He}$  nucleus (alpha particle) has been measured with high accuracy using spectroscopy on muonic helium ions [29]. By using Equation 1.8, the 1S-2S transition frequency in  $^4\text{He}^+$  and the alpha particle charge radius can be combined to obtain a value for the Rydberg constant. Comparing this value with the one obtained from hydrogen spectroscopy will be a sensitive test of QED in this yet unexplored system.

Figure 1.4 shows the relevant levels of  $^4\text{He}^+$ . Like in hydrogen, the 2S state is metastable which leads to a natural linewidth of the 1S-2S transition of only 84 Hz [14]. The  $Z^2$  scaling of the energy levels results in a two-photon transition wavelength of 60.8 nm which lies in the extreme ultraviolet (XUV) wavelength range. Working in this wavelength range is extremely challenging since it lies far below the transparency range of any bulk material. This means that no refractive optics and no laser sources are available. It also precludes the use of nonlinear crystals for efficiently converting narrow-band laser light into the XUV.

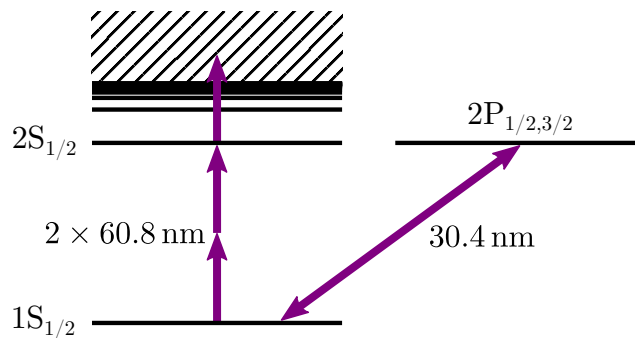


Figure 1.4: Level scheme of  $^4\text{He}^+$ . The two times larger nuclear charge leads to four times shorter transition wavelengths compared to hydrogen. Since the alpha particle has zero spin, there is no hyperfine structure. The 2S state can be ionized by radiation with a wavelength below 91.1 nm.

Instead, high-order harmonic generation (HHG) can be used for generating XUV radiation [30]. This process occurs when highly intense short (usually sub-ps) laser pulses are focused into a target. The large electric field strength inside the laser pulses creates a strong nonlinear response in the target. This results in the emission of harmonics of the driving radiation. In isotropic media, such as gases, only odd-order harmonics are being generated. At first glance, using short pulses appears incompatible with the goal of performing precision spectroscopy on a narrow spectral line. The bandwidth of a laser pulse is on the order of the inverse pulse duration. For sub-ps pulses we therefore expect bandwidths of at least hundreds of GHz which is more than nine orders of magnitude larger than the natural linewidth of the 1S-2S transition. However, the picture changes when the spectrum of the entire *pulse train* emitted by a mode-locked pulsed laser is considered. As we will show in chapter 3, the spectrum consists of a *comb* of individual modes which can be as narrow as the best continuous-wave lasers. Already in 1977, Ye. Baklanov and V. Chebotayev pointed out that this mode structure could be used for efficient excitation of two-photon transitions [31]. It turns out that the excitation rate is equal to that of a continuous-wave laser with the same average power. Furthermore, the spectral width of the resonance is only limited by the width of the individual modes and of the atomic line, not by the broad spectral envelope of the pulses. An impressive demonstration of this scheme is the spectroscopy on the 1S-3S transition in hydrogen which was performed in our group at MPQ [16]. In this experiment, spectroscopy light at 205 nm was generated by fourth-harmonic generation of the output of a mode-locked Ti:sapphire laser in nonlinear crystals. The high intensity of the ps pulses enabled a significantly higher conversion efficiency compared to continuous-wave sources. The experiment achieved a relative uncertainty of  $2.5 \times 10^{-13}$  which makes it the second most precise measurement on atomic hydrogen, only surpassed by spectroscopy on the much narrower 1S-2S line.

The pulsed two-photon excitation scheme requires a high degree of phase coherence between the pulses. This has so far only been demonstrated for mode-locked laser oscillators with pulse repetition rates of at least tens of MHz. At such high repetition rates, a given amount of average power is distributed over a large number of pulses. This makes it challenging to achieve the required intensity for driving the HHG process. One solution is to use a resonant optical cavity to enhance the available peak intensity [32].

Figure 1.5 shows a schematic overview of the setup we have constructed for performing spectroscopy on the 1S-2S transition in  $\text{He}^+$ . Due to the low efficiency of HHG, it is advantageous to start with a powerful driving laser system. We use a system based on Yb-doped gain crystals that can produce average powers of a few hundred W with a center wavelength of around 1030 nm [33]. The light is then coupled into an enhancement cavity in which HHG takes place in a xenon gas jet. The generated harmonics are coupled out from the cavity. The spectroscopy radiation at 60.8 nm corresponds to the 17th harmonic of the driving laser light.

This radiation is then sent into an ion trap which holds the  $\text{He}^+$  ions. Direct laser cooling of  $\text{He}^+$  is not feasible since the first dipole-allowed transition from the ground

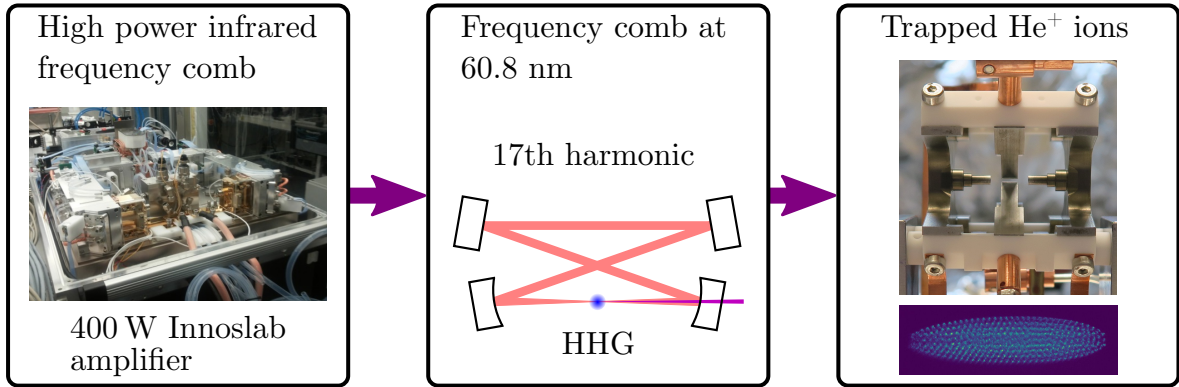


Figure 1.5: Schematic overview of the  $\text{He}^+$  spectroscopy setup. A stabilized Yb-based laser system provides the high power and spectral purity required for XUV generation. The spectroscopy radiation is generated as the 17th harmonic of the driving laser light using cavity-enhanced HHG. Finally, the radiation is sent onto trapped  $\text{He}^+$  ions which are cooled by co-trapped laser cooled  $\text{Be}^+$  ions.

state ( $1S-2P$ ) has a wavelength of 30.4 nm.<sup>7</sup> We therefore indirectly cool the  $\text{He}^+$  ions by mixing them with laser cooled  $\text{Be}^+$  ions. After successful excitation to the  $2S$  state, the  $\text{He}^+$  ions can be ionized to  $\text{He}^{2+}$  by absorbing another photon with a wavelength below 91.1 nm. The production of these ions can be detected with high sensitivity by measuring their characteristic mechanical resonances in the ion trap. This will serve as the signal for performing the spectroscopy.

This thesis is organized as follows. First, the necessary theoretical background is reviewed. This part consists of chapter 2 which focuses on ion trapping and laser cooling, and of chapter 3 in which two-photon direct frequency comb spectroscopy is discussed in detail. Then chapter 4 reports on the design, construction, and characterization of the ion trap system. In chapter 5 a test of the ion detection scheme is presented where real-time detection with single-particle sensitivity was achieved. We furthermore found that the infrared frequency comb that drives the HHG process requires exceptional spectral purity. We have therefore constructed and characterized a low-noise driving laser system which is described in chapter 6. Finally, in chapter 7 two-photon excitation of trapped  $\text{Be}^+$  ions is proposed as a “test experiment” that can be performed before attempting the  $\text{He}^+$  spectroscopy.

In parallel to the work reported here, the enhancement cavity for HHG was set up by J. Weitenberg, A. Ozawa, and J. Moreno. Once this system is fully operational, a first search for the resonance line can be started.

<sup>7</sup>Since this is a one-photon transition, it cannot be efficiently excited with a frequency comb.





# Chapter 2

## Ion trapping and cooling

Trapping particles, i.e. confining them without collisions with the walls of a container, allows studying their fundamental properties with minimal disturbances from the environment. Trapped particles are therefore ideal targets for accurate laser spectroscopy measurements of their energy levels. Important applications are optical atomic clocks in which narrow optical transitions in trapped atoms or ions are used as frequency standards. These clocks have reached relative frequency uncertainties of a few parts in  $10^{18}$  [34–37]. Frequency comparisons of optical clocks are therefore among the most accurate measurements ever performed. Atom trapping also provides almost perfect thermal insulation and prevents the condensation of cold gases that would occur upon contact with a surface. It is therefore an essential ingredient for the preparation of gases at ultra-low temperatures which allows the observation of new phases of matter such as Bose-Einstein condensates [38, 39].

Atomic or molecular ions are particularly well suited for trapping. This is because their net charge allows controlling their motion with external electromagnetic fields. Since ion traps only act on the net charge, they are insensitive to the internal state of the atom or molecule. Stable trapping requires that the ion experiences a restoring force when it leaves the center of the trap along any of the three Cartesian axes. It is easy to see that this cannot be achieved with a static electric potential alone. Any electric potential  $\varphi$  has to fulfill Laplace's equation:

$$\Delta\varphi = \frac{\partial^2\varphi}{\partial x^2} + \frac{\partial^2\varphi}{\partial y^2} + \frac{\partial^2\varphi}{\partial z^2} = 0, \quad (2.1)$$

and can therefore not have a local minimum in all three directions.

One technique for overcoming this limitation is to combine a static quadrupole electric field with a static homogeneous magnetic field. This configuration closely resembles the Penning vacuum gauge where the field configuration is used to maximize the path that electrons travel within a discharge. It was therefore named *Penning trap* by its inventor H. Dehmelt. Penning traps have been used in some extremely accurate measurements, for example in mass comparisons of different atoms and subatomic particles [40, 41], and in the measurement of the  $g$ -factor of the electron [42]. However, the strong magnetic field required for the particle confinement leads to large Zeeman shifts of atomic energy levels.

This makes Penning traps difficult to use for highly accurate atomic spectroscopy. Here, *Paul traps* are commonly employed since they can confine ions in an essentially field-free region.

## 2.1 Paul traps

In 1953, W. Paul and H. Steinwedel described a mass spectrometer that is based on sending ions through an oscillating quadrupole electric field [43]. Such a field can be produced by applying an oscillating voltage to a set of four hyperbolic electrodes as shown in Figure 2.1 (a). As we will show below, the trajectories of ions travelling through such a quadrupole guide fall into two classes of solutions depending on the charge-to-mass ratio of the ions and on the parameters of the applied field. The first class consists of stable trajectories where the ion coordinates remain bounded for any initial conditions. The second class contains solutions that grow exponentially such that the ions collide with the electrode surfaces after a short time. Under appropriate operating conditions, only ions with a small range of charge-to-mass ratios can pass through the device. Such quadrupole mass filters are widely used in commercial mass spectrometers, for example for rest gas analysis in vacuum systems.

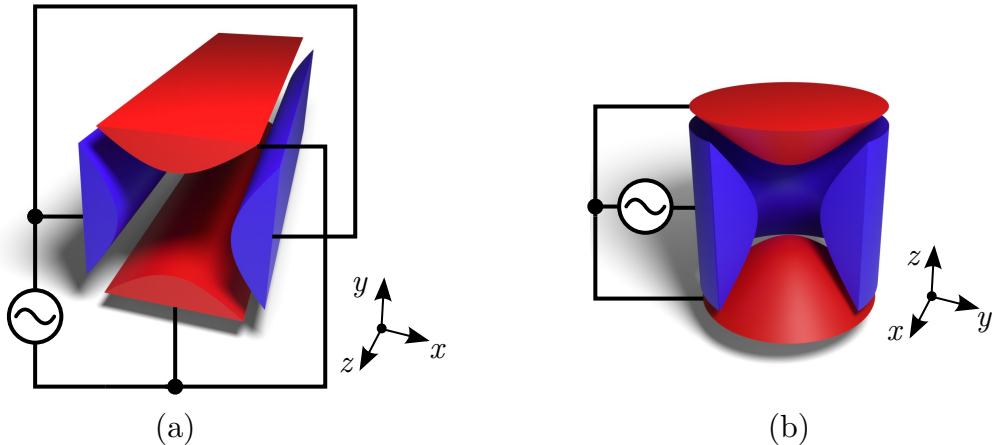


Figure 2.1: (a) Quadrupole ion guide, and (b) Paul trap. Electrodes with matching colors have the same voltage.

Paul and colleagues soon realized that the same principle can be applied to confine ions along all three axes. In 1958, they first described their “Ionenkäfig” (ion cage) which later became known as a Paul trap or radio frequency (RF) ion trap [44]. The trap electrodes have hyperbolic shapes and are split into two “endcap” electrodes and a “ring” electrode between which an oscillating voltage is applied (see Figure 2.1 (b)).

### 2.1.1 Working principle

An electric quadrupole potential with a static component and a component that is sinusoidally oscillating at frequency  $\Omega$  can in general be written as [45]

$$\varphi(x, y, z, t) = \frac{U}{2}(\alpha x^2 + \beta y^2 + \gamma z^2) - \frac{V}{2} \cos(\Omega t)(\alpha' x^2 + \beta' y^2 + \gamma' z^2). \quad (2.2)$$

Since the potential has to fulfill Equation 2.1 at all times, the coefficients are restricted to

$$\alpha + \beta + \gamma = 0, \quad (2.3)$$

$$\alpha' + \beta' + \gamma' = 0. \quad (2.4)$$

We can now analyze the linear quadrupole guide shown in Figure 2.1 (a). If the finite length of the guide can be neglected, we expect no field component in  $z$  direction such that

$$\begin{aligned} \alpha &= -\beta, \\ \alpha' &= -\beta', \\ \gamma &= \gamma' = 0. \end{aligned} \quad (2.5)$$

On the other hand, the Paul trap shown in Figure 2.1 (b) is rotationally symmetric around the  $z$  axis such that

$$\begin{aligned} \alpha &= \beta = -\frac{1}{2}\gamma, \\ \alpha' &= \beta' = -\frac{1}{2}\gamma'. \end{aligned} \quad (2.6)$$

The motion of a charged particle in the potential given by Equation 2.2 is decoupled in the three coordinates. In the following we only treat the motion along  $x$  since the formulas for  $y$  and  $z$  can be obtained by replacing the appropriate coefficients. The equation of motion is

$$m\ddot{x} = -Q \frac{\partial \varphi(x, y, z, t)}{\partial x} = -Q[U\alpha - V \cos(\Omega t)\alpha']x, \quad (2.7)$$

where  $m$  is the mass and  $Q$  is the charge of the ion.

After introducing the constants

$$a_x = \frac{4QU\alpha}{m\Omega^2}, \quad (2.8)$$

$$q_x = \frac{2QV\alpha'}{m\Omega^2}, \quad (2.9)$$

and transforming time into units of RF half-cycles ( $\tau = \Omega t/2$ ), we obtain:

$$\frac{d^2x}{d\tau^2} + [a_x - 2q_x \cos(2\tau)]x = 0. \quad (2.10)$$

This is the *Mathieu differential equation* which was originally derived to describe vibrations of an elliptic membrane [46]. A detailed discussion of Equation 2.10 in the context of ion trapping can be found in the literature [45, 47]. The result is that the  $a$ - $q$ -plane is divided into stable and unstable regions. In stable regions the ion coordinate remains bounded for arbitrary initial conditions, whereas in unstable regions the coordinate grows exponentially with time. The stability diagram is shown in Figure 2.2. Flipping the sign of  $q_x$  in Equation 2.10 is equivalent to shifting the initial phase of the oscillating potential by  $\pi$ . The stability diagram is therefore symmetric with respect to  $q_x$ , and only the positive half is shown in the plot. In our ion trap we only work in the first stable region that includes the origin  $(a_x, q_x) = (0, 0)$ .

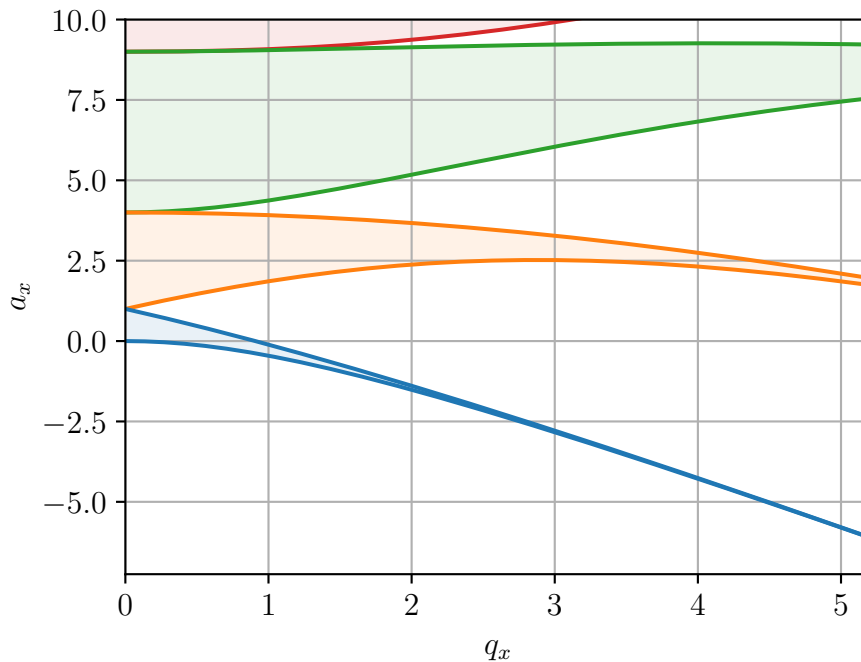


Figure 2.2: Stability diagram of the Mathieu differential equation 2.10. The first four stable regions are shaded in different colors.

Stable solutions of the Mathieu differential equation can be written as [47, p. 20]

$$x(\tau) = A_x \sum_{n=-\infty}^{\infty} c_{2n} \cos[(\beta_x + 2n)\tau] + B_x \sum_{n=-\infty}^{\infty} c_{2n} \sin[(\beta_x + 2n)\tau], \quad (2.11)$$

where  $A_x$  and  $B_x$  depend on the initial conditions. The stability parameter  $\beta_x$  and the coefficients  $c_{2n}$  depend only on  $a_x$  and  $q_x$  and can be iteratively calculated using continued fraction expressions [47, p. 21].

From Equation 2.11 we can see that the ion motion is a superposition of harmonic oscillations with an infinite set of frequencies that are spaced by integer multiples of the

trap drive frequency  $\Omega$ :

$$\omega_{x,n} = \frac{1}{2}\beta_x\Omega + n\Omega. \quad (2.12)$$

The fundamental frequency given by  $n = 0$  is called the *secular frequency*

$$\omega_{\text{sec},x} = \frac{1}{2}\beta_x\Omega. \quad (2.13)$$

### 2.1.2 Pseudopotential approximation

It is instructive to analyze the ion motion in the limit of weak confinement which is defined by

$$|a_x|, q_x^2 \ll 1. \quad (2.14)$$

Then the stability parameter can be approximated by

$$\beta_x \approx \sqrt{a_x + \frac{q_x^2}{2}}, \quad (2.15)$$

and in Equation 2.11 the coefficients  $c_{2n}$  with  $|n| > 1$  can be neglected. The ion motion becomes [47, pp. 24–25]

$$x(t) = x_0 \left[ 1 - \frac{q_x}{2} \cos(\Omega t) \right] \cos(\omega_{\text{sec},x} t + \varphi_{0,x}), \quad (2.16)$$

where  $x_0$  and  $\varphi_{0,x}$  are determined by the initial conditions. The exact solution using Equation 2.11 and the approximation using Equation 2.16 are compared in Figure 2.3.

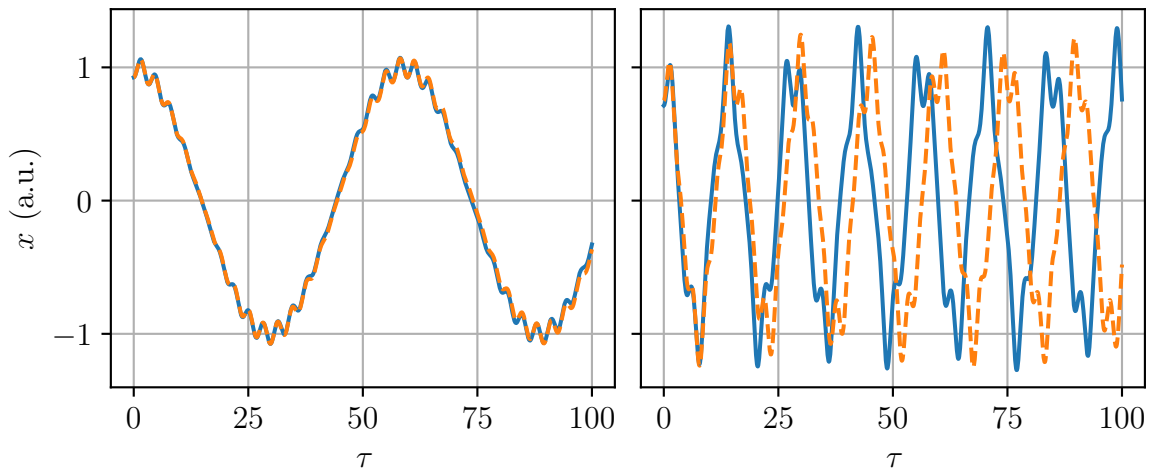


Figure 2.3: Exact (solid blue line) and approximate (dashed orange line) solutions of the Mathieu differential equation 2.10. In the left plot  $a_x = 0$  and  $q_x = 0.1$ , and in the right plot  $a_x = 0.05$  and  $q_x = 0.5$ .

From the condition of weak confinement, it follows that  $\beta \ll 1$  and therefore  $\omega_{\text{sec},x} \ll \Omega$ . We can separate the motion into two terms:

$$x(t) = X(t) + \xi(t), \quad (2.17)$$

where

$$X(t) = x_0 \cos(\omega_{\text{sec},x}t + \varphi_{0,x}) \quad (2.18)$$

is the slow *secular motion* at frequency  $\omega_{\text{sec},x}$ , and

$$\xi(t) = -\frac{q_x}{2} \cos(\Omega t) X(t) \quad (2.19)$$

is the superimposed fast *micromotion* at frequency  $\Omega$ . The micromotion amplitude is proportional to  $X(t)$  and is at most  $q_x/2$  times the secular motion amplitude.

The secular motion can be interpreted as the ion moving in an effective harmonic potential which is called the *pseudopotential* of the trap. The  $x$ -component of this potential is

$$\Phi_x(X) = \frac{1}{2} m \omega_{\text{sec},x}^2 X^2 = \frac{m a_x \Omega^2}{8} X^2 + \frac{m q_x^2 \Omega^2}{16} X^2, \quad (2.20)$$

where we have used Equation 2.13 and Equation 2.15. The first term of Equation 2.20 is the electrostatic potential of the trap which is characterized by the  $a_x$  parameter (see Equation 2.2 and Equation 2.8). The second term is the dynamic confinement due to the oscillating field. It can be related to the micromotion as follows. Since the secular motion is much slower than the micromotion,  $X(t)$  changes only slightly during one period of the micromotion. We can therefore treat it as a time-independent parameter in Equation 2.19. The cycle-averaged kinetic energy of the micromotion becomes

$$E_{\text{mm}}(X) = \frac{1}{2} m \langle \dot{\xi}(t)^2 \rangle \approx \frac{m q_x^2 \Omega^2}{8} X^2 \langle \sin^2(\Omega t) \rangle = \frac{m q_x^2 \Omega^2}{16} X^2, \quad (2.21)$$

where  $\langle \rangle$  signifies averaging over one micromotion cycle. Naively one might expect that the force due to the RF field averages out and should not affect the secular motion. However, it is the micromotion that generates the net attractive force in the pseudopotential. This can be seen by comparing Equation 2.20 and Equation 2.21. The dynamic confinement term of the pseudopotential is given by the mean kinetic energy of the micromotion. Since the micromotion grows with increasing distance from the trap center, this leads to an attractive potential.

In contrast to a purely electrostatic potential, the pseudopotential does not have to fulfill Laplace's equation and can therefore be attractive along all three axes. The pseudopotential of Paul traps can be very deep compared to typical neutral atom traps. If we take for example a secular frequency of  $\omega_{\text{sec},x} = 2\pi \times 1$  MHz and a trap with a radius  $r_0 = 0.5$  mm, a  $\text{Be}^+$  ion ( $m = 9$  u) has to climb a potential of 0.46 eV to get from the trap center to the electrode surface. By dividing this by the Boltzmann constant, we get a characteristic temperature of 5300 K. The trap can therefore easily confine ions at room temperature, and collisions with background gas molecules can only very rarely transfer enough kinetic energy to kick out ions from the trap.

### 2.1.3 Linear Paul traps

We can see from Equation 2.16 that the micromotion vanishes at the node of the oscillating quadrupole field. In the classical Paul trap shown in Figure 2.1 (b), this is only the case in a single point at the center of the trap. If more than one ion is trapped, the ions spread out due to the mutual Coulomb repulsion. This means that at most a single ion can sit in the trap center, and all the other ones experience micromotion. This leads to a number of detrimental effects when addressing the stored ions with laser light.

If the micromotion has a component parallel to the laser beam, the light appears phase modulated in the rest frames of the ions. The resulting modulation sidebands appear at multiples of the trap drive frequency. In Paul traps for atomic ions, this is typically a few tens of MHz which is comparable to the linewidth of atomic transitions used for laser cooling. The micromotion amplitude is  $q_x/2$  times the distance from the trap center [48]. For typical  $q$  parameters in the range of 0.1 to 0.3, already a displacement of a few  $\mu\text{m}$  results in a modulation amplitude on the scale of optical wavelengths. In this case the spectrum is strongly modulated, i.e. the strengths of the modulation sidebands can exceed that of the carrier. Furthermore, the ions experience different laser spectra depending on how far they are located from the trap center. Laser cooling relies on precise control of the detuning between the cooling laser and an atomic resonance (see section 2.2). Micromotion therefore makes it difficult to efficiently laser cool large ensembles of ions in a classical Paul trap [49].

In precision spectroscopy micromotion also leads to systematic shifts of the atomic resonances due to the second-order Doppler effect and due to the Stark effect caused by the oscillating electric field [48]. We will discuss the expected influence of ion micromotion on our  $\text{He}^+$  spectroscopy experiment in subsection 4.7.3.

These micromotion effects can be strongly reduced by using linear Paul traps [50, 51]. These traps are essentially quadrupole guides with an additional static quadrupole electric field preventing the ions from exiting the guide along its axis. One exemplary electrode configuration is shown in Figure 2.4.

In an ideal (infinitely long) linear Paul trap, the node of the oscillating potential forms a line along the trap axis. Linear strings of many ions can be trapped on the nodal line without experiencing micromotion. Furthermore, even ions that are off-axis experience micromotion only in the radial direction. By aligning the laser beam along the trap axis, large numbers of ions can be laser cooled without the detrimental effect of micromotion sidebands. In real linear Paul traps, there is some residual axial micromotion due to the finite length of the electrodes and due to manufacturing imperfections (see subsection 4.7.3). However, the micromotion is typically much weaker than in a classical Paul trap and can be tolerated in many applications.

Linear Paul traps with many different electrode geometries have been demonstrated. These range from traps that still resemble a quadrupole guide to surface-electrode traps in which all electrodes are located in a single plane [52]. We employ linear traps with three-dimensional electrode arrangements and therefore limit our discussion to this type of geometry. A common simplification of the quadrupole guide is to use electrodes with circu-

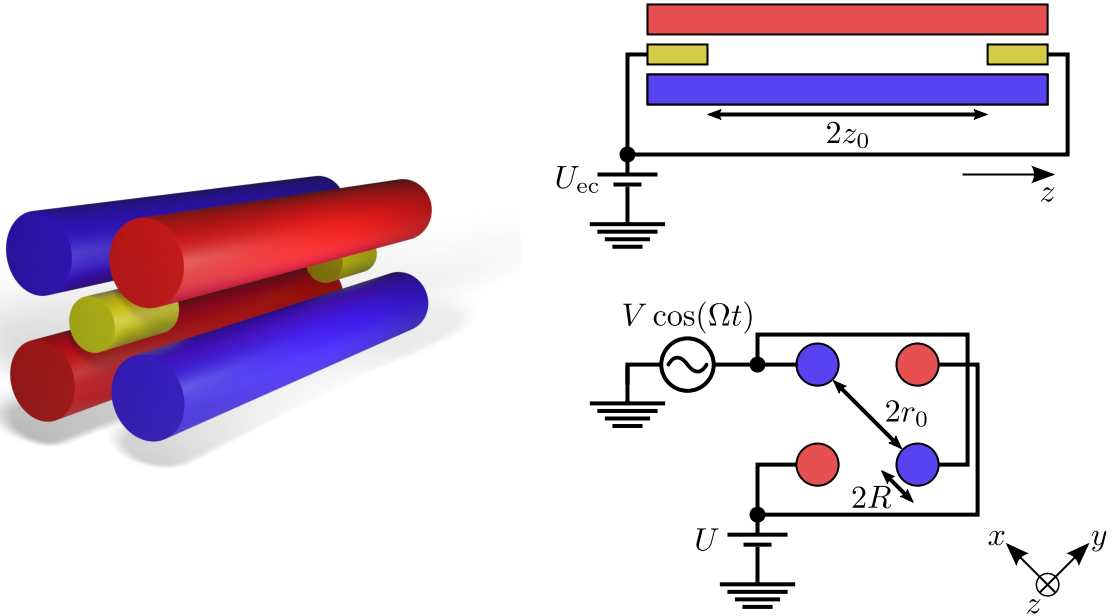


Figure 2.4: Linear Paul trap. The oscillating voltage  $V \cos(\Omega t) - U$  is applied between the red and blue pairs of “rod” electrodes in order to provide radial confinement. The static voltage  $U_{ec}$  is applied to the yellow “endcap” electrodes for axial confinement.

lar cross sections [53]. Since the electrode surfaces no longer correspond to the hyperbolic equipotential surfaces of a quadrupole potential, the potential acquires higher-order terms. The potential can be written in cylindrical coordinates as a multipole expansion [54]:

$$\varphi(\theta, t) = [V \cos(\Omega t) - U] \sum_{n=0}^{\infty} C_n \left(\frac{r}{r_0}\right)^{2(2n+1)} \cos[2(2n+1)\theta]. \quad (2.22)$$

Due to the symmetry of the electrode arrangement, the potential has to change sign upon rotation by  $\pi/2$  around the axis of the guide. Therefore, the expansion only contains terms proportional to  $(r/r_0)^m$ , where  $m = 2, 6, 10, 14, \dots$ . The expansion coefficients  $C_n$  depend on the ratio between the radius of the electrodes  $R$  and the distance  $r_0$  between the electrode surfaces and the center axis (see Figure 2.4). A numerical solution of the boundary value problem shows that  $C_1$ , which is the coefficient of the 12-pole term, vanishes for  $R = 1.146 r_0$  [54]. This ratio is therefore often chosen in order to minimize the anharmonicity of the potential.

### Stability diagram

The radial confinement is generated by the oscillating voltage  $V \cos(\Omega t) - U$  that is applied between the diagonal pairs of electrodes (see Figure 2.4). Near the trap axis we can approximate the potential with the  $n = 0$  (quadrupole) term of Equation 2.22 and get

$$\varphi_{\text{rad}}(x, y, t) = \frac{V \cos(\Omega t) - U}{2r_{\text{eff}}^2} (x^2 - y^2), \quad (2.23)$$



where  $r_{\text{eff}} = r_0/\sqrt{2C_0}$  is the effective radial size of the trap which can be calculated numerically for a given geometry (see section 4.1.2).

The axial confinement is generated by a symmetric pair of electrodes whose surfaces are at a distance  $z_0$  from the center of the trap and which are held at a voltage  $U_{\text{ec}}$ . The shape of the resulting potential depends on the particular electrode shape. Close to the trap center, we can approximate it as a quadrupole potential and obtain

$$\varphi_{\text{ax}}(x, y, z) = \frac{\kappa U_{\text{ec}}}{2z_0^2} \left[ z^2 - \frac{1}{2}(x^2 + y^2) \right], \quad (2.24)$$

where  $\kappa$  is a geometrical factor that depends on the shape of the electrodes and can be determined using numerical simulations. Since the axial confinement is due to a static potential, the motion along  $z$  is stable provided that  $QU_{\text{ec}} > 0$ . In contrast to classical Paul traps, linear traps can confine either positive or negative ions, but not both at the same time. The axial secular frequency is

$$\omega_z = \sqrt{\frac{Q\kappa U_{\text{ec}}}{mz_0^2}}. \quad (2.25)$$

The Mathieu parameters for the radial motion are

$$q_x = -q_y = -\frac{2QV}{m\Omega^2 r_{\text{eff}}^2}, \quad (2.26)$$

$$a_x = -\frac{4QU}{m\Omega^2 r_{\text{eff}}^2} - \frac{2Q\kappa U_{\text{ec}}}{m\Omega^2 z_0^2}, \quad (2.27)$$

$$a_y = \frac{4QU}{m\Omega^2 r_{\text{eff}}^2} - \frac{2Q\kappa U_{\text{ec}}}{m\Omega^2 z_0^2}. \quad (2.28)$$

For weak confinement we can calculate the approximate secular frequencies using Equation 2.13 and Equation 2.15. We get

$$\omega_{\text{sec},x} = \sqrt{\omega_{\text{rf}}^2 - \omega_{\text{dc}}^2 - \frac{1}{2}\omega_z^2}, \quad (2.29)$$

$$\omega_{\text{sec},y} = \sqrt{\omega_{\text{rf}}^2 + \omega_{\text{dc}}^2 - \frac{1}{2}\omega_z^2}, \quad (2.30)$$

where

$$\omega_{\text{rf}}^2 = \frac{Q^2 V^2}{2m^2 \Omega^2 r_{\text{eff}}^4}, \quad (2.31)$$

and

$$\omega_{\text{dc}}^2 = \frac{QU}{mr_{\text{eff}}^2}. \quad (2.32)$$

Due to Laplace's equation, the axial confinement leads to deconfinement along  $x$  and  $y$  which lowers the corresponding secular frequencies. In contrast to that, the static offset

voltage  $U$  leads to confinement along  $x$  and deconfinement along  $y$  or vice versa. The motions along the axes are stable if the respective Mathieu parameters are inside the stable regions shown in Figure 2.2.

Figure 2.5 shows the combined stability diagrams for the radial directions in two special cases. The first is when the axial confinement can be neglected, i.e.  $\omega_z^2 \ll \omega_{\text{rf}}^2$ . In this case  $a_x = -a_y$ , and the linear Paul trap is essentially a quadrupole guide. The second case is when no offset voltage  $U$  is applied to the rod electrodes such that  $\omega_{\text{dc}}^2 = 0$ . This means that the trap potential is radially symmetric and the Mathieu parameters and secular frequencies are identical for the motions along  $x$  and  $y$ .

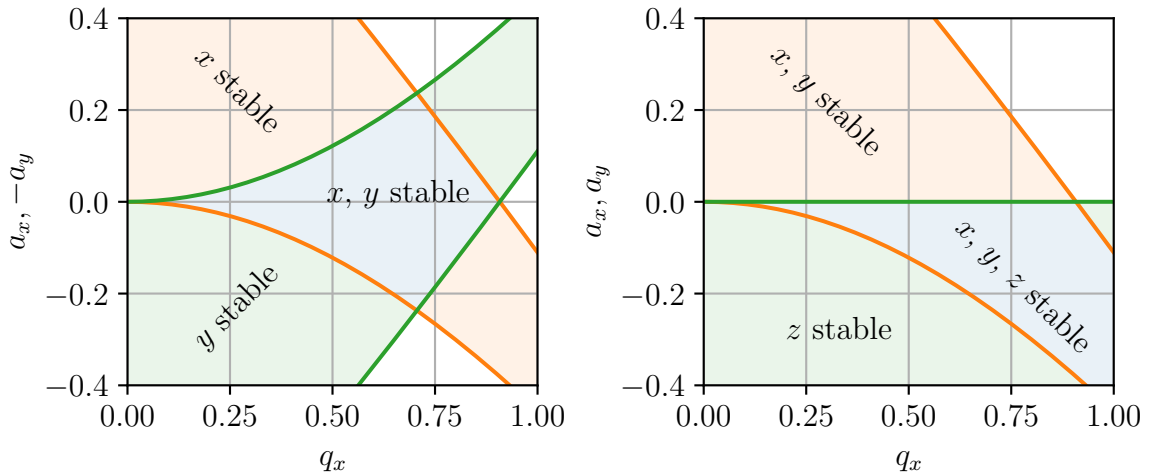


Figure 2.5: Combined stability diagrams for a linear Paul trap for negligible axial confinement strength (left) and for radially symmetric confinement (right). The regions of stable operation are colored blue. In the first case the  $a$  parameter is determined by the static offset voltage  $U$  applied between the rod electrodes. In the second case the  $a$  parameter is due to the axial confinement only. It has to be negative for stable confinement along the trap axis.

### 2.1.4 Trapping different species

The Mathieu  $a$  and  $q$  parameters are proportional to the charge-to-mass ratio  $Q/m$  of the ion species. This means that multiple ion species can be held in the same trap only if their respective stability diagrams overlap. We typically operate our trap with almost symmetrical radial confinement (right plot in Figure 2.5). The relevant species for the  $\text{He}^+$  spectroscopy experiment are  $\text{Be}^+$ ,  $\text{He}^+$ , and  $\text{He}^{2+}$ . Figure 2.6 shows the combined stability diagrams for this case. All three species can be trapped simultaneously if  $q_x \lesssim 0.2$  for  $\text{Be}^+$ . We can also see that the radial deconfinement due to the axial confinement will destabilize the motion of  $\text{Be}^+$  before that of the lighter species.

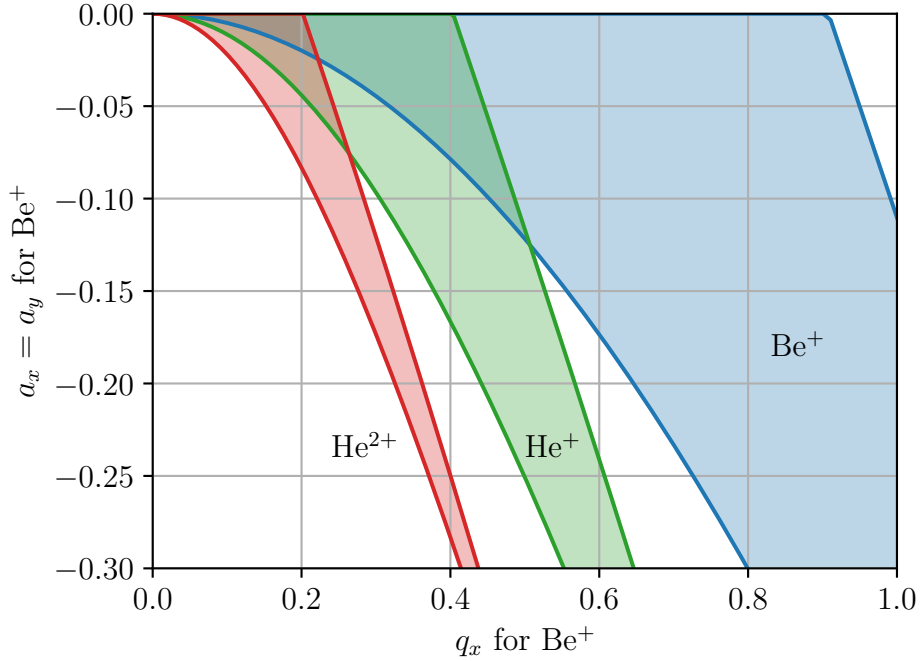


Figure 2.6: Stability diagrams for different ion species relevant for  $\text{He}^+$  spectroscopy in a radially symmetric linear Paul trap ( $U = 0$ ).

### 2.1.5 Trapping many ions

If multiple ions are stored in the same trap, their trajectories and equilibrium positions are affected by the mutual Coulomb repulsion. Since this is an all-to-all interaction, the number of terms in the equations of motion increases with the square of the number of particles, and analytical solutions are usually not possible. Instead, one has to resort to numerical molecular dynamics simulations (see section 5.5). However, we can get an intuition for the dynamics by approximating the ions as a charged fluid at zero temperature. In equilibrium the fluid takes a shape such that a test ion inside it would feel no force. This means for the combined potential [55]:

$$\Phi + Q\phi_i = \text{const.}, \quad (2.33)$$

where  $\Phi$  is the pseudopotential of the trap given by Equation 2.20, and  $\phi_i$  is the electrostatic potential created by the ions. By taking the Laplacian on both sides and using Poisson's equation, we get

$$\frac{1}{Q}\Delta\Phi = -\Delta\phi_i = \frac{\rho}{\varepsilon_0}, \quad (2.34)$$

where  $\rho$  is the charge density of the ions, and  $\varepsilon_0$  is the vacuum electric permittivity. For a linear Paul trap, we use Equations 2.29-2.31 and find

$$\rho = Qn = \frac{2\varepsilon_0 m \omega_{\text{rf}}^2}{Q} = \frac{\varepsilon_0 Q V^2}{m \Omega^2 r_{\text{eff}}^4}, \quad (2.35)$$

where  $n$  is the ion number density.

The ions arrange themselves with a uniform density that only depends on the strength of the dynamic part of the confinement in the trap. The shape of the ion cloud is determined by Equation 2.33 which requires that the potential inside the ion cloud is a quadratic function in the coordinates. This condition is fulfilled for an ellipsoid with a constant charge density [56, p. 194]. The dimensions of the ellipsoid can be calculated by equating the coefficients of the pseudopotential  $\Phi$  with those of the electric potential inside the charge distribution. However, the resulting equations are quite lengthy and in general do not have analytic solutions. We therefore do not give them here and instead refer to the literature [56, pp. 194–195, 57, 58].

## 2.2 Laser cooling

Maxwell's equations predict that light exerts pressure onto objects that reflect or absorb it. This effect was first measured by P. Lebedew in 1901 using a sensitive torsion balance [59]. The forces on macroscopic objects are usually extremely small, but lead to measurable effects on the trajectories of astronomical objects and spacecraft. The situation is different for atoms that are resonantly excited by laser light. In this case the scattering cross section is on the order of the wavelength squared [60, p. 27]. The ratio between the cross section and the mass is many orders of magnitude larger than for macroscopic objects. Light pressure forces can therefore lead to a considerable acceleration of resonantly excited atoms.

Laser cooling was first proposed in 1975 for free atoms [61] and for trapped ions [62]. We limit our discussion to Doppler cooling which is used in the experiment. The basic idea of this method is that the light pressure can be made velocity dependent by employing the Doppler shift of a laser beam in the frame of a moving atom. In the following we further assume that cooling takes place on a strong electric dipole transition whose excited state lifetime  $\tau$  is much shorter than the time scale of the atomic motion. For a trapped ion this is fulfilled if the period of the secular motion along the laser beam is much longer than  $\tau$ , and if micromotion can be neglected. In this case the populations of the atomic levels are in a steady state for each atomic velocity. If an atom absorbs a photon, it receives a momentum kick  $\Delta\mathbf{p} = \hbar\mathbf{k}$ , where  $\hbar$  is the reduced Planck constant, and  $\mathbf{k}$  is the laser wave vector. Spontaneous emission of photons also leads to momentum kicks. However, since the angular distribution of spontaneous emission is symmetric, this contribution averages to zero. The mean force therefore is [45]

$$\mathbf{F}_c(\mathbf{v}) = \hbar\mathbf{k}\Gamma\rho_{ee}(\mathbf{v}), \quad (2.36)$$

where  $\Gamma = 1/\tau$  is the spontaneous decay rate, which is equal to the  $2\pi$  times the full width at half maximum (FWHM) linewidth of the atomic transition, and

$$\rho_{ee}(\mathbf{v}) = \frac{s/2}{1 + s + \left(\frac{\Delta - \mathbf{k}\cdot\mathbf{v}}{\Gamma/2}\right)^2} \quad (2.37)$$

is the steady-state probability of finding the atom in the excited state.  $\Delta = \omega - \omega_0$  is the detuning between the laser frequency  $\omega$  and the transition frequency  $\omega_0$  in an atom at rest,  $-\mathbf{k} \cdot \mathbf{v}$  is the Doppler shift of an atom moving with velocity vector  $\mathbf{v}$ , and  $s$  is the saturation parameter which is proportional to the light intensity. For small velocities, i.e. when  $\mathbf{k} \cdot \mathbf{v} \ll \Delta$ , the force can be linearized in the velocity [45]:

$$\mathbf{F}_c(\mathbf{v}) \approx \mathbf{F}_0(1 + \boldsymbol{\kappa} \cdot \mathbf{v}), \quad (2.38)$$

where

$$\mathbf{F}_0 = \hbar \mathbf{k} \Gamma \frac{s/2}{1 + s + \left(\frac{\Delta}{\Gamma/2}\right)^2} \quad (2.39)$$

is the velocity-independent component of the radiation pressure, and

$$\boldsymbol{\kappa} = \frac{8\Delta/\Gamma^2}{1 + s + \left(\frac{\Delta}{\Gamma/2}\right)^2} \mathbf{k}. \quad (2.40)$$

We can see that for  $\Delta < 0$  (red-detuned laser) the velocity-dependent part of the force acts against the direction of motion and therefore provides damping.

So far we neglected that the force is created by discrete absorption and emission events. The resulting random momentum kicks prevent the atoms from being cooled to zero velocity. At this point it is worth discussing how to apply the concept of “temperature” to small numbers of trapped ions. The temperature of a macroscopic sample is often defined via the mean kinetic energy of the very large number of constituent particles. Since we are dealing with only a few particles, or even a single one, this ensemble average has to be replaced with a time average. Furthermore, the motions along the different trap axes can be almost completely decoupled such that the total kinetic energy is not necessarily evenly distributed among the degrees of freedom. We therefore define the temperature  $T_u$  of a particular degree of freedom  $u$  by the relation  $k_B T_u/2 = E_{\text{kin},u}$ , where  $E_{\text{kin},u}$  is the kinetic energy due to the motion in the degree of freedom, and  $k_B$  is the Boltzmann constant.

An approximate expression for the equilibrium temperature of the motion along the cooling laser direction can be derived by equating the cooling power due to the damping and the heating power due to the momentum kicks [45]. The result is

$$T = \frac{\hbar \Gamma}{8k_B} (1 + \xi) \left[ (1 + s) \frac{\Gamma/2}{|\Delta|} + \frac{|\Delta|}{\Gamma/2} \right], \quad (2.41)$$

where the factor  $\xi = 2/5$  represents the average component of the random emission recoil kicks that is directed along the cooling laser [45].

The temperature only depends on the linewidth of the cooling transition, the saturation parameter, and the cooling laser detuning. Figure 2.7 shows a plot of Equation 2.41 for laser cooling of  $\text{Be}^+$  on the  $\text{D}_2$  line ( $\Gamma = 2\pi \times 18 \text{ MHz}$ ). The minimum temperature is achieved at a detuning of

$$\Delta_{\text{min}} = -\frac{\Gamma}{2} \sqrt{1 + s}, \quad (2.42)$$

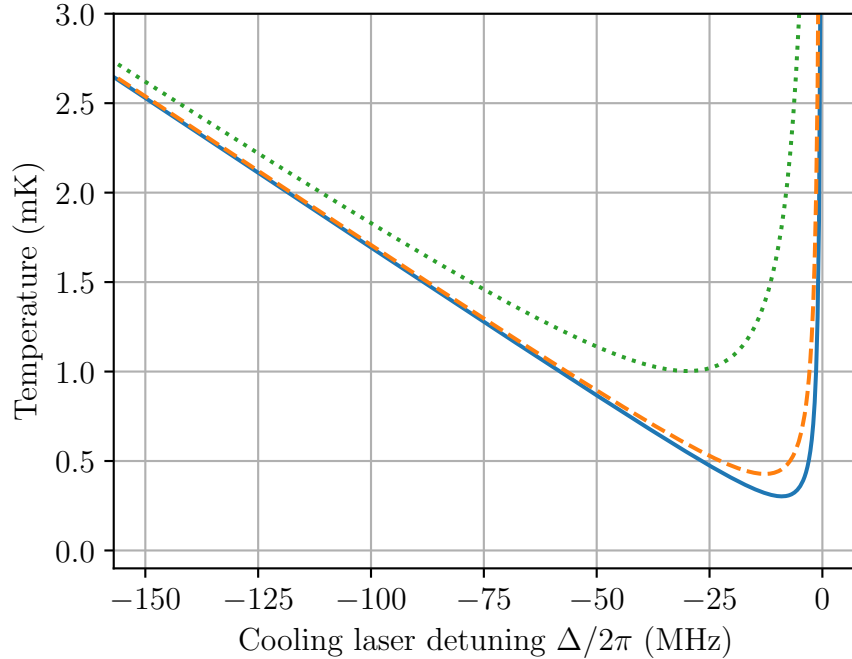


Figure 2.7: Equilibrium temperature for Doppler cooling of  $\text{Be}^+$ . The width of the  $\text{D}_2$  line is  $\Gamma = 2\pi \times 18 \text{ MHz}$  (see section 2.5). The solid blue line is plotted for the limit of small saturation ( $s \rightarrow 0$ ), the dashed orange line for  $s = 1$ , and the dotted green line for  $s = 10$ .

where it takes the value

$$T_{\min} = \frac{\hbar\Gamma}{4k_B}(1 + \xi)\sqrt{1 + s}. \quad (2.43)$$

The minimum attainable temperature is called the *Doppler limit*. For cooling of  $\text{Be}^+$  on the  $\text{D}_2$  line, it is 0.30 mK.

Three orthogonal pairs of counter-propagating laser beams are required to cool all degrees of freedom of a free atom (“optical molasses”). This is different for trapped ions since the direction of motion reverses in each half-cycle of the secular motion. A single laser beam that has a projection onto all three trap axes is therefore sufficient to laser cool single trapped ions. If the trapped ions form a three-dimensional Coulomb crystal (see below), the motion along different trap axes is strongly coupled due to the Coulomb interaction between the ions. In this case cooling is efficient even when the laser beam is aligned parallel to one of the axes. In order to avoid the detrimental effects of micromotion (see subsection 2.1.3), large ion crystals in linear Paul traps are usually laser cooled using a single beam that propagates along the trap axis.

## 2.3 Ion Coulomb crystals

The structural properties of an ensemble of trapped ions depend on the ratio between the Coulomb interaction energy between neighboring particles and the mean kinetic energy of the particles. This is characterized by the *Coulomb correlation parameter* [47, p. 263]

$$\Gamma_c = \frac{1}{4\pi\epsilon_0} \frac{Q^2}{a_{\text{WS}}} \frac{1}{k_B T}, \quad (2.44)$$

where  $a_{\text{WS}}$  is the Wigner-Seitz radius,  $k_B$  is the Boltzmann constant, and  $T$  is the ion temperature.<sup>1</sup> The Wigner-Seitz radius is the radius of a sphere whose volume is equal to the average volume per ion, such that

$$\frac{4}{3}\pi a_{\text{WS}}^3 = \frac{1}{n}, \quad (2.45)$$

where  $n$  is the ion number density.

In an infinitely large system of charges, there is a phase transition from gaseous to liquid for  $\Gamma_c \geq 2$ , and the system crystallizes into a regular lattice at  $\Gamma_c \approx 174$  [63]. For a typical value of  $a_{\text{WS}} \approx 10 \mu\text{m}$ , this corresponds to a temperature of around 10 mK. The behavior of finite systems is different due to surface effects. Molecular dynamics simulations show that this lowers the crystallization point [64]. For example, the phase transition in a spherical cloud of 100 ions is predicted to occur at a three times lower temperature than in an infinite system [64]. Figure 2.8 shows examples for  $\text{Be}^+$  ion crystals of different sizes that were produced in our trap.

Large ion crystals, such as the one shown in Figure 2.8 (d), typically reach temperatures of a few mK under laser cooling. This temperature is significantly higher than the Doppler limit which is due to collisions between the trapped ions and rest gas molecules. Molecular dynamics simulations show that under these conditions the ions are not completely localized, but can diffuse between crystal sites on ms time scales [64–66]. This motion is not resolved in our ion images since we typically use camera exposure times between 200 ms and a few seconds. The images should therefore be interpreted as probability density plots, rather than as images of individual particles [65].

## 2.4 Sympathetic cooling and mixed ion crystals

Laser cooling relies on the ability to resonantly scatter a large number of photons from an atom or molecule (see section 2.2). However, many interesting ionic species do not possess suitable transitions. In general laser cooling of molecules is challenging since they have a large number of rotational and vibrational states, and closed transitions usually do not exist [67]. In atomic ions very short transition wavelengths are often problematic. This is the case in our  $\text{He}^+$  ions where the first electric dipole transition from the ground state is

<sup>1</sup>In a large ensemble of trapped ions, the strong coupling usually leads to good thermalization of the different degrees of freedom. It is therefore possible to uniquely assign the ensemble a single temperature.

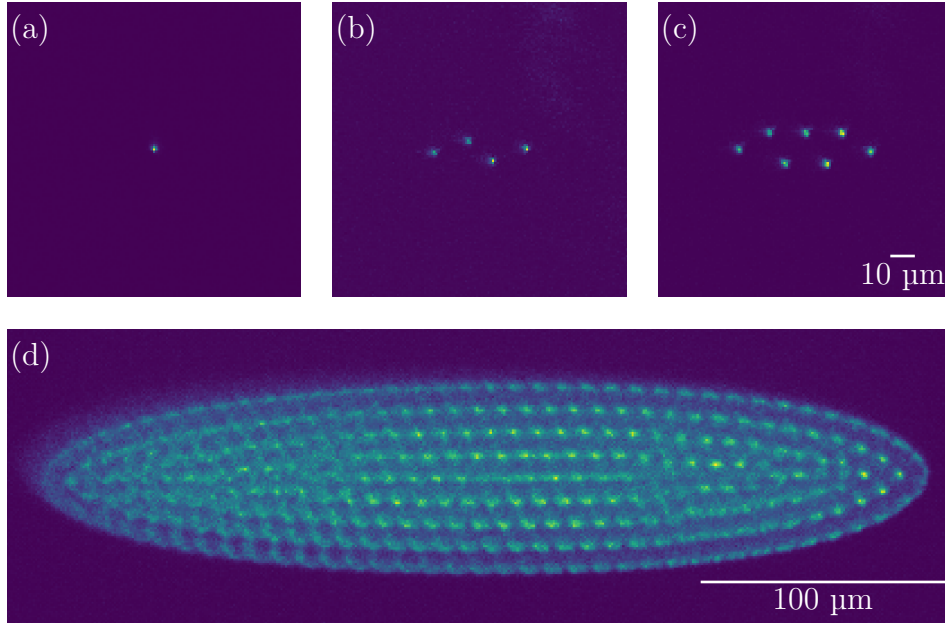


Figure 2.8: Fluorescence images of  $\text{Be}^+$  ion crystals in our trap. The crystals consist of (a) one, (b) four, (c) seven, and (d) around 2000 ions. The ion crystal in (d) is a three-dimensional ellipsoid, and only one “slice” of ions close to the center axis of the crystal is in the focus of the imaging system.

the 1S-2P transition which has a wavelength of 30.4 nm. There is currently no technology that can produce radiation at this wavelength with a linewidth that is narrow enough for laser cooling. Other examples for atomic ions that cannot be laser cooled are  $^{27}\text{Al}^+$ , which is used in some of the best optical atomic clocks [37], and highly charged ions [68].

Sympathetic cooling is a powerful and universal scheme for overcoming these limitations. The basic idea is to mix the ions with another ion species that can be laser cooled. The motion of different ions that are stored in the same trap is strongly coupled due to the mutual Coulomb interaction. The ions therefore quickly thermalize, and cooling one species also indirectly cools all other ones. If a sufficiently low temperature is reached, the ions form a Coulomb crystal.

Figure 2.9 shows an example from our ion trap. The fluorescence image contains eight laser cooled  $\text{Be}^+$  ions that form a regular “zigzag” structure. However, one ion is “missing” from the position marked by the white arrow. This is the location of a sympathetically cooled “dark” ion of a different species. Most likely it is a  $\text{BeH}^+$  ion that can be formed in an exothermic chemical reaction between laser cooled  $\text{Be}^+$  ions and  $\text{H}_2$  molecules from the rest gas in our trap vacuum chamber [69].

In a linear Paul trap, the radial confinement is stronger for an ion with a larger charge-to-mass ratio (see section 2.1.3). Large mixed crystals of equally charged ions therefore separate into a “core” consisting of the lightest species and one or more “shells” of the



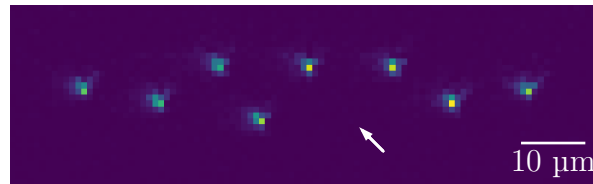


Figure 2.9: Fluorescence image of a mixed ion crystal consisting of eight laser cooled  $\text{Be}^+$  ions and one dark ion (most likely  $\text{BeH}^+$ ).

heavier ions (see Figure 2.10). The separation between the ions increases for larger differences in charge-to-mass ratios. This reduces the motional coupling between the species and therefore limits the sympathetic cooling efficiency [66]. For sympathetic cooling of the very light  $\text{He}^+$  ions, we therefore use  $^9\text{Be}^+$  which is the lightest ion species that can be conveniently laser cooled.

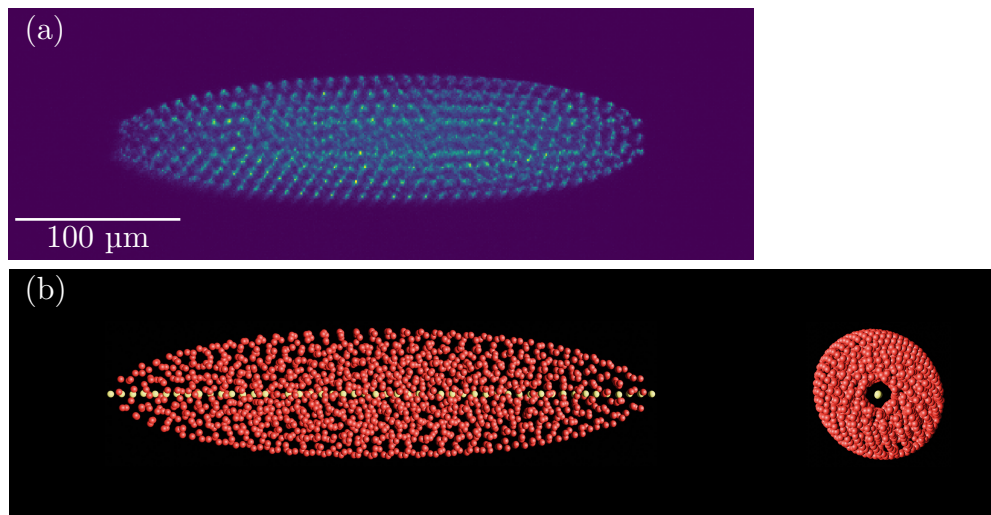


Figure 2.10: (a) Fluorescence image of a mixed  $\text{Be}^+/\text{He}^+$  ion crystal. Only the laser cooled  $\text{Be}^+$  ions are visible. The sympathetically cooled  $\text{He}^+$  ions experience stronger radial confinement and form a dark “core” in the center of the ion crystal. (b) Coulomb crystal structure obtained by a molecular dynamics simulation (see section 5.5). The simulation contains 1450  $\text{Be}^+$  ions (red spheres) and 50  $\text{He}^+$  ions (yellow spheres). Radial view (left) and axial view (right) of the same crystal.

## 2.5 The $\text{Be}^+$ ion

$\text{Be}^+$  is an alkali-like ion with a filled 1s shell and a single valence electron in the 2s subshell. Like other alkalis it features a strong electric dipole transition between the ground state

and the first excited state that is split into a fine structure doublet. The fine structure arises due to the interaction between the intrinsic magnetic moment of the electron and its orbital magnetic moment in the excited state. These characteristic transitions were first observed in the emission spectrum of sodium and are called the D<sub>1</sub> and D<sub>2</sub> lines. In Be<sup>+</sup> the wavelengths of the D<sub>1</sub> (2s <sup>2</sup>S<sub>1/2</sub> → 2p <sup>2</sup>P<sub>1/2</sub>) and D<sub>2</sub> (2s <sup>2</sup>S<sub>1/2</sub> → 2p <sup>2</sup>P<sub>3/2</sub>) transitions are 313.2 nm and 313.1 nm, respectively [70]. In this work we use the D<sub>2</sub> line for laser cooling and fluorescence detection since it can be driven as a cycling transition (see below).

### Transition linewidth

The lifetime of the 2p states was measured by two different groups in the 1960s which yielded somewhat discrepant results of 8.1(4) ns [71] and 9.5(2) ns [72].<sup>2</sup> Z.-C. Yan, M. Tambasco, and G. Drake have performed precise calculations of the oscillator strengths in lithium and lithiumlike ions [74]. For the 2p <sup>2</sup>P<sub>3/2</sub> state in Be<sup>+</sup>, they obtain a lifetime of 8.8519(8) ns, resulting in an FWHM linewidth of 17.9797(16) MHz. For lithium, where accurate lifetime measurements are available, the calculations agree with the measurements to a few parts in 10<sup>4</sup>. We therefore believe that the calculation for Be<sup>+</sup> is more reliable than the measurements and use a linewidth of 18 MHz in this thesis.

### Hyperfine structure

The only naturally occurring isotope <sup>9</sup>Be has a nuclear spin quantum number  $I = 3/2$  and therefore has hyperfine structure. The hyperfine energy shift for a state with electronic angular momentum quantum number  $J$  and total atomic angular momentum quantum number  $F$  is given by [75, p. 26]

$$\Delta E_{\text{hfs}} = \frac{1}{2}AK + B \frac{\frac{3}{2}K(K+1) - 2I(I+1)J(J+1)}{2I(2I-1)2J(2J-1)}, \quad (2.46)$$

where  $K = F(F+1) - I(I+1) - J(J+1)$ , and  $A$  and  $B$  are the magnetic dipole and electric quadrupole hyperfine constants, respectively. Only nuclei with  $I > 1/2$  and electronic states with  $J > 1/2$  can have electric quadrupole moments. Therefore,  $B$  is zero unless both  $I$  and  $J$  are greater than  $1/2$  [75, pp. 26–27].

The ground state hyperfine constant of <sup>9</sup>Be<sup>+</sup> has been accurately measured using radio frequency spectroscopy in Penning traps [76, 77]. The resulting value is  $A_{S_{1/2}}/h = -625\,008\,837.044(12)$  Hz, where  $h$  is the Planck constant. The hyperfine splitting of the 2p <sup>2</sup>P<sub>3/2</sub> state is smaller than the inverse lifetime of the state and is therefore unresolved in optical spectroscopy. Values for the magnetic dipole and electric quadrupole hyperfine constants have been calculated from measured values of the magnetic dipole moment and electric quadrupole moment of the <sup>9</sup>Be nucleus [78]. The values are  $A_{P_{3/2}}/h = -1.026$  MHz and  $B_{P_{3/2}}/h = -2.299\,40$  MHz. Figure 2.11 shows the resulting level scheme of the D<sub>2</sub> line.

<sup>2</sup>[72] is a reanalysis of the data from [73] in which the uncertainty estimate was increased by a factor of 10.

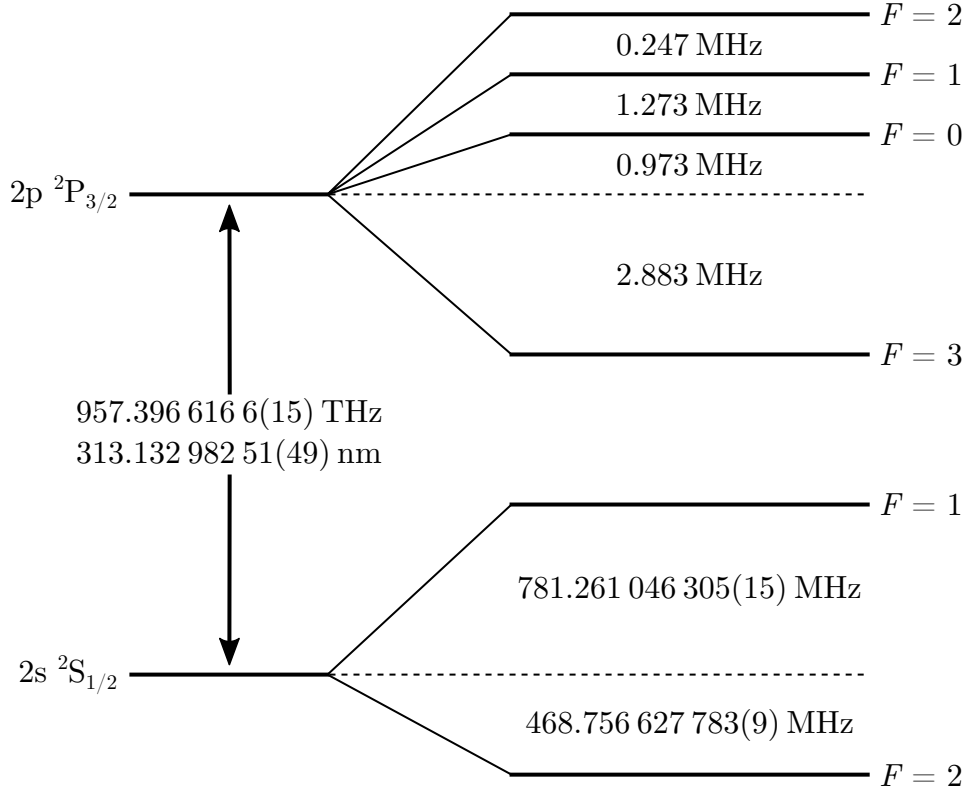


Figure 2.11: Level scheme of the  $^9\text{Be}^+$  D<sub>2</sub> line. The hyperfine centroid frequency is taken from [70]. The hyperfine splittings are calculated with Equation 2.46 using measured [76, 77] and calculated [78] hyperfine constants for the ground state and excited state, respectively. In the excited state the electric quadrupole hyperfine constant has a larger magnitude than the magnetic dipole hyperfine constant. This leads to a somewhat unusual order of the hyperfine levels.

### Cycling transition

Laser cooling and fluorescence detection require scattering many photons from each ion. For  $^9\text{Be}^+$  this can be achieved by driving the D<sub>2</sub> transition with circularly polarized light. If for example  $\sigma^-$  polarization is used, the selection rule for photon absorption is  $\Delta m_F = -1$ , while spontaneous decay can occur with  $\Delta m_F = 0, \pm 1$ . The ion is therefore rapidly pumped into the transition between the “stretched states”  $S_{1/2}(F = 2, m_F = -2)$  and  $P_{3/2}(F = 3, m_F = -3)$  which is indicated by the solid black arrow in Figure 2.12. Since the upper stretched state can only decay into the lower stretched state, this effectively forms a closed two-level system that continuously scatters photons. In practice imperfect laser polarization and misalignment between the magnetic field that defines the quantization axis and the laser beam allows the excitation of states other than the upper stretched state. From these the ion can decay into the  $S_{1/2}(F = 1)$  manifold. The cooling laser which is tuned close to the  $S_{1/2}(F = 2) \rightarrow P_{3/2}(F = 3)$  transition is off-resonant from the

$S_{1/2}(F = 1) \rightarrow P_{3/2}$  transition by roughly the ground state hyperfine splitting of 1.25 GHz. Therefore, the photon scattering rate from the  $S_{1/2}(F = 1)$  ground state is low and the state is called a *dark state*. Optical pumping into the dark state is therefore prevented by adding a second “repumper” laser beam that is resonant with the  $S_{1/2}(F = 1) \rightarrow P_{3/2}$  transition.

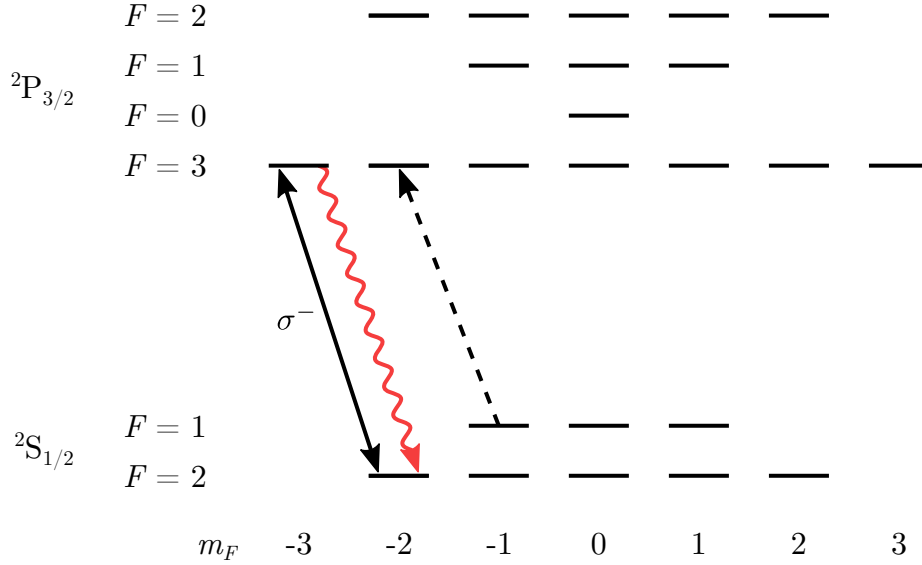


Figure 2.12: Driving the  $S_{1/2}(F = 2) \rightarrow P_{3/2}(F = 3)$  cycling transition with a  $\sigma^-$  polarized laser beam (black solid arrow). The upper state of the cycling transition can only decay into the lower one (red wavy arrow), forming an effective two-level system. Imperfections of the laser polarization or magnetic field alignment can lead to optical pumping of the ion into the  $S_{1/2}(F = 1)$  dark state. This is prevented by a “repumper” beam that is resonant with the  $S_{1/2}(F = 1) \rightarrow P_{3/2}$  transition (black dashed arrow).

# Chapter 3

## Two-photon direct frequency comb spectroscopy on trapped ions

In this section we first review the theory of driving two-photon transitions with frequency combs. Working with trapped particles leads to peculiar features in the excitation dynamics. We briefly summarize the main points that are relevant for our application. Finally, we analyze different potential excitation geometries that could be used for driving the 1S-2S transition in  $\text{He}^+$  and motivate our choice.

### 3.1 Optical frequency combs

An optical frequency comb is a laser which emits a regular train of phase-coherent pulses. Mathematically this means that the electric field of the laser output can be written as

$$E(t) = \frac{1}{2}A(t)e^{-i\omega_c t} + \text{c.c.}, \quad (3.1)$$

where  $\omega_c$  is the carrier frequency, and  $A(t)$  is the pulse envelope function. The pulse repetition rate  $\omega_{\text{rep}} = 2\pi/T$  is defined by the condition  $A(t) = A(t - T)$ . The shape of such a pulse train is illustrated in Figure 3.1 (a).

Since  $A(t)$  is periodic in time, it can be written as a Fourier series [79]:

$$A(t) = \sum_{m=-\infty}^{\infty} \tilde{A}_m e^{-im\omega_{\text{rep}} t}, \quad (3.2)$$

where the Fourier coefficients are given by

$$\tilde{A}_m = \frac{1}{T} \int_{-T/2}^{T/2} A(t) e^{im\omega_{\text{rep}} t} dt. \quad (3.3)$$

By inserting Equation 3.2 into Equation 3.1, we obtain

$$E(t) = \frac{1}{2} \sum_{m=-\infty}^{\infty} \tilde{A}_m e^{-i(m\omega_{\text{rep}} + \omega_c)t} + \text{c.c.}. \quad (3.4)$$

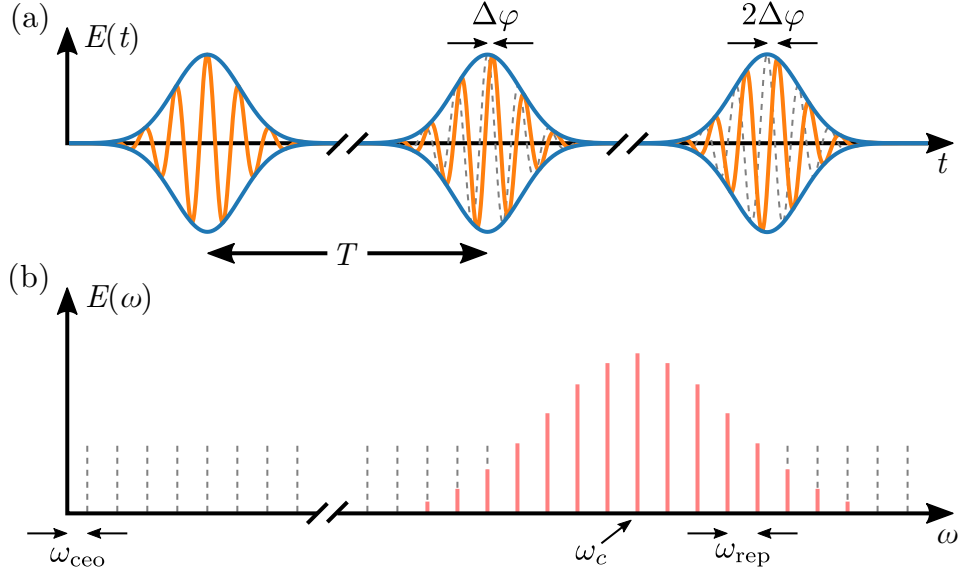


Figure 3.1: Output of an optical frequency comb in the time and frequency domains. (a) The frequency comb pulses (orange lines) can be described as a monochromatic carrier wave that is modulated by an envelope function (blue lines). The shape of the first pulse is repeated in the second and third pulse as a dashed line in order to illustrate the pulse-to-pulse phase slippage  $\Delta\varphi$ . (b) An infinitely long pulse train results in a comb of narrow spectral lines. The phase slippage leads to an offset frequency  $\omega_{\text{ceo}} = \Delta\varphi/T$ .

The spectrum acquires a comb of sidebands around  $\omega_c$  which are spaced by integer multiples of  $\omega_{\text{rep}}$  (see Figure 3.1 (b)). The frequencies of the resulting *comb modes* are given by

$$\omega_m = m\omega_{\text{rep}} + \omega_c. \quad (3.5)$$

Since  $\omega_c$  is in general not an integer multiple of  $\omega_{\text{rep}}$ , the comb structure “misses” the origin if we extrapolate it towards low frequencies. This offset frequency can be determined by re-numbering Equation 3.5:

$$\omega_n = n\omega_{\text{rep}} + \omega_{\text{ceo}}, \quad (3.6)$$

where  $|\omega_{\text{ceo}}| < \omega_{\text{rep}}/2$ . It can be shown that this offset is related to the carrier-envelope phase slippage  $\Delta\varphi$  by  $\omega_{\text{ceo}} = \Delta\varphi/T$  [79]. It is therefore called the *carrier-envelope offset frequency*. While  $\omega_{\text{rep}}$  can be easily measured by sending part of the pulse train onto a photodetector, determining  $\omega_{\text{ceo}}$  is more challenging. The standard technique is to use an  $f - 2f$  interferometer. First, the frequency comb spectrum is broadened, for example by nonlinear interactions in a photonic crystal fiber, until it covers more than one octave. Then there exists a mode number  $n$  such that both  $\omega_n$  and  $\omega_{2n}$  fall within the spectrum of the frequency comb. The spectral components around  $\omega_n$  are then frequency doubled in a nonlinear crystal and are overlapped with the spectral components around  $\omega_{2n}$  on a photodetector. This results in a beat note at [80]

$$2(n\omega_{\text{rep}} + \omega_{\text{ceo}}) - (2n\omega_{\text{rep}} + \omega_{\text{ceo}}) = \omega_{\text{ceo}}. \quad (3.7)$$

Both  $\omega_{\text{rep}}$  and  $\omega_{\text{ceo}}$  are radio frequencies and can therefore be electronically counted and/or controlled with feedback loops acting on the laser. Equation 3.6 then provides a direct link from the radio frequency domain to the optical frequencies of the comb modes [81].

### Elastic tape picture

As a consequence of Equation 3.6, the frequencies of the different comb modes are strongly correlated with each other. Any perturbation of the laser oscillator, whether intentionally applied in order to control the parameters, or caused by noise, has some effect on  $\omega_{\text{rep}}$  and  $\omega_{\text{ceo}}$ . The resulting mode frequencies  $\omega_n$  can be visualized as an “elastic tape” containing equidistant spectral lines that stretches or contracts around a fixed point  $\omega_{\text{fix}}$  on the frequency scale [82]. The position of the fixed point depends on the particular type of perturbation and does not have to lie within the output spectrum of the frequency comb. Fully stabilizing the modes of a frequency comb therefore requires two actuators that affect  $\omega_{\text{rep}}$  and  $\omega_{\text{ceo}}$  in a different way.

One important question is how well the output of a real frequency comb follows the elastic tape picture. We can quantify this by writing [83]

$$\omega_n(t) = n\omega_{\text{rep}}(t) + \omega_{\text{ceo}}(t) + \delta\omega(n, t), \quad (3.8)$$

where  $\delta\omega(n, t)$  are fluctuations of the mode frequencies that do not comply with the elastic tape picture. Frequency combs are used to measure the frequency ratios between different optical frequency standards. In this context extremely small values of  $\delta\omega(n, t)/\omega_n(t)$  on the level of a few parts in  $10^{21}$  have been demonstrated for averaging times of around one day [84–86]. The deviations were attributed to differential drifts of the optical path lengths between the different lasers used in the comparisons. The fundamental limit due to the laser oscillators themselves could therefore be even lower. One explanation for this astonishing level of accuracy is that any deviation from the perfectly equidistant comb mode spacing would lead to a rapid “dissolution” of the pulse circulating inside the laser oscillator. This is prevented by the mode-locking mechanism that forms the laser pulses [79].

In our work we use frequency combs based on passively mode-locked laser oscillators. In such systems the pulsed output is being generated by a fast nonlinear mechanism, such as the Kerr effect, that tightly couples all modes of the frequency comb [82]. It is therefore reasonable to assume that  $\delta\omega(n, t)$  is also very small on much shorter time scales. This is supported by a number of experimental measurements of the correlations between the noise of different comb modes in which good agreement with the elastic tape picture was observed [83, 87–89].

## 3.2 Two-photon transitions

In our experiment we want to drive transitions between the 1S and 2S states in  $\text{He}^+$ . In the electric dipole approximation, the transition strength between the atomic states  $|g\rangle$

and  $|e\rangle$  is governed by the dipole matrix element [60, p. 50]

$$\mathbf{d}_{eg} = \langle e|\hat{\mathbf{d}}|g\rangle = \langle e| -e\hat{\mathbf{r}}|g\rangle, \quad (3.9)$$

where  $e$  is the elementary charge, and  $\hat{\mathbf{r}}$  is the atomic electron position operator. Since the wave functions of both S states have the same even parity, we can immediately see that the dipole matrix element for the 1S-2S transition is zero. We will therefore have to resort to a different mechanism for exciting our transition.

Already in 1931, M. Göppert-Mayer was able to show theoretically that atoms can be excited by the simultaneous absorption of a pair of photons whose frequencies add up to the transition frequency [90]. We start our analysis by considering the interaction between an atom and one or more laser fields. For simplicity we assume that all lasers have the same linear polarization in  $z$  direction.<sup>1</sup> The Hamiltonian for this problem is

$$\hat{H} = \hat{H}_0 + \hat{V}(t), \quad (3.10)$$

where  $\hat{H}_0$  is the atomic Hamiltonian, and

$$\hat{V}(t) = e\hat{z}E(\mathbf{r}, t). \quad (3.11)$$

The total electric field is

$$E(\mathbf{r}, t) = \frac{1}{2} \sum_m \left[ E_m(\mathbf{r}, t)e^{-i\omega_m t} + E_m^*(\mathbf{r}, t)e^{i\omega_m t} \right], \quad (3.12)$$

where  $E_m(\mathbf{r}, t)$  and  $\omega_m$  are the complex amplitude and the frequency of the  $m$ th laser field, respectively. The level scheme of our atom is shown in Figure 3.2. We assume that the atom has two energy levels  $|g\rangle$  and  $|e\rangle$  that have the same parity such that dipole transition between them are not allowed. Furthermore, it has intermediate states  $\{|n\rangle\}$  of opposite parity that are connected to  $|g\rangle$  and  $|e\rangle$  via dipole transitions.

We can write the state of the atom at time  $t$  as

$$|\alpha(t)\rangle = \sum_k c_k(t)e^{-i\tilde{E}_k t/\hbar}|k\rangle, \quad (3.13)$$

where  $|k\rangle$  are the eigenstates of the unperturbed Hamiltonian  $\hat{H}_0$  with energy eigenvalues  $\tilde{E}_k$ , and  $\hbar = h/(2\pi)$  is the reduced Planck constant. Inserting  $|\alpha(t)\rangle$  into the Schrödinger equation yields differential equations for the coefficients [92, p. 319]:

$$i\hbar \frac{d}{dt} c_k(t) = \sum_l V_{kl}(t)e^{i\omega_{kl}t} c_l(t), \quad (3.14)$$

---

<sup>1</sup>High harmonic generation produces linearly polarized light. Furthermore, it turns out that the dynamics of two-photon transitions between S states remain unchanged under rotations of the linear polarization direction [91].



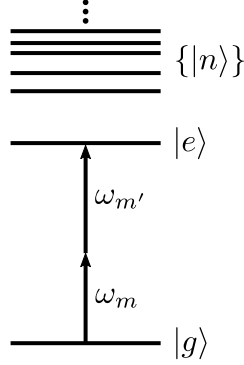


Figure 3.2: Level scheme of the two-photon absorption process. Pairs of fields at frequencies  $\omega_m$  and  $\omega_{m'}$  drive transitions between the ground state  $|g\rangle$  and excited state  $|e\rangle$ . The intermediate states  $|n\rangle$  are connected with  $|g\rangle$  and  $|e\rangle$  via one-photon transitions, but all laser fields are far off-resonant from the transitions.

where  $\omega_{kl} = (\tilde{E}_k - \tilde{E}_l)/\hbar$ , and  $V_{kl}(t) = \langle k|\hat{V}(t)|l\rangle$ . The matrix elements of the operator are

$$V_{kl}(t) = \frac{e}{2} \langle k|\hat{z}|l\rangle \sum_m \left[ E_m(\mathbf{r}, t)e^{-i\omega_m t} + E_m^*(\mathbf{r}, t)e^{i\omega_m t} \right]. \quad (3.15)$$

As discussed above the dipole matrix elements between states of equal parity vanish:

$$\langle g|\hat{z}|e\rangle = \langle n_1|\hat{z}|n_2\rangle = 0, \quad (3.16)$$

where  $|n_1\rangle, |n_2\rangle \in \{|n\rangle\}$ .

We can therefore simplify the differential equations for the coefficients of the states  $|g\rangle$ ,  $|e\rangle$ , and the intermediate states  $\{|n\rangle\}$ :

$$\dot{c}_g(t) = -\frac{ie}{2\hbar} \sum_{\{|n\rangle\}} \sum_m \langle g|\hat{z}|n\rangle \left[ E_m(\mathbf{r}, t)e^{i(\omega_{gn}-\omega_m)t} + E_m^*(\mathbf{r}, t)e^{i(\omega_{gn}+\omega_m)t} \right] c_n(t), \quad (3.17)$$

$$\dot{c}_e(t) = -\frac{ie}{2\hbar} \sum_{\{|n\rangle\}} \sum_m \langle e|\hat{z}|n\rangle \left[ E_m(\mathbf{r}, t)e^{i(\omega_{en}-\omega_m)t} + E_m^*(\mathbf{r}, t)e^{i(\omega_{en}+\omega_m)t} \right] c_n(t), \quad (3.18)$$

$$\begin{aligned} \dot{c}_n(t) = -\frac{ie}{2\hbar} \sum_m \left\{ \langle n|\hat{z}|g\rangle \left[ E_m(\mathbf{r}, t)e^{i(\omega_{ng}-\omega_m)t} + E_m^*(\mathbf{r}, t)e^{i(\omega_{ng}+\omega_m)t} \right] c_g(t) \right. \\ \left. + \langle n|\hat{z}|e\rangle \left[ E_m(\mathbf{r}, t)e^{i(\omega_{ne}-\omega_m)t} + E_m^*(\mathbf{r}, t)e^{i(\omega_{ne}+\omega_m)t} \right] c_e(t) \right\}. \end{aligned} \quad (3.19)$$

If we assume that the atom starts out in the ground state such that  $c_n(t)$  vanishes as  $t \rightarrow -\infty$ , we can write a formal solution of Equation 3.19 as

$$c_n(t) = \int_{-\infty}^t \dot{c}_n(t') dt'. \quad (3.20)$$

The expression contains integrals of the form

$$\int_{-\infty}^t E_m(\mathbf{r}, t') e^{i\Delta t'} c_x(t') dt', \quad (3.21)$$

where  $x = \{g, e\}$ , and  $\Delta = \omega_{nx} \pm \omega_m$ . Since all laser fields are far off-resonant from dipole-allowed transitions,  $e^{i\Delta t}$  oscillates at optical frequencies. We assume that the time evolution of  $c_g(t)$  and  $c_e(t)$ , and variations of the field amplitudes  $E_m(\mathbf{r}, t)$  are slow compared to the time scale set by  $\Delta^{-1}$ . This allows us to make the zeroth-order Markov approximation [93] which means that we replace  $E_m(\mathbf{r}, t')c_x(t') \approx E_m(\mathbf{r}, t)c_x(t)$  in the integral in Equation 3.21. We obtain

$$\int_{-\infty}^t E_m(\mathbf{r}, t')e^{i\Delta t'}c_x(t')dt' \approx \frac{E_m(\mathbf{r}, t)e^{i\Delta t}}{i\Delta}c_x(t). \quad (3.22)$$

With this approximation Equation 3.19 can be solved:

$$c_n(t) \approx -\frac{e}{2\hbar} \sum_m \left\{ \langle n|\hat{z}|g\rangle \left[ \frac{E_m(\mathbf{r}, t)e^{i(\omega_{ng}-\omega_m)t}}{\omega_{ng}-\omega_m} + \frac{E_m^*(\mathbf{r}, t)e^{i(\omega_{ng}+\omega_m)t}}{\omega_{ng}+\omega_m} \right] c_g(t) \right. \\ \left. + \langle n|\hat{z}|e\rangle \left[ \frac{E_m(\mathbf{r}, t)e^{i(\omega_{ne}-\omega_m)t}}{\omega_{ne}-\omega_m} + \frac{E_m^*(\mathbf{r}, t)e^{i(\omega_{ne}+\omega_m)t}}{\omega_{ne}+\omega_m} \right] c_e(t) \right\}. \quad (3.23)$$

We can now substitute this expression for  $c_n(t)$  into Equation 3.17 and Equation 3.18 and apply the rotating wave approximation. This means that we neglect all terms that oscillate at optical frequencies. We obtain

$$\dot{c}_g(t) \approx \frac{ie^2}{4\hbar^2} \sum_{\{n\}} \sum_{m, m'} \left\{ \right. \\ \left. |\langle g|\hat{z}|n\rangle|^2 \left[ \frac{E_m(\mathbf{r}, t)E_{m'}^*(\mathbf{r}, t)e^{-i(\omega_m-\omega_{m'})t}}{\omega_{ng}+\omega_{m'}} + \frac{E_m^*(\mathbf{r}, t)E_{m'}(\mathbf{r}, t)e^{i(\omega_m-\omega_{m'})t}}{\omega_{ng}-\omega_{m'}} \right] c_g(t) \right. \\ \left. + \langle g|\hat{z}|n\rangle \langle n|\hat{z}|e\rangle \frac{E_m^*(\mathbf{r}, t)E_{m'}^*(\mathbf{r}, t)e^{-i[\omega_{eg}-(\omega_m+\omega_{m'})]t}}{\omega_{ne}+\omega_{m'}} c_e(t) \right\}, \quad (3.24)$$

and

$$\dot{c}_e(t) \approx \frac{ie^2}{4\hbar^2} \sum_{\{n\}} \sum_{m, m'} \left\{ \right. \\ \left. |\langle e|\hat{z}|n\rangle|^2 \left[ \frac{E_m(\mathbf{r}, t)E_{m'}^*(\mathbf{r}, t)e^{-i(\omega_m-\omega_{m'})t}}{\omega_{ne}+\omega_{m'}} + \frac{E_m^*(\mathbf{r}, t)E_{m'}(\mathbf{r}, t)e^{i(\omega_m-\omega_{m'})t}}{\omega_{ne}-\omega_{m'}} \right] c_e(t) \right. \\ \left. + \langle e|\hat{z}|n\rangle \langle n|\hat{z}|g\rangle \frac{E_m(\mathbf{r}, t)E_{m'}(\mathbf{r}, t)e^{i[\omega_{eg}-(\omega_m+\omega_{m'})]t}}{\omega_{ng}-\omega_m} c_g(t) \right\}. \quad (3.25)$$

A comparison of Equation 3.24 and Equation 3.25 with Equation 3.14 shows that we have obtained an effective two-level system where the interaction is given by the two-photon operator

$$\hat{V}_{2p}(t) = \begin{pmatrix} \hbar\Delta\omega_g(t) & V_{ge}(t) \\ V_{eg}(t) & \hbar\Delta\omega_e(t) \end{pmatrix}, \quad (3.26)$$

where

$$\Delta\omega_g = - \left( \frac{e}{2\hbar} \right)^2 \sum_{\{n\}} \sum_{m,m'} |\langle g|\hat{z}|n\rangle|^2 \left[ \frac{E_m(\mathbf{r}, t)E_{m'}^*(\mathbf{r}, t)e^{-i(\omega_m - \omega_{m'})t}}{\omega_{ng} + \omega_{m'}} + \frac{E_m^*(\mathbf{r}, t)E_{m'}(\mathbf{r}, t)e^{i(\omega_m - \omega_{m'})t}}{\omega_{ng} - \omega_{m'}} \right], \quad (3.27)$$

$$\Delta\omega_e = - \left( \frac{e}{2\hbar} \right)^2 \sum_{\{n\}} \sum_{m,m'} |\langle e|\hat{z}|n\rangle|^2 \left[ \frac{E_m(\mathbf{r}, t)E_{m'}^*(\mathbf{r}, t)e^{-i(\omega_m - \omega_{m'})t}}{\omega_{ne} + \omega_{m'}} + \frac{E_m^*(\mathbf{r}, t)E_{m'}(\mathbf{r}, t)e^{i(\omega_m - \omega_{m'})t}}{\omega_{ne} - \omega_{m'}} \right], \quad (3.28)$$

$$\frac{V_{ge}}{\hbar} = - \left( \frac{e}{2\hbar} \right)^2 \sum_{\{n\}} \sum_{m,m'} \langle g|\hat{z}|n\rangle \langle n|\hat{z}|e\rangle \frac{E_m^*(\mathbf{r}, t)E_{m'}(\mathbf{r}, t)e^{i(\omega_m + \omega_{m'})t}}{\omega_{ne} + \omega_{m'}}, \quad (3.29)$$

$$\frac{V_{eg}}{\hbar} = - \left( \frac{e}{2\hbar} \right)^2 \sum_{\{n\}} \sum_{m,m'} \langle e|\hat{z}|n\rangle \langle n|\hat{z}|g\rangle \frac{E_m(\mathbf{r}, t)E_{m'}(\mathbf{r}, t)e^{-i(\omega_m + \omega_{m'})t}}{\omega_{ng} - \omega_{m'}}. \quad (3.30)$$

The diagonal elements  $\Delta\omega_g$  and  $\Delta\omega_e$  change the effective energy levels of the atom, but do not lead to transitions between the states. This effect is called the *ac Stark shift*. Transitions between the states are mediated by the off-diagonal elements.

Figure 3.3 (a) shows an intuitive picture for the two-photon absorption process. The first photon at frequency  $\omega_m$  off-resonantly excites the atom to an intermediate state  $|n\rangle$ . From there the second photon at frequency  $\omega_{m'}$  completes the transition to the final state  $|e\rangle$ . From this picture it is clear that two-photon transitions connect two states of the same parity such as our 1S and 2S states. Another interpretation of the same process is shown in Figure 3.3 (b). The presence of one of the light fields perturbs the ground state  $|g\rangle$  into a virtual intermediate state  $|\delta g\rangle$ . From there the other field can drive the transition to the final state  $|e\rangle$  [91]. The *ac Stark shifts* can be interpreted as transitions where the initial and final states are the same.

### 3.2.1 Frequency comb excitation

We are now ready to analyze the dynamics of two-photon excitation driven by a frequency comb. The electric field of a frequency comb is given in Equation 3.4. By comparison with Equation 3.12, we can identify  $\omega_m = m\omega_{\text{rep}} + \omega_c$  and  $E_m(\mathbf{r}, t) = \tilde{A}_m$  (the spatial dependence of the field is included in the next section). The double sums over  $m$  and  $m'$  in the two-photon operator (Equations 3.27-3.30) can be simplified as follows. We re-number the comb modes such that

$$E(t) = \frac{1}{2} \sum_{m=-\infty}^{\infty} \tilde{A}'_m e^{-i(m\omega_{\text{rep}} + \omega_0)t} + \text{c.c.}, \quad (3.31)$$

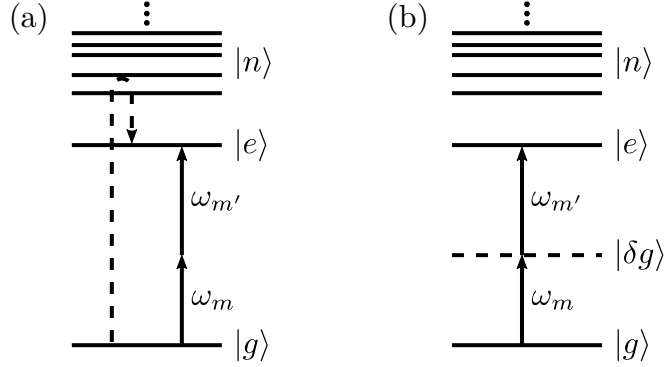


Figure 3.3: Two interpretations of the two-photon transition process. The solid arrows show a pair of fields at frequencies  $\omega_m$  and  $\omega_{m'}$  that drive the transition. (a) The dashed arrow shows the excitation of the atom from the ground state  $|g\rangle$  via one of the intermediate states  $|n\rangle$  to the final state  $|e\rangle$ . (b) The field at frequency  $\omega_m$  perturbs the atomic ground state into a virtual intermediate state  $|\delta g\rangle$ . From there the second field at frequency  $\omega_{m'}$  completes the transition to the final state  $|e\rangle$ .

where  $\omega_0$  is the frequency of the comb mode that is closest to  $\omega_{eg}/2$ , and the coefficients are given by

$$\tilde{A}'_m = \tilde{A}_{m-\mu}, \quad (3.32)$$

where  $\mu = (\omega_c - \omega_0)/\omega_{\text{rep}}$ .

The condition for achieving two-photon resonance is  $\omega_m + \omega_{m'} = (m + m')\omega_{\text{rep}} + 2\omega_0 \approx \omega_{eg}$ . In our new numbering scheme, this corresponds to  $m = -m'$ . Non-resonant terms with  $m \neq -m'$  are detuned from the resonance by integer multiples of  $\omega_{\text{rep}}$ . In our experiment we use a laser with  $\omega_{\text{rep}} = 2\pi \times 40$  MHz, while the expected transition linewidth is a few kHz at most (see section 3.3). The contribution of the non-resonant terms is therefore negligible, and they are dropped in the following. The time domain picture of this approximation is that the pulsed excitation is replaced with a continuous time averaged excitation. This is valid since the atomic state lifetime is much longer than the time interval between the individual pulses.

We further make the assumption that the bandwidth of the frequency comb is much smaller than its carrier frequency  $\omega_c$ . The spectrum of our XUV frequency comb at 60.8 nm has not been accurately characterized yet. However, we expect that the bandwidth will be around 0.4 nm such that this approximation is well justified. This allows us to replace  $\omega_{m'}$  by  $\omega_c$  in the denominator in Equation 3.30. We obtain

$$\frac{V_{eg}}{\hbar} = -\frac{e^2}{4\hbar} \sum_{\{n\}} \frac{\langle e|\hat{z}|n\rangle\langle n|\hat{z}|g\rangle}{\tilde{E}_n - \tilde{E}_g - \hbar\omega_c} \sum_m \tilde{A}'_m \tilde{A}'_{-m} e^{-i2\omega_0 t}. \quad (3.33)$$

The ac Stark shifts in Equation 3.26 can be taken into account by adjusting the effective energy levels. Then the resulting two-photon operator is equivalent to the well known operator that describes the dynamics of a two-level atom with a dipole-allowed transition

between the levels (see for example chapter 5 in [94]). We can identify the *two-photon detuning* [91]

$$\Delta\omega = 2\omega_0 - \omega_{eg} - (\Delta\omega_e - \Delta\omega_g), \quad (3.34)$$

and the *two-photon Rabi frequency*

$$\Omega_{2p} = -\frac{e^2}{2\hbar} \sum_{\{n\}} \frac{\langle e|\hat{z}|n\rangle\langle n|\hat{z}|g\rangle}{\tilde{E}_n - \tilde{E}_g - \hbar\omega_c} \sum_m \tilde{A}'_m \tilde{A}'_{-m}. \quad (3.35)$$

The excitation process is visualized in Figure 3.4. The sum  $\sum_m \tilde{A}'_m \tilde{A}'_{-m}$  in Equation 3.35 can be interpreted as the pairwise interaction of frequency comb modes that lie symmetrically around  $\omega_{eg}/2$  and whose photon energies add up to the transition energy.

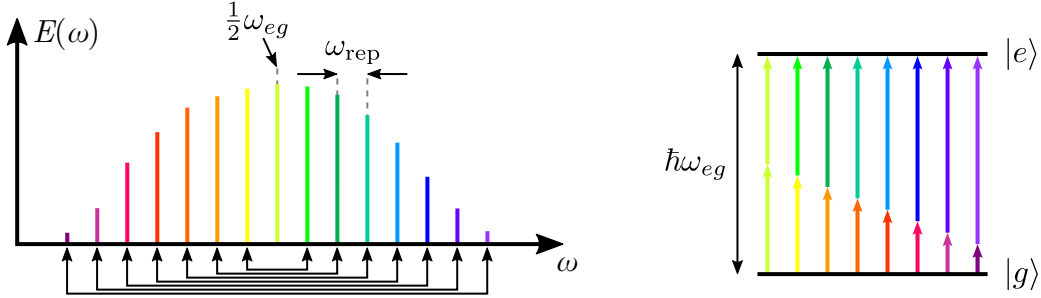


Figure 3.4: Illustration of two-photon excitation with a frequency comb. Two-photon resonance is achieved if  $\omega_{eg}/2$  coincides with a comb mode, or lies exactly in the center between two modes. In this case all modes contribute pairwise to the excitation. If the frequency of the entire comb is scanned, the excitation spectrum repeats every  $\omega_{\text{rep}}/2$ .

### Motional effects

As a next step the spatial dependence of the electric field is introduced. We assume that the frequency comb pulses propagate along the  $x$  axis. The field is then given by replacing  $t$  with  $t - x/c$  in Equation 3.4:<sup>2</sup>

$$\begin{aligned} E(x, t) = E(t - x/c) &= \frac{1}{2} \sum_{m=-\infty}^{\infty} \tilde{A}_m e^{-i(m\omega_{\text{rep}} + \omega_c)(t - x/c)} + \text{c.c.} \\ &= \frac{1}{2} \sum_{m=-\infty}^{\infty} \tilde{A}_m(x) e^{-i(m\omega_{\text{rep}} + \omega_c)t} + \text{c.c.}, \end{aligned} \quad (3.36)$$

where we have defined the position-dependent Fourier coefficients

$$\tilde{A}_m(x) = \tilde{A}_m e^{i(m\omega_{\text{rep}} + \omega_c)x/c}. \quad (3.37)$$

<sup>2</sup>The refractive index is set to 1 since our experiments generally take place in vacuum.

This allows us to use the results from the previous section by replacing  $\tilde{A}_m$  with  $\tilde{A}_m(x)$  in the formulas.

As we will show below, motional effects can be strongly suppressed by exciting the atom with two counter-propagating pulse trains. For mathematical convenience we assume that the individual pulses have a Gaussian envelope:

$$\mathcal{E}_I(t) = \sqrt{\frac{I}{\varepsilon_0 c}} \sqrt{2} \sqrt[4]{\frac{2}{\pi}} \sqrt{\frac{T}{\tau}} e^{-(t/\tau)^2}, \quad (3.38)$$

where  $I$  is the average intensity of the pulse train,  $\varepsilon_0$  is the vacuum electric permittivity,  $c$  is the speed of light, and  $T$  is the pulse repetition time. The intensity FWHM of the pulses is  $\Delta t_{1/2} = \sqrt{2 \ln(2)} \tau$ . The corresponding position-dependent Fourier coefficients are given by

$$\begin{aligned} \tilde{A}_{m,I}(x) &= e^{i(m\omega_{\text{rep}} + \omega_c)x/c} \frac{1}{T} \int_{-T/2}^{T/2} \mathcal{E}_I(t) e^{im\omega_{\text{rep}}t} dt \approx e^{i(m\omega_{\text{rep}} + \omega_c)x/c} \frac{1}{T} \int_{-\infty}^{\infty} \mathcal{E}_I(t) e^{im\omega_{\text{rep}}t} dt \\ &= 2 \sqrt{\frac{I}{\varepsilon_0 c}} \sqrt[4]{\frac{2}{\pi}} \sqrt{\frac{\tau}{T}} e^{-\frac{1}{4}(m\omega_{\text{rep}}\tau)^2} e^{i(m\omega_{\text{rep}} + \omega_c)x/c}, \end{aligned} \quad (3.39)$$

where in the second step we assumed that the pulse duration  $\tau$  is much shorter than the pulse repetition time  $T$ .

The total electric field of the two pulse trains is

$$E(x, t) = \frac{1}{2} \sum_{m=-\infty}^{\infty} [\tilde{A}_{m,I_1}(x) + \tilde{A}_{m,I_2}(-x)] e^{-i(m\omega_{\text{rep}} + \omega_c)t} + \text{c.c.}, \quad (3.40)$$

where  $I_1$  and  $I_2$  are the intensities of the two pulse trains. By comparing Equation 3.40 and Equation 3.36, we identify:

$$\begin{aligned} \tilde{A}_m(x) &= \tilde{A}_{m,I_1}(x) + \tilde{A}_{m,I_2}(-x) \\ &= \frac{2}{\sqrt{\varepsilon_0 c}} \sqrt[4]{\frac{2}{\pi}} \sqrt{\frac{\tau}{T}} e^{-\frac{1}{4}(m\omega_{\text{rep}}\tau)^2} \left[ \sqrt{I_1} e^{i(m\omega_{\text{rep}} + \omega_c)x/c} + \sqrt{I_2} e^{-i(m\omega_{\text{rep}} + \omega_c)x/c} \right]. \end{aligned} \quad (3.41)$$

For simplicity we assume that the spectrum of the frequency comb is centered with respect to the two-photon resonance, i.e.  $2\omega_c = 2\omega_0 \approx \omega_{eg}$ . This corresponds to  $\mu = 0$  in Equation 3.32 such that  $\tilde{A}'_m(x) = \tilde{A}_m(x)$ . From Equation 3.35 we then get the two-photon Rabi frequency:

$$\Omega_{2p} = -\frac{e^2}{2\hbar} \sum_{\{|n\rangle\}} \frac{\langle e|\hat{z}|n\rangle \langle n|\hat{z}|g\rangle}{\tilde{E}_n - \tilde{E}_g - \hbar\omega_c} \sum_m \tilde{A}'_m(x) \tilde{A}'_{-m}(x). \quad (3.42)$$

The product of the two position-dependent Fourier coefficients is

$$\begin{aligned} \tilde{A}'_m(x) \tilde{A}'_{-m}(x) &= 2 \frac{\sqrt{2\pi} \tau}{\varepsilon_0 c T} e^{-\frac{1}{2}(m\omega_{\text{rep}}\tau)^2} \left[ I_1 e^{i2\omega_c x/c} + I_2 e^{-i2\omega_c x/c} \right. \\ &\quad \left. + \sqrt{I_1 I_2} \left( e^{i2m\omega_{\text{rep}}x/c} + e^{-i2m\omega_{\text{rep}}x/c} \right) \right]. \end{aligned} \quad (3.43)$$

The expected 0.4 nm intensity FWHM of our XUV frequency comb corresponds to a bandwidth of 32 THz. With a pulse repetition rate of 40 MHz, the comb therefore contains around one million modes. We can therefore replace the sum over the modes in Equation 3.42 by an integral using  $\sum_m \approx \frac{1}{\omega_{\text{rep}}} \int_{-\infty}^{\infty} d(m\omega_{\text{rep}})$ . The integral can be evaluated, and we arrive at the final expression for the two-photon Rabi frequency:

$$\Omega_{2p} = 2(2\pi\beta_{ge}) \left[ I_1 e^{i2\omega_c x/c} + I_2 e^{-i2\omega_c x/c} + 2\sqrt{I_1 I_2} e^{-2[x/(c\tau)]^2} \right], \quad (3.44)$$

where

$$\beta_{ge} = -\frac{e^2}{2hc\varepsilon_0} \sum_{\{|n\rangle\}} \frac{\langle e|\hat{z}|n\rangle \langle n|\hat{z}|g\rangle}{\tilde{E}_n - \tilde{E}_g - \hbar\omega_c} \quad (3.45)$$

is the *two-photon matrix element*. For hydrogen-like atoms  $\beta_{ge}$  can be calculated analytically. Values for a number of two-photon transitions in hydrogen are tabulated in [91]. The results can be applied to other two-body Coulomb systems by multiplying with the factor [91]

$$\frac{1}{Z^4} \left( \frac{m_e}{\mu} \right)^3, \quad (3.46)$$

where  $Z$  is the nuclear charge number,  $m_e$  is the electron mass, and  $\mu$  is the reduced mass of the two particles forming the system. For the two-photon excitation of the 1S-2S transition in  $\text{He}^+$  driven at 60.8 nm, the value is [95]

$$\beta_{ge} = 2.301\,64 \times 10^{-6} \text{ Hz (W/m}^2\text{)}^{-1}. \quad (3.47)$$

Remarkably, we find that at  $x = 0$  the two-photon Rabi frequency given by Equation 3.44 is identical to the one obtained for a pair of continuous-wave lasers of the same average intensities [91]. One can also show that the ac Stark shifts are given by the *average* intensities of the excitation lasers, and not by the much higher peak intensities of the laser pulses [96].

The first two terms in Equation 3.44, which are proportional to  $I_1$  and  $I_2$ , correspond to two-photon absorption where both photons come from a single beam. They have  $x$ -dependent phase factors with the effective wave vectors  $\pm 2\omega_c/c$ . This *collinear* excitation process is therefore affected by motional effects such as Doppler shifts and recoil effects.

The third term, which is proportional to  $\sqrt{I_1 I_2}$ , corresponds to *anticollinear* excitation where one photon is absorbed from either beam. One peculiar feature is that away from the coordinate origin, the term drops off exponentially on the scale of  $c\tau$ . This shows that the absorption process can only take place inside the *pulse collision volume* where the counter-propagating pulses meet. The size of the pulse collision volume can be defined by the distance between the points where the Rabi frequency has dropped by one half. The resulting FWHM size is

$$\Delta x_{1/2} = \sqrt{2 \ln(2)} c\tau = c\Delta t_{1/2}. \quad (3.48)$$

The phase factor is absent in this term which shows that, like in the continuous-wave laser case, the anticollinear absorption process is not affected by the first-order Doppler shift.

However, due to the finite bandwidth of the frequency comb, only the *average* wave vector is zero. The absorbed photon pairs in general have nonzero total momenta such that the process is not entirely decoupled from the atomic motion. We will come back to this point in section 3.4.

### 3.3 Excitation dynamics

The electronic state of a  $\text{He}^+$  ion is described by the density matrix in the rotating frame [91]:

$$\rho = \begin{pmatrix} \rho_{gg} & \rho'_{ge} \\ \rho'_{eg} & \rho_{ee} \end{pmatrix}, \quad (3.49)$$

where  $\rho_{gg}$  and  $\rho_{ee}$  are the populations of the 1S ground state and the 2S excited state, respectively, and  $\rho'_{ge}$  and  $\rho'_{eg} = \rho_{ge}^*$  are the coherences in the rotating frame. The time evolution of the density matrix is determined by the *optical Bloch equations* [91]:

$$\dot{\rho}_{gg} = -\Omega_{2p} \text{Im}(\rho'_{ge}) + \Gamma_s \rho_{ee}, \quad (3.50)$$

$$\dot{\rho}'_{ge} = -i\Delta\omega\rho'_{ge} + i\frac{\Omega_{2p}}{2}(\rho_{gg} - \rho_{ee}) - \frac{\Gamma_s + \Gamma_i}{2}\rho'_{ge}, \quad (3.51)$$

$$\dot{\rho}_{ee} = \Omega_{2p} \text{Im}(\rho'_{ge}) - (\Gamma_s + \Gamma_i)\rho_{ee}, \quad (3.52)$$

where  $\Gamma_s$  is the spontaneous decay rate of the 2S state. One feature of all hydrogen-like systems is that a laser that can excite the 1S-2S two-photon transition has sufficient photon energy to ionize the 2S state.<sup>3</sup> This is taken into account by the decay terms in Equation 3.51 and Equation 3.52 which are proportional to the 2S ionization rate

$$\Gamma_i = 2\pi\beta_{\text{ioni}}I, \quad (3.53)$$

where  $I$  is the mean laser intensity, and  $\beta_{\text{ioni}}$  is the ionization rate coefficient. For hydrogen-like atoms  $\beta_{\text{ioni}}$  can be calculated analytically. The expression and values for several transitions in hydrogen are given in [91]. Like the two-photon matrix elements, the rate coefficients can be applied to other two-body Coulomb systems by scaling them with Equation 3.46. For ionization of the 2S state of  $\text{He}^+$  by 60.8 nm radiation, one finds [95]

$$\beta_{\text{ioni}} = 7.51609 \text{ Hz (W/m}^2\text{)}^{-1}. \quad (3.54)$$

The interplay between decay and ionization of the 2S state leads to rich dynamics which cannot be described by simple rate equations (see [91] and [95] for detailed descriptions of the dynamics). In our experiment the first challenge will be to find the resonance line. The 1S-2S transition frequency in  $\text{He}^+$  can be calculated with an estimated uncertainty of

---

<sup>3</sup>Our high-harmonic source generates all odd harmonics of the driving laser at 1033 nm. The 2S state of  $\text{He}^+$  can be ionized by the 13th and higher harmonics. The calculations in this chapter are done for the 17th harmonic only since the output spectrum of the high harmonic source has not been accurately characterized yet.



70 kHz which is limited both by QED theory, and by the uncertainty of the alpha particle charge radius [12, 29]. This contrasts with a natural linewidth of only 84 Hz [14]. To search the line we will step the laser frequency over a range that covers a few standard deviations around the calculated value. At each frequency point the  $\text{He}^+$  ions will be exposed to the spectroscopy laser for a certain amount of time. Then the generation of  $\text{He}^{2+}$  ions will be measured by exciting the secular motion of the trapped ions (see chapter 5). The exposure time and frequency step size have to be carefully chosen. If the time is too short or the step size is too large, we could “miss” the line during the scan. On the other hand, very long exposure times and small step sizes lead to very long measurement times.

Equations 3.50-3.52 are numerically integrated for an exposure time of  $t_0 = 5$  s and different spectroscopy laser intensities  $I$  and two-photon detunings  $\Delta\omega$ . In this section we ignore all motional effects and give values for collinear excitation with a single laser beam (this corresponds to setting  $I_1 = I$  and  $I_2 = 0$  in Equation 3.44). The ionization probability at the end of the exposure, which is given by  $1 - \rho_{ee}(t_0) - \rho_{gg}(t_0)$ , is shown in Figure 3.5.

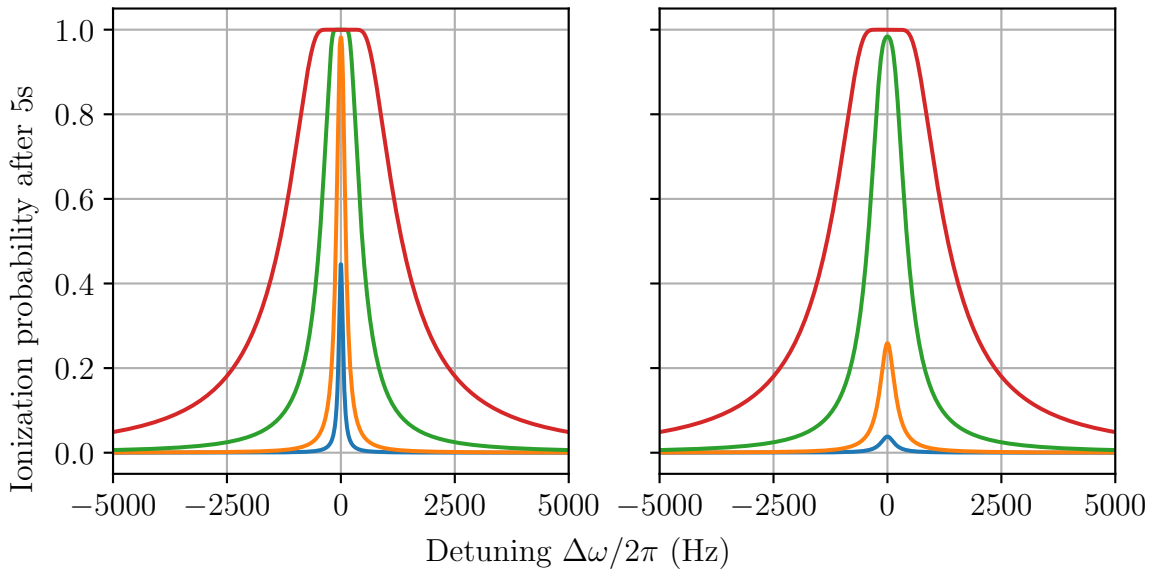


Figure 3.5: Calculated ionization probabilities after exposing a  $\text{He}^+$  ion with resonant XUV radiation for 5 s for  $\Gamma_s = 2\pi \times 84$  Hz (left), and for  $\Gamma_s = 2\pi \times 350$  Hz (right). From top to bottom the curves correspond to intensities of 10, 5, 2, and 1  $\mu\text{W}/\mu\text{m}^2$ .

In the left plot the 2S decay rate was set to the natural linewidth ( $\Gamma_s = 2\pi \times 84$  Hz). If a  $\text{He}^+$  ion experiences an electric field, the 2S and 2P states are mixed which reduces the 2S lifetime [95]. While a trapped ion arranges itself such that it feels no electric field on average, the *mean square* field can be nonzero if the ion experiences micromotion. In the right plot we have set  $\Gamma_s = 2\pi \times 350$  Hz which is a typical value we expect due to micromotion in our setup (see subsection 4.7.3). The plots show that achieving a sufficiently high laser intensity is crucial for the success of the experiment. Besides ensuring

reliable excitation on resonance, high intensities also saturate and broaden the spectral line which allows using a larger step size in the frequency scan. Furthermore, the comparison between the two plots shows that at low intensities the expected lifetime reduction of the 2S state will strongly reduce the ionization rate. On the other hand, at high intensities the ionization process dominates over the 2S decay such that the ionization probabilities are hardly affected.

### 3.4 Motional dynamics

In precision laser spectroscopy the interaction between the atomic motion and the field of the laser is an important source of line shifts and broadening. In the rest frame of a moving atom, the laser frequency appears shifted due to the Doppler effect. If the atomic velocities follow a thermal distribution, this leads to Doppler broadening of the spectral line [27, pp. 151–153]. Furthermore, if one or more photons excite a transition, the atom absorbs their total momentum  $\hbar\mathbf{k}_{\text{eff}}$ , where  $\mathbf{k}_{\text{eff}}$  is the sum of the wave vectors of the contributing photons. In free atoms this leads to a shift of the observed transition frequency which is given by the *recoil frequency* [27, pp. 149–150]

$$\Delta\omega_{\text{rec}} = \frac{\hbar k_{\text{eff}}^2}{2m}, \quad (3.55)$$

where  $k_{\text{eff}} = |\mathbf{k}_{\text{eff}}|$ , and  $m$  is the atomic mass.

The dynamics are quite different if the spectroscopy target is a trapped particle. We first discuss some general features using the simple example of a single trapped ion before treating the more realistic scenario of multiple ions trapped together. We assume that the ion is trapped in a one-dimensional harmonic potential with a secular frequency  $\omega_{\text{sec}}$ . The effective wave vector is for now assumed to be parallel to the direction of motion. The motion is then described by a quantum harmonic oscillator [45, 97]. The motional state can be written as a superposition of orthogonal *Fock states*  $|n\rangle$ :

$$|\psi\rangle = \sum_{n=0}^{\infty} c_n |n\rangle, \quad (3.56)$$

where  $n$  is the motional quantum number.

The absorption or emission of photons changes the motional state of the atom. The strength of this motional coupling is quantified by the *Lamb-Dicke parameter* [45, 95]

$$\eta = k_{\text{eff}} x_0 = k_{\text{eff}} \sqrt{\frac{\hbar}{2m\omega_{\text{sec}}}} = \sqrt{\frac{\Delta\omega_{\text{rec}}}{\omega_{\text{sec}}}}, \quad (3.57)$$

where  $x_0 = \sqrt{\hbar/(2m\omega_{\text{sec}})}$  is the size of the ground state wave function of the harmonic oscillator. The Lamb-Dicke parameter is small if the ground state wave function is much smaller than  $1/k_{\text{eff}}$ , or, equivalently, if the recoil frequency is much smaller than the secular frequency.

Frequency standards that rely on trapped atoms or ions are usually operated in the *Lamb-Dicke regime* which is defined by the condition [45]:

$$k_{\text{eff}}\sqrt{\langle\hat{x}^2\rangle} = \eta\sqrt{\langle(\hat{a} + \hat{a}^\dagger)^2\rangle} \ll 1, \quad (3.58)$$

where  $\sqrt{\langle\hat{x}^2\rangle}$  is the root mean square size of the motional wave function, and the atomic position operator is expressed as

$$\hat{x} = x_0(\hat{a} + \hat{a}^\dagger), \quad (3.59)$$

where  $\hat{a}$  and  $\hat{a}^\dagger$  are the annihilation and creation operators of the harmonic oscillator, respectively. Note that  $\eta \ll 1$  is a necessary, but not sufficient condition for achieving the Lamb-Dicke regime since the ground state is the smallest harmonic oscillator state.

In the Lamb-Dicke regime, the absorption spectrum of the ion is dominated by the so-called *carrier resonance*. Driving this resonance does not change the motional state, and the spectral line is free of Doppler broadening and of the recoil shift. Its width is therefore only limited by the natural linewidth of the atomic transition.

The recoil frequencies for a number of narrow transitions in atomic or ionic species are compared in Table 3.1. Due to the low atomic mass and short transition wavelength, the recoil frequency when collinearly exciting the 1S-2S transition in  $\text{He}^+$  is orders of magnitude larger than typical values in optical frequency standards. Our ion trap achieves secular frequencies of up to a few MHz for  $^4\text{He}^+$  which is much smaller than the recoil frequency. We therefore have  $\eta > 1$  and cannot reach the Lamb-Dicke regime.

Table 3.1: Recoil frequencies for a number of narrow transitions used in optical atomic frequency standards. The numbers for the  $\text{He}^+$  isotopes refer to collinear excitation of the 1S-2S two-photon transition.

Species	Transition wavelength (nm)	Recoil frequency $\Delta\omega_{\text{rec}}/(2\pi)$ (MHz)
$^3\text{He}^+$	30.4	71.7
$^4\text{He}^+$	30.4	54.0
$^{27}\text{Al}^+$	267.4	0.103
$^{40}\text{Ca}^+$	729.3	0.009
$^{87}\text{Sr}$	698.4	0.005
$^{171}\text{Yb}$	578.4	0.003
$^{171}\text{Yb}^+$	466.9	0.005
$^{199}\text{Hg}^+$	281.6	0.013

The coupling between photon absorption and atomic motion is described by transitions of the type  $|g\rangle|n\rangle \rightarrow |e\rangle|n+s\rangle$ . As a result the atomic spectrum acquires sidebands which are spaced by  $\Delta\omega = s\omega_{\text{sec}}$  from the carrier. The Rabi frequency for the  $s$ th sideband is given by [45]

$$\Omega_{n,n+s} = \Omega_{n+s,n} = \Omega \left| \langle n+s | e^{ik_{\text{eff}}\hat{x}} | n \rangle \right| = \Omega \left| \langle n+s | e^{i\eta(\hat{a}+\hat{a}^\dagger)} | n \rangle \right|, \quad (3.60)$$

where  $\Omega$  is the Rabi frequency in the absence of motional effects. The Rabi frequency is scaled by a matrix element for the transition between the motional states which is given by [45, 95]

$$\langle n + s | e^{i\eta(\hat{a} + \hat{a}^\dagger)} | n \rangle = e^{-\eta^2/2} (i\eta)^{|s|} \sqrt{\frac{n_{<}!}{n_{>}!}} L_{n_{<}}^{|s|}(\eta^2), \quad (3.61)$$

where  $n_{<} = \min(n + s, n)$ ,  $n_{>} = \max(n + s, n)$ , and  $L_n^\alpha(X)$  is the generalized Laguerre polynomial.

Figure 3.6 shows Equation 3.60 evaluated for a collinearly excited  ${}^4\text{He}^+$  ion that is trapped with a secular frequency of  $\omega_{\text{sec}} = 2\pi \times 10$  MHz. The ion is assumed to start out in the motional ground state  $|\psi\rangle = |0\rangle$ . Even then, the Lamb-Dicke regime is not reached ( $\eta = 2.3$ ), and the spectrum consists of a number of sidebands. The recoil frequency of  $\Delta\omega_{\text{rec}} = 2\pi \times 54$  MHz is a few times larger than the sideband spacing. As a result the strongest sideband is not the carrier at  $\Delta\omega = 0$ , but the one that is closest to  $\Delta\omega_{\text{rec}}$ .

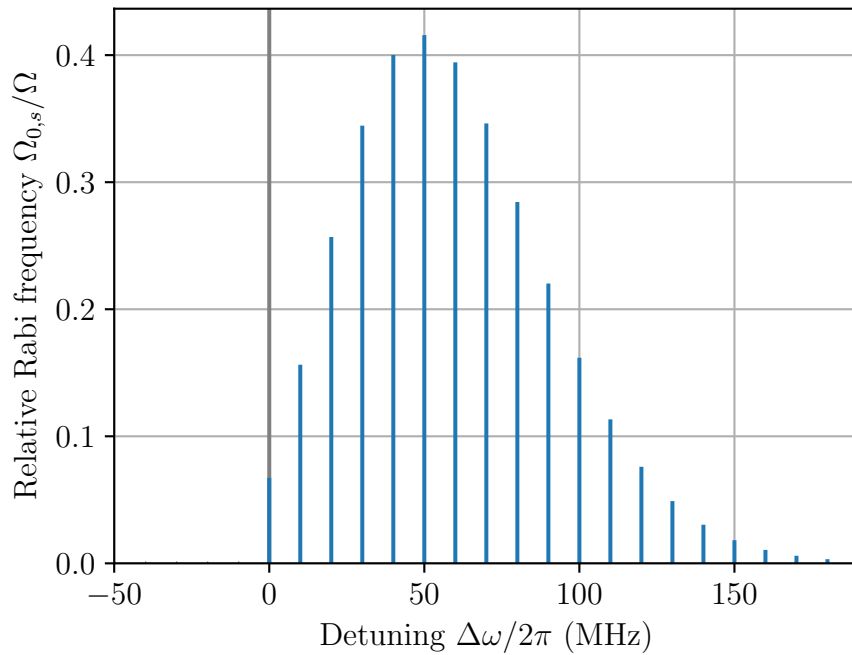


Figure 3.6: Sideband spectrum of a single collinearly excited  ${}^4\text{He}^+$  ion trapped with a secular frequency of  $\omega_{\text{sec}} = 2\pi \times 10$  MHz. The ion is initially in the motional ground state  $|\psi\rangle = |0\rangle$ . Since the recoil shift is much larger than the secular frequency, the Lamb-Dicke regime is not reached. As a result the spectrum contains a number of sidebands whose envelope is shifted away from the carrier (thick gray vertical line). Negative sidebands vanish since there is no motional state whose energy is below the ground state.

### 3.4.1 Multiple ions

Since laser cooling of  $\text{He}^+$  is currently not feasible, it has to be combined with at least one other ion for sympathetic cooling. The mutual Coulomb interaction couples the motion of the ions such that the spectrum becomes more complicated. In the following we treat the general case of  $N$  ions that are trapped together and are cold enough such that they form a Coulomb crystal. The derivation closely follows [98], but we do not make the simplifying assumption that the ions are arranged in a one-dimensional string.

The position of the  $j$ th ion in the Coulomb crystal is  $\mathbf{r}_j$ . The dynamics of the crystal are determined by the total potential energy

$$V(\mathbf{r}_1, \dots, \mathbf{r}_N), \quad (3.62)$$

which contains the effect of the trap, as well as the Coulomb interaction between the ions. We use the pseudopotential approximation for the ion trap such that  $V$  does not explicitly depend on time. The equilibrium configuration of the Coulomb crystal can be found by minimizing  $V$  with respect to the ion positions [99]. The equilibrium position of the  $j$ th ion is denoted  $\mathbf{r}_j^{(0)}$ . The ion positions are then expressed as [100]

$$\mathbf{r}_j = \mathbf{r}_j^{(0)} + q_j \mathbf{e}_x + q_{N+j} \mathbf{e}_y + q_{2N+j} \mathbf{e}_z, \quad (3.63)$$

where the parameters  $q_i$  ( $i = 1, \dots, 3N$ ) are the displacements from the equilibrium positions, and  $\mathbf{e}_x$ ,  $\mathbf{e}_y$ , and  $\mathbf{e}_z$  are Cartesian unit vectors along the trap axes. The potential energy is rewritten as

$$V(\mathbf{r}_1, \dots, \mathbf{r}_N) = V(\mathbf{r}_1^{(0)}, \dots, \mathbf{r}_N^{(0)}) + \tilde{V}(q_1, \dots, q_{3N}). \quad (3.64)$$

Since we are interested in small oscillations of the ions around their equilibrium positions,  $\tilde{V}$  is approximated by a Taylor series up to second order<sup>4</sup> [98]:

$$\tilde{V}(q_1, \dots, q_{3N}) \approx \frac{1}{2} \sum_{i,j=1}^{3N} V_{ij} q_i q_j, \quad (3.65)$$

where

$$V_{ij} = \frac{\partial^2}{\partial q_i \partial q_j} \tilde{V}(q_1, \dots, q_{3N})|_{q_i, q_j=0}. \quad (3.66)$$

The  $3N$  coupled equations of motion for the parameters are then given by

$$m_i \ddot{q}_i + \sum_{j=1}^{3N} V_{ij} q_j = 0, \quad (3.67)$$

where  $m_i$  is the mass of the  $i$ th ion, and  $m_{N+i} = m_{2N+i} = m_i$  for  $i = 1, \dots, N$ .

---

<sup>4</sup>The first-order terms vanish since the expansion is performed around an equilibrium position.

We now introduce the *mass-weighted coordinates*  $q'_i = \sqrt{m_i}q_i$ . The equations of motion then simplify to

$$\ddot{q}'_i + \sum_{j=1}^{3N} V'_{ij} q'_j = 0, \quad (3.68)$$

where  $V'_{ij} = V_{ij}/\sqrt{m_i m_j}$ . A general solution of Equation 3.68 consists of a superposition of oscillations at a set of *resonance frequencies*  $\omega_\alpha$  ( $\alpha = 1, \dots, 3N$ ) [101, p. 250]:

$$q'_i = \sum_{\alpha=1}^{3N} C_\alpha \beta_i^\alpha e^{-i\omega_\alpha t}, \quad (3.69)$$

where  $C_\alpha$  is a complex amplitude factor that determines the amplitude and phase of the oscillation at frequency  $\omega_\alpha$ , and  $\beta_i^\alpha$  is the  $i$ th component of the normalized *eigenvector*  $\beta^\alpha$ . Inserting Equation 3.69 into Equation 3.68 yields an eigenvalue problem for the matrix  $V'_{ij}$  from which the resonance frequencies  $\omega_\alpha$  and eigenvectors  $\beta^\alpha$  can be obtained:

$$\sum_{j=1}^{3N} V'_{ij} \beta_j^\alpha = \omega_\alpha^2 \beta_i^\alpha. \quad (3.70)$$

The eigenvectors define an orthogonal transformation into a set of  $3N$  new coordinates:

$$\pi_\alpha = \sum_{i=1}^{3N} \beta_i^\alpha q'_i. \quad (3.71)$$

It can be shown that each of the coordinates  $\pi_\alpha$  performs oscillations at only the frequency  $\omega_\alpha$  [101, p. 252]. They are therefore called the *normal coordinates* of the system, and the vibrations are called the *normal modes*. A quantum description of the normal mode oscillations is obtained by introducing the position operators for the normal coordinates

$$\hat{\pi}_\alpha = \sqrt{\frac{\hbar}{2\omega_\alpha}} (\hat{a}_\alpha + \hat{a}_\alpha^\dagger), \quad (3.72)$$

where  $\hat{a}_\alpha$  and  $\hat{a}_\alpha^\dagger$  are the annihilation and creation operators for the normal mode  $\alpha$ , respectively. Since the eigenvectors are orthogonal, Equation 3.71 can be inverted to express the original coordinates  $q_i$  in terms of the normal mode coordinates:

$$q_i = \frac{1}{\sqrt{m_i}} \sum_{\alpha=1}^{3N} \beta_i^\alpha \pi_\alpha. \quad (3.73)$$

Position operators for the original coordinates are then obtained by inserting Equation 3.72 into Equation 3.73 [98]:

$$\hat{q}_i = \frac{1}{\sqrt{m_i}} \sum_{\alpha=1}^{3N} \beta_i^\alpha \sqrt{\frac{\hbar}{2\omega_\alpha}} (\hat{a}_\alpha + \hat{a}_\alpha^\dagger). \quad (3.74)$$

The motional state of the ion crystal can in general be written as a superposition of Fock states for the normal modes [100]:

$$|\psi\rangle = \sum_{\{n_\alpha\}=0}^{\infty} c_{\{n_\alpha\}} |\{n_\alpha\}\rangle, \quad (3.75)$$

where  $\{n_\alpha\}$  is a shorthand notation for  $n_1, \dots, n_{3N}$ .

We can now analyze how the excitation of one of the ions changes the motional state of the ion crystal. If the ion crystal is initially in the motional state  $|\psi_i\rangle$ , and the  $j$ th ion absorbs photons with an effective wave vector  $\mathbf{k}_{\text{eff}}$ , the motional state of the ion crystal changes to [98]

$$|\psi_f\rangle = e^{i\mathbf{k}_{\text{eff}} \cdot \hat{\mathbf{r}}_j} |\psi_i\rangle, \quad (3.76)$$

where  $\hat{\mathbf{r}}_j = \mathbf{r}_j^{(0)} + \hat{q}_j \mathbf{e}_x + \hat{q}_{N+j} \mathbf{e}_y + \hat{q}_{2N+j} \mathbf{e}_z$  is the position operator for the  $j$ th ion. The operator in Equation 3.76 is called the *kick operator*. It can be rewritten as

$$e^{i\mathbf{k}_{\text{eff}} \cdot \hat{\mathbf{r}}_j} = e^{i\phi_j} e^{i\mathbf{k}_{\text{eff}} \cdot \hat{\mathbf{q}}_j}, \quad (3.77)$$

where  $\phi_j = \mathbf{k}_{\text{eff}} \cdot \mathbf{r}_j^{(0)}$  is a constant phase term that depends on the equilibrium position of the ion, and  $\hat{\mathbf{q}}_j = \hat{q}_j \mathbf{e}_x + \hat{q}_{N+j} \mathbf{e}_y + \hat{q}_{2N+j} \mathbf{e}_z$ .

Inserting Equation 3.74 into Equation 3.77 finally yields

$$e^{i\mathbf{k}_{\text{eff}} \cdot \hat{\mathbf{r}}_j} = e^{i\phi_j} \prod_{\alpha=1}^{3N} e^{i\eta_j^\alpha (\hat{a}_\alpha + \hat{a}_\alpha^\dagger)}, \quad (3.78)$$

where the *generalized Lamb-Dicke parameter* for the  $j$ th ion and the normal mode  $\alpha$  was introduced:

$$\eta_j^\alpha = \mathbf{k}_{\text{eff}} \cdot (\beta_j^\alpha \mathbf{e}_x + \beta_{N+j}^\alpha \mathbf{e}_y + \beta_{2N+j}^\alpha \mathbf{e}_z) \sqrt{\frac{\hbar}{2m_j \omega_\alpha}}. \quad (3.79)$$

If we assume that the ion crystal is in an energy eigenstate  $|\{n_\alpha\}\rangle = |n_1\rangle |n_2\rangle \dots |n_{3N}\rangle$ , the excitation of the  $j$ th ion can induce transitions to the final states  $|\{n_\alpha + s_\alpha\}\rangle$ . These transitions lead to sidebands which are spaced by  $\Delta\omega = \sum_{\alpha=1}^{3N} s_\alpha \omega_\alpha$  from the carrier. As in the single-ion case, the Rabi frequencies for the sideband transitions are scaled by the magnitude of the transition matrix elements which are given by [100]:

$$\begin{aligned} \langle \{n_\alpha + s_\alpha\} | e^{i\mathbf{k}_{\text{eff}} \cdot \hat{\mathbf{r}}_j} | \{n_\alpha\} \rangle &= e^{i\phi_j} \langle \{n_\alpha + s_\alpha\} | \prod_{\alpha=1}^{3N} e^{i\eta_j^\alpha (\hat{a}_\alpha + \hat{a}_\alpha^\dagger)} | \{n_\alpha\} \rangle \\ &= e^{i\phi_j} \prod_{\alpha=1}^{3N} \langle n_\alpha + s_\alpha | e^{i\eta_j^\alpha (\hat{a}_\alpha + \hat{a}_\alpha^\dagger)} | n_\alpha \rangle \\ &= e^{i\phi_j} \prod_{\alpha=1}^{3N} e^{-(\eta_j^\alpha)^2/2} (i\eta_j^\alpha)^{|s_\alpha|} \sqrt{\frac{n_{\alpha<}!}{n_{\alpha>}!}} L_{n_{\alpha<}}^{|s_\alpha|} \left( (\eta_j^\alpha)^2 \right), \end{aligned} \quad (3.80)$$

where in the last step we have used Equation 3.61.

### 3.4.2 Comparison of excitation geometries

$\text{Be}^+$  can be efficiently photoionized by the absorption of a single photon with a wavelength shorter than 68.1 nm [102, 103]. It is therefore important to choose a geometry that allows illuminating the  $\text{He}^+$  ions with the XUV spectroscopy radiation while avoiding the  $\text{Be}^+$  ions. Two possible options are shown in Figure 3.7. The first option (“radial collinear excitation”) is to prepare a linear string of  $\text{He}^+$  and  $\text{Be}^+$  ions along the trap axis (the simplest case is having one of each). The spectroscopy radiation can then be focused onto one of the  $\text{He}^+$  ions along the radial plane of the trap [104]. The second option (“axial anticollinear excitation”) is to load a large mixed ion crystal of  $\text{Be}^+$  and  $\text{He}^+$  ions. If suitable ion numbers are chosen, the lighter  $\text{He}^+$  ions displace the  $\text{Be}^+$  ions from the center of the ion crystal and form a linear string along the trap axis (see also Figure 2.10). The spectroscopy radiation is then aligned parallel to the trap axis and is sent through the center of the ion crystal. As we will show below, anticollinear excitation is a prerequisite for achieving narrow linewidths in large ion crystals. This is achieved by back-reflecting the frequency comb pulses with an XUV mirror.

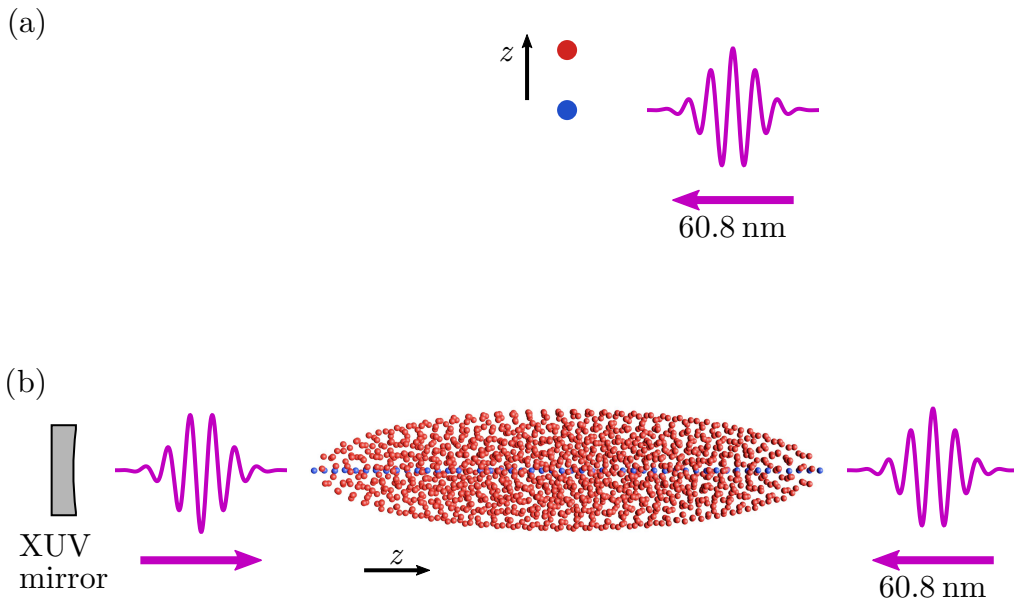


Figure 3.7: Possible excitation geometries for the trapped  $\text{He}^+$  ions. (a) Radial collinear excitation, and (b) axial anticollinear excitation. Blue dots are  $\text{He}^+$  ions, and red dots are  $\text{Be}^+$  ions used for sympathetic cooling and ion detection. The axis of the linear Paul trap is along  $z$ . Anticollinear excitation is achieved by back-reflecting the frequency comb pulses using an XUV mirror. In this case the pulses have to collide at the position of the ions.



### Radial collinear excitation

We start the discussion with the radial excitation of one  $\text{He}^+$  ion that is sympathetically cooled by one  $\text{Be}^+$  ion as shown in Figure 3.7 (a). For simplicity we assume that the ion trap is radially symmetric such that the secular frequencies in  $x$  direction and  $y$  direction are the same. We then choose the coordinates such that the spectroscopy laser beam is aligned along the  $x$  axis. The single-particle radial secular frequencies of the ions are given by Equation 2.29:

$$\omega_{\text{sec},x,\{\text{He,Be}\}} = \sqrt{\omega_{\text{rf},\{\text{He,Be}\}}^2 - \frac{1}{2}\omega_{z,\{\text{He,Be}\}}^2}, \quad (3.81)$$

where  $\omega_{\text{rf},\{\text{He,Be}\}}$  and  $\omega_{z,\{\text{He,Be}\}}$  are given by inserting the ion mass  $m = \{m_{\text{He}}, m_{\text{Be}}\}$  into Equation 2.31 and Equation 2.25, respectively.

For a string of ions along the axis of a linear Paul trap, the motions along the three trap axes are decoupled [100]. The spectroscopy laser therefore interacts only with the two radial modes of motion in  $x$  direction. The eigenvalue problem for the coupled oscillations of the two ions in  $x$  direction can be solved analytically [105]. The motion consists of an in-phase mode ( $i$ ) where the ions move in the same direction, and an out-of-phase mode ( $o$ ) where the ions move in opposite directions. The resonance frequencies of the modes are given by

$$\omega_i = \sqrt{-\frac{\mu + \mu^2 - \epsilon^2(1 + \mu^2) - a}{2\mu^2}} \omega_{z,\text{He}}, \quad (3.82)$$

$$\omega_o = \sqrt{-\frac{\mu + \mu^2 - \epsilon^2(1 + \mu^2) + a}{2\mu^2}} \omega_{z,\text{He}}, \quad (3.83)$$

where  $a = \sqrt{\epsilon^4(\mu^2 - 1)^2 - 2\epsilon^2(\mu - 1)^2\mu(1 + \mu) + \mu^2[1 + (\mu - 1)\mu]}$ ,  $\mu = m_{\text{Be}}/m_{\text{He}}$ , and  $\epsilon = \omega_{\text{sec},x,\text{He}}/\omega_{z,\text{He}}$ . The eigenvectors are

$$\beta^i = \begin{pmatrix} b_1 \\ b_2 \end{pmatrix}, \quad (3.84)$$

$$\beta^o = \begin{pmatrix} -b_2 \\ b_1 \end{pmatrix}, \quad (3.85)$$

where

$$b_1 = \sqrt{\frac{\mu - \mu^2 + \epsilon^2(-1 + \mu^2) + a}{2a}}, \quad (3.86)$$

$$b_2 = \sqrt{-\frac{\mu - \mu^2 + \epsilon^2(-1 + \mu^2) - a}{2a}}. \quad (3.87)$$

The results are visualized in Figure 3.8. The strength of the motional coupling between the two ions depends on the axial secular frequency  $\omega_{z,\text{He}}$ . For  $\omega_{z,\text{He}} \ll \omega_{\text{rf},\text{He}}$  the ions are spaced far apart such that their radial motions are almost independent. In the other limit when

$\omega_{z,\text{He}}$  becomes comparable to  $\omega_{\text{rf,He}}$ , the motions are strongly coupled and both components of the mode eigenvectors become significant. If  $\omega_{z,\text{He}}$  becomes too large, the resonance frequency of the out-of-phase mode vanishes. At this point the linear configuration of the ions along the trap axis becomes unstable, and the ion crystal turns into a linear radial configuration [105].

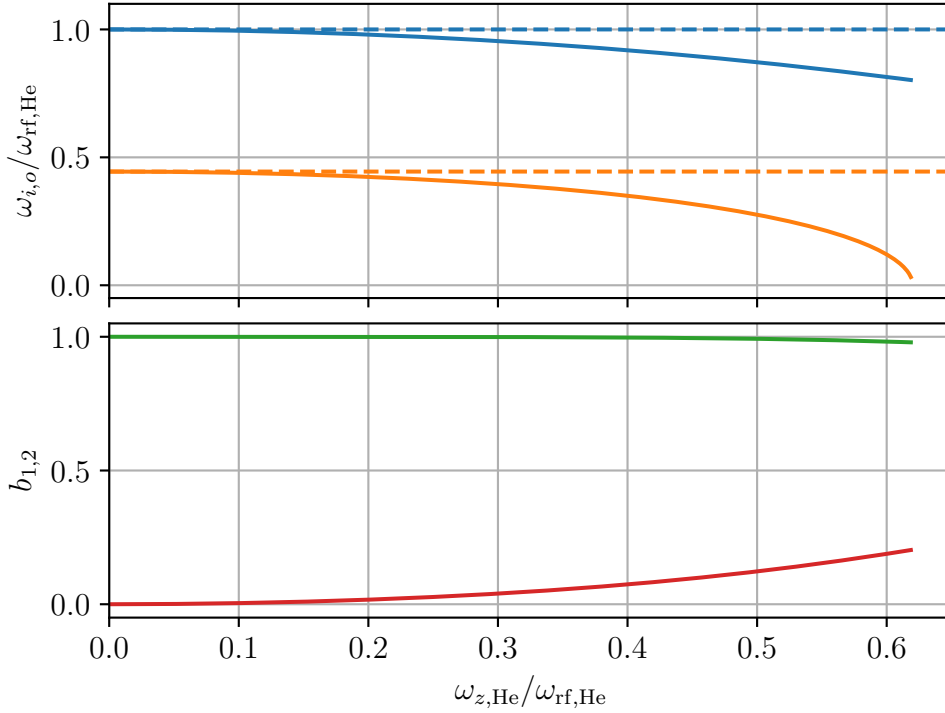


Figure 3.8: Radial modes of a  $\text{He}^+/\text{Be}^+$  two-ion crystal. The top plot shows the resonance frequencies of the in-phase mode (blue) and out-of-phase mode (orange). In the limit of weak axial confinement ( $\omega_{z,\text{He}} \rightarrow 0$ ), the motions of the two ions are decoupled. The resonance frequencies then are those of only the  $\text{He}^+$  ion (blue dashed line), and of only the  $\text{Be}^+$  ion (orange dashed line). The bottom plot shows the two components of the eigenvectors,  $b_1$  (green) and  $b_2$  (red). The closer the two values are to each other, the stronger the ion motion is coupled.

The generalized Lamb-Dicke parameters are obtained by inserting Equations 3.82-3.85 into Equation 3.79. With these, the Rabi frequencies for the different motional sidebands can be calculated using Equation 3.80. Figure 3.9 shows the resulting sideband spectrum for collinear excitation of the 1S-2S transition in the  $\text{He}^+$  ion. It is assumed that both modes of motion are initially in the ground state. In the left plot  $\omega_{z,\text{He}} = 2\pi \times 1.0$  MHz is much smaller than  $\omega_{\text{rf,He}} = 2\pi \times 10$  MHz. The two ions are therefore essentially decoupled and the spectrum closely matches the single-ion case shown in Figure 3.6. In the right plot  $\omega_{z,\text{He}}$  is increased to  $2\pi \times 5.0$  MHz. The motion of the  $\text{He}^+$  ion is therefore strongly coupled to both modes such that the spectrum acquires many more sidebands.

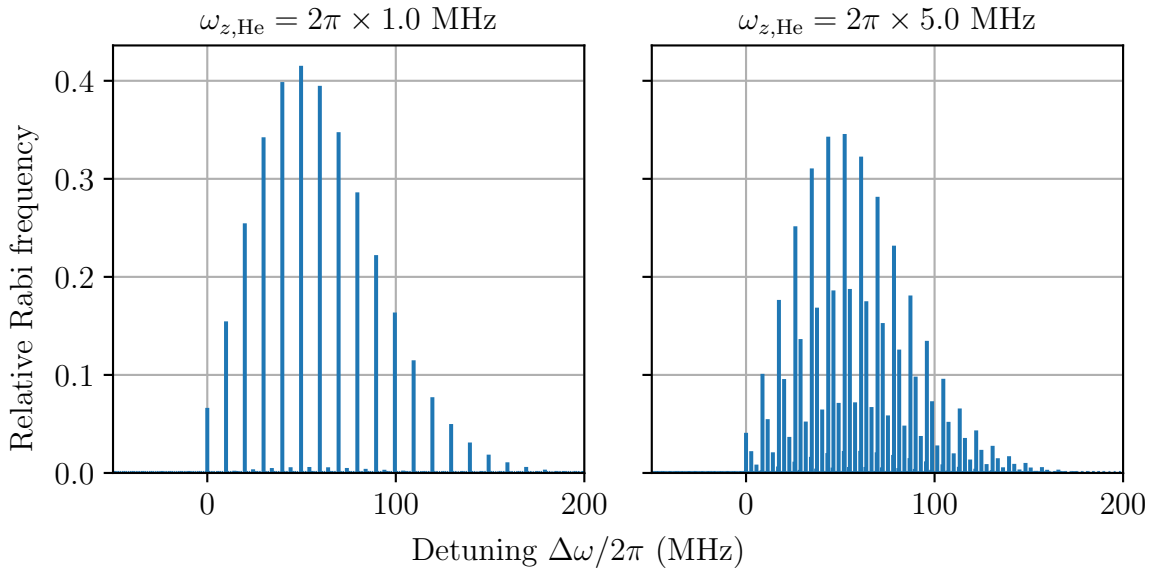


Figure 3.9: Sideband spectrum for collinear radial excitation of the  $\text{He}^+$  ion in a  $\text{He}^+/\text{Be}^+$  two-ion crystal. In both plots  $\omega_{\text{rf,He}} = 2\pi \times 10$  MHz. The mode frequencies are (left)  $\omega_i = 2\pi \times 10.0$  MHz and  $\omega_o = 2\pi \times 4.4$  MHz, and (right)  $\omega_i = 2\pi \times 8.7$  MHz and  $\omega_o = 2\pi \times 2.8$  MHz. It is assumed that both modes are initially in the ground state.

In principle it is possible to perform precision spectroscopy on a motional sideband instead of on the carrier. The resonance frequencies of the normal modes can typically be measured to  $\sim$  kHz accuracy (see section 4.7). If the transition frequency is known with an uncertainty that is much lower than the sideband spacing, the sideband orders  $s_i$  and  $s_o$  can be determined. Then the carrier frequency is calculated by subtracting  $s_i\omega_i + s_o\omega_o$  from the measured line position. In practice the excitation spectrum will be even more complex than is shown in Figure 3.9. Since we excite the transition with a frequency comb, the spectrum repeats every  $\omega_{\text{rep}}/2$ . In the weak axial confinement case, the repetition rate can be set to a multiple of the frequency  $\omega_i$  of the dominant in-phase mode. The frequency comb excitation will then drive multiple sideband simultaneously, and no “new” sidebands are created in the spectrum [95]. However, sympathetic cooling becomes inefficient if the ion motion is only weakly coupled [105]. In the case of strong axial confinement, the more dense and irregular sideband spacing could make it challenging to identify the correct sideband. One possible solution would be to bring the ions close together for cooling, and then to separate them during the excitation of the  $\text{He}^+$  ion [104]. This could for example be achieved by changing the endcap electrode voltage of the linear Paul trap. One additional benefit is that the probability of accidentally ionizing the  $\text{Be}^+$  ion with the XUV spectroscopy radiation is reduced for larger ion spacing.

### Axial anticollinear excitation

Large mixed ion crystals, like the one shown in Figure 3.7 (b), typically contain at least a few hundred ions and therefore have hundreds or even thousands of normal modes. Motional sidebands can occur at sums and differences of integer multiples of all mode frequencies. The sideband spectrum is therefore extremely dense and merges into a continuum. Achieving Doppler-free spectral lines in large ion crystals consequently requires working in the Lamb-Dicke regime where the carrier dominates the spectrum [106]. As we will show, this can be achieved by anticollinear excitation of the 1S-2S transition in the  $\text{He}^+$  ions.

In the following we assume that the laser beams are aligned along the  $z$  axis of the trap. We introduce the operator for the  $z$  coordinate of the  $j$ th ion  $\hat{z}_j = \hat{\mathbf{r}}_j \cdot \mathbf{e}_z$ , and  $z_j^{(0)} = \mathbf{r}_j^{(0)} \cdot \mathbf{e}_z$ . We assume that this is the  $\text{He}^+$  ion for which we want to determine the excitation dynamics. The Rabi frequency for exciting a two-photon transition with counter-propagating Gaussian pulse trains was derived in the previous section. From Equation 3.42, Equation 3.43, and Equation 3.45 we obtain

$$\hat{\Omega}_{2p} = 2(2\pi\beta_{ge})\sqrt{2\pi}\frac{\tau}{T} \sum_m e^{-\frac{1}{2}(m\omega_{\text{rep}}\tau)^2} \left[ I_1 e^{i2\omega_c \hat{z}_j/c} + I_2 e^{-i2\omega_c \hat{z}_j/c} + \sqrt{I_1 I_2} \left( e^{i2m\omega_{\text{rep}} \hat{z}_j/c} + e^{-i2m\omega_{\text{rep}} \hat{z}_j/c} \right) \right], \quad (3.88)$$

where we have replaced the coordinate  $x$  with the operator  $\hat{z}_j$ . The first two terms inside the square brackets in Equation 3.88 contain kick operators with effective wave vectors  $\pm 2\omega_c/c$  and correspond to collinear excitation. The third term describes anticollinear excitation driven by the  $m$ th comb mode of one pulse train and the  $-m$ th comb mode of the other pulse train. Here, the effective wave vector is given by the wave vector difference between the comb modes  $\pm 2m\omega_{\text{rep}}/c$ .

If the ion crystal is initially in an energy eigenstate  $|\{n_\alpha\}\rangle$ , the carrier Rabi frequency is given by

$$\langle \{n_\alpha\} | \hat{\Omega}_{2p} | \{n_\alpha\} \rangle. \quad (3.89)$$

However, it is usually not possible to prepare a large ion crystal in such a state. This is because the dense sideband spectrum precludes the use of resolved sideband techniques that are employed for cooling single ions or small ion crystals below the Doppler limit [45]. The ion motion is therefore thermal, and a probabilistic description of the motional states has to be used. The probability of finding the mode  $\alpha$  with a motional quantum number  $n_\alpha$  is given by [100]

$$P(n_\alpha) = \frac{(\bar{n}_\alpha)^{n_\alpha}}{(\bar{n}_\alpha + 1)^{n_\alpha + 1}}. \quad (3.90)$$

The mean motional quantum number  $\bar{n}_\alpha$  is [97]

$$\bar{n}_\alpha = \left( e^{\hbar\omega_\alpha/(k_B T)} - 1 \right)^{-1}, \quad (3.91)$$

where  $T$  is the ion temperature, and  $k_B$  is the Boltzmann constant.

In the probabilistic description, the  $\text{He}^+$  ion is no longer in a well-defined motional state. The time evolution of its internal state can therefore also not be given directly. Instead, only statistical averages over the thermal distribution can be calculated. How this averaging has to be performed, depends on the relative time scale of the motional dynamics and the excitation dynamics of the  $\text{He}^+$  ion. If the motional state of the  $\text{He}^+$  ion fluctuates much more rapidly than the time scale of its excitation dynamics, the excitation can be described by a “mean Rabi frequency” that is obtained by averaging over the thermal distribution. In the other limit, when the excitation dynamics are much faster than the motional dynamics, the ion is in a well-defined motional state for each excitation event. In this case, the *result* of the excitation process, for example the scattering or ionization probability, has to be averaged over the thermal distribution (see chapter 3.8 in [107] for a more formal treatment of this problem in the context of Mößbauer spectroscopy). The excitation dynamics of a driven  $\text{He}^+$  ion are governed by the two-photon Rabi frequency, the excited state decay rate, and the 2S ionization rate. For the envisioned experimental parameters, these give a ms time scale. The motional time scale is determined by the *relaxation time* which quantifies how quickly a motionally excited  $\text{He}^+$  ion distributes its kinetic energy to the other ions in the crystal [107, p. 87]. Using our molecular dynamics simulations (see section 5.5), we have determined that this happens on a time scale of a few  $\mu\text{s}$  under our envisioned experimental conditions. We are therefore in the first regime such that the excitation dynamics can be described by averaging Equation 3.89 over the thermal distribution.

Equation 3.89 contains terms of the form

$$\langle \{n_\alpha\} | e^{ik_{\text{eff}} \hat{z}_j} | \{n_\alpha\} \rangle, \quad (3.92)$$

where  $k_{\text{eff}} = \{\pm 2\omega_c/c, \pm 2m\omega_{\text{rep}}/c\}$ . Averaging these terms over the thermal distribution in each mode gives [100]:

$$\begin{aligned} \overline{\langle \{n_\alpha\} | e^{ik_{\text{eff}} \hat{z}_j} | \{n_\alpha\} \rangle} &= e^{ik_{\text{eff}} z_j^{(0)}} \prod_{\alpha=1}^{3N} \left[ \sum_{n_\alpha=0}^{\infty} P(n_\alpha) \langle n_\alpha | e^{in_j^\alpha (\hat{a}_\alpha + \hat{a}_\alpha^\dagger)} | n_\alpha \rangle \right] \\ &= e^{ik_{\text{eff}} z_j^{(0)}} \prod_{\alpha=1}^{3N} \left[ \sum_{n_\alpha=0}^{\infty} \frac{(\bar{n}_\alpha)^{n_\alpha}}{(\bar{n}_\alpha + 1)^{n_\alpha + 1}} e^{-(\eta_j^\alpha)^2/2} L_{n_\alpha}^0 \left( (\eta_j^\alpha)^2 \right) \right] \\ &= e^{ik_{\text{eff}} z_j^{(0)}} \prod_{\alpha=1}^{3N} e^{-(\eta_j^\alpha)^2 (\bar{n}_\alpha + \frac{1}{2})}. \end{aligned} \quad (3.93)$$

In the last step we have used the Laguerre polynomial sum identity [100]

$$\sum_{n=0}^{\infty} z^n L_n^0(x) = \frac{e^{-\frac{zx}{1-z}}}{1-z}, \quad (3.94)$$

where  $x = (\eta_j^\alpha)^2$  and  $z = \bar{n}_\alpha / (\bar{n}_\alpha + 1)$ .

We now insert Equation 3.79 into Equation 3.93 and obtain:

$$\begin{aligned} \overline{\langle \{n_\alpha\} | e^{ik_{\text{eff}} \hat{z}_j} | \{n_\alpha\} \rangle} &= e^{ik_{\text{eff}} z_j^{(0)}} \prod_{\alpha=1}^{3N} e^{-(k_{\text{eff}} \beta_{2N+j}^{\alpha'})^2 (\bar{n}_\alpha + \frac{1}{2}) \hbar / (2m_j \omega_\alpha)} \\ &= e^{ik_{\text{eff}} z_j^{(0)}} \prod_{\alpha=1}^{3N} e^{-\frac{1}{2} (k_{\text{eff}} \beta_{2N+j}^{\alpha'})^2 \langle \hat{\pi}_\alpha^2 \rangle / m_j}, \end{aligned} \quad (3.95)$$

where we have used that the mean square of the normal coordinate  $\pi_\alpha$  is given by [97]

$$\langle \hat{\pi}_\alpha^2 \rangle = \frac{\hbar}{\omega_\alpha} \left( \bar{n}_\alpha + \frac{1}{2} \right). \quad (3.96)$$

Using Equation 3.73, the root mean square fluctuation  $z_j^{\text{rms}}$  of the coordinate  $z_j$  around its equilibrium position  $z_j^{(0)}$  can be expressed in terms of the mean squares of the normal coordinates:

$$\begin{aligned} (z_j^{\text{rms}})^2 &\equiv \langle (\hat{z}_j - z_j^{(0)})^2 \rangle = \frac{1}{m_j} \sum_{\alpha=1}^{3N} \sum_{\gamma=1}^{3N} \langle \beta_{2N+j}^\alpha \beta_{2N+j}^\gamma \hat{\pi}_\alpha \hat{\pi}_\gamma \rangle \\ &= \frac{1}{m_j} \sum_{\alpha=1}^{3N} (\beta_{2N+j}^\alpha)^2 \langle \hat{\pi}_\alpha^2 \rangle, \end{aligned} \quad (3.97)$$

where we have used that the normal coordinates are uncorrelated. By inserting Equation 3.97 into Equation 3.95, we obtain:

$$\overline{\langle \{n_\alpha\} | e^{ik_{\text{eff}} \hat{z}_j} | \{n_\alpha\} \rangle} = e^{ik_{\text{eff}} z_j^{(0)}} e^{-\frac{1}{2} (k_{\text{eff}} z_j^{\text{rms}})^2}. \quad (3.98)$$

The exponential reduction of the carrier due thermal motion of atoms is well known in the fields of X-ray diffraction and Mößbauer spectroscopy where the term is called the *Debye-Waller factor* [107, p. 45].

In the classical regime where the amplitude of ion motion is much larger than the size of the ground state wave functions of the ions,  $z_j^{\text{rms}}$  can be determined from molecular dynamics simulations. We obtain simulated ion trajectories for a mixed Be<sup>+</sup>/He<sup>+</sup> ion crystal at different temperatures as described in section 5.5. The resulting root mean square motions of the He<sup>+</sup> ions along the trap axis are shown in Figure 3.10. Typical amplitudes at temperatures of a few mK are several hundred nm.

Using Equation 3.98 we can now write down an expression for the mean carrier Rabi frequency:

$$\begin{aligned} \overline{\langle \{n_\alpha\} | \hat{\Omega}_{2p} | \{n_\alpha\} \rangle} &= 2(2\pi\beta_{ge}) \sqrt{2\pi} \frac{\tau}{T} \sum_m e^{-\frac{1}{2} (m\omega_{\text{rep}}\tau)^2} \left[ \right. \\ &\quad e^{-\frac{1}{2} (2\omega_c z_j^{\text{rms}}/c)^2} \left( I_1 e^{i2\omega_c z_j^{(0)}/c} + I_2 e^{-i2\omega_c z_j^{(0)}/c} \right) \\ &\quad \left. + \sqrt{I_1 I_2} e^{-\frac{1}{2} (2m\omega_{\text{rep}} z_j^{\text{rms}}/c)^2} \left( e^{i2m\omega_{\text{rep}} z_j^{(0)}/c} + e^{-i2m\omega_{\text{rep}} z_j^{(0)}/c} \right) \right]. \end{aligned} \quad (3.99)$$

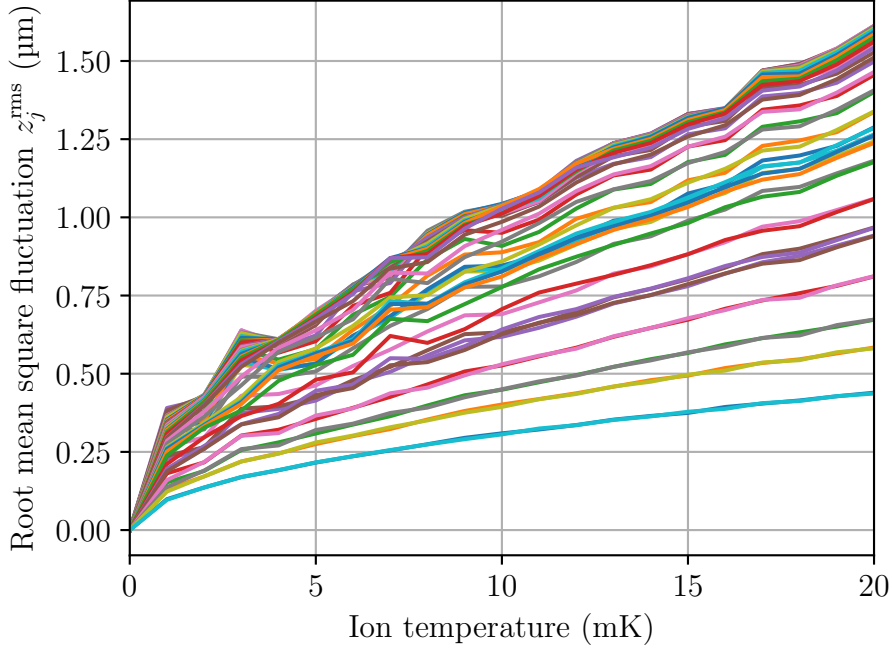


Figure 3.10: Ion position fluctuations obtained from a molecular dynamics simulation. The motion of an ion crystal containing 50  $\text{He}^+$  ions and 1450  $\text{Be}^+$  ions (see Figure 2.10) was simulated for 5 ms at different temperatures. Each line corresponds to the root mean square fluctuation of the  $z$  coordinate of one  $\text{He}^+$  ion in the chain. The ions near the ends of the chain are surrounded by fewer  $\text{Be}^+$  ions and move significantly less than the ones in the center of the chain.

As in the previous section, we replace the sum over the frequency comb modes with an integral using  $\sum_m \approx \frac{1}{\omega_{\text{rep}}} \int_{-\infty}^{\infty} d(m\omega_{\text{rep}})$ . After evaluating the integral, we obtain the final result:

$$\overline{\langle \{n_\alpha\} | \hat{\Omega}_{2p} | \{n_\alpha\} \rangle} \approx 2(2\pi\beta_{ge}) \left[ e^{-\frac{1}{2}(2\omega_c z_j^{\text{rms}}/c)^2} \left( I_1 e^{i2\omega_c z_j^{(0)}/c} + I_2 e^{-i2\omega_c z_j^{(0)}/c} \right) + 2\sqrt{I_1 I_2} \frac{c\tau}{\sqrt{(2z_j^{\text{rms}})^2 + (c\tau)^2}} e^{-2(z_j^{(0)})^2 / [(2z_j^{\text{rms}})^2 + (c\tau)^2]} \right]. \quad (3.100)$$

The first term inside the square brackets gives the contribution to the Rabi frequency due to collinear excitation. The effective wave vector for this process is  $k_{\text{eff}} = 2\omega_c/c = 2\pi/30.4 \text{ nm}$ . Typical motion amplitudes of a few hundred nm are much larger than  $1/k_{\text{eff}}$ . Collinear excitation of the carrier is therefore strongly suppressed by the Debye-Waller factor.

The anticollinear excitation process has not just one effective wave vector, but a range of values that are given by the wave vector differences of the contributing comb modes. The reduction of the carrier Rabi frequency therefore takes a different form and is given

by the term

$$\frac{c\tau}{\sqrt{(2z_j^{\text{rms}})^2 + (c\tau)^2}} e^{-2(z_j^{(0)})^2 / [(2z_j^{\text{rms}})^2 + (c\tau)^2]}, \quad (3.101)$$

which also contains the exponential drop of the Rabi frequency if the ion is located outside the pulse collision volume ( $|z_j^{(0)}| > c\tau$ ).

The pulse duration  $\tau$  is connected to the intensity FWHM of the frequency comb spectrum  $\Delta\omega_{1/2}$  by

$$\tau = \frac{2\sqrt{2\ln(2)}}{\Delta\omega_{1/2}}. \quad (3.102)$$

Figure 3.11 shows Equation 3.101 evaluated for an ion in the center of the pulse collision volume ( $z_j^{(0)} = 0$ ). Typical motional amplitudes of few hundred nm correspond to a reduction of the carrier Rabi frequency by around 10%.

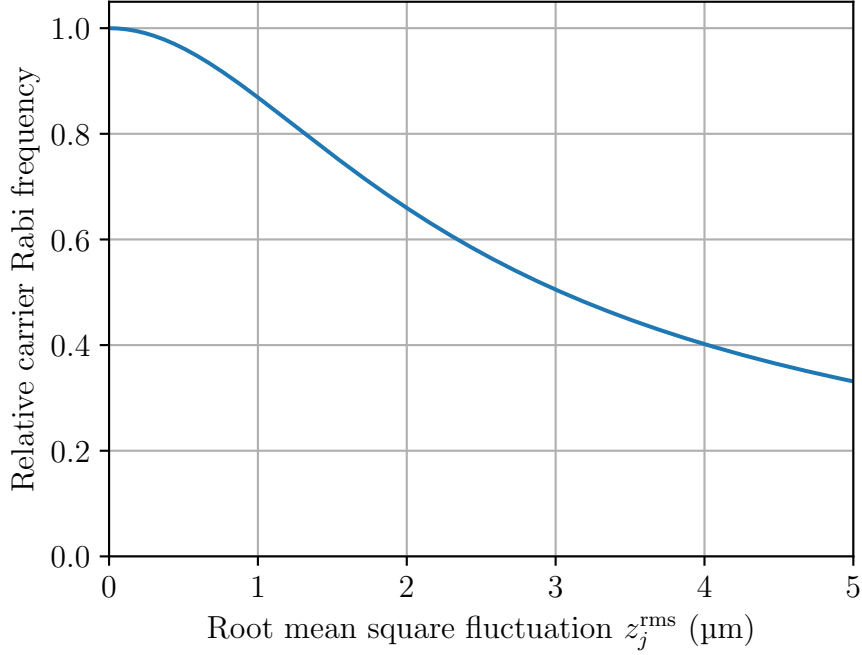


Figure 3.11: Reduction of the carrier Rabi frequency due to ion position fluctuations for anticollinear excitation. The ion is located in the center of the pulse collision volume, and an intensity FWHM of the frequency comb spectrum of  $\Delta\omega_{1/2} = 2\pi \times 32$  THz is assumed.

## Conclusion

In conclusion, we expect that both radial collinear excitation and axial anticollinear excitation are viable in our experiment. On the other hand, for axial collinear excitation in a large ion crystal, the carrier is completely suppressed by the Debye-Waller factor. For



example, even relatively small rms position fluctuations of 300 nm lead to a Debye-Waller factor of  $\exp(-2000)$ .

One drawback of collinear radial excitation is the complicated sideband spectrum that has to be accounted for as described above. However, the configuration would allow detecting the  $\text{He}^+$  1S-2S excitation with a scheme similar to quantum logic spectroscopy [104]. The first step is to cool at least one mode of the mixed ion crystal to the ground state using Raman sideband cooling on the  $\text{Be}^+$  ion. In the ground state, the red ( $s_\alpha < 0$ ) sidebands vanish since there are no lower lying states. If the  $\text{He}^+$  ion is excited on a motional sideband, the motional state of the ion crystal changes. This can then be detected by performing spectroscopy on the red sidebands in the Raman spectrum of the  $\text{Be}^+$  ion [108]. In comparison to detecting  $\text{He}^{2+}$  created by resonant three-photon ionization, this detection scheme has the advantage that it is nondestructive if the laser intensity is low enough such that ionization is avoided. It could therefore allow for much faster experimental cycles since the ion does not have to be reloaded after each excitation. However, Raman sideband cooling requires significant additional experimental effort compared to Doppler cooling. Furthermore, the limited fidelity of the motional state measurement leads to a background which could obscure a very weak excitation signal. Alternatively, the ionization of  $\text{He}^+$  to  $\text{He}^{2+}$  could be easily detected by a position shift of the  $\text{Be}^+$  ion.

Anticollinear axial excitation has the advantage that the motional spectrum consists only of the carrier resonance. Another advantage is that having many  $\text{Be}^+$  ions makes the scheme somewhat more robust against accidentally losing some of them due to ionization or collisions with background gas. As we will show in chapter 5, the production of  $\text{He}^{2+}$  ions can be detected also in large ion crystals with single-particle sensitivity. We therefore believe that this scheme is well suited for a first observation of the transition and have decided to implement it in our setup.



# Chapter 4

## Ion trap setup

This chapter provides a detailed description of the ion trap setup we built for the  $\text{He}^+$  spectroscopy experiment.

### 4.1 Ion trap

#### 4.1.1 Trap electrodes

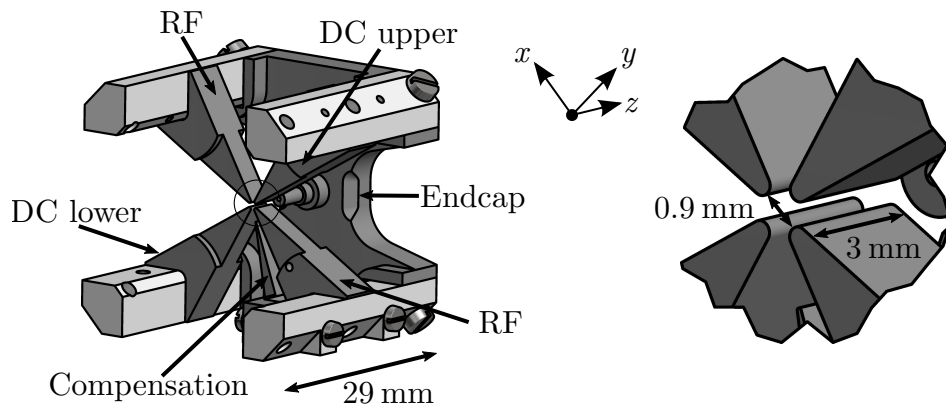


Figure 4.1: Geometry of the ion trap. The trap axis is in  $z$  direction. Radial confinement is provided by four blade electrodes. An RF voltage is applied to one diagonal pair, while the other two electrodes are held at DC voltages. Two endcap electrodes are used for the axial confinement. For clarity, only one of the endcaps is shown. Holes are drilled through the endcaps in order to allow for optical access along the trap axis. The compensation electrode can be used to compensate for field asymmetries due to stray electric fields and electrode misalignment.

Figure 4.1 shows the geometry of our ion trap. It consists of four blade electrodes with an axial length of 3.00 mm. The electrodes have cylindrical tips with a radius  $R = 0.225$  mm, and their surfaces have a distance of  $r_0 = 0.45$  mm from the trap axis. This

relatively small size was chosen such that a sufficiently large Mathieu  $q$  parameter can be achieved with a moderate RF voltage. The ratio  $R/r_0 = 0.5$  is smaller than the “ideal” value of 1.146 for which the 12-pole term of the potential vanishes (see subsection 2.1.3). This value was chosen since smaller tip diameters increase the gap between the electrodes which allows for more convenient optical access to the stored ions.

A radio frequency signal is applied to one diagonal pair of blade electrodes in order to generate the radial confinement. We call these the RF electrodes. The other pair consists of the two DC electrodes which are held at constant voltages. Axial confinement is provided by a pair of endcap electrodes that are held at a positive high voltage. Their surfaces are located 3.50 mm from the trap center. In order to allow axial optical access to the ions, holes with 0.5 mm diameter are drilled through the endcaps. An additional compensation electrode is located between two of the blade electrodes. By adjusting the voltages of the DC electrodes and the compensation electrode, unwanted electric fields in the trap center can be compensated. Here, the relatively large gap between the blade electrodes helps to make the compensation electrode more effective.

During trap operation, the trapping volume is illuminated with ultraviolet laser beams for beryllium ionization,  $\text{Be}^+$  laser cooling, and  $\text{He}^+$  spectroscopy. Furthermore, an electron gun is used to produce  $\text{He}^+$  ions. It is therefore difficult to avoid charge buildup on any electrical insulators in the trap structure. If insulators are located close to the ions, the resulting patch potentials can lead to large electric fields that displace the ions from the trap center. The trap electrodes are therefore machined from molybdenum which does not oxidize at ordinary temperatures and has a low and uniform surface potential [109, p. 356]. The electrodes are held by insulating spacers that are manufactured from a machinable ceramic.<sup>1</sup>

### 4.1.2 Trap potential

We use a commercial finite element analysis software<sup>2</sup> to simulate the electric potential created by the trap electrode structure shown in Figure 4.1. The software can directly import the trap geometry from the computer-aided design (CAD) files that were used to machine the electrodes. The simulated geometry consists of the blade electrodes, endcap electrodes, and compensation electrode. Small unimportant features, such as screw holes, were removed to reduce the computation times. The software divides up space into a three-dimensional mesh and numerically solves Laplace’s equation for given voltages applied to the electrodes.

#### Radial potential

To analyze the radial confinement, a voltage of 1 V is applied to the RF electrodes while all other electrodes are grounded. Figure 4.2 shows cuts through the resulting potential on connection lines between the opposing surfaces of the two RF electrodes.

---

<sup>1</sup>Corning MACOR.

<sup>2</sup>COMSOL Multiphysics.

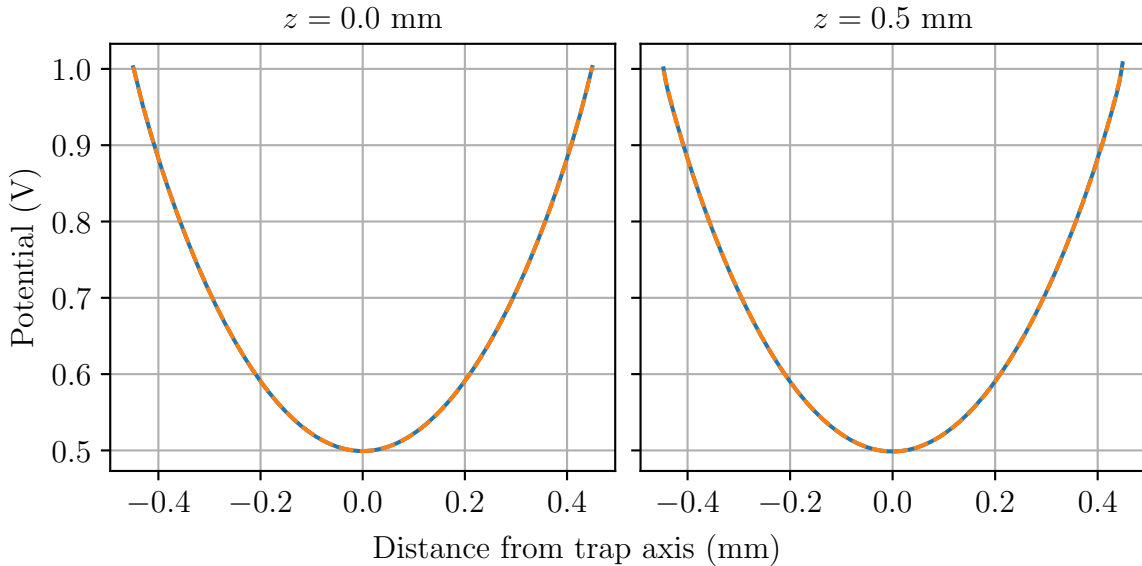


Figure 4.2: Simulated trap potential on connection lines between opposing RF electrode surfaces at different axial positions. The solid blue lines are the results of the simulation, and the dashed orange lines are polynomial fits according to Equation 2.22.

As discussed in subsection 2.1.3, the potential contains terms beyond the quadrupole term since the electrodes do not have the ideal hyperbolic shape. In order to quantify the higher-order contributions, we fit the simulated potential with the multipole expansion given in Equation 2.22 up to the  $(r/r_0)^{14}$  term. Typical large ion crystals in our setup have axial lengths of a few hundred  $\mu\text{m}$  and radial diameters of less than 200  $\mu\text{m}$  (see Figure 2.8). It is evident from Figure 4.2 that the potential does not change very much for an axial distance of up to  $\pm 0.5$  mm from the trap center. From the fit we obtain an effective trap size of  $r_{\text{eff}} = 0.468$  mm in the center and  $r_{\text{eff}} = 0.469$  mm at  $z = 0.5$  mm. The total contribution of anharmonic terms up to  $(r/r_0)^{14}$  is less than 0.1% of the quadrupole term for  $r < 100$   $\mu\text{m}$ . In the radial direction we therefore do not expect significant deviations from the dynamics of an ideal Paul trap.

### Axial potential

The static axial potential is simulated by applying 1 V to the endcap electrodes and grounding the other ones. Figure 4.3 shows the resulting potential along the trap axis. We can see that the blade electrodes surrounding the trapping region lead to a strong shielding of the potential produced by the endcap electrodes.

We fit the potential in the range of  $|z| \leq 0.5$  mm with an even polynomial up to fourth order:

$$\varphi_{\text{ax}}(z) = \frac{U_{\text{ec}}}{2} \left[ \kappa \left( \frac{z}{z_0} \right)^2 + C_4 \left( \frac{z}{z_0} \right)^4 \right] + U_0, \quad (4.1)$$

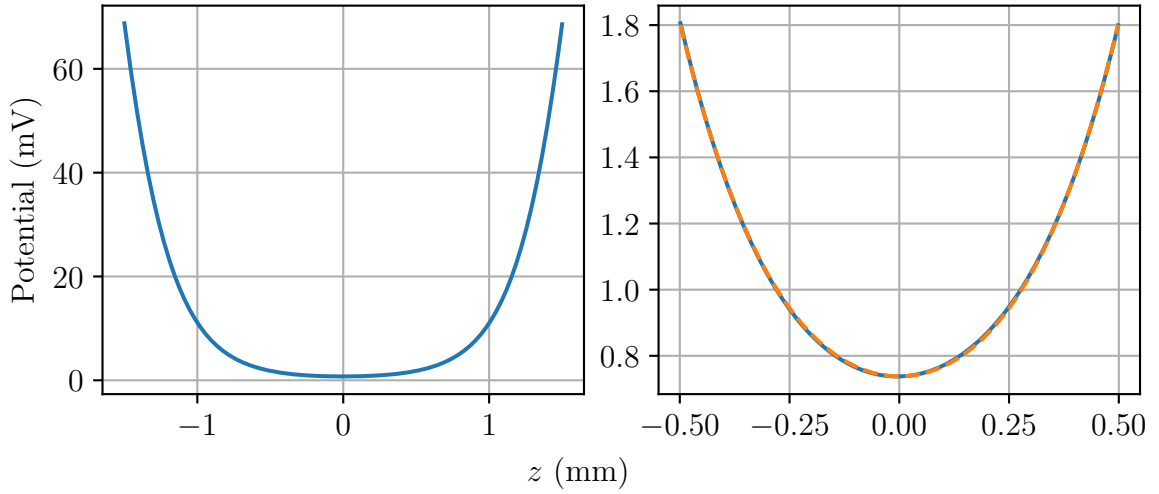


Figure 4.3: Simulated axial trap potential due to the endcap electrodes along the trap axis. The left plot shows the potential along the entire length of the blade electrodes, while the right plot is limited to  $\pm 0.5$  mm around the trap center. The solid blue lines are the results of the simulation, and the dashed orange line is a fit of Equation 4.1.

where  $U_{ec} = 1$  V is the voltage applied to the endcaps,  $U_0$  is the potential in the trap center,  $z_0 = 3.5$  mm is the distance between the endcap electrodes and the trap center,  $\kappa$  is the geometrical factor defined in Equation 2.24, and  $C_4$  is the coefficient of the cubic component of the potential. We obtain a geometrical factor of  $\kappa = 0.073$ . At a distance of 0.5 mm from the trap center, the cubic term contributes 31% to the total potential.

### 4.1.3 RF resonator

Paul traps for atomic and molecular ions are typically driven with radio frequencies of a few tens of MHz such that secular frequencies in the MHz range can be achieved. The trap electrodes constitute an almost entirely capacitive load which is badly matched to the  $50 \Omega$  characteristic impedance of RF sources and amplifiers. If an ion trap is directly connected to an RF source, a complex voltage divider is formed between the output impedance of the source and the reactance of the trap. This means that the voltage across the trap electrodes can be at most twice the voltage that the source delivers into a  $50 \Omega$  load. Typical RF amplitudes required for driving Paul traps are above 100 V. Very high RF powers would be required in order to reach such amplitudes directly from an RF amplifier. A more efficient technique is to use a resonant transformer for matching the  $50 \Omega$  source impedance to the capacitive ion trap. Another benefit of using a resonant circuit is that due to the limited bandwidth, electrical noise is filtered out that could otherwise heat up the motion of the ions.

### Helical resonators

In our frequency range helical resonators [110–112] with dimensions of a few cm are well suited for this task. Figure 4.4 shows a schematic of such a resonator. It consists of a large helical main coil that is housed in a cylindrical shield. The inductance of the main coil and the resistance and capacitance of the resonator and the attached trap electrodes form a resonant RLC circuit. The signal is inductively coupled in through a smaller antenna coil that is placed close to the main coil. The design of our helical resonators is described in detail in [113], and we only summarize the main results here.

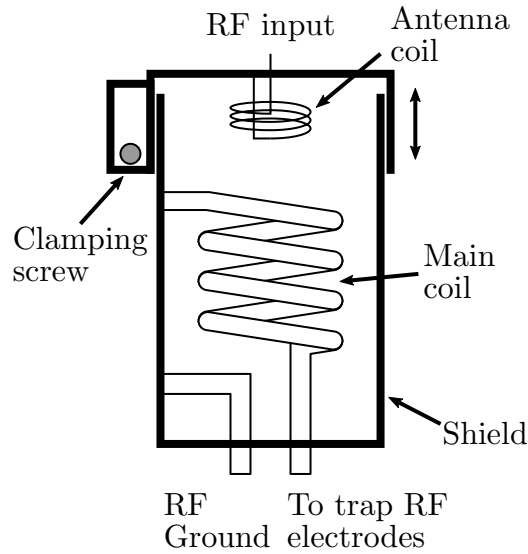


Figure 4.4: Schematic of a helical resonator. A resonant RLC circuit is formed by the inductance of the main coil and the overall capacitance and resistance of the resonator and the attached ion trap. The RF signal is coupled in through the antenna coil which is mounted to the lid that closes the resonator body. The coupling between the coils can be adjusted by sliding the lid up or down. It is then clamped in place with a screw.

Figure 4.5 shows the equivalent circuit that we use to describe the system. The RF source consists of a signal generator<sup>3</sup> and an amplifier<sup>4</sup> with a characteristic impedance of  $Z_0 = 50\ \Omega$ . The helical resonator is modelled as the main coil with inductance  $L_c$  that is inductively coupled to the antenna coil with inductance  $L_a$ . The main coil and the cylindrical shield have resistances  $R_c$  and  $R_s$ , respectively. The overall parallel capacitance of the resonator is  $C_h$ . The ion trap consists of a capacitance  $C_t$  and a series resistance  $R_t$ . Typically, the resistance of the trap  $R_t$  is much smaller than its reactance  $1/(\omega C_t)$ , where  $\omega$  is the frequency at which the circuit operates. In this case the resistances and capacitances of the helical resonator and the ion trap can be lumped together as shown in the bottom of Figure 4.5. Here,  $C = C_h + C_t$  is the combined capacitance of the trap

<sup>3</sup>Rohde & Schwarz SMC100A.

<sup>4</sup>Mini-Circuits ZHL-20W-13.

and the helical resonator, and  $R_{\text{ESR}} = R_c + R_s + R_t[C_t/(C_h + C_t)]^2$  is the equivalent series resistance of the circuit.

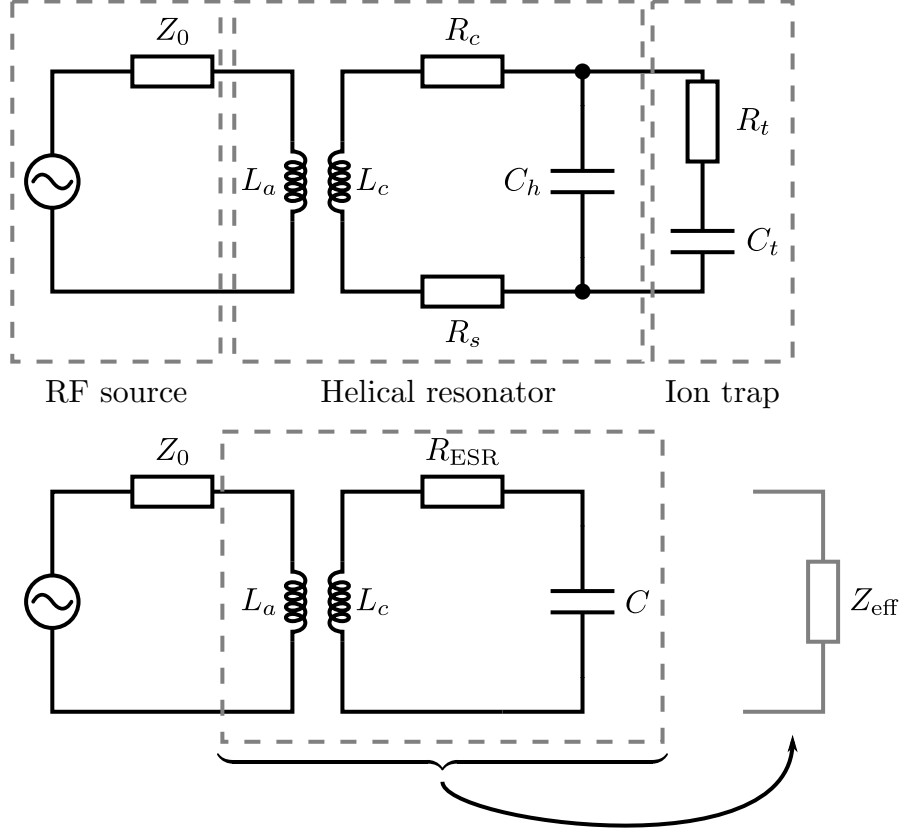


Figure 4.5: Equivalent circuit of the ion trap RF supply (top) and simplified version (bottom). The symbols are explained in the main text.

The power dissipated in  $R_{\text{ESR}}$  is maximal when the circuit is impedance matched to the RF source. Since  $R_{\text{ESR}}$  and  $C$  are connected in series, this condition also maximizes the voltage drop across the ion trap. Impedance matching means that the effective impedance  $Z_{\text{eff}}$  of the helical resonator and ion trap is equal to the characteristic impedance  $Z_0$  of the RF source. In practice this matching is achieved by adjusting the distance between the antenna coil and the main coil until the back-reflected RF power is minimized. From this condition the resonance frequency of the circuit can be calculated:

$$\omega_0 = \frac{1}{\sqrt{L_c C - \frac{R_{\text{ESR}}}{Z_0} L_a C}}, \quad (4.2)$$

and the resulting voltage enhancement of the resonator is

$$\eta = \frac{U_{\text{out}}}{U_{\text{in}}} = \frac{1}{\omega_0 C \sqrt{Z_0 R_{\text{ESR}}}}, \quad (4.3)$$

where  $U_{\text{in}}$  is the voltage amplitude produced by the RF source, and  $U_{\text{out}}$  is the voltage amplitude across the trap electrodes.



### Resonator design

If the circuit parameters are known, Equation 4.2 can be used to calculate the expected resonance frequency of the helical resonator. The capacitance of an ion trap can be directly measured with an LCR meter. We used a network analyzer<sup>5</sup> that has an impedance analysis function and obtained  $C_t = 16$  pF for our trap. Empirical expressions for the inductance  $L_c$  and capacitance  $C_h$  of a helical resonator are [110]

$$L_c = 39.37 b \frac{0.025 d^2 [1 - (d/D)^2]}{\tau^2} \times 10^{-6} \text{ H/m}, \quad (4.4)$$

$$C_h = 39.37 b \frac{0.75}{\log_{10}(D/d)} \times 10^{-12} \text{ F/m}, \quad (4.5)$$

where  $b$  is the height of the main coil,  $\tau$  is its winding pitch,  $d$  is its diameter, and  $D$  is the inner diameter of the cylindrical shield.

The resistances  $R_c$ ,  $R_s$ , and  $R_t$  are more difficult to estimate. However, since typically  $R_{\text{ESR}} \ll Z_0$  and  $L_a \lesssim L_c$ , we can neglect the second term under the square root in Equation 4.2 and get

$$\omega_0 \approx \frac{1}{\sqrt{L_c(C_h + C_t)}}. \quad (4.6)$$

We chose an inner shield diameter of  $D = 7.6$  cm and a main coil with diameter  $d = 3$  cm, height  $b = 5$  cm, and winding pitch  $\tau = 11$  mm. The calculated inductance and capacitance are  $L_c = 309$  nH and  $C_h = 3.66$  pF, respectively. This results in an expected resonance frequency of  $\omega_0 = 2\pi \times 65$  MHz.

In order to minimize ohmic losses, the main coil is wound from thick copper wire with 5 mm diameter. One end is soldered to the copper shield, while the other end is terminated with a connector that is used to attach the resonator to the ion trap electrodes. At the other end the resonator is closed with a copper lid that also holds the antenna coil. The antenna coil is hand wound from 1 mm wire. We found that 2.5 windings with a diameter of 2 cm and 5 mm winding pitch work well. The lid can be slid along the shield in order to optimize the coupling between the two coils. A small amount of lubricant had to be used to prevent galling of the copper surfaces. Once good impedance matching is achieved, the lid can be clamped in place with a screw.

### Characterization

The helical resonator is characterized by connecting the network analyzer to the antenna coil and measuring the frequency dependence of the  $S_{11}$  parameter:

$$S_{11} = \frac{P_{\text{ref}}}{P_{\text{in}}} = \frac{P_{\text{in}} - P_{\text{diss}}}{P_{\text{in}}}, \quad (4.7)$$

where  $P_{\text{in}}$  is the input power,  $P_{\text{ref}}$  is the reflected power, and  $P_{\text{diss}}$  is the power dissipated in the circuit.

---

<sup>5</sup>Keysight E5061B.

The resonance is visible as a dip in the  $S_{11}$  value, and the impedance matching is optimized by maximizing the depth of the dip. As shown in Figure 4.6, a resonance frequency of 65.3 MHz is achieved which is in very good agreement with the theoretical calculation. On resonance the  $S_{11}$  parameter reaches almost  $-30$  dB such that essentially the entire available RF power is coupled into the resonator.

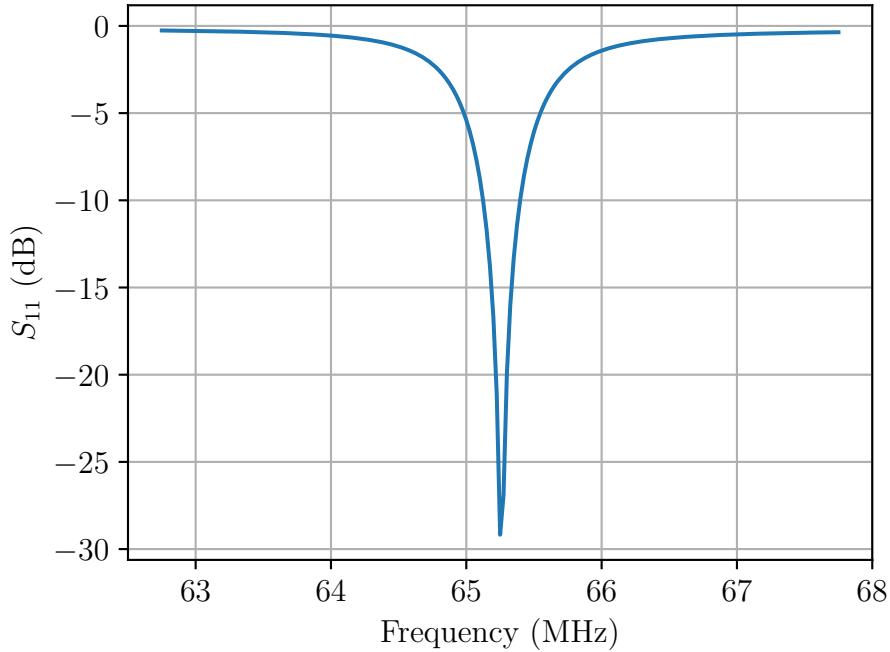


Figure 4.6:  $S_{11}$  parameter of the impedance matched helical resonator showing a strong resonance at 65.3 MHz.

The network analyzer can also be used to determine the equivalent series resistance  $R_{\text{ESR}}$  of the circuit. The equations describing an RLC circuit are of the same form as those of a damped harmonic oscillator. This means that the resonance has a Lorentzian shape whose width is determined by the losses of the system. The  $Q$  factor of a resonator is given by the ratio between the resonance frequency and bandwidth:

$$Q = \frac{\omega_0}{\Delta\omega}, \quad (4.8)$$

where  $\Delta\omega$  is the FWHM bandwidth of the power dissipated in the lossy part of the system. The  $Q$  factor of the circuit shown in Figure 4.5 is quite sensitive to the coupling between the antenna coil and the main coil since the output impedance  $Z_0$  of the RF source damps the oscillation in addition to  $R_{\text{ESR}}$  [114]. We therefore increased the distance between the antenna coil and main coil such that  $L_a$  and  $L_c$  are only weakly coupled. Under this condition the influence of  $Z_0$  and  $L_a$  on the circuit is small, and the helical resonator and ion trap can be treated as a series RLC circuit consisting of the effective series resistance

$R_{\text{ESR}}$ , the main coil inductance  $L_c$ , and the total capacitance  $C = C_h + C_t$ . The  $Q$  factor of this circuit is

$$Q = \frac{1}{R_{\text{ESR}}} \sqrt{\frac{L_c}{C_h + C_t}}. \quad (4.9)$$

From Equation 4.7 we can see that the bandwidth of  $P_{\text{diss}}$  is equivalent to the bandwidth of  $1 - S_{11}$ . Figure 4.7 shows the measurement result for our resonator. The curve has a sloped background which we attribute to the frequency dependent loss in the coaxial cable from the network analyzer to the helical resonator. To extract the resonance width, we therefore fit the curve with the sum of a linear function and a Lorentzian function. We obtain an FWHM bandwidth of 379 kHz, corresponding to  $Q = 172$ . From Equation 4.9 we obtain an effective series resistance of  $R_{\text{ESR}} = 0.73 \Omega$ . The resulting voltage enhancement given by Equation 4.3 is  $\eta = 21$ .

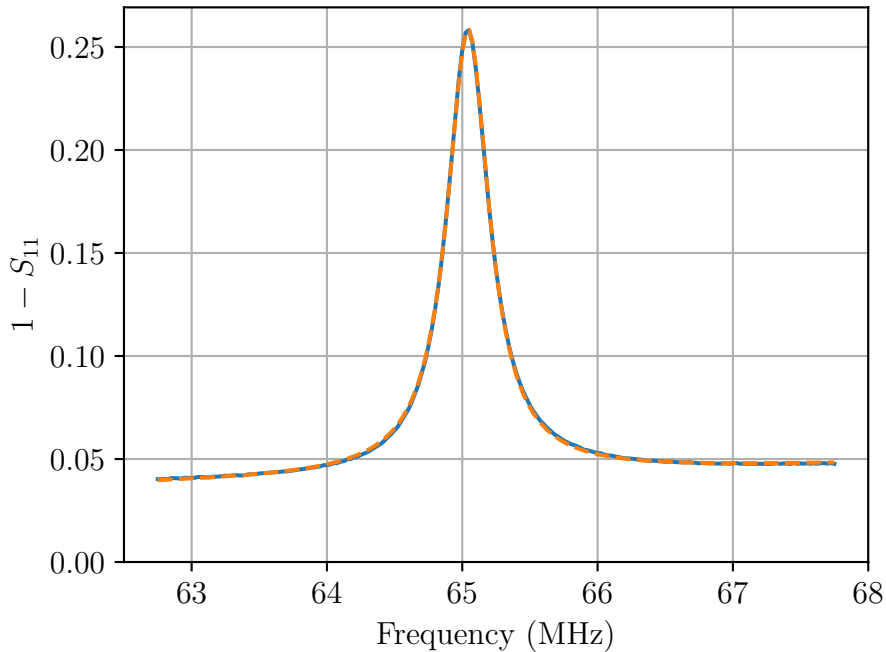


Figure 4.7: Power coupled into the resonator for weak coupling between the antenna coil and main coil (solid blue line). A fit with the sum of a Lorentzian and a sloped background (dashed orange line) yields  $Q = 172$ .

We later remeasured the  $Q$  factor and obtained lower values between 70 and 90. This corresponds to  $R_{\text{ESR}}$  between  $1.4 \Omega$  and  $1.8 \Omega$  and voltage enhancements of 13 to 15. We attribute this to increased contact resistance due to surface oxidization of the bare copper connectors between the helical resonator and the vacuum feedthrough going to the ion trap. We typically operate the RF amplifier well below its rated power. The decrease in voltage enhancement can therefore be easily compensated by increasing the input RF power. If higher  $Q$  factors are required, connectors plated with a corrosion resistant material such

as silver or gold could be used.

#### 4.1.4 Electrode connections

Figures 4.8 and 4.9 show the electrical connections of the trap electrodes. The endcap electrodes are connected to two independent channels of a high voltage power supply<sup>6</sup> that can output up to 2 kV. The DC electrodes are connected to analog outputs of a multifunction I/O card<sup>7</sup> which have a range of  $\pm 10$  V. Since the compensation electrode is placed further away from the ions than the DC electrodes, it requires a higher voltage to be effective. A bipolar high voltage amplifier<sup>8</sup> is therefore used to increase the range of the I/O card to  $\pm 200$  V.

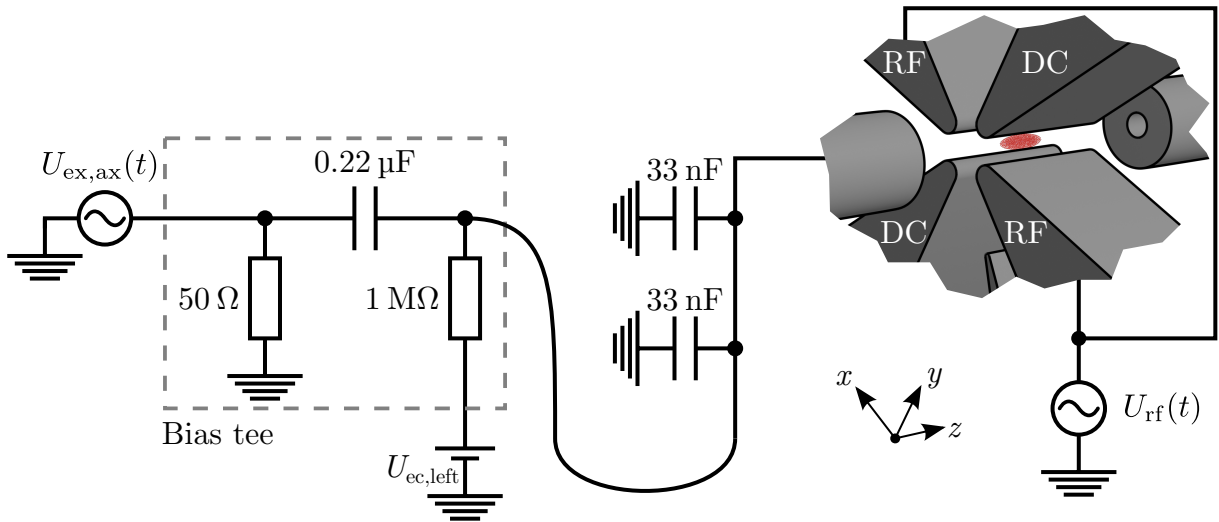


Figure 4.8: Electrical connections of the endcap electrodes and RF electrodes. The RF electrodes are driven by the helical resonator which is not shown here. The circuit for the right endcap is identical to the one for the left endcap. The secular excitation voltage  $U_{\text{ex,ax}}(t)$  is only applied to one of the endcaps.

Due to their close proximity, the other trap electrodes are capacitively coupled to the RF electrodes. To reduce the resulting RF pickup, the electrodes are shorted to ground at high frequencies using capacitors. We use 1 nF for the DC electrodes and compensation electrode, and 33 nF for the endcap electrodes. The capacitors are soldered to a small circuit board that is located as close as possible to the air side of the vacuum feedthrough used for the electrode connections. This minimizes the cable inductance between the electrodes and capacitors. A too large inductance would lead to a large impedance at high frequency which makes the capacitors ineffective at providing an RF ground path.

<sup>6</sup>iseg NHR 40 20r\_SHV.

<sup>7</sup>National Instruments USB-6229.

<sup>8</sup>Thorlabs HVA200.

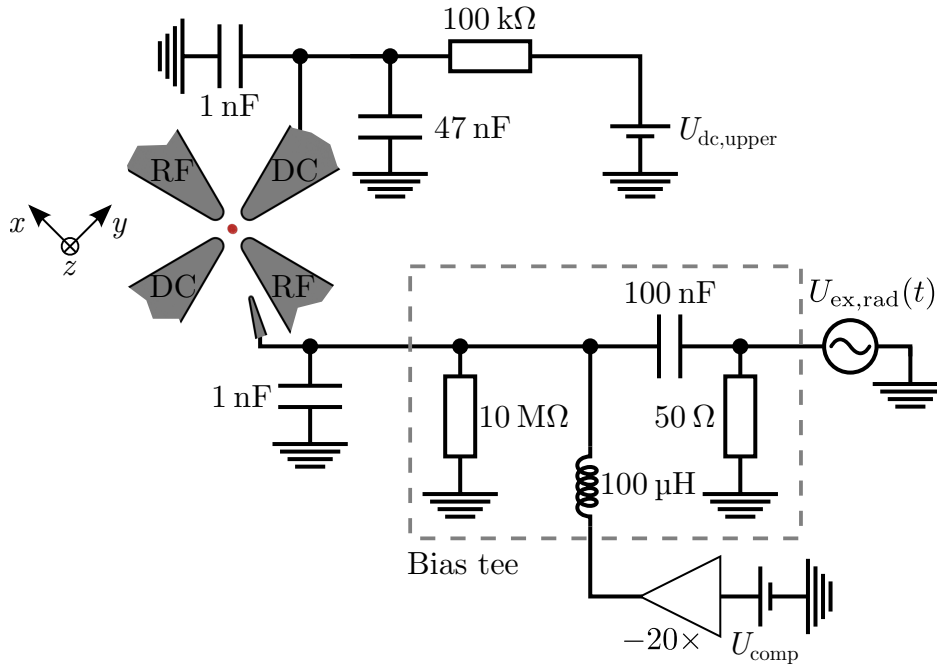


Figure 4.9: Electrical connections of the DC electrodes and compensation electrode. The circuit for the lower DC electrode is identical to the one for the upper DC electrode.

In order to measure the secular frequencies of the trapped ions (see section 4.7 and section 5.3), we have to apply additional oscillating electric fields to excite the motion of the ions. The endcap electrodes and compensation electrode are therefore equipped with bias tees that allow adding the excitation voltages  $U_{\text{ex,ax}}(t)$  and  $U_{\text{ex,rad}}(t)$  to the DC voltages. Since the high voltage amplifier for the compensation electrode turned out to be sensitive to RF pickup, we added a  $100\ \mu\text{H}$  inductor for protection. The  $10\ \text{M}\Omega$  resistor at the output of the bias tee circuit discharges the capacitor when the amplifier is disconnected.

Noise on the trap voltages creates fluctuating forces on the ions which heat their motion. The trap electrodes are therefore equipped with low-pass filters. The DC electrodes are particularly sensitive since they are closest to the ions. Their voltages are filtered with a  $100\ \text{k}\Omega$  resistor and a  $47\ \text{nF}$  capacitor which results in a cutoff frequency of  $34\ \text{Hz}$ . The filtering for the endcap voltages is provided by the  $1\ \text{M}\Omega$  current limiting resistor built into the bias tee and a  $33\ \text{nF}$  capacitor. For exciting radial secular resonances, frequencies of up to several MHz have to be applied to the compensation electrode. We therefore added no additional filtering beyond the one provided by the  $1\ \text{nF}$  capacitor, the inductor contained in the bias tee, and the output impedance of the high voltage amplifier.

#### 4.1.5 Magnetic field coils

As described in section 2.5,  $\text{Be}^+$  can be efficiently laser cooled by driving a cycling transition between stretched states using circularly polarized light. This requires that the

magnetic field is aligned parallel with the cooling laser beam. Our setup contains three perpendicular pairs of coils that allow full adjustment of the magnetic field vector. The coils have 100 windings and are located just outside the vacuum chamber that houses the ion trap. Currents of a few hundred mA are sufficient to overcome the background due to the earth's magnetic field and stray fields from the ion pumps and vacuum gauges. The coil currents are adjusted by maximizing the fluorescence from the laser cooled ions while the repumper is turned off.

## 4.2 Fluorescence detection

In all ion trap experiments described in this thesis, the detected signal is the fluorescence emitted by the trapped  $\text{Be}^+$  ions. Our setup contains two imaging systems that allow the observation of the trapped ions from the horizontal and vertical direction.

### 4.2.1 Objectives

Objectives for imaging trapped ions can either be placed inside the vacuum chamber, or the ions can be imaged from the outside through a vacuum window. In-vacuum optics has the advantage that the distance between the objective and the ions can be made much shorter. This means that the desired numerical aperture can be reached with much smaller optical elements than when the objective is located outside the vacuum chamber. However, there are also a number of drawbacks. The insulating surface of the first lens can get electrically charged due to exposure to electrons from the electron gun and ultraviolet light from the ionization and cooling lasers. This leads to stray fields at the position of the ions which can interfere with the operation of the trap. Another issue is that the objective can only contain vacuum compatible materials and has to withstand the bake out temperatures of around  $200^\circ\text{C}$  that are required to achieve ultra-high vacuum.

We therefore decided to use objectives placed outside the vacuum chamber as shown in Figure 4.10. The windows used for imaging are made from fused silica. Horizontal imaging is performed through a 6.35 mm thick “re-entrant” window whose vacuum side is located 69.5 mm from the center of the ion trap. The top window of the trap vacuum chamber is 9.5 mm thick and its vacuum side is located 64.5 mm from the center of the ion trap.

### Objective design

Our application requires a long working distance and operation at 313 nm which lies in the ultraviolet. These relatively unusual requirements make it difficult to find suitable commercial standard objectives. Furthermore, the vacuum window between the ions and the objective introduces spherical aberrations [115] that would degrade the performance of the imaging system if not taken into account in the design. A relatively simple and cost effective way of constructing custom imaging objectives is to combine a number of catalog singlet lenses. The basic design procedure is the following [116, 117]. First, an existing

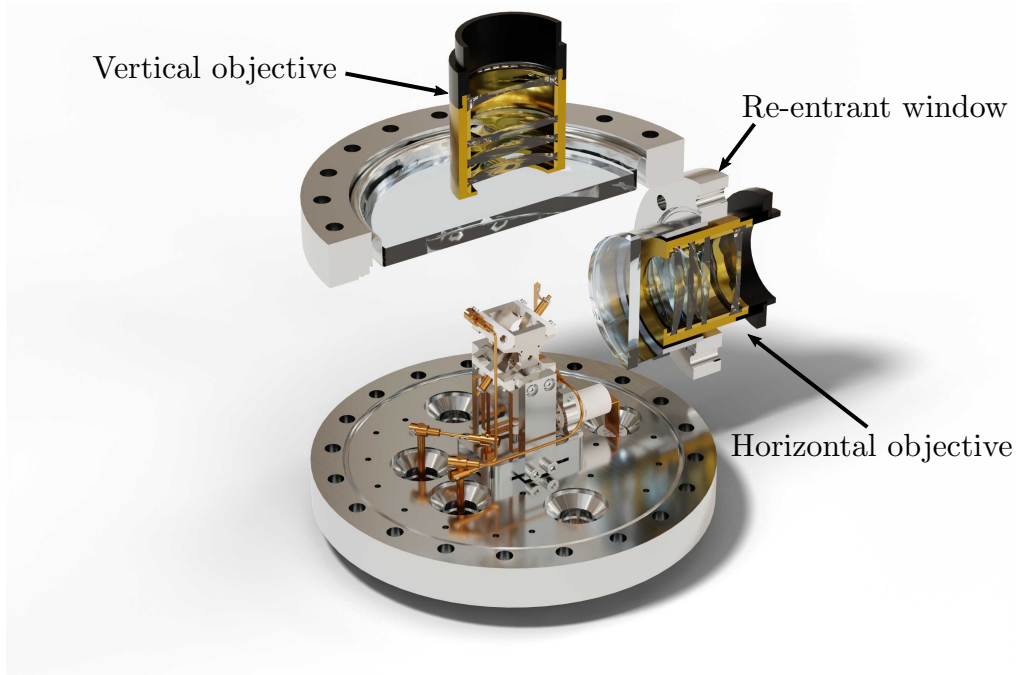


Figure 4.10: Overview of the ion imaging objectives. The re-entrant window allows placing the horizontal objective closer to the ion trap than a flat window would allow. For simplicity, components other than the ion trap are not shown.

objective design is used as a starting point. Ray tracing software is then used to numerically optimize the performance of the objective by adjusting the radii of curvature of the lens surfaces and the spacings between the surfaces. The lenses are then successively replaced with the closest available catalog parts. At each step the remaining free lens parameters and the spacings between the lenses are re-optimized.

One important parameter is the magnification of the imaging system. It should be large enough to ensure that the pixel size of the camera sensor is not limiting the imaging resolution. At the same time, a too large magnification would limit the field of view. Our cameras have sensor sizes of  $8 \times 8 \text{ mm}^2$  and pixel sizes of  $8 \times 8 \mu\text{m}^2$ . We therefore chose a target magnification of  $M \approx -8$  in order to achieve a field of view of around  $1 \times 1 \text{ mm}^2$ . This allows fitting even large ion crystals with a few hundred  $\mu\text{m}$  axial length into the frame. The resulting digital resolution due to the finite pixel size is  $1 \times 1 \mu\text{m}^2$ . This is smaller than the optical resolution of the imaging system and is therefore not limiting the image quality.

We decided to use fused silica lenses with 50.8 mm diameter and employed a commercial ray tracing software<sup>9</sup> for the numerical optimization. Ray tracers simulate the propagation of light rays through a lens system using the law of refraction. In an ideal aberration-free imaging system, all rays originating from a point in the object plane converge in a single

<sup>9</sup>Qioptiq WinLens3D.

point in the image plane. At the same time it follows from Fermat's principle that the optical path lengths of all the rays are identical [115]. WinLens3D traces bundles of rays from points in the object plane to the image plane such that the entire entrance pupil of the objective is covered. We chose one object point on the optical axis and one 0.5 mm off-axis such that both the center and the edge of the field of view are covered. One popular visualization of the resulting ray data consists of spot diagrams that are shown in Figure 4.11. They show the coordinates at which the rays intersect the image plane relative to the aberration-free image position. The deviations from the center are called *transverse ray aberrations*.

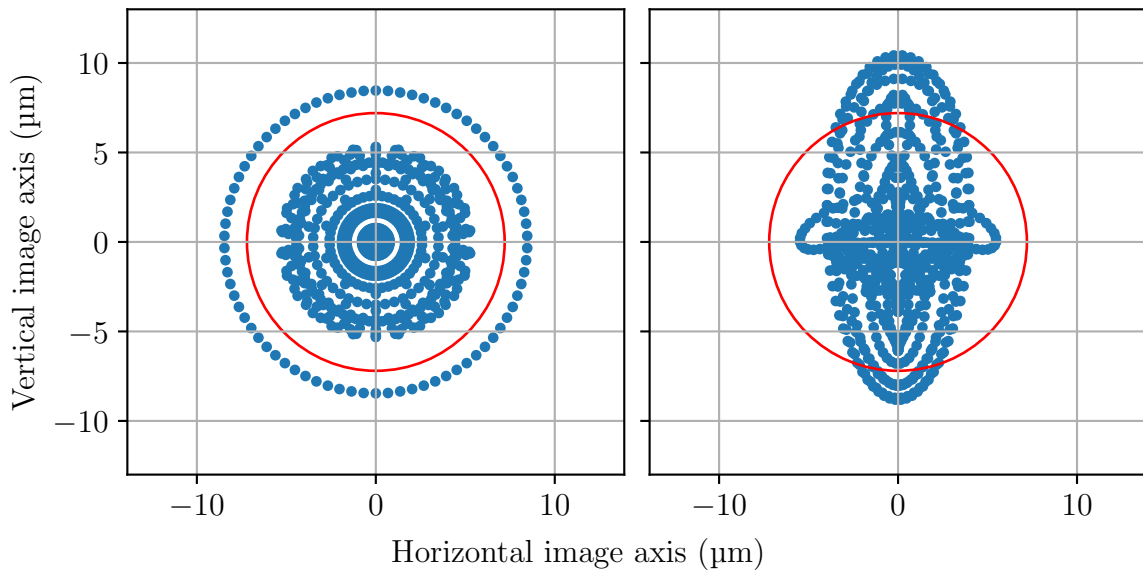


Figure 4.11: Spot diagrams of the horizontal objective simulated by the ray tracing software. The plots show how much rays originating from a single reference point in the object plane spread out in the image plane due to aberrations. In the left plot the reference point is on the axis of the objective, and in the right plot it is 0.5 mm from the axis. The red circles indicate the sizes of the Airy disks. This is a common measure for the spot size of a diffraction-limited imaging system [115].

Another visualization consists of optical path difference (OPD) plots which are shown in Figure 4.12. Here, the path differences between the rays and a reference ray that crosses the center of the input aperture of the imaging system are plotted. For off-axis object points, ray fans are aligned along the meridional and sagittal planes (see for example section 10.2.4 in [115]).

For the numerical optimization, WinLens3D calculates a merit function as the quadratic sum of a user-defined set of aberration parameters. Another term ensures that the overall magnification of the imaging system remains close to the design value. The merit function also contains additional terms that penalize designs that are difficult to manufacture, for example due to the lenses becoming too thin at the edges. WinLens3D then uses a damped



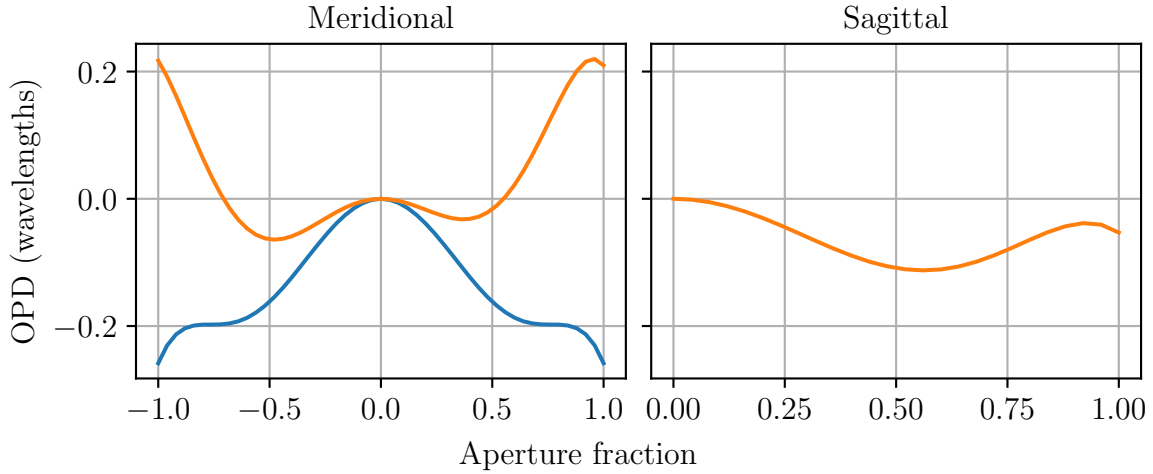


Figure 4.12: Optical path difference (OPD) plots for the horizontal objective. The path differences are measured relative to a reference ray that crosses the center of the input aperture of the imaging system. The rays originate on-axis (blue) and 0.5 mm off-axis (orange). The aperture fraction measures how far from the center the rays cross the input aperture. A value of 1 corresponds to marginal rays that hit the edge of the aperture.

least squares method to minimize the merit function by adjusting the parameters of the imaging system. We found that good results could be achieved by minimizing the transverse ray aberrations, i.e. the spread of the points in Figure 4.11. After some trial and error we found a suitable design for the horizontal imaging system that combines four catalog lenses as shown in Figure 4.13.

In the absence of aberrations, the achievable resolution of an imaging system is limited by diffraction from the aperture. For a circular aperture the intensity in the image plane follows the Airy distribution [115]:

$$I(r) \propto \left[ \frac{2J_1\left(\frac{2\pi}{\lambda} \frac{ar}{R}\right)}{\frac{2\pi}{\lambda} \frac{ar}{R}} \right]^2, \quad (4.10)$$

where  $J_\alpha(x)$  are the Bessel functions of the first kind,  $r$  is the distance from the spot center in the image plane,  $\lambda$  is the wavelength,  $R$  is the distance between the aperture and the image plane, and  $a$  is the radius of the aperture. The Airy distribution has its first zero at

$$r_0 \approx 0.61R \frac{\lambda}{a}, \quad (4.11)$$

which defines the radius of the *Airy disk*.

An objective design is considered “diffraction limited” if the spot diagrams obtained by ray tracing are much smaller than the sizes of the Airy disks (red circles in Figure 4.11) [115]. Another common criterion for a diffraction limited imaging system is

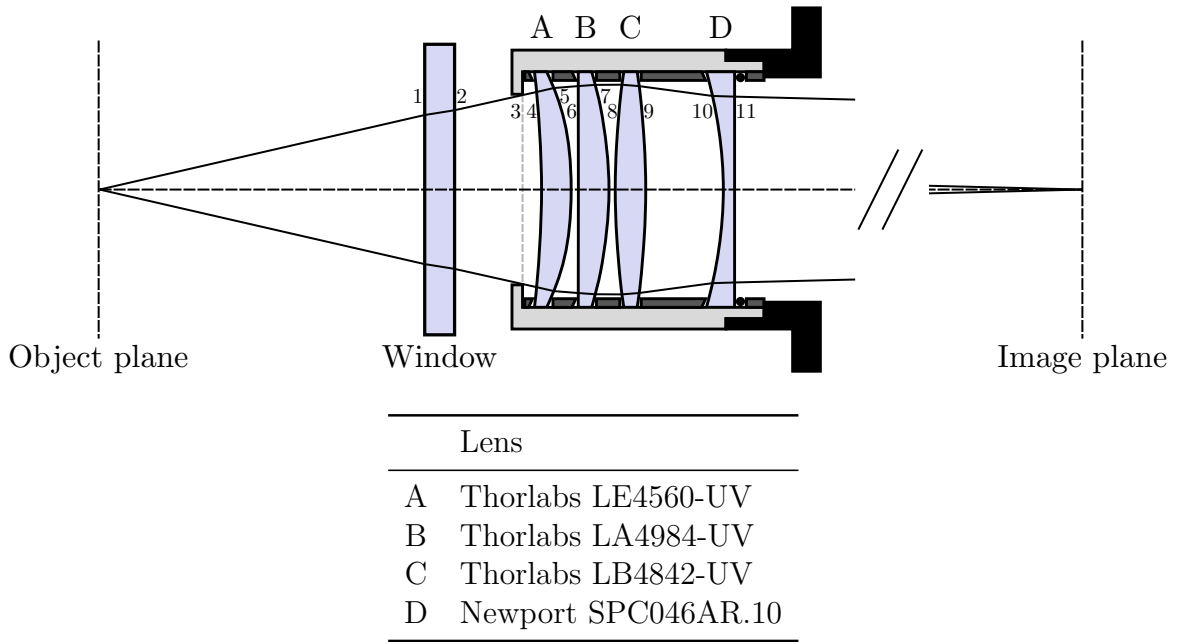


Figure 4.13: Schematic of the objective designed from catalog lenses. The gray dashed line shows the input aperture. The surfaces are numbered and their curvatures and spacings are given in Tables A.1 and A.2 for the two variants of the objective.

that the optical path differences are less than one quarter of the wavelength [118]. According to both criteria our design is on the edge of being diffraction limited. The aberrations of an imaging system can be reduced by stopping down the aperture size. This is because a smaller aperture reduces the largest angle at which rays can strike the lens surfaces. However, it comes at the cost that a smaller aperture increases the spot size due to diffraction and reduces the light gathering ability of the objective. For our application we decided that maximizing the light gathering ability is more important than achieving a slightly higher resolution by stopping down the lens. The aperture diameter was therefore chosen such that the marginal rays pass just through the specified clear apertures of the lenses. The resulting numerical aperture of the objective is  $NA = \sin(\theta) = 0.23$ , where  $2\theta$  is the apex angle of the cone of light that can enter the aperture. The solid angle covered by the cone is

$$\Omega = 4\pi \sin^2(\theta/2) = 2\pi \left(1 - \sqrt{1 - (NA)^2}\right). \quad (4.12)$$

The objective can therefore gather  $\Omega/4\pi = 1.3\%$  of the light emitted by an isotropic source.

The horizontal and vertical imaging systems only differ in the position and thickness of the vacuum window. We found that this difference could be compensated by changing only the spacings between the objective lenses. The resulting spot diagrams and optical path difference plots are qualitatively similar to those of the horizontal objective. The ray tracing results and surface data are given in Appendix A.

A schematic of the mechanical design of the objectives is shown in Figure 4.13. The

lenses are placed in a brass tube, and spacer rings are used to precisely locate them at the design positions. The stack of lenses and spacer rings is held together by a rubber O-ring and a cap that is screwed into the lens tube.

### Objective performance

The assembled horizontal objective was first tested outside the ion trap setup. As a stand-in for the vacuum window, a fused silica flat of the same thickness was used. We used a  $1\ \mu\text{m}$  pinhole as a test object that was illuminated by a  $313\ \text{nm}$  laser beam. The pinhole was placed on a 3-axis stage which allowed moving it through the field of view of the imaging system. Figure 4.14 shows the image of the pinhole at different positions in the field of view. Fitting a 2D Gaussian to the center image yields a slightly elliptical spot with  $1/e^2$  waist diameters of  $21\ \mu\text{m}$  and  $17\ \mu\text{m}$  which is in rough agreement with the simulated spot diagrams. At the edges of the field of view, the spots show aberrations that are not symmetric with respect to the center of the image. We believe that this is due to manufacturing imperfections of the lenses, the lens tube, and the spacer rings. These lead to a slight asymmetry of the assembled objective. Nonetheless, an imaging resolution of less than a few  $\mu\text{m}$  is achieved across the field of view which is sufficient for resolving the individual ions in a Coulomb crystal.

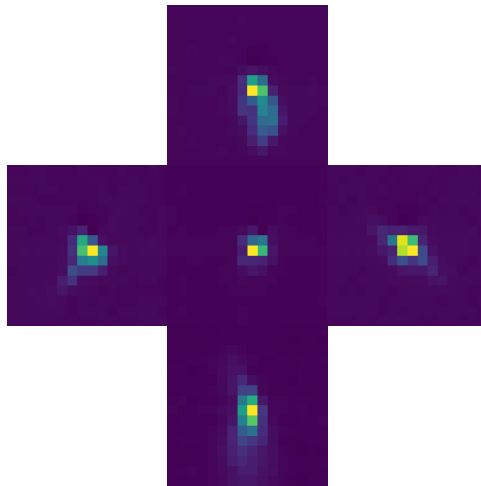


Figure 4.14: Image of a  $1\ \mu\text{m}$  pinhole in the center of the field of view, and shifted by around  $\pm 0.4\ \text{mm}$  along the horizontal and vertical axes.

### 4.2.2 Detectors

The requirements for the detectors that record the fluorescence emitted by the  $\text{Be}^+$  ions vary by application. For example, taking pictures of ion crystals requires spatially resolved photon detection, while time resolution is less important. On the other hand, the detection

of excess micromotion with the photon-correlation method (see subsection 4.7.3) requires tagging the photon arrival times with ns resolution, while spatial resolution is not required.

We therefore use two different detector types in the fluorescence detection system. Electron-multiplying CCD (EMCCD) cameras are used for spatially resolved imaging with low time resolution, while photomultiplier tubes (PMTs) are used to measure photon arrival times with ns resolution. The detection system is shown in Figure 4.15. The PMTs are located in light-tight boxes that are attached to the front of the cameras. The boxes contain movable beam splitters that allow sending half of the light onto the PMTs.

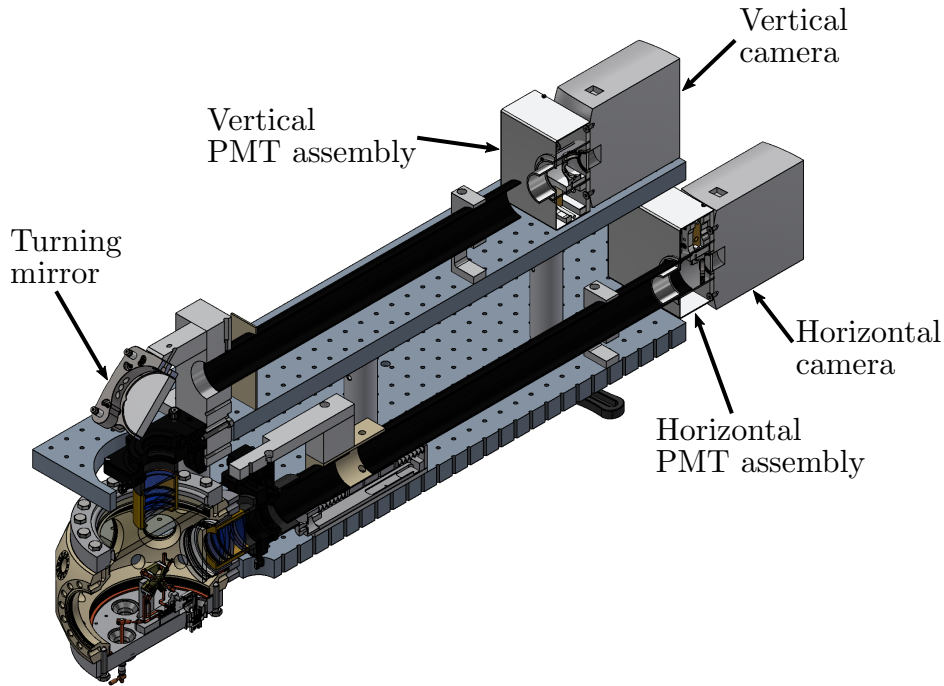


Figure 4.15: Detectors used in the imaging system. The cameras are used for spatially resolved imaging, while the PMTs allow measuring photon arrival times with ns time resolution.

### Cameras

We use two similar EMCCD cameras for the horizontal<sup>10</sup> and vertical<sup>11</sup> imaging systems. Both cameras contain identical EMCCD image sensors with a pixel size of  $8 \times 8 \mu\text{m}^2$  and a resolution of  $1004 \times 1002$  pixels. The sensor quantum efficiency at 313 nm is specified to be 25%. The sensors of the horizontal and vertical cameras are cooled to  $-75^\circ\text{C}$  and  $-85^\circ\text{C}$ , respectively, using thermoelectric coolers. This reduces the dark currents to below  $0.028$  and  $0.01 \text{ e}^- \text{ px}^{-1} \text{ s}^{-1}$ , respectively. Since each ion is imaged onto a spot of a few px size and we use exposure times of a few s at most, these dark counts are essentially negligible in our

<sup>10</sup>Andor iXon DV885LC-VP.

<sup>11</sup>Andor iXon DU-885K-CS-0#VP.

application. When photons strike the pixels of a CCD sensor, they create charges due to the photoelectric effect. After the exposure time has elapsed, the charges are shifted across the sensor and are sequentially read out by an amplifier and analog to digital converter. For our cameras the noise created in this process amounts to around 20 to 30 e<sup>-</sup> px<sup>-1</sup>. The EMCCD sensors suppress the influence of this readout noise by multiplying up the number of electrons accumulated in a pixel before they reach the readout amplifier. This is achieved by shifting the charges through a series of special amplification registers that are operated at a relatively high voltage. With a certain probability this can lead to the creation of further charges due to impact ionization. Hundreds of these registers are stacked in order to achieve gains of up to a few thousand. In this regime the readout noise becomes smaller than the signal due to a single photon. To reject room light, 313 nm band-pass filters<sup>12</sup> with 10 nm FWHM bandwidth are mounted directly in front of the image sensors.

### Photomultiplier tubes

For time-resolved photon detection, we use integrated photon counting heads<sup>13</sup> which contain a PMT, the required high voltage power supply, and pulse detection circuitry. For each detected photon they output a 10 ns long pulse with 2.2 V amplitude into a 50 Ω load. The specified quantum efficiency at 313 nm is 29 %. Room light is rejected using the same filters used for the cameras. Even when the cooling laser beams are well aligned through the ion trap, some light is being scattered from the trap electrodes which creates background counts on the PMTs. We therefore spatially filter the light using pinholes that are placed in the image planes of the objectives directly in front of the PMTs. Different pinhole diameters can be chosen depending on the application. For experiments with single ions and large ion crystals, we typically used 100 μm and 1 mm pinholes, respectively.

## 4.3 Be<sup>+</sup> cooling laser

Laser cooling of Be<sup>+</sup> requires ultraviolet light at 313.1 nm (see section 2.5). The cooling laser system is based on a design pioneered in the group of D. Wineland and D. Leibfried at the NIST<sup>14</sup> [119]. It was originally designed and built by V. Batteiger and is described in detail in his dissertation [120]. In the following, we summarize the main features of the system and explain the changes made during this thesis work. Figure 4.16 shows a schematic of the optical setup for generating 313 nm light.

---

<sup>12</sup>Edmund Optics #34-977.

<sup>13</sup>Hamamatsu H10682-210.

<sup>14</sup>National Institute of Standards and Technology, Boulder, United States.

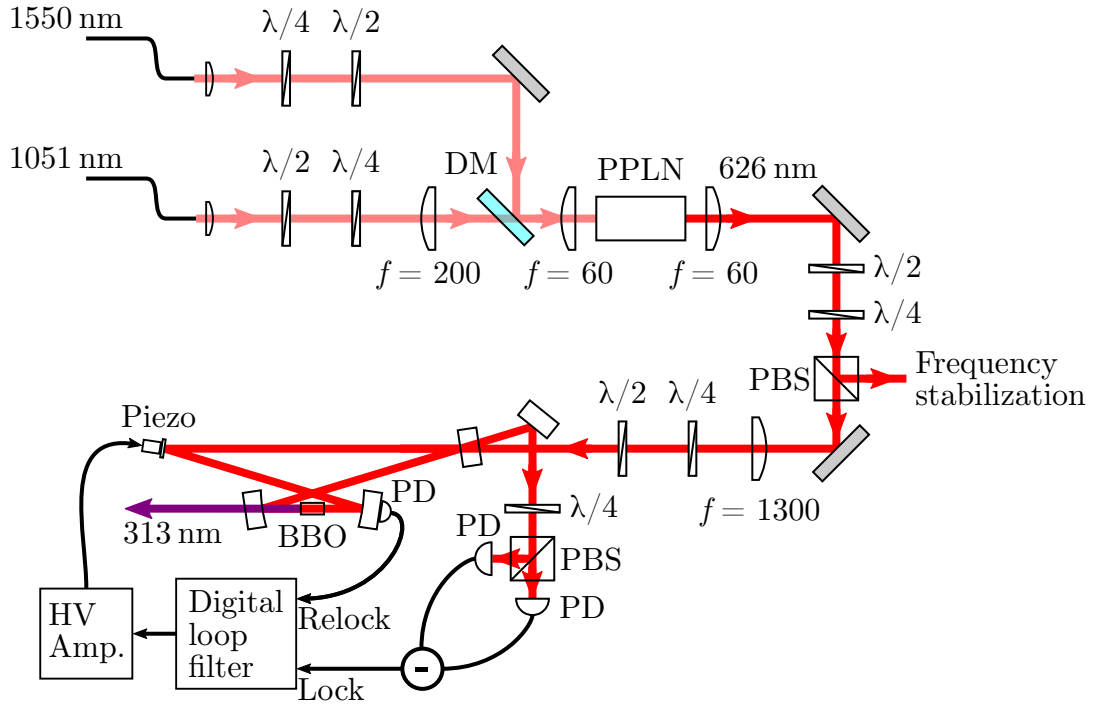


Figure 4.16: Setup for generating 313 nm light. DM, dichroic mirror; PBS, polarizing beam splitter; PD, photodiode. Focal lengths are given in mm.

### Sum frequency generation

Fundamental radiation at 1051 nm and 1550 nm is generated by two fiber lasers.<sup>15</sup> The beams are overlapped on a dichroic mirror and focused into a periodically poled lithium niobate (PPLN) crystal for sum frequency generation. Phase matching is achieved at a crystal temperature of around 161 °C. When operating the fiber lasers at their maximum output power, more than 2 W of optical power can be generated at 626 nm [120]. This is significantly more power than we need in the experiment. In order to reduce the stress on the components, we therefore typically use an input power of 2.79 W at 1051 nm and 1.93 W at 1550 nm. This results in about 500 mW of 626 nm light.

### Second harmonic generation

The 626 nm light is then frequency doubled in a  $\beta$ -barium borate (BBO) crystal in a bow-tie enhancement cavity. The crystal is 8 mm long and is critically phase-matched. In the original design the cavity was constructed from mirror mounts on optical posts that were clamped to a breadboard. We found that this made the cavity very sensitive to mechanical disturbances, for example when someone was walking around in the lab. We therefore replaced the optomechanics with a construction similar to the one used for the

<sup>15</sup>Originally we used two Menlo Systems Orange One lasers. After multiple failures of the 1051 nm system, we replaced it with a new laser (Keopsys CYFL-KILO).

Be ionization laser (see Figure 4.29). The mirror mounts are directly screwed into a 35 mm thick machined aluminum plate. With this more rigid construction, the cavity is almost completely insensitive to typical mechanical disturbances in the lab environment.

In the original setup the optical surfaces had to be cleaned from dust every few days in order to maintain sufficient enhancement [120]. We therefore sealed the housing of the cavity and use an air circulator to circulate filtered and dry air through the system. With these modifications we found that no regular cleaning is required.

The resonator length is stabilized using the Hänsch-Couillaud method [121]. We replaced the original analog loop filter with the digital one we developed (see section 4.6.1) and added a monitor photodiode behind one of the cavity focusing mirrors. The diode is used to measure the power circulating in the cavity. The digital loop filter uses the signal to automatically reacquire the lock when necessary. When the system is well aligned, it generates around 160 mW to 180 mW at 313 nm from 500 mW of input power at 626 nm.

### Repumper

As described in section 2.5, imperfections in the cooling laser polarization and in the alignment of the magnetic field axis lead to pumping of the Be<sup>+</sup> ions into the  $S_{1/2}(F = 1)$  dark states. We use a resonant electro-optic modulator<sup>16</sup> (EOM) to create 1.25 GHz sidebands on the cooling laser. When the carrier is on resonance with the  $S_{1/2}(F = 2) \rightarrow P_{3/2}(F = 3)$  cycling transition, the lower sideband drives transitions from the  $S_{1/2}(F = 1)$  manifold to the  $P_{3/2}$  state which re-pumps the ions out of the dark states. The sideband strength is around 6 % of the carrier which is sufficient for this application. To prevent drifts of the resonance frequency of the EOM, its temperature is actively stabilized using the built-in temperature sensor and a Peltier element.

#### 4.3.1 Frequency stabilization

To achieve laser cooling, the laser frequency has to be held at a fixed detuning relative to the transition frequency of the Be<sup>+</sup> ions. For stable operation the frequency fluctuations should be kept well below the transition linewidth, i.e. in the range of a few MHz. Commercial Fizeau wavelength meters achieve measurement resolutions below 1 MHz. However, they are subject to environmental drifts and require frequent recalibration. In our setup we use such a wavelength meter for coarse frequency determination only. The cooling laser is stabilized using a frequency offset lock to a self-referenced frequency comb. Figure 4.17 shows a schematic of the frequency stabilization setup.

A half-wave plate and a polarizing beam splitter are used to split off a few mW of 626 nm light after the sum frequency generation. The light is coupled into a polarization maintaining fiber and is split into two outputs by a fiber beam splitter. 10 % of the light are sent to a Fizeau wavelength meter.<sup>17</sup> An adjustable fiber attenuator is used for exposure control. The wavelength meter features a fiber switch that can be used to switch

<sup>16</sup>Qubig PM-Be+\_1.3P3.

<sup>17</sup>HighFinesse WSU-2.





between the signal to be measured and a calibration source. For this we use a stabilized helium-neon laser.<sup>18</sup> We found that back reflections from the fiber coupling disturb the frequency stabilization of the helium-neon laser and therefore added an optical isolator directly in front of the laser aperture. Every few minutes, the wavelength meter software automatically calibrates the device using the calibration source.

The other 90 % of the light are sent through a 100 m long polarization maintaining fiber to another lab which contains a commercial self-referenced frequency comb.<sup>19</sup> The comb is based on an erbium-doped fiber laser and operates with a central wavelength of around 1560 nm. It contains an internal fiber amplifier and a second harmonic generation stage that produces 180 mW of output power with a spectrum centered at 780 nm. This light is then spectrally broadened in a photonic crystal fiber to produce a broadband spectrum with a specified wavelength range from 600 nm to 973 nm. This light is overlapped with the light from the cooling laser system on a polarizing beam splitter (PBS). A half-wave plate and another PBS are used to project the two beams onto the same polarization axis. To ensure good spatial mode matching, both beams are then coupled into the same single-mode optical fiber. The fiber output is collimated and sent onto a diffraction grating. An  $f = 75$  mm lens is placed one focal length behind the grating in order to convert the angular dispersion produced by the grating into a spatial separation of the different wavelengths. An adjustable slit placed in the focal plane of the lens is then used to filter out the wavelength components of the comb light that lie far from the wavelength of the cooling laser. These components would reduce the signal to noise ratio of the detected beat note since they do not contribute to the signal, but increase the noise level due to shot noise and technical amplitude noise on the light (see also subsection 6.3.2). Finally, the light is focused by an  $f = 50$  mm lens onto an amplified silicon photodetector.<sup>20</sup>

Figure 4.18 shows the resulting beat note between the cooling laser and the closest frequency comb mode. The beat note frequency is given by

$$f_{\text{beat}} = |f_{\text{cool}} - f_n|, \quad (4.13)$$

where  $f_{\text{cool}}$  is the frequency of the cooling laser at 626 nm, and  $f_n$  is the frequency of the  $n$ th comb mode which is given by the frequency comb equation (see section 3.1):

$$f_n = n f_{\text{rep}} + f_{\text{ceo}}, \quad (4.14)$$

where  $f_{\text{rep}} = 250$  MHz is the pulse repetition rate of the frequency comb, and  $f_{\text{ceo}} = -2 \times 45$  MHz is the carrier-envelope offset frequency.<sup>21</sup>

A 100 MHz low-pass filter is used to select only the lowest-order beat note from the electronic signal which is then amplified by an RF amplifier. The signal is sent back to the He<sup>+</sup> experiment using a 100 m long low-loss coaxial cable.<sup>22</sup>

<sup>18</sup>Thorlabs HRS015B.

<sup>19</sup>Menlo Systems FC1500-250-ULN.

<sup>20</sup>Thorlabs PDA10A-EC.

<sup>21</sup>The frequency comb is stabilized at a carrier-envelope offset frequency of  $-45$  MHz. The factor 2 is due to the second harmonic generation in the 780 nm output.

<sup>22</sup>Type RG-214/U.

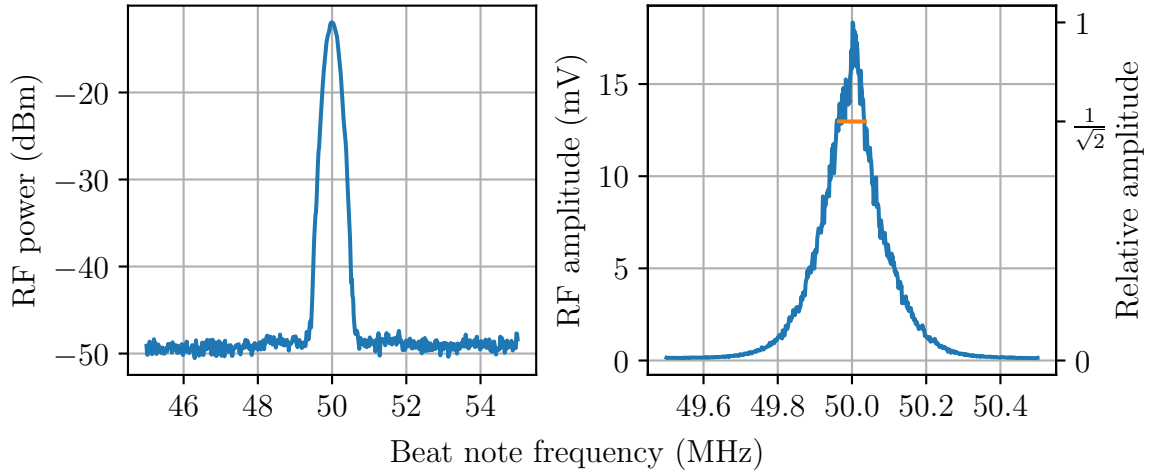


Figure 4.18: Beat note between the cooling laser light at 626 nm and a frequency comb mode. Logarithmic scale with 300 kHz resolution bandwidth (left) and linear scale with 9.1 kHz resolution bandwidth (right). The orange line shows the intensity FWHM linewidth of around 70 kHz.

The left plot in Figure 4.18 is recorded with a resolution bandwidth of 300 kHz which is more than the linewidth of the beat note. A signal-to-noise ratio (SNR) of 37 dB in 300 kHz bandwidth can be read off. The noise spectrum in the photodiode signal is approximately flat and is band-limited to 100 MHz by the low-pass filter. The resulting SNR of the entire beat note signal is  $37 \text{ dB} - 10 \log_{10}(100 \text{ MHz}/300 \text{ kHz}) \text{ dB} = 12 \text{ dB}$  which we found to be insufficient for a reliable phase lock. At this stage we could insert a band-pass filter to reduce the noise contribution to the signal. One challenge is that we want to be able to change the beat note frequency in order to tune the frequency of the laser. This is required since we work with cooling laser detunings from a few MHz to more than 100 MHz, depending on the requirements of each particular experiment. This would require synchronous tuning of the center frequency of the band-pass filter which is technologically difficult.

Instead, after further amplification the beat note signal is mixed with a local oscillator signal from a function generator. This shifts the beat note to an intermediate frequency

$$f_{\text{IF}} = |f_{\text{beat}} - f_{\text{LO}}|, \quad (4.15)$$

where  $f_{\text{LO}}$  is the local oscillator frequency which is adjusted such that an intermediate frequency of 10 MHz is reached. The mixer output is filtered with a band-pass that has a center frequency of 10.7 MHz and a 3 dB bandwidth of 3.8 MHz. The filtering increases the SNR to around 26 dB which is sufficient for reliable phase tracking. A digital phase and frequency detector (PFD) [122, 123] is then used to obtain the phase difference between the intermediate frequency signal and a fixed 10 MHz reference. An analog loop filter is finally used to close the phase locked loop by giving feedback to the frequency tuning input of one of the two fiber lasers in the cooling laser setup.



misalignment of the diffracted beam is avoided when the AOM frequency is changed [124]. This dramatically increases the usable bandwidth of the setup compared to using a single pass through the AOM. A quarter-wave plate is used to rotate the polarization of the back-reflected beams by  $90^\circ$  with respect to the incoming beams. The 1st order diffracted beam gets diffracted by the AOM again which doubles the frequency shift. Finally, the output beam is separated from the incoming beam by the PBS. One disadvantage of this configuration is that the diffraction efficiencies of AOMs for ultraviolet light, which are usually made from quartz glass, are strongly polarization dependent. We measured a diffraction efficiency of up to 81 % with vertical polarization, but only 19 % with horizontal polarization. This limits the maximum overall efficiency of the frequency shifter to around 13 %. Nonetheless, this still leaves us ample power for efficient laser cooling.

One feature of this setup is that the component that is not diffracted by the AOM (“0th order”) is overlapped with the one that is diffracted twice (“1st order”) [120]. A fast mechanical shutter is placed close to the mirror of the cat’s eye to selectively block or unblock the 0th order beam. Since the shutter is located close to the focal plane where the beam is small, it achieves rise/fall times of only 33  $\mu\text{s}$  and has a switching delay of around 1.6 ms. If the shutter is open, the output of the system contains two frequency components that are separated by twice the AOM frequency. We call the component that is due to the 1st order diffraction the “near-detuned” component, and the one due to the 0th order the “far-detuned” component. We make use of the far-detuned component during trap loading in order to efficiently cool the hot ions (see subsection 4.6.1).

The output of the frequency shifter is finally coupled into a photonic crystal fiber that has been hydrogen loaded in order to prevent degradation due to the intense ultraviolet light [125]. The fiber delivers the light to the ion trap setup which is located on another optical table. Figure 4.20 shows the relative output power after the fiber for different AOM drive frequencies. The FWHM of the curve is around 40 MHz, corresponding to a frequency shifting range of 80 MHz. Over time we have observed damage to the fiber input facet that has been attributed to contamination due to particles and aerosols getting burned into the surface [126]. We mitigate this by flushing the input fiber collimator with nitrogen.

## 4.4 Vacuum system

Delivering the extreme ultraviolet (XUV) spectroscopy radiation at 60.8 nm to the trapped  $\text{He}^+$  ions comes with a number of challenges. XUV radiation is strongly absorbed in all gases such that the XUV source has to be connected to the ion trap with a vacuum system. The XUV radiation is being generated using high harmonic generation (HHG) in a gas jet. In our system the resulting gas load leads to pressures in the HHG vacuum chamber of up to a few times  $10^{-3}$  mbar. At the same time we aim to keep the pressure in the ion trap chamber below  $1 \times 10^{-10}$  mbar to minimize collisions between the trapped ions and background gas molecules. One possibility would be to separate the different regions with a thin aluminum foil (hundreds of nm thickness) which has some transparency in the XUV and would also provide spectral filtering [95]. However, the extreme fragility of

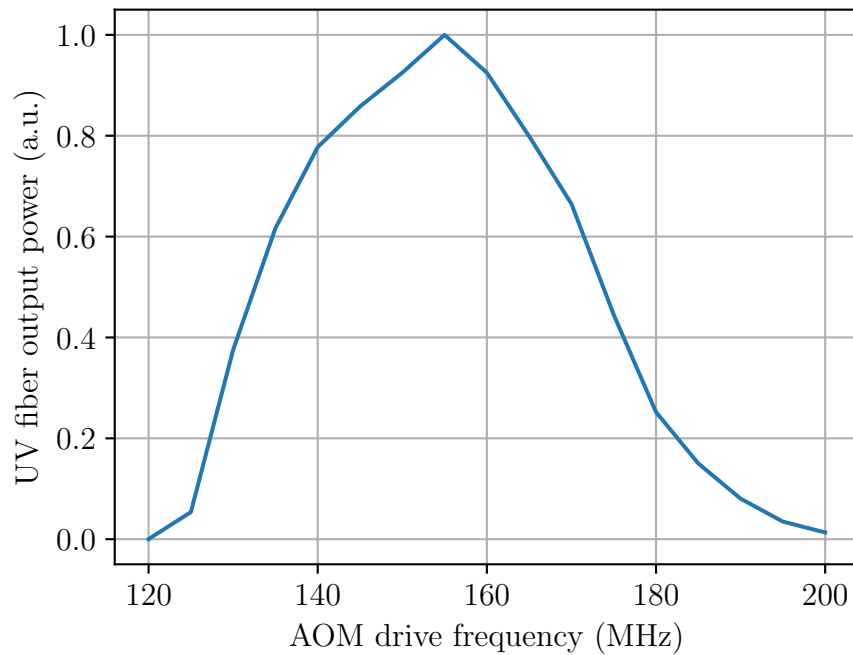


Figure 4.20: Efficiency curve of the frequency shifter setup. The FWHM is around 40 MHz. Since the AOM is used in a double-pass configuration, the achievable frequency shifting range is twice as large.

such foils makes them difficult to use as windows, and the large transmission losses would reduce the achievable signal rate. We therefore constructed a differential pumping setup for maintaining the required pressure difference while leaving a path for the laser beam.

#### 4.4.1 Differential pumping

The vacuum system is shown in Figure 4.21. The XUV frequency comb is being generated in an enhancement cavity located inside the HHG chamber. The XUV radiation is then sent through a series of vacuum chambers until it reaches the ion trap. The various laser beam paths are described in the following section, while this section focuses on the vacuum components. For reference a detailed schematic containing all main vacuum components is shown in Figure 4.22.

The HHG chamber is evacuated using a 4501/s turbomolecular pump (TMP).<sup>24</sup> In addition a metal tube with a small hole is placed opposite to the nozzle that produces the xenon gas jet used for the HHG. The tube is directly connected to a roughing pump. This “gas catcher” significantly reduces the gas load and the base pressure in the chamber when the gas jet is being operated. The next vacuum chamber is a small differential pumping section. In order to minimize the amount of gas flowing through, it is connected to the

<sup>24</sup>Edwards STP-iX457.

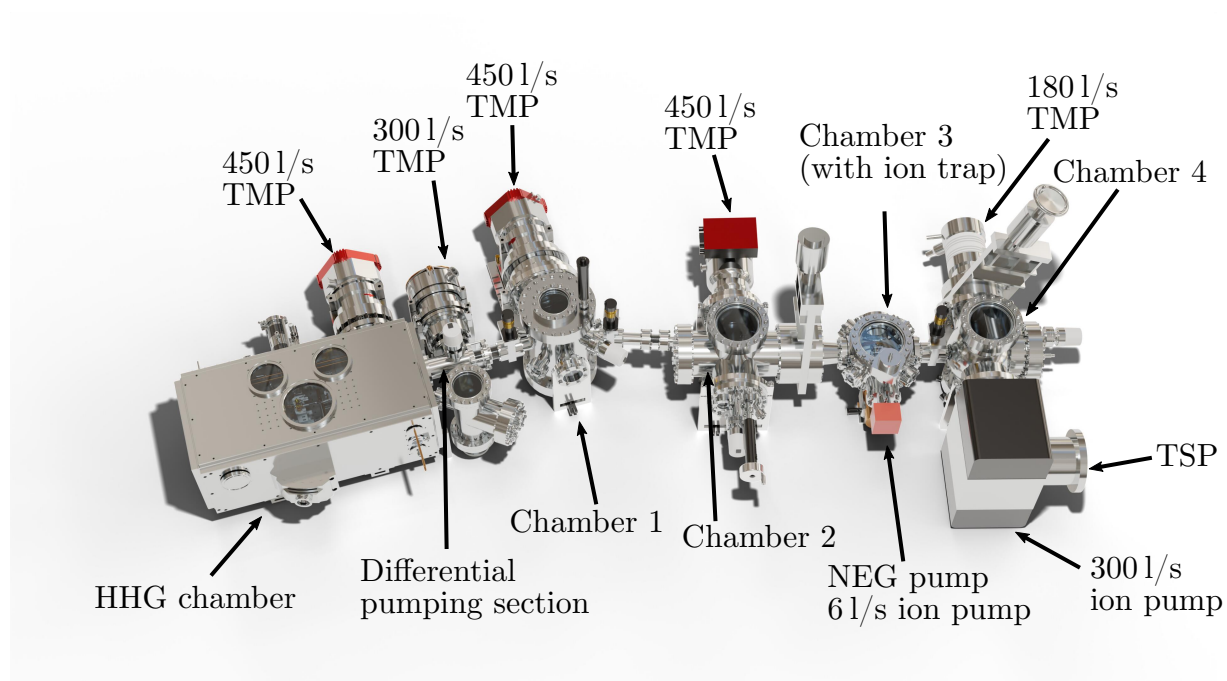


Figure 4.21: Overview of the vacuum system. The generated XUV radiation is guided to the ion trap through several stages of differential pumping. Chambers 1, 3, and 4 contain mirrors for steering and focusing the XUV radiation (see Figure 4.24). TMP, turbomolecular pump; NEG pump, non-evaporable getter pump; TSP, titanium sublimation pump.

HHG chamber with a 1.8 mm diameter hole and to the following vacuum chamber with a 3.2 mm diameter hole. The positions of the holes are adjustable such that the XUV beam can be sent through the chamber without clipping. The differential pumping section and chamber 1 are being evacuated with 300 l/s<sup>25</sup> and 450 l/s<sup>26</sup> TMPs, respectively. Under normal operating conditions the pressure in chamber 2 already reaches the limit set by the compression ratio of its 450 l/s TMP.<sup>27</sup> A second identical TMP is therefore used in series to reduce the foreline pressure of the first pump (not shown in the figure). Chambers 3 and 4 form the ultra-high vacuum (UHV) section of the setup. Chamber 3 houses the ion trap and contains a non-evaporable getter (NEG) pump.<sup>28</sup> After being activated by heating, the NEG chemically binds reactive gases such as H<sub>2</sub>, O<sub>2</sub>, and N<sub>2</sub> and is specified for a pumping speed of a few hundred l/s. Highly inert gases, such as argon or xenon, cannot be pumped by the NEG. It is therefore combined with a small ion element which reaches 6 l/s of pumping speed for argon. Chamber 4 is pumped by a 300 l/s ion pump<sup>29</sup> which also contains a titanium sublimation pump (TSP) for additional pumping of reactive gases. A

<sup>25</sup>Edwards STP-301.

<sup>26</sup>Edwards STP-iX457.

<sup>27</sup>Edwards STP-iX455.

<sup>28</sup>SAES NEX Torr D 500-5.

<sup>29</sup>Varian VacIon Plus 300 StarCell.



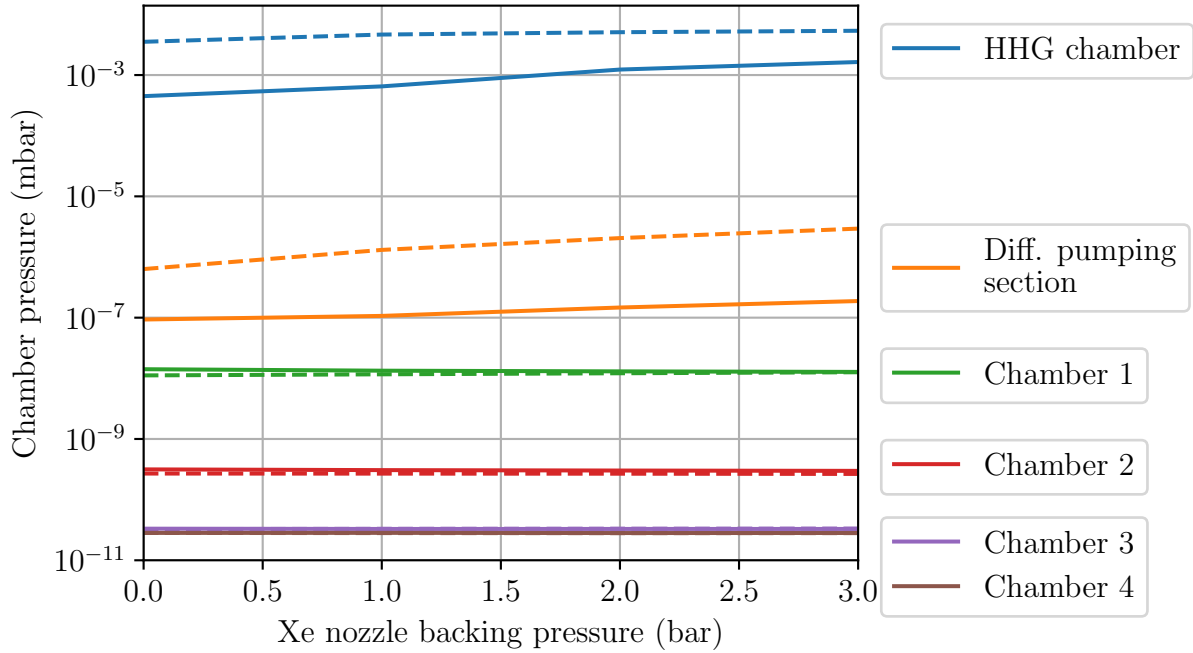


Figure 4.23: Performance of the differential pumping system. The pressures in the vacuum chambers are measured for different xenon backing pressures in the HHG setup. Solid lines show pressures with the gas catcher enabled, and dashed lines without the gas catcher.

1801/s TMP<sup>30</sup> connected to chamber 4 allows initially pumping down the UHV section. In normal operation it is isolated from the setup using a gate valve. After baking the UHV section to remove adsorbed water and hydrocarbons from the chamber walls [109, p. 144], a base pressure of around  $3 \times 10^{-11}$  mbar is reached in chambers 3 and 4.

All vacuum chambers are equipped with cold cathode ion gauges<sup>31</sup> for measuring the individual pressures. The gas load in the HHG chamber depends on the xenon backing pressure that is being applied to the nozzle. Figure 4.23 shows the chamber pressures for backing pressures of up to 3 bar.<sup>32</sup> Even without the gas catcher, the pressures in chambers 1-4 are essentially unaffected by the xenon gas jet in the HHG chamber. This shows the effectiveness of the differential pumping section with its small apertures strongly limiting the gas flow. Comparing the data with the gas catcher (solid lines) to the data without (dashed lines) however shows a clear reduction of the gas load in the HHG chamber and in the differential pumping section. The gas catcher therefore allows switching to larger nozzle

<sup>30</sup>Pfeiffer TMU 200M P.

<sup>31</sup>HHG chamber and differential pumping section: Pfeiffer PKR 251 (full range gauge with additional Pirani sensor). Chambers 1, 2, and 4: Pfeiffer IKR 270. Chamber 3: VACOM COLDION extended.

<sup>32</sup>In these measurements, chamber 1 was evacuated by a 10001/s TMP (Pfeiffer TMH 1000M P). This pump was later found to cause excess vibrations and was replaced with the 4501/s TMP listed above. Since the pressure in chamber 1 barely rises above the base pressure, we do not expect this to significantly influence the system performance.



backing pressures if necessary. One planned upgrade of the HHG system is to replace the xenon with a helium/xenon gas mixture. This increases the velocity of the molecules in the gas jet and has been shown to reduce detrimental steady-state plasma accumulation in an enhancement cavity [127]. However, the pressure of the gas mixture will have to be larger in order to keep the xenon partial pressure constant.

#### 4.4.2 Laser beam lines

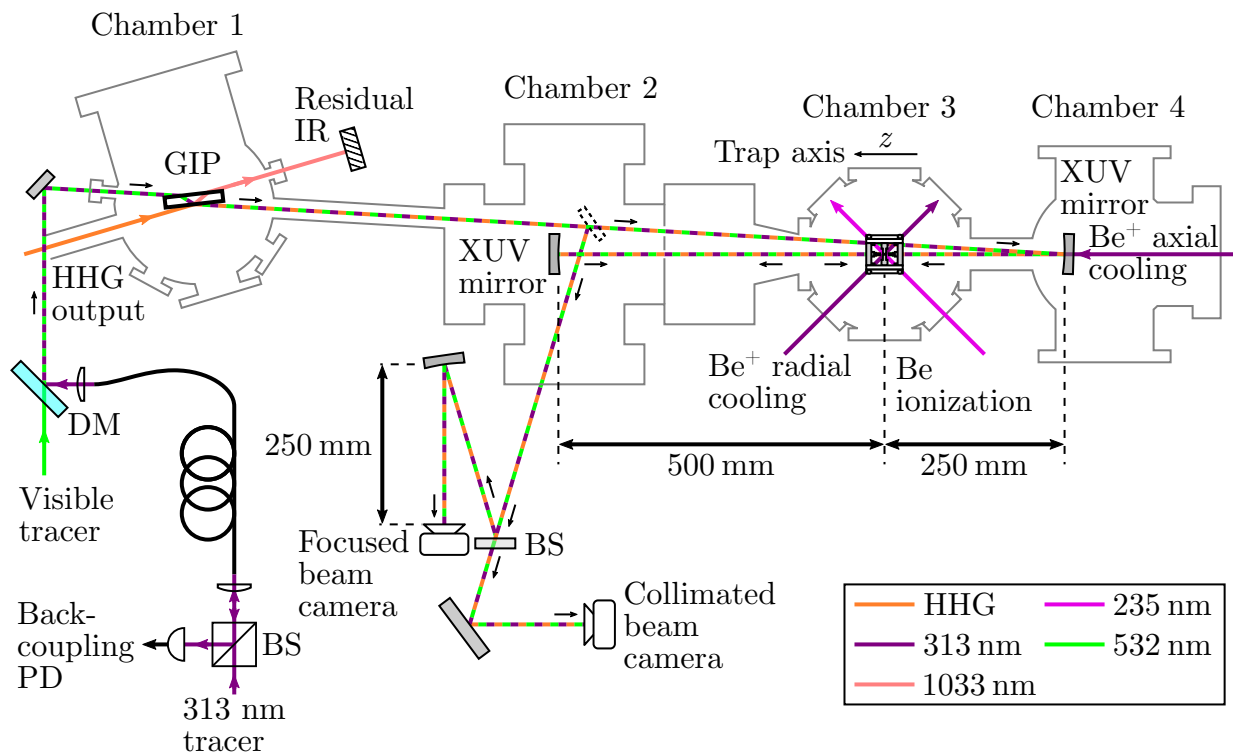


Figure 4.24: Schematic of the laser beam line delivering radiation to the ion trap (not to scale). The grazing incidence plate (GIP) steers the radiation from the high harmonic generation setup and splits off residual infrared light. It is also used for overlapping the HHG output with tracer beams. An insertable mirror (dashed) can send the light out of the setup for adjusting the relative alignment of the wavelength components. The beam is focused onto the ions by a concave XUV mirror (500 mm radius of curvature). A second identical mirror is used as a retroreflector. BS, beam splitter; DM, dichroic mirror.

The setup for sending radiation into the ion trap is shown schematically in Figure 4.24. The radiation that is coupled out from the HHG enhancement cavity can contain up to a few W of residual infrared light at the fundamental wavelength (centered around 1033 nm). This light could lead to thermal damage in the subsequent optical components. The infrared light is therefore strongly attenuated by a “grazing incidence plate” which is

anti-reflection coated for this wavelength.<sup>33</sup> Since the plate is hit at a very large angle of incidence ( $80^\circ$ ), we expect a reflectivity of around 70 % at 60.8 nm from the top  $\text{SiO}_2$  layer of the anti-reflection coating [128]. The plate is mounted in a motorized mirror mount<sup>34</sup> and can be used for steering the beam through the setup. The plate is partially transparent for visible and ultraviolet light. It is therefore also used for overlapping the HHG output with tracer beams. The first tracer has a wavelength of 532 nm and is used to make the beam alignment visible through the windows of the vacuum chambers. The second tracer is derived from the  $\text{Be}^+$  cooling laser at 313 nm. This light makes the trapped  $\text{Be}^+$  ions fluoresce and can be used for fine tuning the alignment onto the ions.

The tracers have to be carefully overlapped with the HHG output. For this purpose a metallic broadband mirror can be inserted into the beam path using a mechanical vacuum feedthrough (dashed mirror in Figure 4.24). The mirror sends the light out of the vacuum chamber through a window. Besides the tracer beams, the fundamental (1033 nm), 3rd harmonic (344 nm), and 5th harmonic (207 nm) contained in the HHG output can pass through the fused silica vacuum window. The light is then split into two paths by a wedged beam splitter.<sup>35</sup> The reflection is focused onto a camera using a concave metallic broadband mirror with 500 mm radius of curvature. This geometry matches the beam path that focuses the radiation onto the trapped ions (see below). The transmitted light is sent onto a second camera without focusing optics. Overlapping the spot positions in the images from the first camera ensures that the beams meet at the focus, but does not yet fix their relative angles. This is achieved by also overlapping the spots in the images from the second camera.

Without the mirror inserted, the beam passes through chambers 2 and 3 and encounters the first concave XUV mirror which is located in chamber 4. The mirror has a radius of curvature of 500 mm and is coated with a custom  $\text{B}_4\text{C}$  multi-layer coating<sup>36</sup> which achieves a measured reflectivity of 33.4 % at 60.8 nm.<sup>37</sup> The mirror focuses the light into the ion trap. As discussed in chapter 3, we plan to excite the 1S-2S transition in  $\text{He}^+$  using two counter-propagating laser beams. This is achieved by placing a second identical XUV mirror 500 mm behind the ion trap which reflects the beam back onto itself. The XUV mirrors are mounted in motorized mirror mounts<sup>38</sup> which are placed on motorized linear stages<sup>39</sup> for focus adjustment. The 313 nm tracer beam makes the  $\text{Be}^+$  ions fluoresce. If a large ion crystal is loaded into the trap, the position and size of the focus can be observed in the horizontal and vertical plane using the ion imaging system (see section 4.2). The light for the 313 nm tracer beam is delivered to the setup using a hydrogen loaded photonic crystal fiber [125]. If the second XUV mirror is adjusted correctly, the tracer beam is sent

---

<sup>33</sup>Custom coating from Layertec.

<sup>34</sup>Newport 8822-UHV.

<sup>35</sup>Thorlabs BSF10-UV.

<sup>36</sup>Produced by optiX fab.

<sup>37</sup>Mirrors in this wavelength range exhibit large losses due to material absorption in the multi-layer stack.

<sup>38</sup>SmarAct STT-25.4-UHV.

<sup>39</sup>SmarAct SLC-2445-O30-UHV.

back through the setup, passes through the grazing incidence plate again, and is coupled back into the fiber. This back-coupled light is monitored using a beam splitter and a photodiode which are placed before the fiber. The signal of this photodiode is used to precisely adjust the alignment of the second XUV mirror.

### Cooling and ionization lasers

For laser cooling single ions, the laser beam has to have a projection onto all three trap axes. On the other hand, it is advantageous to align the laser beam parallel to the trap axis when working with three-dimensional Coulomb crystals (see section 2.2). The former is achieved by sending a laser beam diagonally through chamber 3 (“radial cooling” beam in Figure 4.24). The light is focused by an  $f = 200$  mm lens to a spot size of  $2w_0 \approx 70$   $\mu\text{m}$ . Direct optical access along the trap axis is blocked by the XUV mirrors. However, the mirrors transmit around 7% at 313 nm such that the axial cooling beam can be sent through the first XUV mirror. The light is focused by an  $f = 500$  mm lens which results in a spot size of  $2w_0 \approx 180$   $\mu\text{m}$  in the center of the ion trap.

## 4.5 Experiment control system

The ion trap setup contains a large number of individual components whose settings have to be adjusted during operation. Figure 4.25 shows a high-level overview of the computer system used to control the setup.

Modern PC hardware and operating systems are optimized for throughput, i.e. to maximize the amount of data and number of calculations that can be processed per unit time. On the other hand, the exact timing of the program execution is usually much less important and can fluctuate wildly depending on factors such as system load. This makes them unsuitable for controlling experimental sequences in which accurate timing is required. Our control system therefore combines a desktop PC with a dedicated real-time controller that is specifically designed for atomic physics experiments.<sup>40</sup>

The PC controls many lab devices, such as the EMCCD cameras, power supplies, signal generators, and the I/O card that generates the DC trap voltages. We wrote a custom software in Python (“ion trap software”) that provides a graphical user interface<sup>41</sup> for adjusting the device settings and for viewing the camera images.

The real-time controller is based on a field-programmable gate array (FPGA). It features digital inputs and outputs, analog inputs, and several independent signal generator channels based on direct digital synthesis (DDS). The FPGA controls the timing sequence of the digital output signals and DDS settings with 1 ns resolution. The digital inputs are used for digitizing the pulses generated by the PMT modules, and the analog inputs record voltages from several photodiodes that monitor power levels in the setup. The controller is programmed in a Python-based language. The compiled programs and the acquired

---

<sup>40</sup>ARTIQ Sinara [129].

<sup>41</sup>The interface is implemented using the Qt framework: <https://www.qt.io/>.

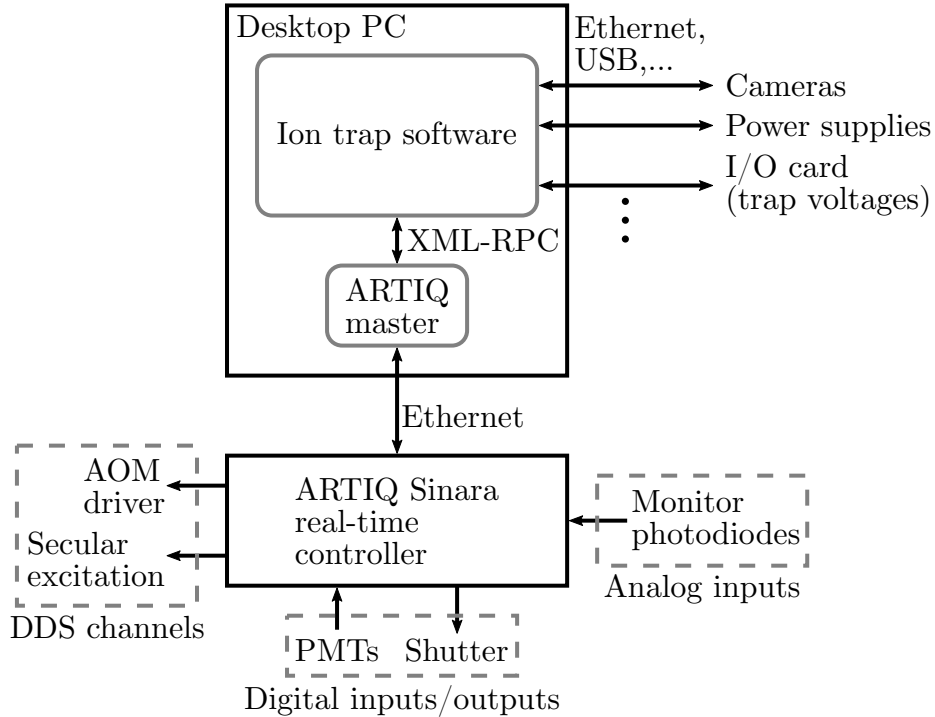


Figure 4.25: Overview of the experiment control system. A software running on a desktop PC provides a graphical user interface and controls a range of devices that do not require accurate timing. A dedicated real-time controller produces accurately timed signals and records the pulses generated by the PMT modules.

data are exchanged between the controller and the PC via Ethernet. A program named “ARTIQ master” handles the communication and controls the program execution.

Sometimes the real-time controller has to work together with the ion trap software. For example, during  $\text{Be}^+$  loading (see section 4.6.1), the real-time controller measures the ion fluorescence and controls the cooling laser frequency shifter (see subsection 4.3.2), while the ion trap software records camera images and measures the ion crystal size. The real-time controller queries the ion trap software for the ion crystal size using remote procedure calls that are transmitted by the ARTIQ master software.<sup>42</sup> Using the same method the real-time controller can also access the other devices that are managed by the ion trap software.

## 4.6 Ion loading

This section describes how we load different ion species into our trap. Besides  $\text{Be}^+$  and  $\text{He}^+$ , we can also load  $\text{H}_2^+$  molecular ions. These have the same charge-to-mass ratio as

<sup>42</sup>We use the XML-RPC method that is implemented as part of the Python standard library: <https://docs.python.org/3/library/xmlrpc.html>.

$\text{He}^{2+}$  and are therefore used for testing the ion detection (see chapter 5). Figure 4.26 shows an overview of the components that are involved. Neutral beryllium is evaporated in an oven and is sent through the trapping region. There, the atoms are resonantly ionized by a 235 nm laser beam and are subsequently laser cooled using 313 nm light. Since helium and hydrogen are gases at room temperature, they can be leaked into the vacuum chamber. An electron gun is used for ionizing the atoms or molecules. In the following the individual components and the loading sequences are described in detail.

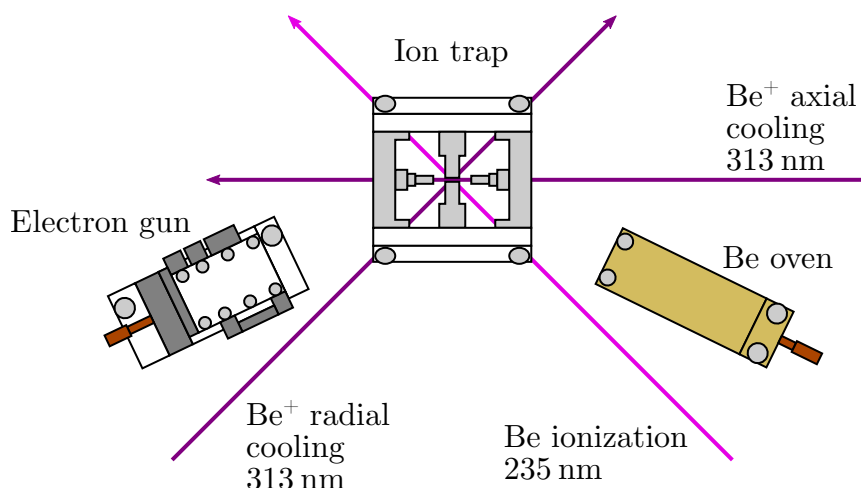


Figure 4.26: Overview of the ion loading setup. A beryllium atomic beam is produced in an oven and is sent through the trapping region. The atoms are ionized by a 235 nm laser beam. Helium and molecular hydrogen can be leaked into the vacuum chamber with a motorized valve and are ionized by electron impact.

### 4.6.1 $\text{Be}^+$ loading

#### Be oven

Beryllium has a relatively high melting point of  $1287^\circ\text{C}$ . This is considerably higher than that of typical aluminum alloys ( $\lesssim 650^\circ\text{C}$ ) and only around 140 K lower than that of 304 stainless steel [130]. It is therefore more challenging to construct an oven for evaporating beryllium than for many other elements used in atomic physics experiments.

The design of our oven is described in detail in [131]. At its core it contains a short piece of beryllium wire that is placed in an aluminum oxide ceramic tube. The tube is heated by passing a current through a tantalum wire wound around it. We typically work with currents between 1.9 A and 2.3 A, corresponding to heating powers of 6.2 W to 9.7 W. The evaporated beryllium is then formed into a diverging atomic beam by an aperture. The oven is aligned such that the beam crosses the trapping region.

### Resonant laser ionization

We use a 235 nm laser to resonantly ionize the beryllium atoms. Figure 4.27 shows the level scheme of the process. The atoms are first excited from the  $2s^2 \ ^1S_0$  ground state to the  $2s2p \ ^1P_1$  excited state. The transition has a wavelength of 234.932 321(7) nm [132] and a linewidth of 86 MHz [133], corresponding to a saturation intensity of 8.6 kW/m<sup>2</sup>. From the excited state the atoms can then be ionized by the 235 nm light.

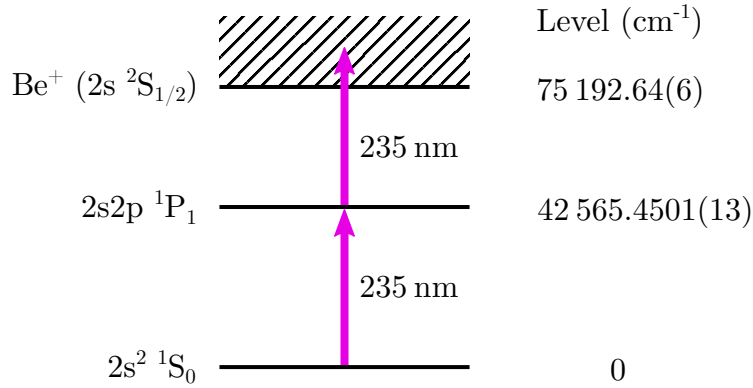


Figure 4.27: Relevant levels and transitions for resonant photoionization of beryllium. The transition wavelength is taken from [132] and the ionization limit from [134].

Resonant photoionization has a number of advantages over electron impact ionization. When operating an electron gun near the ion trap, it is difficult to avoid electrons hitting the various surfaces of the setup. This can lead to patch charges on insulators that create stray fields in the trapping region. The DC trap electrodes are connected to their voltage sources through low-pass filters with large resistors (see subsection 4.1.4). If they are struck by electrons, the dissipated currents significantly change their voltages which can destabilize the trap. An ultraviolet laser beam can also create surface charges due to the photoelectric effect. However, it is easy to focus the beam to the trapping region which minimizes the illuminated surfaces.

Another advantage is species selectivity. While electron impact can ionize any atom, the resonant laser ionization relies on a spectral line in beryllium.<sup>43</sup> This avoids contaminating the trap with unwanted ion species that can be produced from the background gas.

### Ionization laser system

We generate the 235 nm light for ionization by frequency quadrupling the output of a diode laser system. Figure 4.28 shows a schematic of the setup.

A grating-stabilized external-cavity diode laser [135] generates around 70 mW of light at 940 nm. The power is boosted to 400 mW in a tapered amplifier. Optical isolators

<sup>43</sup>In many atomic species contamination by other isotopes is a concern. This is not an issue in beryllium since all isotopes besides <sup>9</sup>Be have relatively short lifetimes such that their natural abundances are negligible.

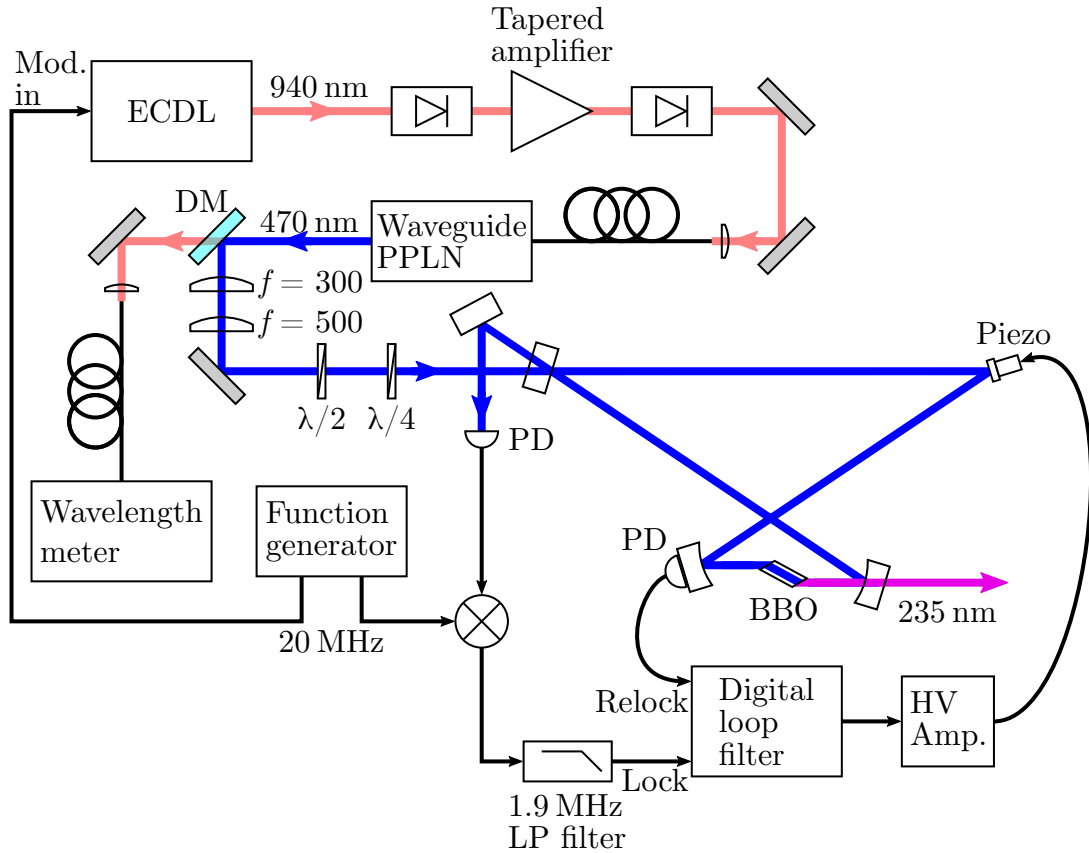


Figure 4.28: Schematic of the ionization laser system. ECDL, external-cavity diode laser; DM, dichroic mirror; PD, photodiode; LP filter, low-pass filter. Focal lengths are given in mm.

protect the diode laser and the tapered amplifier from back reflections that can disturb the single-mode operation of the laser and can cause damage to the amplifier.

The light is then sent into a fiber-coupled frequency doubling module.<sup>44</sup> In the module second harmonic generation takes place in a periodically poled lithium niobate (PPLN) crystal that is shaped to also act as a waveguide. In this way high optical intensity can be maintained over a longer interaction length than is possible by focusing a laser beam into a bulk crystal. This allows for efficient single-pass frequency conversion at relatively low input power levels [136]. The temperature of the crystal has to be fine tuned and stabilized in order to maintain quasi-phase matching. This is achieved using the built-in thermistor and Peltier element of the module, and an external temperature controller. In our setup the module produces an output power of around 30 mW at 470 nm.

A dichroic mirror is used to split off the residual infrared light. Part of this light is sent to a wavelength meter<sup>45</sup> for monitoring the ECDL wavelength. At the melting point

<sup>44</sup>NTT WH-0470-000-A-B-C.

<sup>45</sup>HighFinesse WS7.

of beryllium, the FWHM Doppler width of the photoionization transition is 12 GHz [137, p. 84]. Due to space constraints in our vacuum chamber, the atomic beam has an angle of  $19^\circ$  to the ionization laser beam (see Figure 4.26). We therefore do not expect a significant reduction of the Doppler width due to having an atomic beam. At the fundamental wavelength this corresponds to an FWHM width of 3 GHz. The passive frequency stability of the ECDL is therefore sufficient to maintain resonance, and no active feedback system is required.

The 470 nm light is then frequency doubled to 235 nm in a  $\beta$ -barium borate (BBO) crystal in a bow-tie enhancement cavity. Critical type I phase matching is achieved at an angle of  $58.2^\circ$ . We decided to use a Brewster-cut uncoated crystal to avoid potential degradation of anti-reflection coatings due to the generated ultraviolet light.

For a given power the efficiency of second harmonic generation depends on the crystal length, and on the size and shape of the focus inside the crystal. This was studied theoretically in a seminal paper by G. Boyd and D. Kleinman [138]. They found that the efficiency depends on the parameter  $\xi = l/b$ , where  $l$  is the length of the crystal, and  $b$  is the confocal parameter of the focused light. The optimum value varies from  $\xi = 2.84$  in the absence of walk-off (noncritical phase matching) to  $\xi = 1.39$  for large walk-off. The results were later generalized to the case of elliptical beams [139].

In an enhancement cavity the focus parameters are determined by the cavity mode. For a given cavity geometry, the mode can be calculated using the ABCD matrix formalism for the propagation of Gaussian beams [140]. We found it convenient to implement the calculations in a Python program<sup>46</sup> such that the resulting mode for different cavity configurations could be quickly evaluated. The theoretical efficiency is then calculated by performing the numerical optimization described in [139]. After analyzing different possible configurations, we decided to use the same cavity geometry that was previously used in a similar system [141]. In this design the beam in the collimated arm of the cavity (opposite to the crystal) is round which simplifies mode matching. The crystal has a length of 10 mm. The angle of incidence on the focusing mirrors, which have a radius of curvature of 38 mm, is  $16.9^\circ$ . The total optical path length of the cavity is 373 mm, resulting in a free spectral range of 803 MHz. The focus inside the crystal is elliptic with a Gaussian waist radius  $w_h = 22.2 \mu\text{m}$  in the horizontal direction and  $w_v = 14.5 \mu\text{m}$  in the vertical direction. The resulting single-pass conversion efficiency is calculated to be  $\Gamma = P_{\text{out}}/P_{\text{in}}^2 = 1.0 \times 10^{-4} \text{ W}^{-1}$ , where  $P_{\text{in}}$  is the input power at the fundamental wavelength, and  $P_{\text{out}}$  is the generated power. This is 47% smaller than the maximum that can be achieved with an elliptical beam [139]. However, we found that this “ideal focusing” would be difficult to achieve since the Brewster-cut crystal introduces ellipticity in the wrong direction [139].

Another degree of freedom is the transmission of the input coupler mirror. The conversion efficiency is maximum for an impedance matched cavity [142], i.e. when the input coupler transmission is equal to the round-trip loss (excluding the input coupler). Since it is difficult to precisely estimate the losses before the cavity is built, we obtained different

<sup>46</sup>The source code is available at <https://github.com/schmidf/shg-cavity-calculator>.



mirrors with reflectivities of 99.7%, 99.5%, and 99.1%. The best efficiency was achieved with 99.1% reflectivity.

One of the cavity mirrors is mounted on a piezoelectric actuator for active length stabilization. The error signal is obtained using the Pound-Drever-Hall method [143], and the required sidebands are generated by modulating the ECDL current.

Figure 4.29 shows the mechanical construction of the cavity. The mirror mounts are directly screwed into a 37 mm thick aluminum base plate which makes the setup very rigid. Their positions are fixed according to the design by alignment pins that slot into precisely machined holes in the plate. The BBO crystal is mounted on a linear stage and a kinematic rotation mount<sup>47</sup> for fine tuning of the focusing and phase matching. To prevent thermal drifts of the phase matching, its temperature is actively stabilized with a temperature sensor and a heater. In order to prevent contamination of the optical surfaces, the cavity has an airtight enclosure, and filtered and dry air is circulated through the system.

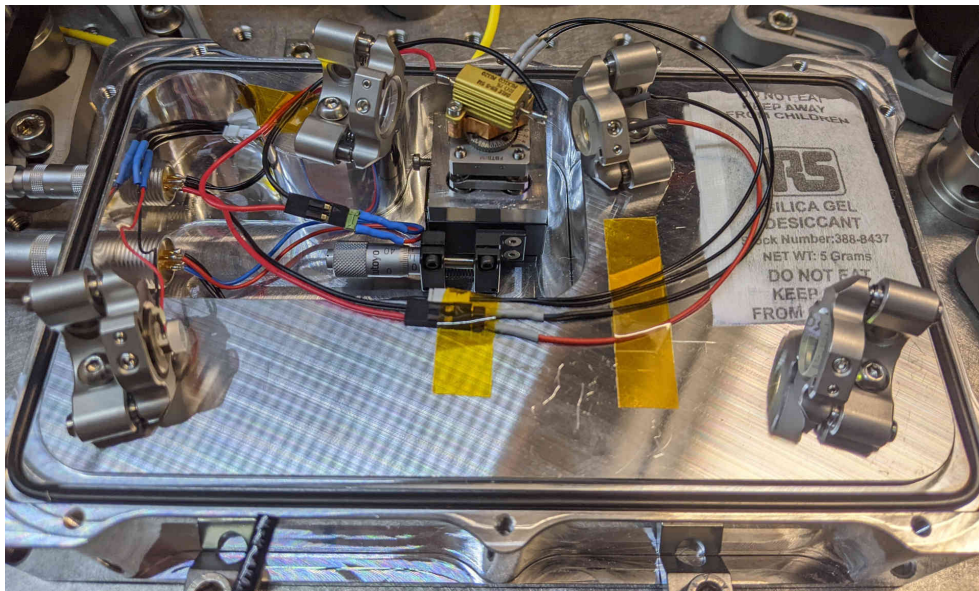


Figure 4.29: Cavity for resonant second harmonic generation. The light at 470 nm is coupled in through the mirror in the bottom right. The mirror on the top left is dichroic and transmits the generated light at 235 nm. The base plate is machined from a 37 mm thick block of aluminum and provides good mechanical stability.

The cavity produces an output power of a few hundred  $\mu\text{W}$  which is sufficient for efficient trap loading. The light is loosely focused into the trapping region using an  $f = 200$  mm lens.

<sup>47</sup>Thorlabs FBTB/M.

### Crystal degradation and digital loop filter

Despite the relatively low power levels, we observed significant degradation of the BBO crystal due to the generated ultraviolet light. This manifests itself as a drop in the generated output power over time. Furthermore, the cavity resonance “splits” into a double-peak structure which we attribute to increased absorption of the fundamental Gaussian cavity mode. The output power is typically restored after shifting the position of the crystal which indicates that it is responsible for the degradation. A number of crystals from several manufacturers were tested. While some showed rapid degradation on the time scale of a few minutes, others lasted for many hours of operation. However, none were entirely immune to degradation. The longevity of the system can be significantly improved by only turning on the cavity lock during ion loading.

We therefore developed a digital loop filter that can be remote controlled and that automatically acquires the cavity lock. It is based on a commercial RF signal acquisition and generation board.<sup>48</sup> The board is based on a system on a chip that contains an ARM processor and an FPGA. The FPGA controls two 14-bit analog to digital converters (ADCs) and two 14-bit digital to analog converters (DACs) which operate at 125 MS/s. It also has four auxiliary analog input channels with 12-bit resolution and 100 kS/s sampling rate.

We implemented a custom FPGA firmware<sup>49</sup> for cavity locking. The error signal is sampled by one of the ADC channels. A digital proportional-integral-derivative (PID) controller implemented in the FPGA calculates a correction signal which is output using the DAC. We also added the automatic relocking algorithm from [144] to our firmware. A photodiode is placed behind one of the cavity mirrors and records the leakage power which is proportional to the power circulating in the cavity. This signal is digitized by one of the auxiliary analog inputs of the FPGA. If the signal drops below a configured threshold, the FPGA freezes the state of the PID controller and starts sweeping the output voltage in a triangle pattern with increasing amplitude (see Figure 4.30). Once the signal exceeds the threshold again, the sweep is stopped and the PID controller is re-engaged. This algorithm reliably acquires the lock when the feedback controller is enabled, or after a mechanical disturbance has unlocked the cavity.

### Loading sequence

The beryllium loading sequence is fully automated using the experiment control system. First, the beryllium oven and the ionization laser are turned on. The  $\text{Be}^+$  ions generated in the trapping region are initially very hot. This leads to a large Doppler broadening, making laser cooling inefficient. We found that it is difficult to crystallize the ions when the cooling laser detuning is too small. In the beginning of the loading cycle, the AOM in the frequency shifter setup is therefore turned off and the 0th order shutter is opened such that only the far-detuned frequency component is applied (see subsection 4.3.2). This

---

<sup>48</sup>Red Pitaya STEMLab 125-14.

<sup>49</sup>The firmware is available at <https://github.com/schmidf/rp-lockbox>.

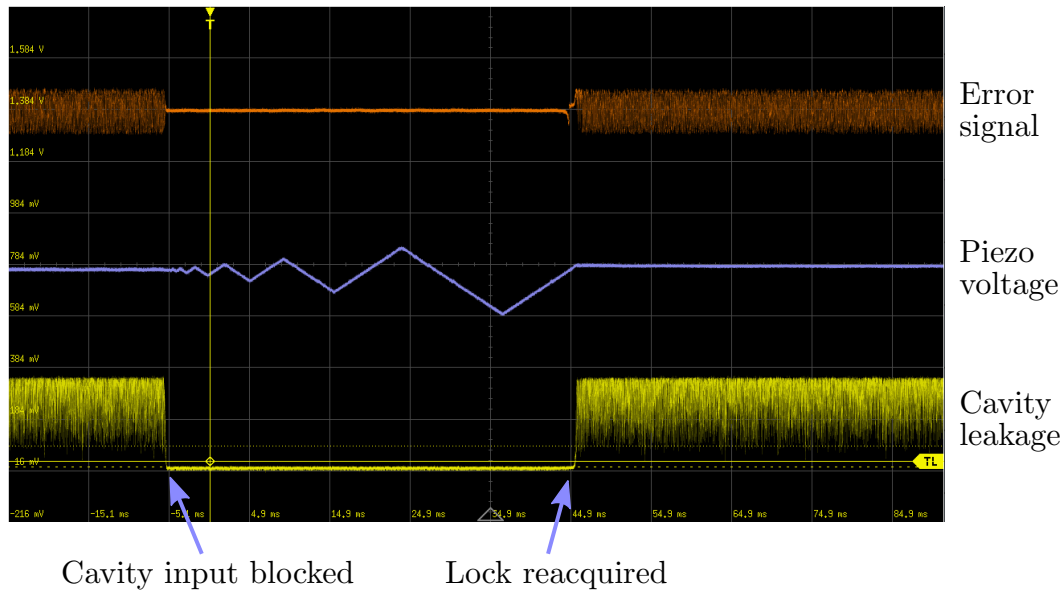


Figure 4.30: Demonstration of automatic cavity relocking. The cavity input is blocked for a short time such that the lock is lost. The drop in cavity leakage power is registered by the FPGA which then sweeps the Piezo voltage to search for a cavity resonance. Once a sufficiently high leakage power is detected again, the sweep is stopped and the PID controller is re-engaged. The linewidth of the enhancement cavity is not much larger than that of the 470 nm laser. This leads to a relatively high noise level visible in the leakage and error signals.

component is red-detuned from the resonance by a few hundred MHz.

Once the first ions are crystallized into a Coulomb crystal, the fluorescence recorded with the PMTs increases. The experiment control system detects this and turns on the AOM in the frequency shifter setup. This enables the near-detuned frequency component which strongly increases the scattering from the trapped ions. The ion crystal shape can then be monitored using the cameras. At this point the loading process also becomes more efficient since the already crystallized ions sympathetically cool the newly generated ones. The images from one of the cameras are automatically analyzed to determine the ion crystal size. The image analysis is implemented in Python using the scikit-image library [145] and is illustrated in Figure 4.31. First, foreground and background pixels are separated according to a threshold brightness value that is calculated using the triangle algorithm [146]. The region covering the ion crystal contains holes due to image noise and gaps between the ions. These are removed using a morphological closing operation on the binary image [147]. The largest contiguous region is then identified as the ion crystal. Its ellipse parameters [147] finally give an estimate for the height and width of the ion crystal.

When the ion crystal width has reached a configured target value, the ionization laser and beryllium oven are automatically turned off which ends the loading sequence. In this way we can reliably produce nearly identical ion crystals despite the stochastic nature of

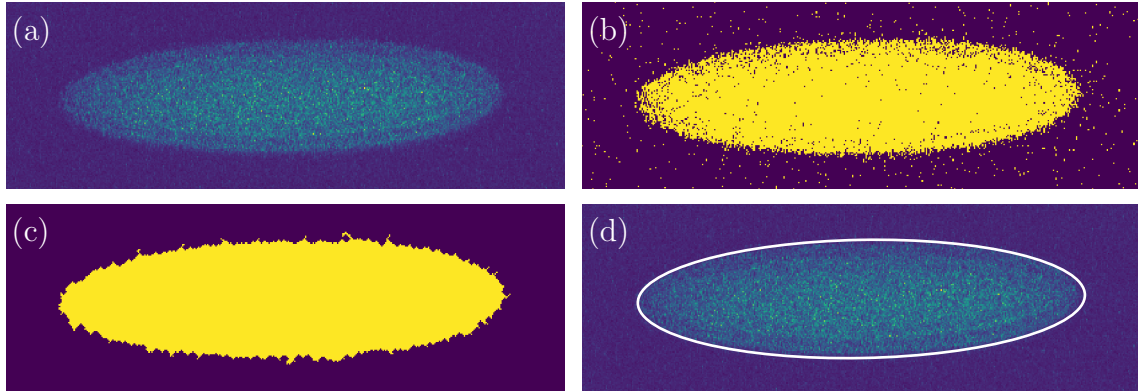


Figure 4.31: Automated measurement of the ion crystal size in a camera image. (a) Input image. (b) Binary separation between foreground and background pixels. (c) Identified ion crystal region after holes have been closed by a closing operation. (d) Extracted ellipse parameters of the ion crystal region.

the loading process.

#### 4.6.2 $\text{He}^+/\text{H}_2^+$ loading

The first dipole-allowed transition from the ground state of neutral helium ( $1s^2 \ ^1S_0$  to  $1s2p \ ^1P_1$ ) has a wavelength of only 58.4 nm [148]. Resonant laser ionization is therefore not feasible, and electron impact ionization is used instead. As mentioned above, electron beams can lead to detrimental effects in ion traps due to patch charges created on insulating surfaces. In our setup operating the electron gun leads only to weak stray fields in the trapping region. These can be easily compensated by adjusting the voltages of the DC trap electrodes and the compensation electrode. However, operating the electron gun for more than a few seconds significantly increases the background pressure in the vacuum chamber which leads to ion loss. Large  $\text{Be}^+$  ion crystals can therefore only be loaded using resonant photoionization in our setup. This is not a significant limitation for loading typical numbers of  $\text{He}^+$  or  $\text{H}_2^+$  ions which takes a few seconds at most.

#### Gas system

Figure 4.32 shows the setup that allows filling the ion trap chamber with a controlled partial pressure of hydrogen or helium gas. The gas reservoir is first evacuated with a turbo pumping station.<sup>50</sup> The pumps are then isolated, and the reservoir is filled with a few ten mbar of hydrogen or helium. A motorized leak valve<sup>51</sup> introduces a small amount of gas into the ion trap chamber. The pressure in the chamber is measured with a cold

<sup>50</sup>Edwards T-Station 85H Dry.

<sup>51</sup>VAT Series 590.

cathode ion gauge, and the built-in feedback controller of the leak valve adjusts its setting to maintain a configured pressure value.

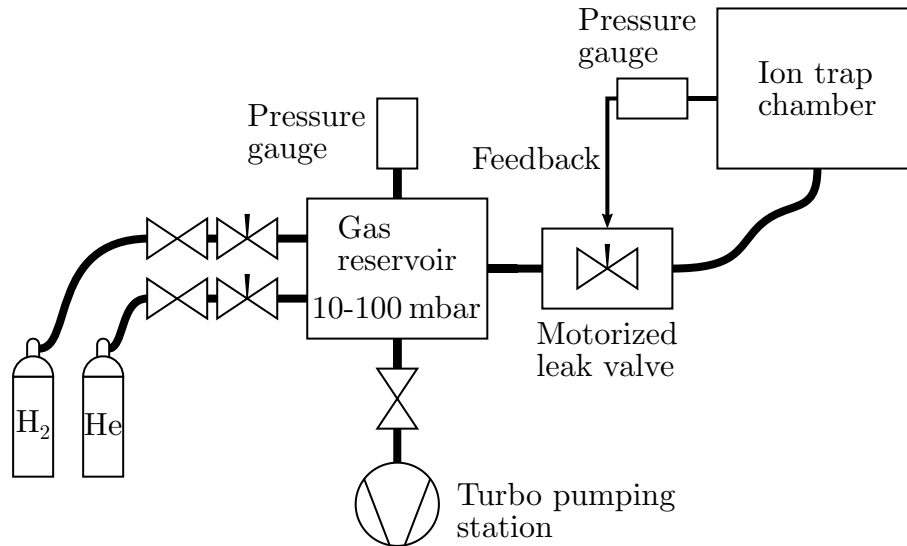


Figure 4.32: Gas system for introducing hydrogen or helium into the ion trap chamber. The rest of the vacuum system is not shown (see section 4.4).

### Electron gun

Our electron gun was designed by B.-m. Ann and is described in detail in [149]. A cross section of the design is shown in Figure 4.33.

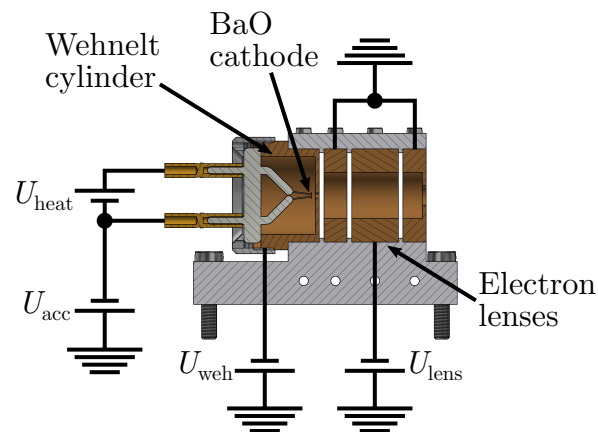


Figure 4.33: Cross section view of the electron gun. See the main text for details.

The electrons are emitted by a BaO coated cathode<sup>52</sup> which is heated by a DC current. The coating leads to a lower work function compared to a standard tungsten cathode.

<sup>52</sup>Kimball Physics ES-015.

It can therefore operate at a lower temperature which increases the lifespan and reduces the amount of light that is emitted which could otherwise overwhelm the fluorescence imaging system. The acceleration voltage  $U_{\text{acc}} = -200 \text{ V}$  is applied to the filament. It is placed inside a Wehnelt cylinder which is held at  $U_{\text{weh}} = -160 \text{ V}$ . The potential difference accelerates the electrons through a small hole in the cylinder. They are then focused by three lens electrodes. The outer ones are grounded, and the voltage  $U_{\text{lens}} = -120 \text{ V}$  is applied to the middle one. This produces a collimated electron beam with 200 eV electron energy. The emission current depends on the temperature of the filament and can be controlled by adjusting the heater voltage  $U_{\text{heat}}$ . Typically, we use currents between 50  $\mu\text{A}$  and 100  $\mu\text{A}$ .

### Loading sequence

To produce a mixed ion crystal, we first load a  $\text{Be}^+$  ion crystal as described in the previous section. The  $\text{He}^+/\text{H}_2^+$  loading sequence is automated using the experiment control system.

First, the pressure setpoint of the motorized leak valve is configured. The feedback system reaches the target value after a few seconds. We typically use pressures between  $5 \times 10^{-10} \text{ mbar}$  and  $5 \times 10^{-9} \text{ mbar}$ . The electron beam has to pass close to one of the endcap electrodes to reach the trapping region (see Figure 4.26). This leads to a deflection of the beam since the electron gun acceleration voltage is on the same order of magnitude as typical endcap voltages. The endcap voltages are therefore ramped down to 100 V during the loading process. This is sufficient for stable trapping, but low enough that the electron beam is not affected too much. The electron gun is then turned on for a few seconds to ionize the gas. Finally, the leak valve is closed, and the endcap voltages are ramped back up to their original values. Figure 4.34 shows a  $\text{Be}^+$  ion crystal before and after  $\text{He}^+$  ions were loaded into the trap. Since the  $\text{He}^+$  ions are lighter than the  $\text{Be}^+$  ions, they are more tightly confined and arrange themselves along the trap axis (see Equation 2.20). This displaces  $\text{Be}^+$  ions from the center of the ion crystal resulting in a dark “core” visible in the images.

## 4.7 Trap characterization

In subsection 4.1.2 the expected potential for our ion trap geometry obtained using a finite element analysis software was shown. This section describes the experimental characterization of the potential of our realized ion trap.

### 4.7.1 Radial secular frequencies

We characterize the radial potential of our trap by exciting the radial secular motion of a single trapped  $\text{Be}^+$  ion. We do this by applying an additional oscillating voltage to the compensation electrode (see subsection 4.1.4). The ion is laser cooled using the radial cooling beam (see Figure 4.24) with a saturation parameter  $s \approx 10$ . The cooling laser is



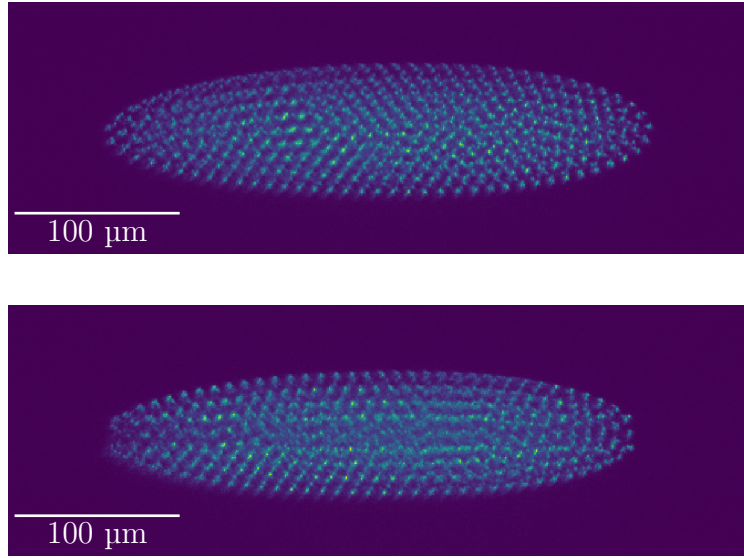


Figure 4.34: Fluorescence image of a  $\text{Be}^+$  ion crystal before (top) and after (bottom) loading  $\text{He}^+$  ions into the trap. The  $\text{He}^+$  ions do not fluoresce and are visible as a dark “core” in the ion crystal. The focus of the imaging system is adjusted close to the center of the ion crystal. However, some of the fluorescence from the  $\text{Be}^+$  ions located in front and behind of the  $\text{He}^+$  ions is visible in the bottom image such that the region containing the  $\text{He}^+$  ions is not entirely dark.

red-detuned from the cooling transition by 112 MHz. The excitation frequency is scanned in 250 steps over a range of a few hundred kHz around the resonances. At each frequency step ion fluorescence is collected for 10 ms using the PMTs. Figure 4.35 shows a typical resulting secular spectrum. Under the experimental conditions, the secular excitation leads to an increase in the fluorescence emitted by the ion. The radial secular resonance is split into a pair of resonances. This shows that the potential of our trap is not perfectly radially symmetric (see section 2.1.3).

The measurement is repeated for different RF powers applied to the helical resonator. The endcaps are held at a fixed voltage of 400 V which results in an axial secular frequency of  $\omega_z = 2\pi \times 748$  kHz (see below). The results are shown in Figure 4.36.

The secular frequencies along the two radial axes of a linear Paul trap are given by Equations 2.29 and 2.30. In general the frequency of a radial secular resonance can be written as

$$\omega_{\text{sec}} = \sqrt{\omega_{\text{rf}}^2 \pm \omega_{\text{dc}}^2 - \frac{1}{2}\omega_z^2}, \quad (4.17)$$

where  $\omega_{\text{rf}}$  is the dynamic confinement created by the oscillating trap field, and  $\omega_{\text{dc}}$  is the confinement or deconfinement due to the DC electrodes. From Equation 2.31, we find

$$\omega_{\text{rf}} \propto V \propto \sqrt{P_{\text{rf}}}, \quad (4.18)$$

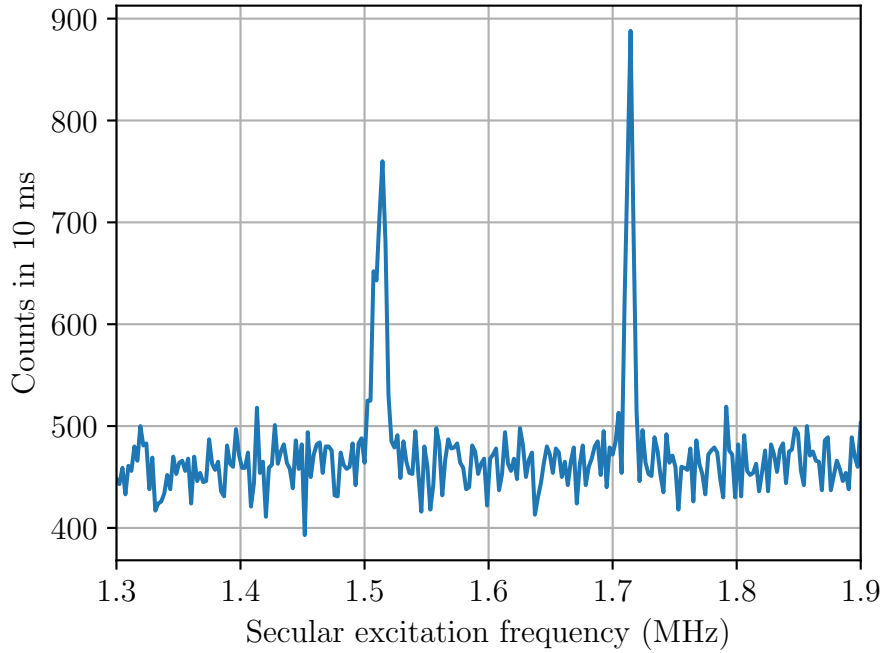


Figure 4.35: Typical secular scan spectrum showing the radial excitation of a single  $\text{Be}^+$  ion. On resonance the ion starts to move which increases the fluorescence intensity. The resonance is split into a pair of resonances which indicates that the radial symmetry of the ion trap is broken.

where  $V$  is the amplitude of the RF signal at the trap RF electrodes, and  $P_{\text{rf}}$  is the RF power applied to the helical resonator. We therefore fit the experimental points with the following function:

$$\omega_{\text{sec}} = \sqrt{\alpha P_{\text{rf}} + \beta}, \quad (4.19)$$

where  $\alpha$  and  $\beta$  are the fit parameters.

For the upper resonance we obtain  $\alpha_{\text{upper}} = (2\pi \times 2.03 \text{ MHz})^2/W$ ,  $\beta_{\text{upper}} = -(2\pi \times 598 \text{ kHz})^2$ , and for the lower resonance we obtain  $\alpha_{\text{lower}} = (2\pi \times 2.02 \text{ MHz})^2/W$ ,  $\beta_{\text{lower}} = -(2\pi \times 985 \text{ kHz})^2$ .

The amplitude of the RF signal is given by

$$V = \eta \sqrt{2Z_0 P_{\text{rf}}}, \quad (4.20)$$

where  $Z_0 = 50 \Omega$  is the characteristic impedance of the RF amplifier, and  $\eta$  is the voltage enhancement of the helical resonator. We obtain a theoretical value for the parameter  $\alpha$  by inserting Equation 4.20 into Equation 2.31:

$$\omega_{\text{rf}}^2 = \frac{Q^2 V^2}{2m^2 \Omega^2 r_{\text{eff}}^4} = \frac{Q^2 \eta^2 Z_0}{m^2 \Omega^2 r_{\text{eff}}^4} P_{\text{rf}} = \alpha_{\text{theor}} P_{\text{rf}}, \quad (4.21)$$



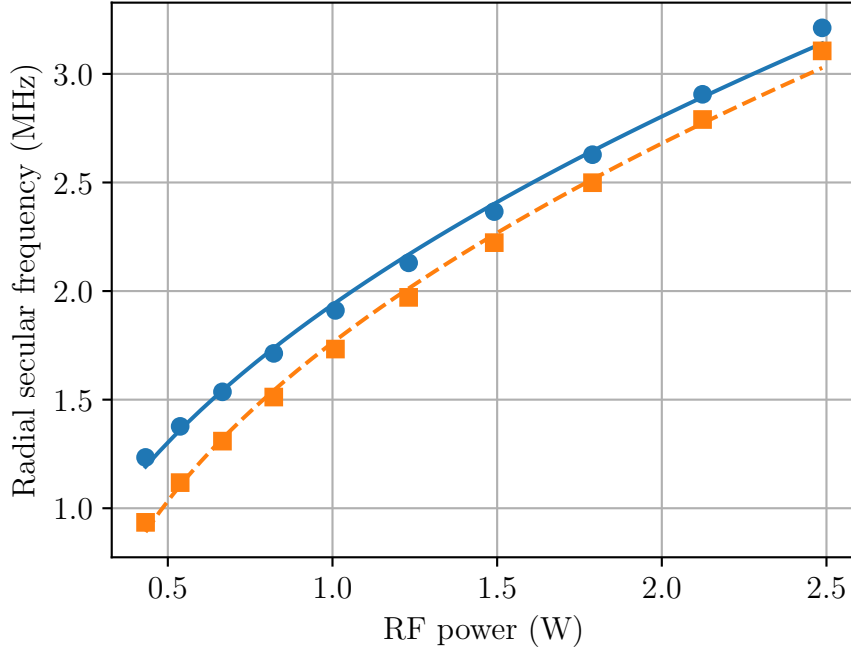


Figure 4.36: Radial secular frequencies of a single  $\text{Be}^+$  ion measured for different RF powers applied to the helical resonator. The blue circles show the position of the upper resonance and the orange squares that of the lower resonance. The solid and dashed lines are fits of Equation 4.19 to the upper and lower resonance data, respectively.

where  $Q$  and  $m$  are the charge and mass of a  $\text{Be}^+$  ion,  $\Omega = 2\pi \times 66.05$  MHz is the radio frequency applied to the trap, and  $r_{\text{eff}} = 0.468$  mm is the effective size of the trap (see section 4.1.2). As discussed in section 4.1.3, we observed that the voltage enhancement of the RF resonator has degraded somewhat over time. If we take a typical value  $\eta \approx 14$ , we get  $\alpha_{\text{theor}} = (2\pi \times 1.78 \text{ MHz})^2/W$  which is in reasonable agreement with the experimental values. This indicates that the radial trap potential agrees with the shape obtained from the simulations.

### 4.7.2 Axial secular frequencies

The axial potential of the trap is characterized in a similar way by exciting the axial secular motion of a single trapped  $\text{Be}^+$  ion. In this case the excitation signal is applied to one of the endcap electrodes (see subsection 4.1.4). The ion is laser cooled with the radial cooling beam only. Good results were achieved for the secular excitation spectra with a saturation parameter  $s \approx 1$  and with the cooling laser red-detuned from the resonance by 9 MHz. A typical axial secular spectrum is shown in Figure 4.37. At the chosen parameters the excitation leads to a strong decrease in the fluorescence emitted by the ion.

The secular frequency is measured for different voltages  $U_{\text{ec}}$  applied to the endcap electrodes. The results are shown in Figure 4.38.

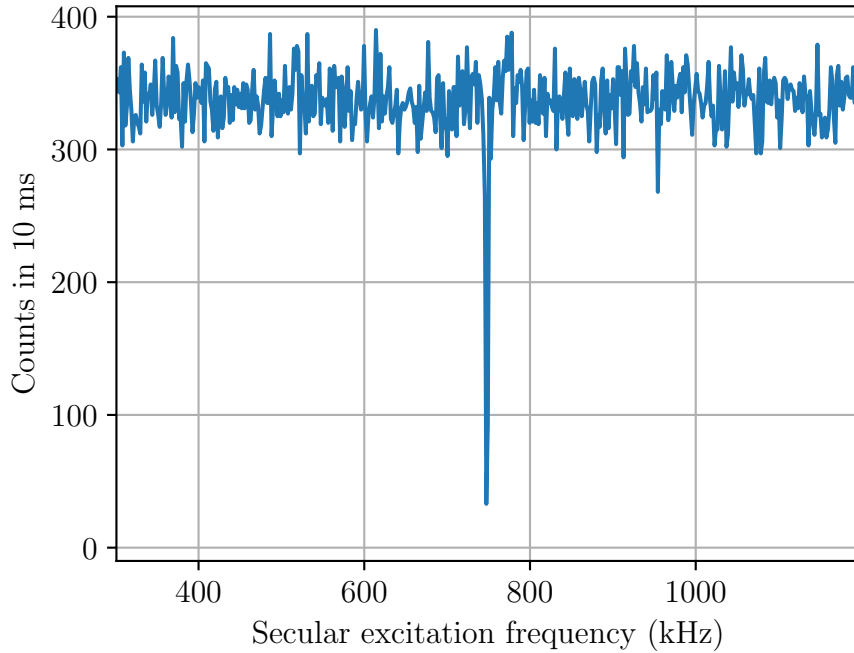


Figure 4.37: Typical secular scan spectrum showing the axial excitation of a single  $\text{Be}^+$  ion. The ion motion on resonance leads to a significant drop in the fluorescence intensity.

For an ideal linear Paul trap, the axial secular frequency is given by Equation 2.25 and scales with the square root of the endcap voltage  $U_{\text{ec}}$ . The geometrical factor  $\kappa$  can be obtained by fitting this function to the data. However, we found that the fit is unsatisfactory for our experimental data. Instead, we use the following fit function:

$$\omega_z = \sqrt{\frac{Q\kappa U_{\text{ec}}}{mz_0^2} + \omega_0^2}, \quad (4.22)$$

where  $z_0 = 3.5$  mm is the distance between the endcap electrodes and the trap center. The fit parameters are the geometrical factor  $\kappa$ , and  $\omega_0$  which characterizes a contribution to the axial confinement that is independent of the endcap voltage. The fit results are  $\kappa = 0.054$  and  $\omega_0 = 2\pi \times 291$  kHz. This disagrees with the finite element method simulation of the trap potential (see section 4.1.2) which predicts  $\kappa = 0.073$  and no endcap voltage-independent term  $\omega_0$ . The finite length of the trap electrodes can in principle lead to RF confinement along the trap axis. We have used the finite element analysis software<sup>53</sup> to evaluate this effect for our trap geometry. According to the simulation results, the axial RF confinement is around 1000 times weaker than the radial RF confinement and can therefore not explain the discrepancy. This was confirmed experimentally by measuring the axial secular frequency for different radial secular frequencies. The endcap voltage was set to a relatively low value of 100 V such that  $\omega_0$  contributes significantly to the axial secular

<sup>53</sup>COMSOL Multiphysics.

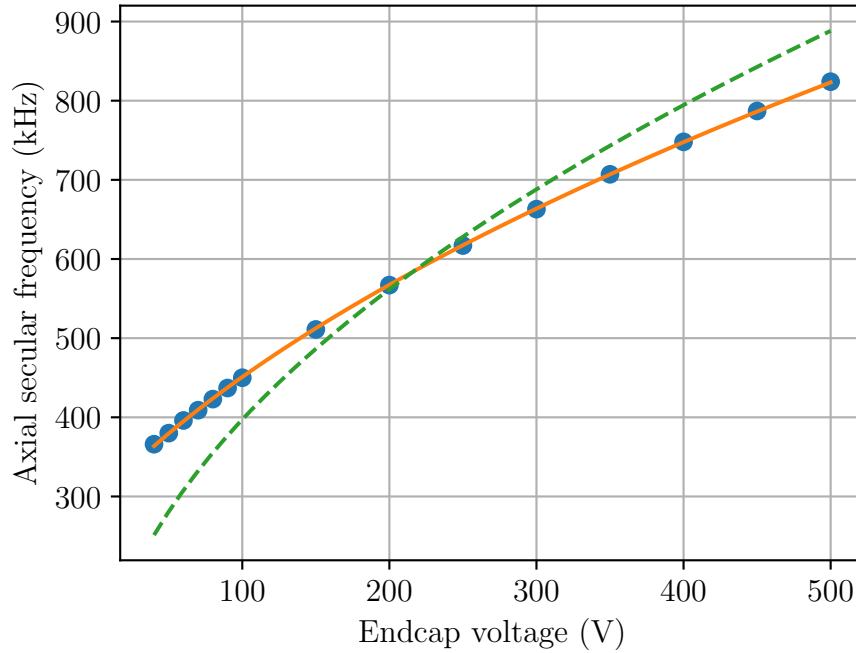


Figure 4.38: Axial secular frequencies of a single  $\text{Be}^+$  ion measured at different endcap voltages (blue circles). The theoretical expression for the axial secular frequency in an ideal linear Paul trap (Equation 2.25) gives an unsatisfactory fit to the experimental data (green dashed line). The orange line is a fit of Equation 4.22 where an endcap voltage-independent axial confinement was added.

frequency. Under these conditions changing the radial secular frequency by a factor of three led to no significant change of the axial secular frequency.

As we will show in the next section, small manufacturing imperfections that change the positions of the blade electrodes can lead to significant deviations from the theoretical potential. While the origin of the spurious axial confinement remains unclear, we suspect that it might be caused by such imperfections.

### 4.7.3 Excess micromotion

So far we have focused only on the secular ion motion in the effective pseudopotential of the trap. As discussed in subsection 2.1.2 and subsection 2.1.3, the oscillating trap potential causes an additional micromotion component at the trap drive frequency  $\Omega$ . In this section the theory of ion micromotion is reviewed, and measurements of the micromotion amplitude in our trap are presented. Finally, the resulting effects of micromotion on the  $\text{He}^+$  spectroscopy are estimated.

### Stray fields

Micromotion is often caused by stray electric fields that displace the ions from the node of the RF potential. We write the position of an ion in the trap as  $\mathbf{u} = u_x \mathbf{e}_x + u_y \mathbf{e}_y + u_z \mathbf{e}_z$ , where  $\mathbf{e}_x$ ,  $\mathbf{e}_y$ , and  $\mathbf{e}_z$  are unit vectors along the three trap axes. The coordinate system is shown in Figure 4.1, Figure 4.8, and Figure 4.9. The ion is affected by a static electric field  $\mathbf{E}_{\text{dc}}$ . Such a field can for example be caused by surface charges on the trap electrodes. If multiple ions are trapped together,  $\mathbf{E}_{\text{dc}}$  also contains the fields created by the other ions. The resulting equations of motion are inhomogeneous forms of the Mathieu differential equation [48, 150]:

$$\ddot{u}_i + [a_i + 2q_i \cos(\Omega t)] \frac{\Omega^2}{4} u_i = \frac{Q \mathbf{E}_{\text{dc}} \cdot \mathbf{e}_i}{m}, \quad (4.23)$$

where  $a_i$  and  $q_i$  are the Mathieu parameters (see subsection 2.1.3), and  $Q$  and  $m$  are the charge and mass of the ion.

An approximate solution of Equation 4.23 for  $|a_i|, q_i^2 \ll 1$  is [48]

$$u_i(t) = [u_{0,i} + u_{1,i} \cos(\omega_{\text{sec},i} t + \varphi_{0,i})] \left[ 1 + \frac{q_i}{2} \cos(\Omega t) \right], \quad (4.24)$$

where  $u_{1,i}$  is the amplitude of the secular motion,  $\varphi_{0,i}$  is a constant that depends on the initial conditions,

$$\omega_{\text{sec},i} = \frac{\Omega}{2} \sqrt{a_i + \frac{q_i^2}{2}} \quad (4.25)$$

is the secular frequency along trap axis  $i$ , and

$$u_{0,i} = \frac{Q \mathbf{E}_{\text{dc}} \cdot \mathbf{e}_i}{m \omega_{\text{sec},i}^2} \quad (4.26)$$

is the displacement of the average ion position from the trap center due to  $\mathbf{E}_{\text{dc}}$ . Equation 4.24 contains two terms that oscillate at frequency  $\Omega$ . The term proportional to the secular motion is called the ‘‘intrinsic micromotion’’. It does not depend on  $\mathbf{E}_{\text{dc}}$  and is strongly reduced by laser cooling since this damps the secular motion. The term proportional to  $u_{0,i}$  is called the ‘‘excess micromotion’’. Since it is a driven motion, it cannot be significantly reduced by laser cooling [48].

### Residual RF fields

More generally, excess micromotion is due to a residual RF electric field at the equilibrium position of the ion:

$$\mathbf{E}_{\text{rf}}(t) = \sum_{i=x,y,z} \tilde{E}_{\text{rf},i} \cos(\Omega t + \varphi_{\text{rf},i}) \mathbf{e}_i, \quad (4.27)$$

where  $\tilde{E}_{\text{rf},i}$  and  $\varphi_{\text{rf},i}$  are the amplitude and phase of the residual RF electric field component along the trap axis  $i$ . In the case of stray electric fields, it is the displacement of the ion from the node of the RF potential that leads to a residual RF electric field. Another possible

source is a phase shift between the signals applied to the RF electrodes. This leads a residual RF electric field that cannot be compensated by shifting the ion position [48]. In our trap the lengths of the wires connecting the RF resonator to the electrodes are precisely matched to minimize this effect. We therefore expect that all field components present in the trap are in phase such that we can set  $\varphi_{\text{rf},i} = 0$ . We obtain

$$\mathbf{E}_{\text{rf}}(t) = \tilde{\mathbf{E}}_{\text{rf}} \cos(\Omega t), \quad (4.28)$$

where  $\tilde{\mathbf{E}}_{\text{rf}} = \sum_i \tilde{E}_{\text{rf},i} \mathbf{e}_i$  is the vector amplitude of the residual RF electric field.

A real linear Paul trap may not be perfectly symmetric due to manufacturing imperfections. As we will show below, this can lead to an axial component of  $\mathbf{E}_{\text{rf}}(t)$  which does not vanish anywhere along the trap axis. It is therefore also not possible to minimize this component by shifting the ion position.

The equation of motion for the excess micromotion velocity  $\mathbf{v}_{\text{emmm}}$  is [150]

$$m \dot{\mathbf{v}}_{\text{emmm}} = Q \tilde{\mathbf{E}}_{\text{rf}} \cos(\Omega t). \quad (4.29)$$

By integrating Equation 4.29, we find

$$\mathbf{v}_{\text{emmm}} = \frac{Q}{m\Omega} \tilde{\mathbf{E}}_{\text{rf}} \sin(\Omega t). \quad (4.30)$$

The excess micromotion increases the average kinetic energy of the trapped ion by

$$\langle E_{\text{kin,emmm}} \rangle = \frac{1}{2} m \langle |\mathbf{v}_{\text{emmm}}|^2 \rangle = \frac{1}{m} \left( \frac{Q}{2\Omega} \tilde{E}_{\text{rf}} \right)^2, \quad (4.31)$$

where  $\tilde{E}_{\text{rf}} = |\tilde{\mathbf{E}}_{\text{rf}}|$ , and  $\langle \rangle$  signifies temporal averaging.

The trajectory of the excess micromotion around the equilibrium position is obtained by integrating Equation 4.30 once more:

$$\mathbf{u}_{\text{emmm}} = -\frac{Q}{m\Omega^2} \tilde{\mathbf{E}}_{\text{rf}} \cos(\Omega t). \quad (4.32)$$

### Micromotion measurements

A variety of different methods have been used for measuring micromotion amplitudes (an overview is given in [150]). A conceptually simple one is to monitor changes in the ion position when the strength of the RF potential is being raised or lowered [48]. If the secular frequency along the axis  $i$  is changed from  $\omega_{\text{sec},i}$  to  $\omega'_{\text{sec},i}$ , the average ion position along that axis changes from  $u_{0,i}$  to  $u'_{0,i}$ . By using Equation 4.26, the stray electric field component along the axis  $i$  can be calculated:

$$\mathbf{E}_{\text{dc}} \cdot \mathbf{e}_i = \frac{m}{Q} \left( \frac{1}{\omega_{\text{sec},i}^2} - \frac{1}{\omega'_{\text{sec},i}{}^2} \right)^{-1} (u'_{0,i} - u_{0,i}). \quad (4.33)$$

Figure 4.39 shows an exemplary measurement with this method. A single  $\text{Be}^+$  ion was

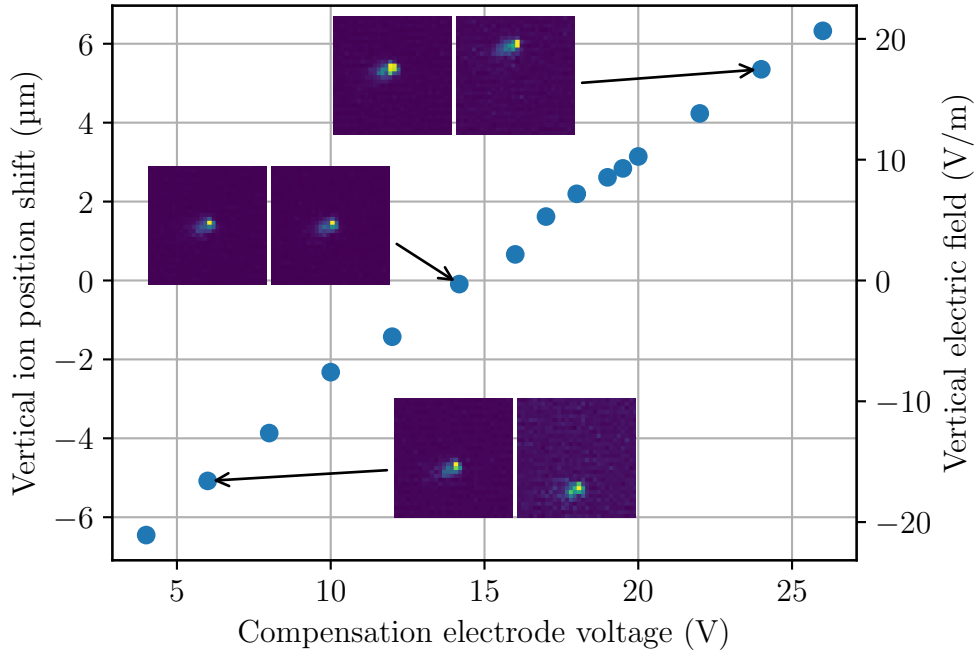


Figure 4.39: Electric field determination by ion position measurements. The relative shift of the ion position is measured when the radial secular frequency is reduced from 1470 kHz to 793 kHz. A minimal displacement is obtained for a compensation electrode voltage of 14.18 V. In the insets the left image shows the ion with the stronger confinement and the right image with the weaker confinement. The scale of the right vertical axis is calculated using Equation 4.33.

loaded into the trap. The voltages of the two DC electrodes and the compensation electrode (see Figure 4.1 and Figure 4.9) were first optimized such that the equilibrium position of the ion changes as little as possible when lowering the strength of the RF potential. The voltage applied to the compensation electrode was then swept over a range from 4 V to 26 V. At each point an image of the ion was taken with strong confinement ( $\omega_{\text{sec},x} = \omega_{\text{sec},y} = 2\pi \times 1470$  kHz) and with weak confinement ( $\omega'_{\text{sec},x} = \omega'_{\text{sec},y} = 2\pi \times 793$  kHz). Due to the electrode geometry, the field created by the compensation electrode is predominantly in the vertical direction (along  $(\mathbf{e}_x + \mathbf{e}_y)/\sqrt{2}$ ). The vertical shift of the ion position was extracted by fitting a 2D Gaussian to each image. A minimum position shift is achieved for a compensation electrode voltage of 14.18 V.

While the position shift method is fast and easy to implement, it can only detect micromotion due to stray electric fields. It is insensitive to residual RF electric fields that do not shift the equilibrium position of the ion.

A more direct technique is the “photon-correlation method” [48, 150]. Micromotion along the cooling laser beam leads to an effective phase modulation in the rest frame of

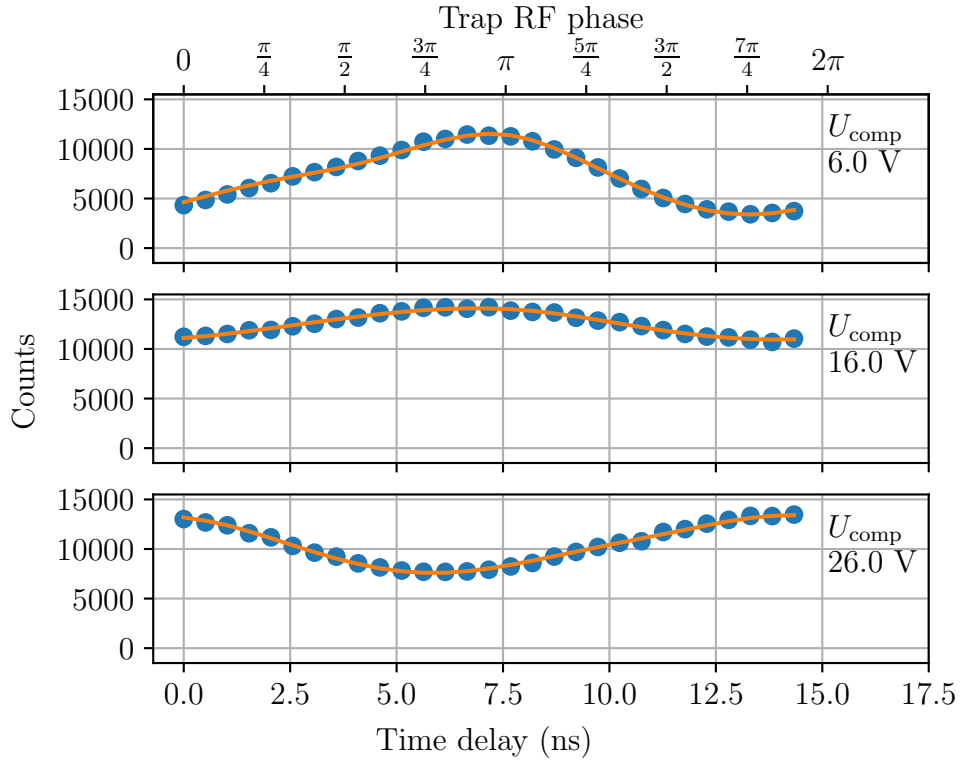


Figure 4.40: Photon correlation signals recorded with the TCSPC (blue circles) for different compensation electrode voltages. The orange lines are fits based on a numerical solution of the optical Bloch equations (see Appendix B).

the ion:

$$\Delta\phi(t) = \mathbf{k} \cdot \mathbf{u}_{\text{em}} = -\frac{Q}{m\Omega^2} \mathbf{k} \cdot \tilde{\mathbf{E}}_{\text{rf}} \cos(\Omega t), \quad (4.34)$$

where  $\mathbf{k}$  is the wave vector of the cooling laser. The strength of the modulation is characterized by the modulation index

$$\beta = \frac{Q}{m\Omega^2} \mathbf{k} \cdot \tilde{\mathbf{E}}_{\text{rf}}. \quad (4.35)$$

The phase modulation can be interpreted as a periodic Doppler shift that changes the detuning of the cooling laser in the rest frame of the ion. Therefore, the fluorescence intensity emitted by the ion is modulated in sync with the trap RF signal. We use the PMTs to detect the fluorescence with very high time resolution (see section 4.2.2). A time-correlated single photon counter<sup>54</sup> (TCSPC) is used to correlate the photon detection events from the PMTs with the trap RF signal. The output of the TCSPC is a histogram of photon counts which are binned according to their arrival time relative to the preceding zero crossing of the trap RF signal (see Figure 4.40).

<sup>54</sup>PicoQuant PicoHarp 300.

The lifetime of the upper state of the  $\text{Be}^+$  cooling transition is around 8.9 ns (see section 2.5) which is on a comparable time scale to the length of one micromotion cycle ( $2\pi/\Omega = 15.1$  ns). The steady-state approximation for the fluorescence modulation derived in [48] is therefore not applicable in our setup. Instead, we numerically solve the optical Bloch equations to obtain a fit function for the modulated fluorescence intensity (see Appendix B).

Figure 4.41 shows the micromotion of a single ion measured with the photon correlation method. The measurement was performed in parallel with the position shift measurement. The ion was illuminated with the radial cooling beam (see Figure 4.24) which propagates along  $\mathbf{u}_{\text{cool}} = \frac{1}{2}(\mathbf{e}_y - \mathbf{e}_x) - \frac{1}{\sqrt{2}}\mathbf{e}_z$ . Note that a *vertical* displacement of the ion (along  $(\mathbf{e}_x + \mathbf{e}_y)/\sqrt{2}$ ) causes *horizontal* excess micromotion (along  $(\mathbf{e}_y - \mathbf{e}_x)/\sqrt{2}$ ). This is illustrated in Figure 4.42 (a). The laser was red-detuned from the cooling transition by 9.5 MHz. A saturation parameter of around  $s = 1.4$  was measured by varying the cooling laser intensity and monitoring the change in emitted fluorescence intensity. At each compensation electrode voltage, a photon-correlation histogram was recorded and the modulation index  $\beta$  was extracted by fitting the theory function to the data. The modulation is minimized at a compensation electrode voltage of 19.5 V.

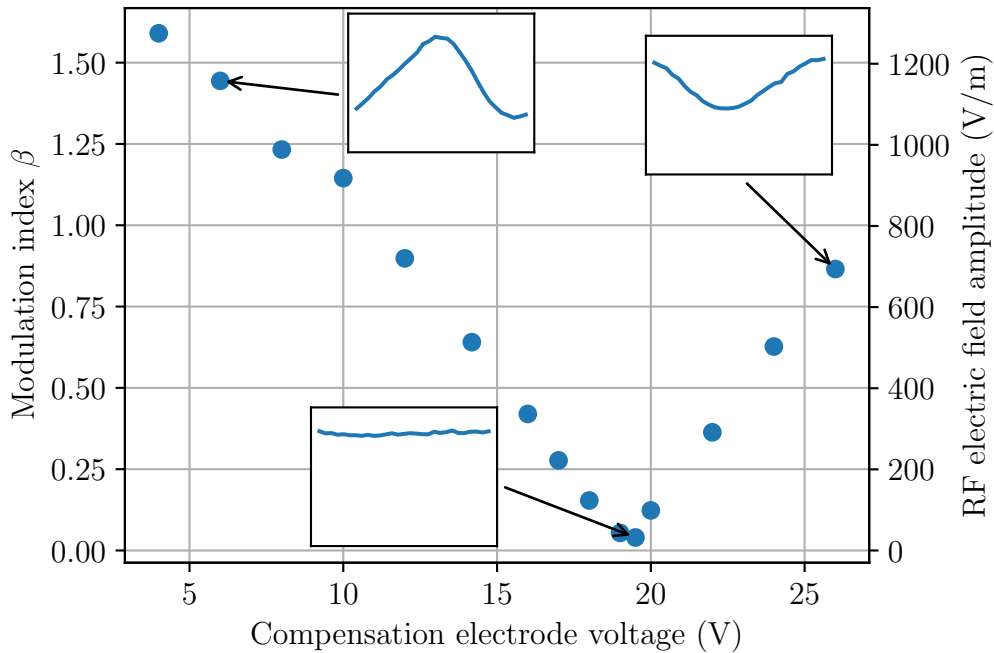


Figure 4.41: Micromotion modulation index  $\beta$  for different compensation electrode voltages measured with the photon-correlation method. The RF electric field amplitude along the cooling laser beam is calculated using Equation 4.35. The insets show correlation signals corresponding to the indicated data points. The modulation is minimized for a compensation electrode voltage of 19.5 V.



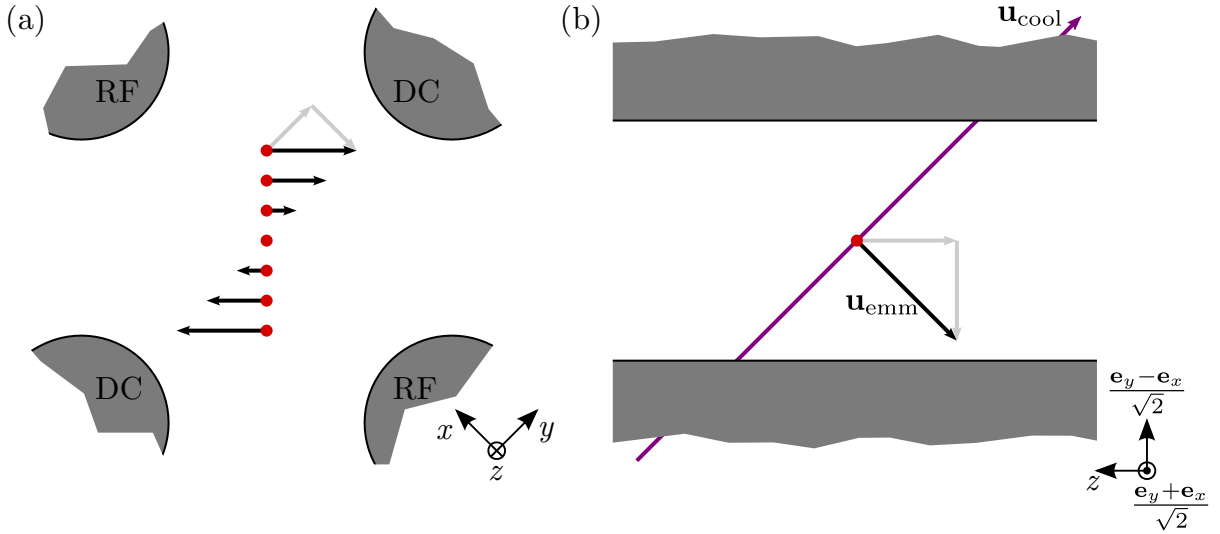


Figure 4.42: Illustration of excess micromotion in a linear Paul trap. (a) Axial view. The micromotion vectors  $\mathbf{u}_{\text{emm}}(t = 0)$  are shown as black arrows for different vertical ion positions. The grey arrows show how the micromotion components along the trap axes  $\mathbf{e}_x$  and  $\mathbf{e}_y$  add up to give horizontal micromotion. (b) Top view. The axial and horizontal micromotion components are shown as grey arrows. There exists a vertical ion position where the two components add up such that  $\mathbf{u}_{\text{emm}} \cdot \mathbf{u}_{\text{cool}} = 0$ .

This does not agree with the optimum voltage of 14.18 V obtained from the position shift measurement. At this point a modulation index of  $\beta = 0.64$  is measured which corresponds to a residual RF electric field amplitude of  $\tilde{\mathbf{E}}_{\text{rf}} \cdot \mathbf{u}_{\text{cool}} = 514 \text{ V/m}$ . As mentioned above there are two mechanisms that can cause residual RF electric fields that are not associated with the ion being shifted from the center of the trap. The first is a phase mismatch between the RF electrodes. This creates an effective field which is directed along the connection line of the two RF electrodes ( $\mathbf{e}_x$ ) and which is out of phase with respect to the trapping field [48]. This contribution therefore does not vanish at any equilibrium position of the ion which disagrees with our observations.

The disagreement between the two measurement methods can however be explained by a position independent axial component of the residual RF electric field. Shifting the ion vertically from the center of the trap leads to horizontal micromotion that adds to the axial component. As shown in Figure 4.42 (b), the vector sum of the axial and horizontal micromotion components can be such that  $\mathbf{u}_{\text{emm}} \cdot \mathbf{u}_{\text{cool}} = 0$ . The ion then performs micromotion perpendicular to the cooling laser beam which minimizes  $\beta$ . We believe that this is the reason why we observe minimal fluorescence modulation at  $U_{\text{comp}} = 19.5 \text{ V}$ . At  $U_{\text{comp}} = 14.18 \text{ V}$  the micromotion is expected to be only along the trap axis. The axial component of the residual RF electric field can then be estimated to be

$$\tilde{\mathbf{E}}_{\text{rf}} \cdot \mathbf{e}_z \approx \sqrt{2} \tilde{\mathbf{E}}_{\text{rf}} \cdot \mathbf{u}_{\text{cool}} = \sqrt{2} \times 514 \text{ V/m} = 727 \text{ V/m}. \quad (4.36)$$

We have used a finite element analysis software<sup>55</sup> (see subsection 4.1.2) to study the axial RF electric field introduced by imperfect alignment of the trap electrodes. We found that the observed axial RF electric field could for example be created by rotating one of the RF trap electrodes by less than  $1^\circ$  with respect to the trap axis (see Figure 4.43). Even though our trap electrodes were carefully aligned under a microscope during assembly, deviations on this scale cannot be excluded.

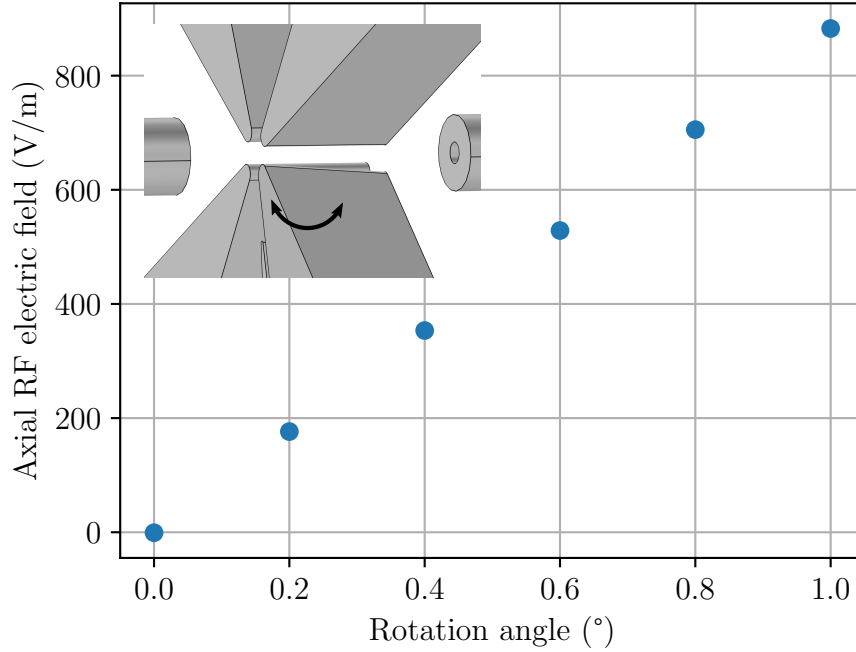


Figure 4.43: Simulated effect of rotating one of the trap electrodes on the axial RF electric field. The simulation is performed for an RF voltage of 100 V which is a typical value in our setup. In the inset the rotation angle is set to  $5^\circ$  to make the effect more visible.

### Effects on $\text{He}^+$ spectroscopy

We plan to drive the 1S-2S two-photon transition in  $\text{He}^+$  in a Doppler-free way using counter-propagating pulses (see chapter 3). Micromotion is therefore not expected to cause modulation sidebands on the spectroscopy signal. However, the excess micromotion increases the mean square velocity of the ions which gives rise to a relativistic second-order Doppler shift of [150]

$$\Delta\nu_{\text{D2}} = -\nu \frac{\langle E_{\text{kin,emm}} \rangle}{m_{\text{He}} c^2} = -\nu \left( \frac{Q}{2m_{\text{He}} c \Omega} E_{\text{rf}} \right)^2, \quad (4.37)$$

where we have used Equation 4.31 in the last step.  $\nu$  is the 1S-2S transition frequency, and  $m_{\text{He}}$  is the mass of a helium ion.

<sup>55</sup>COMSOL Multiphysics.

Furthermore, the ion experiences a nonzero mean square electric field  $\langle E^2 \rangle = E_{\text{rf}}^2/2$  which affects the atomic states. First, it leads to a second-order Stark shift of [150]

$$\Delta\nu_S = \sigma_S \langle E^2 \rangle = \sigma_S \frac{E_{\text{rf}}^2}{2}, \quad (4.38)$$

where  $\sigma_S$  is the Stark shift constant. For the 1S-2S transition in  $\text{He}^+$ , we have  $\sigma_S = 0.005641 \text{ Hz m}^2/\text{V}^2$  [95]. The Stark shift and the second-order Doppler shift are both proportional to  $E_{\text{rf}}^2$  and have opposite signs. The two effects can therefore be made to cancel each other by choosing the proper value for the trap frequency  $\Omega$ . This condition is achieved for  $^4\text{He}^+$  at  $\Omega = 2\pi \times 11.98 \text{ MHz}$  and for  $^3\text{He}^+$  at  $\Omega = 2\pi \times 15.97 \text{ MHz}$ .

A peculiar feature of hydrogen-like systems is that the  $2S_{1/2}$  state and the  $2P_{1/2}$  state are only separated by the Lamb shift which is 14.0 GHz in  $^4\text{He}^+$  [151]. Electric fields therefore lead to a significant mixing of the two states. The  $2P_{1/2}$  state has a lifetime of only 100 ps [28] since it can decay to the 1S ground state via the emission of a single photon. The mixing therefore significantly reduces the lifetime of the  $2S_{1/2}$  state. The lifetime against this quenching process is [95]

$$\tau' = \frac{\eta}{\langle E^2 \rangle} = \frac{2\eta}{E_{\text{rf}}^2}, \quad (4.39)$$

where  $\eta = 158 \text{ sV}^2/\text{m}^2$ . The  $2S_{1/2}$  state has a natural lifetime of  $\tau = 1.899 \text{ ms}$  [14]. As a result the total decay rate of the  $2S_{1/2}$  state is

$$\Gamma_{2S} = \frac{1}{\tau} + \frac{1}{\tau'} = \frac{1}{\tau} + \frac{E_{\text{rf}}^2}{2\eta}. \quad (4.40)$$

The expected line shifts and broadening in our experiment are shown in Figure 4.44. The axial residual RF electric field given in Equation 4.36 shifts the resonance frequency by around 1.4 kHz. The 1S-2S transition frequency in  $\text{He}^+$  can be calculated with an estimated uncertainty of 70 kHz [12]. The micromotion line shift is significantly smaller and therefore does not increase the required search range for finding the line. The decay rate is increased from  $\Gamma = 2\pi \times 84 \text{ Hz}$  to  $\Gamma = 2\pi \times 350 \text{ Hz}$ . The decay and photoionization of the 2S state are competing processes. As discussed in section 3.3, the effect of an increased decay rate depends on the available laser power. For low power levels it is expected to significantly reduce the ionization rate, whereas for high power levels the dynamics are essentially unaffected. While the increased decay rate broadens the resonance line, the off-resonant ionization rate does not increase due to the much lower overall rate (see Figure 3.5). The broadening is therefore not expected to be useful for locating the line.

If the micromotion effects turn out to be limiting factors in the future, a different trap design should be used. For example, the group of T. Mehlstäubler at the PTB<sup>56</sup> has designed traps that are optimized for low amounts of micromotion [152]. Their design is based on stacked laser-cut AlN ceramic wafers with manufacturing tolerances below 10  $\mu\text{m}$ .

<sup>56</sup>Physikalisch-Technische Bundesanstalt, Braunschweig, Germany.

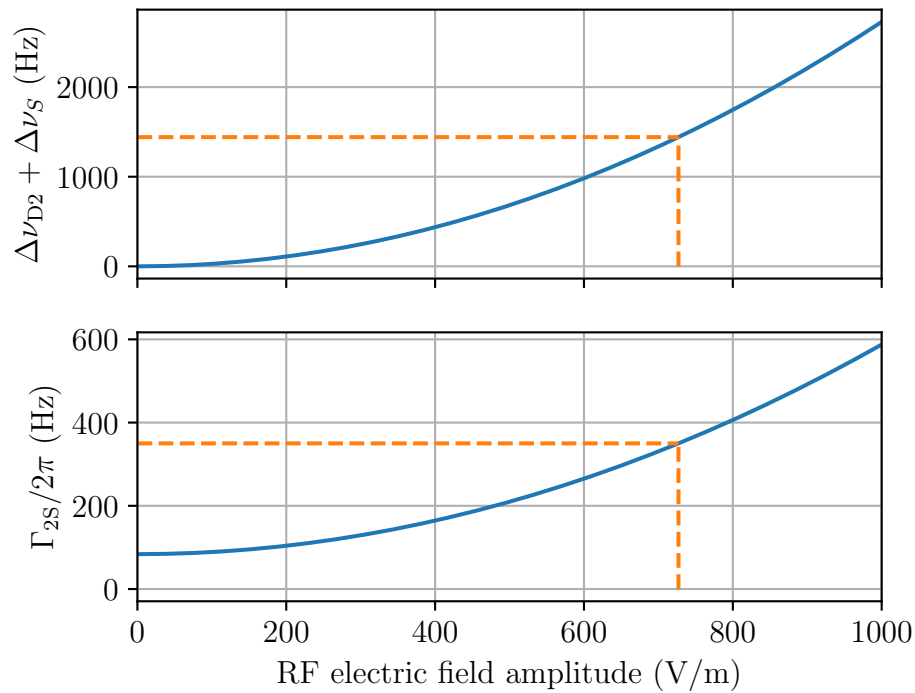


Figure 4.44: Expected line shift (top) and broadening (bottom) due to micromotion. The shift is calculated using Equations 4.37 and 4.38, and the broadening using Equation 4.40. The dashed orange line shows the estimated axial RF electric field amplitude in our trap.

They have demonstrated an axial RF electric field of less than 80 V/m over an entire 1 mm long segment of the trap at an RF amplitude of 800 V. For comparison, our trap was driven with an RF amplitude of only 119 V and suffers from an almost 10 times larger axial RF electric field.

# Chapter 5

## Detecting individual dark ions

In our  $\text{He}^+$  spectroscopy experiment, the production of  $\text{He}^{2+}$  ions will be the signal for the successful excitation of the 1S-2S transition. While it is straightforward to count laser cooled trapped ions by fluorescence imaging, detecting the number of dark ions embedded and sympathetically cooled in a mixed ion crystal is more challenging.

In this chapter we demonstrate a method to track the number of dark ions in real time with single-particle sensitivity. We demonstrate the scheme by detecting  $\text{H}_2^+$  and  $\text{H}_3^+$  ions embedded in a  $\text{Be}^+$  ion crystal. Our method allows observing the generation and destruction of individual ions simultaneously for different types of ions. Since  $\text{H}_2^+$  and  $\text{He}^{2+}$  have the same charge-to-mass ratio, their motional dynamics are identical in an ion trap. The detection of  $\text{H}_2^+$  therefore serves as a test for the detection of  $\text{He}^{2+}$ . Besides high-resolution spectroscopy on dark ions, another application is the detection of chemical reactions in real time with single-particle sensitivity. The contents of this chapter have been published in Physical Review A [153]. The manuscript has been edited to fit into the structure of this thesis.

### 5.1 Introduction

While the number of laser cooled ions can be easily measured by fluorescence imaging, identification and counting of the non-fluorescing dark ions is more difficult. One method is to eject the ions from the trap and to accelerate them onto a detector in an electric field. The different ion species can be distinguished by their arrival times [154–157]. While this method allows a quantitative measurement of the number of ions of each species, it has the disadvantage that it is destructive, and a new ion crystal has to be prepared after each measurement.

In linear Paul traps lighter ions are more tightly confined than heavier ions (see Equation 2.20). Lighter sympathetically cooled ions therefore form a dark region in the center of the fluorescence image of an ion crystal consisting of a heavier coolant species (see Figure 4.34). The number of dark ions can then be obtained by comparing experimental images with simulated ones [158–160]. This method is nondestructive, and the ion im-

ages can be acquired quickly and post-processed later. However, different dark ion species cannot be distinguished.

Instead, secular excitation has been used for nondestructive detection of trapped ions. In this method the secular motion of the ions, i.e. the harmonic motion in the time averaged trap potential, is excited resonantly by applying an additional oscillating electric field. This transfers energy into the motion of the surrounding coolant ions and thereby increases their temperature. Due to the temperature dependence of the Doppler broadening, this leads to a change in the amount of fluorescence that can be observed from the coolant ions. The secular motion of the ions in three-dimensional Coulomb crystals has rich dynamics that can complicate the analysis of the secular excitation spectra. For example, the frequencies of the secular resonances are influenced by space charge effects and the mechanical coupling between the ions [65, 161, 162]. The energy transfer to the coolant ions is expected to increase with an increasing number of dark ions. Therefore, the fluorescence change induced by motional excitation serves as a measure of the number of dark ions. However, the relationship between the fluorescence change and the number of excited dark ions is in general nonlinear and is influenced by various experimental parameters such as the strength of the motional excitation, the geometry of the mixed ion crystal, and the intensity and detuning of the cooling laser. Therefore, evaluating the number of dark ions quantitatively is challenging and often requires intricate modeling and calibration of the signal using molecular dynamics simulations [163, 164]. This problem has been limiting the usage of the secular excitation method for highly precise spectroscopy so far.

In this chapter we show that by properly choosing experimental parameters, discrete steps in the secular excitation signal can be observed that are identified with individual dark ions leaving the trap or being generated within the trap. Hence such a signal is auto-calibrating, and counting the number of ions gives the ultimate accuracy. The signal does not have to be calibrated using a physical model of the secular excitation. Spurious signals at other frequencies that may arise from motional coupling have no influence on the counting process and can be safely ignored.

We experimentally demonstrate this method by resonantly exciting the radial motion of  $\text{H}_2^+$  and  $\text{H}_3^+$  ions embedded in a laser cooled  $\text{Be}^+$  ion crystal. We observe concomitant changes in the amount of fluorescence from the  $\text{Be}^+$  ions when the number of trapped  $\text{H}_2^+$  or  $\text{H}_3^+$  ions changes due to chemical reactions with neutral rest gas molecules.

Spectroscopy on dark ions requires a scheme for detecting that the target transition is being excited. This can for example be achieved by monitoring that new ion species are created by state-dependent photoionization [165] or resonance-enhanced multiphoton dissociation [164, 166–168]. The reliable detection of single dark ions demonstrates that this detection scheme can be single-event sensitive and that the spectroscopy will be limited by quantum projection noise only. Nonlinearities in the signal intensity may introduce a systematic frequency shift, especially when the spectrum consists of multiple overlapping lines [164]. Accurate counting of the dark ions gives rise to a spectroscopy signal with negligible nonlinearity.

Chemical reactions at ultracold temperatures can be investigated precisely for a small number of atoms or ions after careful quantum-state preparation [169]. Our detection

scheme can be employed to efficiently capture such events with single-particle sensitivity.

## 5.2 Experimental setup

In this experiment we operate the trap with an RF amplitude of around 120 V and an endcap voltage of 400 V. For  $\text{Be}^+$  this results in a radial secular frequency of around 1.6 MHz, corresponding to a Mathieu stability parameter  $q \approx 0.07$ , and an axial secular frequency of 645 kHz. The single-particle radial secular frequency scales proportional to the ion's charge-to-mass ratio (see subsection 2.1.3). The theoretical values are 4.8 MHz and 7.2 MHz for  $\text{H}_3^+$  and  $\text{H}_2^+$ , respectively.

The  $\text{Be}^+$  ions are laser cooled using two frequency components that are red-detuned from the cooling transition by 130 MHz and 460 MHz. We found that adding the far-detuned component makes the system more robust against losing the trapped ions when strongly driving secular excitations. Both frequency components have similar intensities of around  $I_{\text{sat}}$ , where  $I_{\text{sat}} = 765 \text{ W/m}^2$  is the saturation intensity of the cooling transition (see section 2.5). The cooling beam is aligned parallel to the trap axis and propagates through the holes in the endcap electrodes.<sup>1</sup>

$\text{Be}^+$  ions are loaded into the trap as described in section 4.6. We then turn on the electron gun for 1 s with a current of about 95  $\mu\text{A}$ . The electrons ionize some of the hydrogen molecules from the residual gas in our vacuum chamber, and the resulting molecular ions become embedded in the ion crystal.

Figure 5.1 (a) and (b) show typical fluorescence images of the ion crystals used in the experiment. We believe that the asymmetric shape visible in Figure 5.1 (b) is due to the imperfect alignment of the trap electrodes which also causes excess micromotion (see section 4.7.3).

## 5.3 Secular scans

In order to measure the radial secular frequencies of the trapped ions, we excite their motion by applying a sinusoidal voltage to the compensation electrode. We sweep the frequency range between 2 MHz and 10 MHz in 500 steps and for each frequency collect photon counts with one of the PMTs for 10 ms. This is slow enough that the ion motion reaches steady state for each frequency point. Figure 5.2 shows a typical resulting secular spectrum. Two peaks at 4.6 MHz and 7.1 MHz can be observed which we attribute to  $\text{H}_3^+$  and  $\text{H}_2^+$  ions, respectively. As described in subsection 4.1.4, the compensation electrode is low-pass filtered with a 1 nF capacitor and is not impedance matched to the  $50 \Omega$  output impedance of the function generator that produces the excitation signal. This makes the electric field amplitude at the position of the ions frequency dependent. In addition, the efficiency of the motional excitation might be different for  $\text{H}_3^+$  and  $\text{H}_2^+$  ions. We therefore

<sup>1</sup>We do not use the radial cooling beam for three-dimensional ion crystals since the radial micromotion leads to strong modulation sidebands that impede laser cooling.

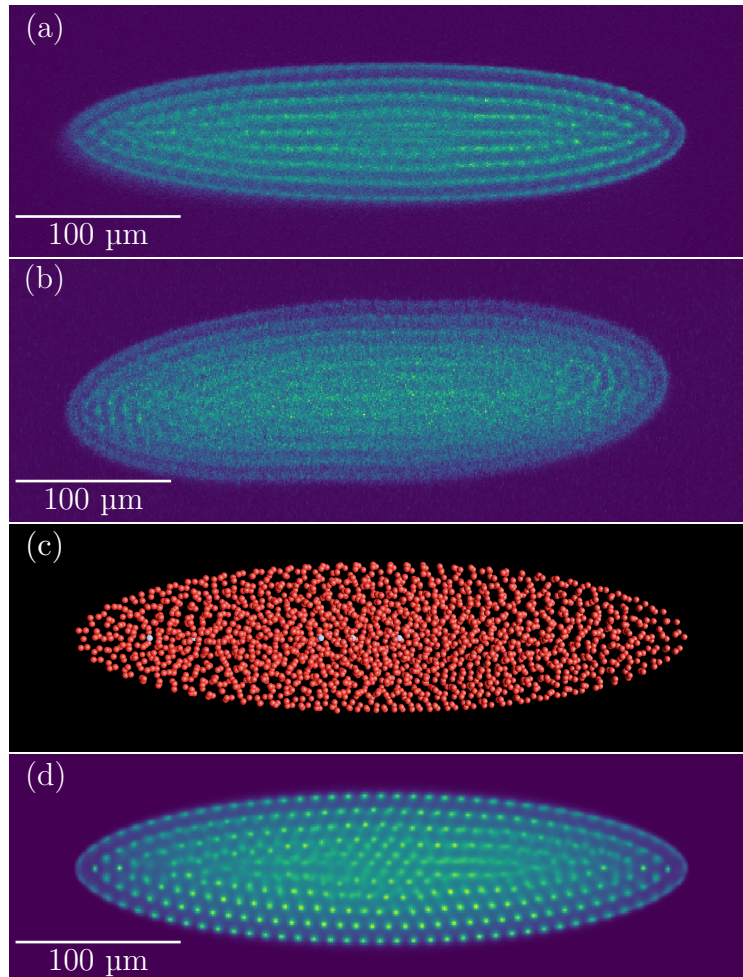


Figure 5.1: Fluorescence images of an ion crystal consisting of around 2000 Be<sup>+</sup> ions with a few embedded H<sub>2</sub><sup>+</sup> and H<sub>3</sub><sup>+</sup> ions, horizontal (a) and vertical (b) view. (c) Coulomb crystal containing 2000 Be<sup>+</sup> ions (red spheres) and 5 H<sub>2</sub><sup>+</sup> ions (light blue spheres) obtained by the molecular dynamics simulation. (d) Simulated ion image for the crystal shown in (c) at 10 mK.



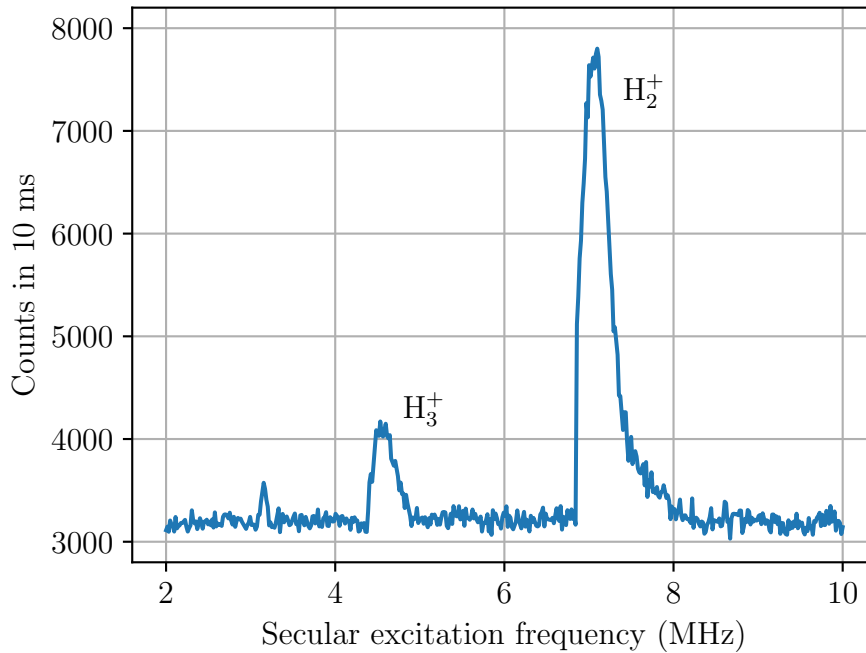


Figure 5.2: Secular spectrum showing the presence of  $\text{H}_2^+$  and  $\text{H}_3^+$  ions embedded in the  $\text{Be}^+$  coolant ions. The origin of the small peak close to 3 MHz has not been conclusively identified.

use two different excitation amplitudes for the frequency range from 2 MHz to 5.5 MHz and from 5.5 MHz to 10 MHz. The amplitudes are chosen to give roughly the same signal strength per ion for the  $\text{H}_2^+$  and  $\text{H}_3^+$  resonances.

## 5.4 Detecting individual $\text{H}_2^+$ and $\text{H}_3^+$ ions

We then repeatedly perform secular scans over a period of a few minutes. Figure 5.3 shows how the heights of the secular resonances change over time in a typical experiment.

We normalize the peak heights of each scan to the off-resonant scattering rate. This compensates for small drifts in the cooling laser power and  $\text{Be}^+$  ion loss during the measurement. The height of the  $\text{H}_2^+$  signal drops in steps until after around 360 s no peak is visible anymore. The height of the  $\text{H}_3^+$  signal increases in steps that coincide with drops of the  $\text{H}_2^+$  signal. We attribute this to individual  $\text{H}_2^+$  ions reacting with molecular hydrogen from the residual gas to form neutral hydrogen and  $\text{H}_3^+$  according to the exothermic chemical reaction  $\text{H}_2^+ + \text{H}_2 \rightarrow \text{H}_3^+ + \text{H}$  [170]. The clearly visible steps in the signals show that we are observing individual ions being destroyed or created within the Coulomb crystal. Sometimes the  $\text{H}_2^+$  signal drops without a corresponding increase in  $\text{H}_3^+$  signal. One possible explanation is that the  $\text{H}_2^+$  ion reacted with a different residual gas molecule such as  $\text{N}_2$ ,  $\text{O}_2$ , or  $\text{H}_2\text{O}$  [171]. Another possibility is that the kinetic energy transferred to the

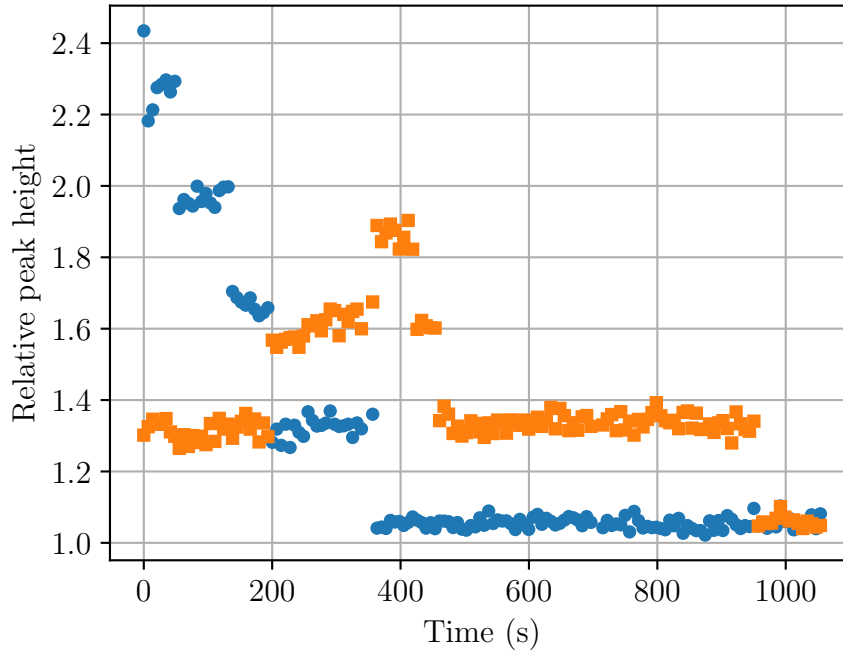


Figure 5.3: Change of the fluorescence peak heights at the  $\text{H}_2^+$  (blue circles) and  $\text{H}_3^+$  (orange squares) resonances over time. For each measurement the peak heights are normalized to the off-resonant scattering rate. The stepwise changes of the peak heights are caused by individual ions undergoing chemical reactions with residual gas molecules. Within each step the peak heights scatter by much less than the step-to-step difference. Each secular scan therefore allows a reliable determination of the ion numbers.

$\text{H}_3^+$  molecule in the chemical reaction is large enough to sometimes allow the product to escape from the trap. Rate constants for the chemical reactions between  $\text{H}_2^+$  and typical residual gas molecules are in the range of  $2\text{--}7 \times 10^{-9} \text{ cm}^3 \text{ s}^{-1}$  [170, 171]. An exponential fit to the  $\text{H}_2^+$  ion number yields a total decay rate of  $0.006 \text{ s}^{-1}$  which corresponds to a residual gas pressure in the range of  $4 \times 10^{-11} \text{ mbar}$  to  $1 \times 10^{-10} \text{ mbar}$ , in rough agreement with the pressure of  $4 \times 10^{-11} \text{ mbar}$  indicated by the vacuum gauge of the ion trap chamber. The number of  $\text{H}_3^+$  ions subsequently drops in similar steps over the time scale of a few minutes. We attribute this to proton transfer reactions of the type  $\text{H}_3^+ + \text{X} \rightarrow \text{HX}^+ + \text{H}_2$  which are possible with a number of residual gas molecules such as  $\text{N}_2$ ,  $\text{CO}$ ,  $\text{CO}_2$ , and  $\text{H}_2\text{O}$  [172].

## 5.5 Molecular dynamics simulations

One striking feature of Figure 5.3 is that the fluorescence peak heights are nearly linear in the number of dark ions. We use the LAMMPS molecular dynamics code [173, 174] to further investigate this behavior. The ion trap is modelled as the sum of an oscillating and

a static quadrupole electric field (see section 2.1):

$$\mathbf{E}(\mathbf{r}, t) = \frac{U_{\text{rf}} \cos(\Omega t) + U_{\text{dc}}}{r_0^2} (y\mathbf{e}_y - x\mathbf{e}_x) + \kappa \frac{U_{\text{ec}}}{2z_0^2} (x\mathbf{e}_x + y\mathbf{e}_y - 2z\mathbf{e}_z), \quad (5.1)$$

where  $U_{\text{rf}}$  and  $\Omega$  are the amplitude and frequency of the trap radio frequency drive,  $r_0$  is the radial size of the trap (see subsection 4.1.2),  $U_{\text{dc}}$  is the static offset voltage between the two diagonal pairs of trap electrodes (see subsection 4.1.4),  $U_{\text{ec}}$  is the voltage applied to the endcap electrodes,  $z_0$  is the distance between the endcap electrodes and the trap center, and  $\kappa$  is a geometrical factor that depends on the trap geometry (see subsection 4.7.2).  $\mathbf{e}_x$ ,  $\mathbf{e}_y$ , and  $\mathbf{e}_z$  are orthogonal unit vectors that define the Cartesian coordinate system as shown in Figure 4.1. Table 5.1 shows the parameters used in our simulations.

Table 5.1: Parameters used in the molecular dynamics simulations.

Parameter	Value
$U_{\text{rf}}$	121 V
$\Omega$	$2\pi \times 66.05$ MHz
$r_0$	0.469 mm
$U_{\text{dc}}$	0.1 V
$U_{\text{ec}}$	400 V
$z_0$	3.5 mm
$\kappa$	0.0469
$\Delta_1$	$-2\pi \times 130$ MHz
$\Delta_2$	$-2\pi \times 460$ MHz
$s_1$	1
$s_2$	1
$N_{\text{Be}}$	2000

The lifetime of the excited state of the  $\text{Be}^+$  cooling transition is 8.9 ns (see section 2.5). This is much shorter than the axial secular oscillation period of the  $\text{Be}^+$  ions in the trap (1.6  $\mu\text{s}$ ). In this unresolved sideband regime, we model the laser cooling as a velocity-dependent average force (see section 2.2) that only acts on the  $\text{Be}^+$  ions:

$$\mathbf{F}_c(v_z) = \sum_{j=1}^2 \hbar k \Gamma \frac{s_j/2}{1 + s_j + (\frac{\Delta_j - kv_z}{\Gamma/2})^2} \mathbf{e}_z, \quad (5.2)$$

where  $\Delta_j$  and  $s_j$  are the detunings and the saturation parameters of the two cooling laser frequency components (see Table 5.1),  $\Gamma = 2\pi \times 18$  MHz is the FWHM linewidth of the  $\text{Be}^+$  cooling transition,  $k = 2\pi/(313 \text{ nm})$  is the cooling laser wave number, and  $v_z$  is the  $z$ -component of the ion velocity.

The secular excitation is implemented as an oscillating electric field perpendicular to the trap axis:

$$\mathbf{E}_{\text{ex}}(t) = E_{\text{ex}} \cos(\Omega_{\text{ex}} t) \frac{1}{\sqrt{2}} (\mathbf{e}_x + \mathbf{e}_y), \quad (5.3)$$

where  $E_{\text{ex}}$  and  $\Omega_{\text{ex}}$  are the amplitude and frequency of the excitation.

The fluorescence signal measured in the experiment is proportional to the rate of photons scattered by the  $\text{Be}^+$  ions:

$$R(t) = \sum_{i=1}^{N_{\text{Be}}} \sum_{j=1}^2 \Gamma \frac{s_j/2}{1 + s_j + \left(\frac{\Delta_j - kv_{z,i}(t)}{\Gamma/2}\right)^2}, \quad (5.4)$$

where  $N_{\text{Be}}$  is the number of  $\text{Be}^+$  ions, and  $v_{z,i}$  is the  $z$ -component of the velocity of the  $i$ th  $\text{Be}^+$  ion.

### Ion numbers and temperatures

We use the simulations to determine the number of trapped ions and their temperature. For a given number of ions, a simulated ion crystal is initialized as follows. First, we randomly place all ions in the simulation volume. Then, they are brought close to an equilibrium configuration by using the potential energy minimization routine of LAMMPS in a static pseudopotential as described in [174]. With that the  $\text{H}_2^+$  and  $\text{H}_3^+$  ions are located close to the trap axis because the pseudopotential is deeper for them than for the  $\text{Be}^+$  ions. A resulting ion configuration is shown in Figure 5.1 (c). The ions are brought to a finite temperature by coupling their motion to a Langevin bath [174]. We generate simulated fluorescence images, taking into account the motion of the ions and the spot size and depth of field of the imaging objective. We then estimate the number of trapped ions in the experiment and their temperature by comparing the simulated images with the experimental ones [65, 158–160]. A good agreement is obtained between experimental and simulated images for around 2000  $\text{Be}^+$  ions at 10 mK mixed with a few dark ions as shown in Figure 5.1 (d). Since micromotion has no visible effect on the simulated ion images, we found it sufficient to perform these simulations in the pseudopotential approximation.

### Secular excitation spectra

For each number of  $\text{H}_2^+$  and  $\text{H}_3^+$  ions, a simulated ion crystal is initialized as described above. The pseudopotential is then replaced by the trap electric field given in Equation 5.1. Instead of the Langevin bath, laser cooling according to Equation 5.2 is applied to the  $\text{Be}^+$  ions. The disordered secular motion of the many interacting ions in large Coulomb crystals behaves like the motion of a gas in thermal equilibrium and can therefore be assigned a temperature [65]. The laser cooling force damps this motion until the ions reach a secular temperature below 1 mK.

Then the secular excitation field given in Equation 5.3 is turned on, and the ion trajectories are simulated for 10 ms. The secular excitation heats up the secular motion until a thermal equilibrium is reached after a few ms. We apply an artificial damping force to the motion of the  $\text{H}_2^+$  and  $\text{H}_3^+$  ions during the first 3 ms of the simulation. This prevents the ion temperature from rising too quickly which occasionally leads to numerical instabilities in our simulation. The fluorescence signal observed in the experiment is simulated

by averaging the  $\text{Be}^+$  scattering rate calculated using Equation 5.4 over the last 5 ms of the simulation. The simulation is then repeated with the same initial ion crystal for a range of secular excitation frequencies in order to obtain a secular spectrum. At typical secular temperatures reached in the experiment and simulations, the ions diffuse through the crystal on a ms time scale [65, 66]. This provides enough averaging such that one run is sufficient for each combination of ion numbers and excitation frequencies.

Figure 5.4 (a) and (b) show experimental secular excitation spectra for different numbers of  $\text{H}_3^+$  and  $\text{H}_2^+$  ions, and Figure 5.4 (c) and (d) show the corresponding simulated spectra. The stepwise change of the fluorescence peak height for different numbers of ions is reproduced in the simulations. Both the simulation and the measurement suggest that the change in the amount of fluorescence is roughly proportional to the number of dark ions that are being excited at their secular frequency.

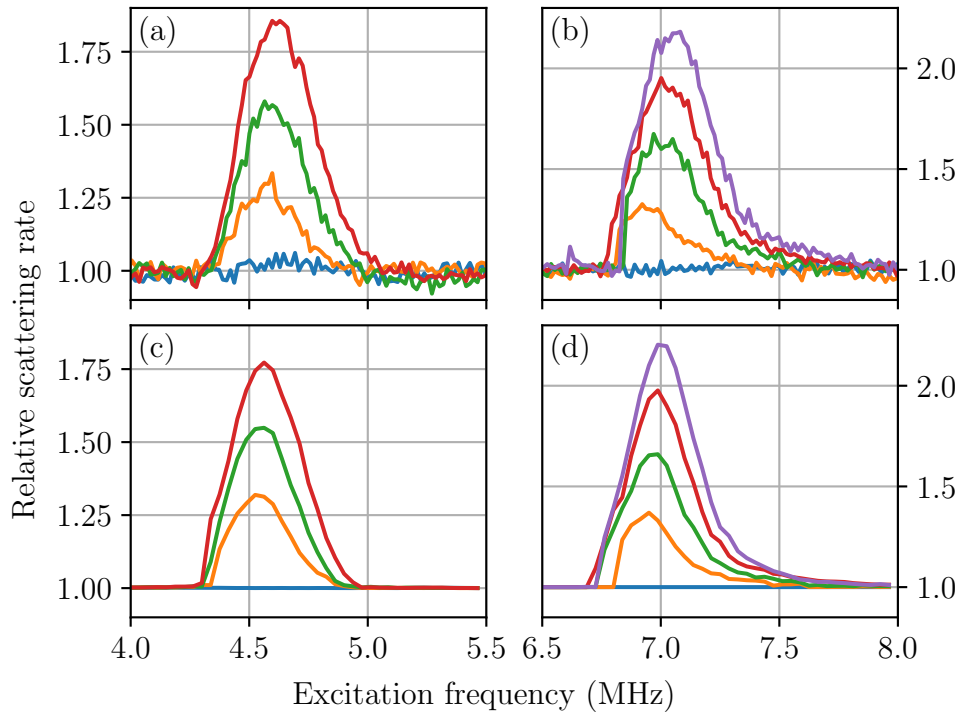


Figure 5.4: Experimental secular excitation spectra for (a) 0–3  $\text{H}_3^+$  ions and (b) 0–4  $\text{H}_2^+$  ions. (c) and (d) are spectra obtained from molecular dynamics simulations with 2000  $\text{Be}^+$  ions and the same numbers of  $\text{H}_2^+$  and  $\text{H}_3^+$  ions as in the experiment. The simulated excitation amplitudes are 2.9 V/m for the  $\text{H}_3^+$  resonance and 2.5 V/m for the  $\text{H}_2^+$  resonance.

The all-to-all Coulomb interaction between the ions makes simulating large ion crystals computationally expensive. In our case simulating the system evolution for 10 ms takes around one day on 8 CPU cores. We found that adding more cores did not speed up the simulation due to communication overhead between the cores. We therefore performed the simulations for the different excitation frequencies and ion numbers in parallel on a

computer cluster.<sup>2</sup>

## 5.6 Theoretical description

We now derive a model for the dependence of the scattering rate at the secular resonance frequency on the number of ions that are being excited. For a cycling cooling transition in an atom at rest, the photon scattering rate is given by

$$w(\Delta) = \frac{s\Gamma/2}{1 + s + \left(\frac{\Delta}{\Gamma/2}\right)^2}, \quad (5.5)$$

where  $\Delta$  is the laser detuning, and  $s = I/I_{\text{sat}}$  is the saturation parameter. During the secular excitation, the temperature of the coolant ions increases to  $T_s$ , and the scattering rate per  $\text{Be}^+$  ion is given by [164]

$$R(T_s) = \int_{-\infty}^{\infty} w(\Delta - kv)p(v, T_s)dv, \quad (5.6)$$

where  $p(v, T) = \sqrt{m_{\text{Be}}/(2\pi k_{\text{B}}T)} \exp[-m_{\text{Be}}v^2/(2k_{\text{B}}T)]$  is the Maxwell-Boltzmann distribution.  $v$  is the velocity of the ion along the cooling laser beam,  $k$  is the cooling laser wave number, and  $m_{\text{Be}}$  is the  $\text{Be}^+$  mass. We assume that the coolant ion temperature  $T_s$  during the secular excitation is determined by the balance between the heating due to the motional excitation and the average laser cooling power. This condition is expressed as

$$N_{\text{Be}}p_c(T_s) = N_{\text{ex}}p_h, \quad (5.7)$$

where  $N_{\text{Be}}$  is the number of  $\text{Be}^+$  ions, and  $N_{\text{ex}}$  is the number of dark ions that are being excited.  $p_h$  is the heating power per excited dark ion. Note that the average cooling power per coolant ion  $p_c(T_s)$  is temperature dependent because of the Doppler broadening of the cooling transition:

$$p_c(T_s) = -\hbar k \int_{-\infty}^{\infty} vw(\Delta - kv)p(v, T_s)dv. \quad (5.8)$$

We use the molecular dynamics simulations to confirm the validity of the underlying assumptions of Equation 5.7. The first one is that the total heating power due to the secular excitation is proportional to the number of  $\text{H}_2^+$  or  $\text{H}_3^+$  ions that are being resonantly excited. The second one is that the secular excitation is the only heating mechanism which is balanced by the laser cooling power in steady state. The molecular dynamics simulation allows us to access such thermodynamic quantities of the system that cannot directly be measured in the experiment. The total heating power due to the excitation field is given by

$$p_{h,\text{tot}}(t) = \sum_{i=1}^{N_{\text{ion}}} q_i \mathbf{v}_i(t) \cdot \mathbf{E}_{\text{ex}}(t), \quad (5.9)$$

---

<sup>2</sup>Operated by the Max Planck Computing and Data Facility (MPCDF).

where  $N_{\text{ion}}$  is the number of ions in the crystal, and  $q_i$  and  $\mathbf{v}_i(t)$  are the charge and velocity of the  $i$ th ion.

The total laser cooling power is

$$p_{c,\text{tot}}(t) = - \sum_{i=1}^{N_{\text{Be}}} \mathbf{v}_i(t) \cdot \mathbf{F}_c[\mathbf{v}_i(t) \cdot \mathbf{e}_z]. \quad (5.10)$$

As for the scattering rate, we obtain steady-state values of the heating and cooling powers by averaging over the last 5 ms of each simulation. Figure 5.5 shows the heating and cooling powers during secular excitation at the  $\text{H}_2^+$  and  $\text{H}_3^+$  resonance frequencies for ion crystals with 2000  $\text{Be}^+$  ions and different numbers of  $\text{H}_2^+$  and  $\text{H}_3^+$  ions. The simulations confirm the approximately linear dependence between the heating power and number of ions. The simulations also show that the heating power is balanced by the laser cooling and that the trapping field does not transfer a significant amount of energy to the ions (RF heating [175]).

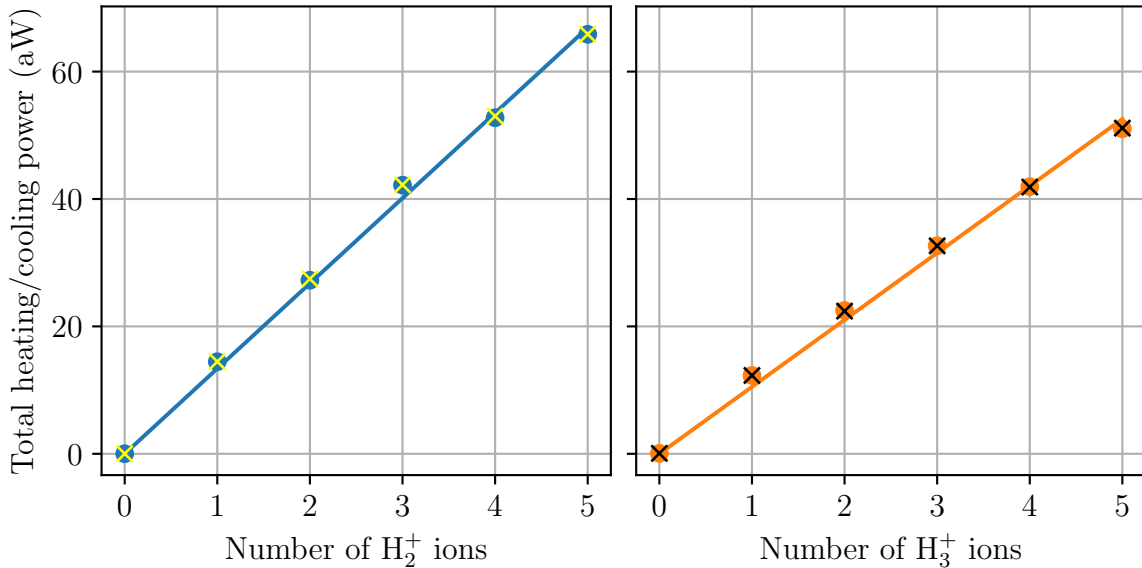


Figure 5.5: Secular heating powers (dots) and laser cooling powers (crosses) when exciting mixed ion crystals at the  $\text{H}_2^+$  (left) and  $\text{H}_3^+$  (right) resonance frequencies. The solid lines are linear fits to the heating powers. The simulated excitation amplitudes are 2.9 V/m for the  $\text{H}_3^+$  resonance and 2.5 V/m for the  $\text{H}_2^+$  resonance.

The relative fluorescence peak heights of the secular resonances shown in Figure 5.3 correspond to  $R(T_s)/R(T_0)$  where  $T_0$  is the equilibrium temperature of the  $\text{Be}^+$  ions in the absence of heating due to secular excitation. Under our experimental conditions,  $T_0$  is around 10 mK. For simplicity we use  $T_0 = 0$  K which introduces a marginal ( $\sim 2\%$ ) difference in the scattering rate. It is difficult to precisely estimate the heating rate  $p_h$  from the experimental parameters. We therefore treat  $\alpha = p_h/N_{\text{Be}}$  as a free parameter in our

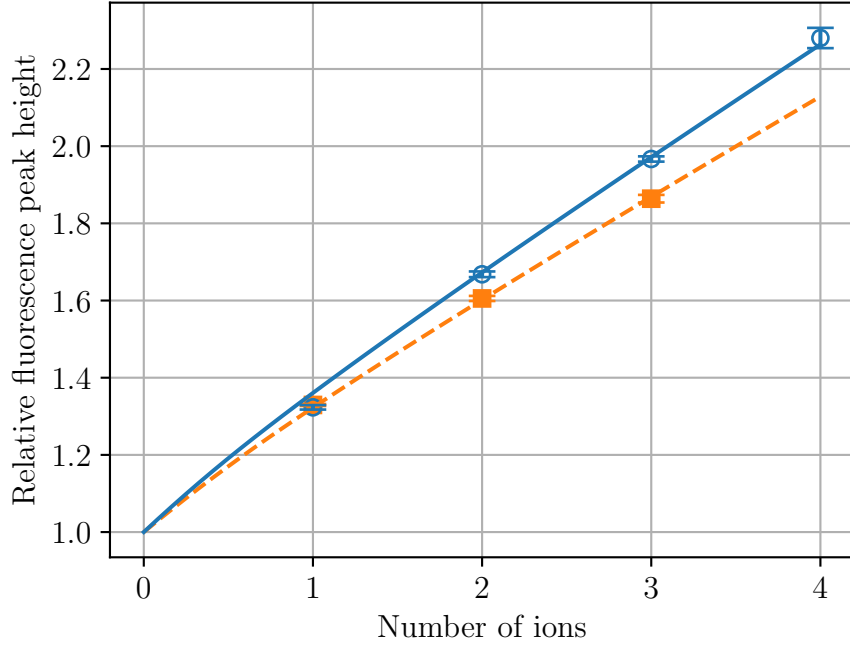


Figure 5.6: Average peak heights of the  $\text{H}_2^+$  (blue circles) and  $\text{H}_3^+$  (orange squares) secular resonances. The error bars show the standard error of the mean. The solid and dashed lines are fits of our model curve  $R(T_s)/R(T_0)$  to the  $\text{H}_2^+$  and  $\text{H}_3^+$  data, respectively. Separate fits are performed for the  $\text{H}_2^+$  and  $\text{H}_3^+$  resonances since the secular excitation strength is different for the two species, and two different fit parameters  $\alpha_{\text{H}_2^+}$  and  $\alpha_{\text{H}_3^+}$  were necessary.

model. We evaluated  $R(T_s)/R(T_0)$  numerically and determined  $\alpha$  to best reproduce the experimental data. No other fit parameters were used. The results are shown in Figure 5.6 for different numbers of  $\text{H}_2^+$  and  $\text{H}_3^+$  ions. For our parameters the model predicts a nearly linear dependence of the scattering rate on the number of dark ions which agrees with the experimental observations.

With a larger number of dark ions, the model predicts that the fluorescence peak height starts to saturate, and the fluorescence steps become smaller accordingly. We have conducted experiments for a larger number of dark ions and confirmed that up to eight dark ions can be reliably counted under our experimental conditions. Additional molecular dynamics simulations with different numbers of dark/coolant ions and different dark-ion species suggest that our method is robust for a wide range of experimental parameters.

In conclusion, we have demonstrated that the secular excitation technique can be used to detect dark ions embedded in laser-cooled ion Coulomb crystals with single-particle resolution. Secular excitation only relies on the Coulomb interaction between the different ion species. We therefore believe that this method could be used for single-particle sensitive detection of a wide range of atomic or molecular ions that do not possess suitable cycling transitions for fluorescence detection.



# Chapter 6

## A low-noise driving laser for high harmonic generation

The output of any real laser has a certain amount of amplitude and phase noise which influences the emitted spectrum. In this chapter we first discuss how laser noise affects spectroscopy experiments. Our XUV frequency comb is generated from an infrared laser using high harmonic generation (HHG). We will see that in order to achieve narrow linewidths in the XUV, it is critical to start with a driving laser with extremely low phase noise. We have therefore developed a laser system based on an Yb:KYW mode-locked oscillator that is tightly phase locked to a cavity-stabilized external-cavity diode laser (ECDL). The second part of the chapter describes the design and characterization of the cavity-stabilized ECDL. We have developed a new technique for characterizing the high-frequency phase noise of this laser system. The corresponding parts of the chapter were published in an article in *Optics Letters* [176]. In the last part of the chapter, the driving laser system for the HHG and its stabilization are described.

### 6.1 Laser noise in spectroscopy experiments

Figure 6.1 shows the spectrum of a beat note between the outputs of two cavity-stabilized ECDLs that are used for hydrogen spectroscopy at MPQ [177, 178]. These lasers have full width at half-maximum (FWHM) linewidths of around 1 Hz. The spectrum contains a narrow carrier whose apparent width is only given by the resolution bandwidth of the spectrum analyzer. Surrounding the carrier there is a broad “pedestal” that is typical for the spectrum of diode lasers. As we will show below, this is mainly caused by high-frequency phase noise. The noise pedestal affects spectroscopy experiments differently depending on the linewidth of the transition. An accurate measurement of a broad transition requires finding the line center within a small fraction of its width (see for example [13]). By beating the spectroscopy laser with a frequency comb, the number of optical cycles per time can be counted, corresponding to the mean frequency of the carrier. As long as the signal-to-noise ratio is sufficient for unambiguous tracking of the optical phase, the high-frequency noise

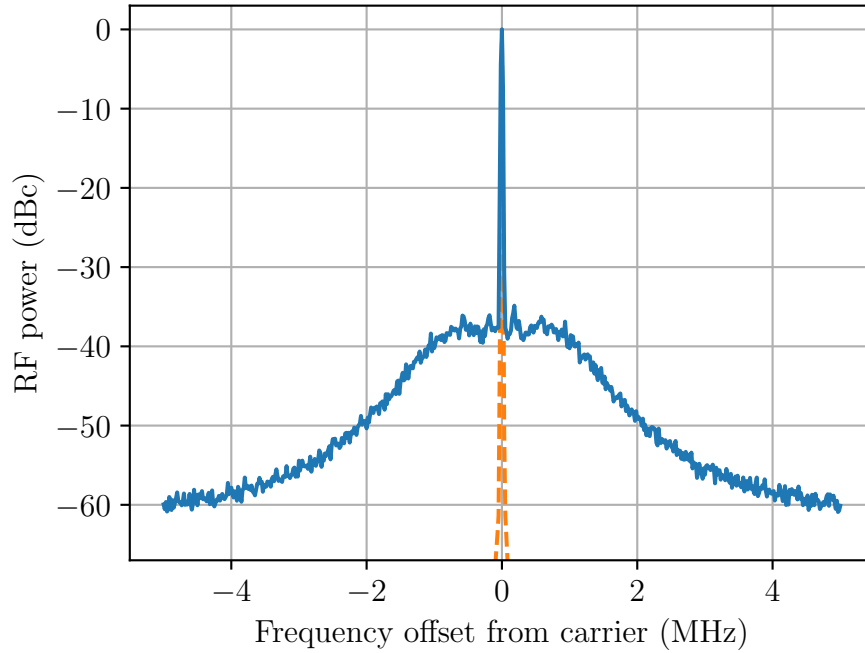


Figure 6.1: Beat note between the outputs of two ECDLs which are stabilized to independent reference cavities and have subhertz linewidths (blue solid trace) recorded with a resolution bandwidth of 20 kHz. The narrow carrier (resolution bandwidth limited) and broad phase-noise pedestal are clearly visible. The frequency axis is shown relative to the carrier frequency of 2.968 GHz. The orange dashed line shows the expected beat note after filtering the output of both lasers through a cavity with an FWHM linewidth of 6.55 kHz (see subsection 6.2.4).

quickly averages out in the carrier frequency measurement. The frequency measurement is therefore mostly unaffected by the shape of the noise pedestal. On the other hand, the observed line shape is a convolution of the laser spectrum with the atomic response. Correlated amplitude and phase noise can lead to an asymmetric noise spectrum [179]. In this case the center of gravity of the laser spectrum is different from the carrier frequency which can lead to a systematic measurement error [165].

The situation is different when spectroscopy is performed on a very narrow transition. In this case high accuracy can be achieved without having to precisely locate the line center within the linewidth. A potential asymmetry in the noise spectrum is therefore less important. However, if the transition is much narrower than the noise spectrum, only the carrier can contribute to driving the excitation. As we will see below, the fraction of power that is “lost” to the noise pedestal can be substantial, especially when harmonics of the laser output are being generated.

### 6.1.1 Amplitude and phase noise basics

We treat the output of a single-mode laser as a sinusoidal oscillation with amplitude and phase noise. The time-dependent part of the electric field emitted by the laser can then be written as [27, p. 47]

$$E(t) = [E_0 + \Delta E_0(t)] \cos[\omega_0 t + \phi(t)], \quad (6.1)$$

where  $\omega_0 = 2\pi\nu_0$  is the unperturbed carrier frequency of the laser. The amplitude exhibits random fluctuations  $\Delta E_0(t)$  around  $E_0$ , and the argument of the cosine function contains the phase noise term  $\phi(t)$ .

#### Amplitude noise

We start our discussion by analyzing pure harmonic amplitude modulation. The laser output becomes

$$E(t) = E_0[1 + M \cos(\omega_m t)] \cos(\omega_0 t), \quad (6.2)$$

where  $M$  is the modulation index, and  $\omega_m$  is the modulation frequency. By using the trigonometric relation  $\cos(\alpha) \cos(\beta) = [\cos(\alpha + \beta) + \cos(\alpha - \beta)]/2$ , we can rewrite Equation 6.2 as

$$E(t) = E_0 \left\{ \cos(\omega_0 t) + \frac{M}{2} \cos[(\omega_0 + \omega_m)t] + \frac{M}{2} \cos[(\omega_0 - \omega_m)t] \right\}. \quad (6.3)$$

The amplitude modulation adds a pair of sidebands to the laser spectrum that are located at  $\pm\omega_m$  from the carrier and have relative amplitudes  $M/2$ . The power contained in the sidebands is  $M^2/2$  times the carrier power [27, p. 17]. In a real laser the amplitude noise is typically due to many small perturbations with different frequencies that can be characterized by a Fourier spectrum [27, pp. 17–18]. The output power of laser sources usually fluctuates only by a small fraction of the average power. Since the HHG process is highly nonlinear, it increases the relative amplitude noise. Typically, this results in root mean square power fluctuations of a few percent of the average power in the XUV output [32]. Therefore, even in the XUV, the amplitude noise sidebands contain much less power than the carrier. Our spectroscopy target, the 1S-2S transition in  $\text{He}^+$ , has a natural linewidth of 84 Hz [14]. We do not expect that the amplitude noise sidebands have a large effect on spectroscopy of such a narrow line. In the following, amplitude noise will therefore be neglected.

#### Noise power spectral densities

Noise is by definition random and therefore has to be described using statistical methods. We want to model a fluctuating physical quantity  $b(t)$  (phase, frequency, voltage, ...). One useful statistical property of  $b(t)$  is its autocorrelation function

$$R_b(\tau) = \lim_{T \rightarrow \infty} \frac{1}{2T} \int_{-T}^T b(t + \tau) b(t) dt. \quad (6.4)$$

The Wiener-Khintchine theorem states that  $R_b(\tau)$  and the *power spectral density*  $S_b^{\text{II}}(f)$  form a Fourier transform pair [27, pp. 57–58]:

$$S_b^{\text{II}}(f) = \int_{-\infty}^{\infty} R_b(\tau) e^{-i2\pi f\tau} d\tau, \quad (6.5)$$

$$R_b(\tau) = \int_{-\infty}^{\infty} S_b^{\text{II}}(f) e^{i2\pi f\tau} df. \quad (6.6)$$

To get an intuition for the meaning of the power spectral density, we insert  $\tau = 0$  in Equation 6.6 and Equation 6.4 and obtain [27, pp. 55–56]

$$R_b(0) = \int_{-\infty}^{\infty} S_b^{\text{II}}(f) df = \lim_{T \rightarrow \infty} \frac{1}{2T} \int_{-T}^T b(t)^2 dt. \quad (6.7)$$

If we integrate the power spectral density over all frequencies, we obtain the mean square value of  $b(t)$  (Parseval's theorem). Hence, the power spectral density quantifies the mean square fluctuations of a signal contained in a certain frequency band. It is therefore measured in units of [unit of  $b$ ]<sup>2</sup>/Hz.<sup>1</sup>

If  $b(t)$  can be described as a stationary process, i.e. its distribution is time-independent, the autocorrelation is an even function. Then the power spectral density is also even.  $S_b^{\text{II}}(f)$  is defined for Fourier frequencies  $-\infty < f < \infty$  and is therefore called the two-sided power spectral density. However, this representation is somewhat redundant since the positive and negative frequency parts contain the same information. It is therefore common to define the one-sided power spectral density

$$S_b^{\text{I}}(f) = 2S_b^{\text{II}}(f), \quad (6.8)$$

which is only defined for  $0 \leq f < \infty$ . Unfortunately, in the literature it is not always clear which definition is used. To avoid confusion, in the following we will use the superscripts I for one-sided and II for two-sided power spectral densities.

If our signal is spectrally filtered such that its Fourier frequencies are limited to a range between  $f_{\text{min}}$  and  $f_{\text{max}}$ , we can calculate the resulting mean square of  $b(t)$  by integrating over the one-sided power spectral density:

$$\langle b(t)^2 \rangle_{\text{bandlim.}} = \int_{f_{\text{min}}}^{f_{\text{max}}} S_b^{\text{I}}(f) df. \quad (6.9)$$

The power spectral density can also be defined via the square magnitude of the Fourier spectrum of  $b(t)$ :

$$S_b^{\text{II}}(f) = \lim_{T \rightarrow \infty} \frac{1}{2T} \left| \int_{-T}^T b(t) e^{-i2\pi ft} dt \right|^2. \quad (6.10)$$

The definitions in Equation 6.5 and Equation 6.10 are equivalent for reasonably well behaved noise processes [27, p. 69].

<sup>1</sup>Sometimes a power spectral density is specified by its *square root* value. In this case the unit becomes [unit of  $b$ ]/ $\sqrt{\text{Hz}}$ .

### Phase and frequency noise power spectral density

When discussing the frequency stability of a laser, the fluctuating quantity of interest is the phase term  $\phi(t)$  in Equation 6.1. The phase noise power spectral density is then defined using Equation 6.4 and Equation 6.5:

$$S_{\phi}^{\text{II}}(f) = \int_{-\infty}^{\infty} R_{\phi}(\tau) e^{-i2\pi f\tau} d\tau, \quad (6.11)$$

$$R_{\phi}(\tau) = \lim_{T \rightarrow \infty} \frac{1}{2T} \int_{-T}^T \phi(t + \tau) \phi(t) dt. \quad (6.12)$$

$S_{\phi}^{\text{II}}(f)$  is measured<sup>2</sup> in units of (rad)<sup>2</sup>/Hz.

It is often useful to work with frequency fluctuations instead of phase fluctuations. The instantaneous frequency of the laser output is given by the time derivative of the argument of the cosine function in Equation 6.1:

$$\nu(t) = \frac{1}{2\pi} \frac{d}{dt} [\omega_0 t + \phi(t)] = \nu_0 + \frac{1}{2\pi} \frac{d\phi(t)}{dt}. \quad (6.13)$$

We can identify the frequency fluctuations

$$\Delta\nu(t) = \frac{1}{2\pi} \frac{d\phi(t)}{dt}. \quad (6.14)$$

The frequency noise power spectral density is defined analogous to the phase noise power spectral density:

$$S_{\nu}^{\text{II}}(f) = \int_{-\infty}^{\infty} R_{\nu}(\tau) e^{-i2\pi f\tau} d\tau, \quad (6.15)$$

$$R_{\nu}(\tau) = \lim_{T \rightarrow \infty} \frac{1}{2T} \int_{-T}^T \Delta\nu(t + \tau) \Delta\nu(t) dt. \quad (6.16)$$

$S_{\nu}^{\text{II}}(f)$  is measured in units of Hz<sup>2</sup>/Hz.

An important property of the Fourier transform is that a derivative in the time domain corresponds to a multiplication with  $2\pi f$  in the frequency domain. By inserting Equation 6.14 into Equation 6.10 and integrating by parts, we find the relationship between the frequency and phase noise power spectral densities:

$$\begin{aligned} S_{\nu}^{\text{II}}(f) &= \lim_{T \rightarrow \infty} \frac{1}{2T} \left| \int_{-T}^T \Delta\nu(t) e^{-i2\pi ft} dt \right|^2 = \lim_{T \rightarrow \infty} \frac{1}{2T} \left| \frac{1}{2\pi} \int_{-T}^T \frac{d\phi(t)}{dt} e^{-i2\pi ft} dt \right|^2 \\ &= f^2 \lim_{T \rightarrow \infty} \frac{1}{2T} \left| \int_{-T}^T \phi(t) e^{-i2\pi ft} dt \right|^2 = f^2 S_{\phi}^{\text{II}}(f). \end{aligned} \quad (6.17)$$

Since the two quantities have the same physical origin, they can be directly converted into each other.

<sup>2</sup>Since the radian is dimensionless, one could argue that it is not really a unit. However, it serves to remind us that a quantity represents a phase difference or an angle.

### Optical spectrum with phase or frequency noise

We now want to know how a given phase or frequency noise power spectral density influences the optical spectrum of our laser. The electric field of a laser output with negligible amplitude noise can be written in complex representation as

$$E(t) = E_0 e^{i[2\pi\nu_0 t + \phi(t)]}. \quad (6.18)$$

The autocorrelation function of the field can then be related to the phase noise power spectral density [27, pp. 64–65]:

$$R_E(\tau) = \langle E(t + \tau) E^*(t) \rangle = E_0^2 e^{i2\pi\nu_0 \tau} e^{-\int_0^\infty S_\phi^I(f) [1 - \cos(2\pi f \tau)] df}, \quad (6.19)$$

where  $\langle \rangle$  signifies temporal averaging.

We obtain the power spectral density of the laser output by taking the Fourier transform of the autocorrelation function. The result is

$$S_E^{\text{II}}(\nu - \nu_0) = E_0^2 \int_{-\infty}^{\infty} e^{-i2\pi(\nu - \nu_0)\tau} e^{-\int_0^\infty S_\phi^I(f) [1 - \cos(2\pi f \tau)] df} d\tau \quad (6.20)$$

$$= E_0^2 \int_{-\infty}^{\infty} e^{-i2\pi(\nu - \nu_0)\tau} e^{-2 \int_0^\infty S_\nu^I(f) \frac{\sin^2(\pi f \tau)}{f^2} df} d\tau, \quad (6.21)$$

where we used Equation 6.17 to obtain the second line.

It is instructive to analyze the laser spectrum for the example of filtered white frequency noise [180, 181]:

$$S_\nu^I(f) = \begin{cases} h_0, & f \leq f_c \\ 0, & f > f_c \end{cases}, \quad (6.22)$$

where  $h_0$  is the noise level, and  $f_c$  is the cutoff frequency. Inserting into Equation 6.21 gives

$$S_E^{\text{II}}(\nu - \nu_0) = E_0^2 \int_{-\infty}^{\infty} e^{-i2\pi(\nu - \nu_0)\tau} e^{-2h_0 \int_0^{f_c} \frac{\sin^2(\pi f \tau)}{f^2} df} d\tau. \quad (6.23)$$

In the limit  $f_c \rightarrow \infty$  (white frequency noise), the integral in the exponent has an analytical solution:

$$\int_0^\infty \frac{\sin^2(\pi f \tau)}{f^2} df = \frac{\pi^2}{2} |\tau|. \quad (6.24)$$

With this, Equation 6.23 can be evaluated. The result is

$$S_E^{\text{II}}(\nu - \nu_0) = \frac{E_0^2}{2} \frac{h_0}{\left(\frac{\pi h_0}{2}\right)^2 + (\nu - \nu_0)^2}. \quad (6.25)$$

A laser with pure white frequency noise has a Lorentzian line shape with an FWHM of  $\pi h_0$ . A physical example for this is the quantum noise caused by the fluctuating photon number in a laser cavity. It can be shown that this leads to a white frequency noise [182]:

$$S_\nu^I(f) = \frac{1}{(2\pi)^2} \frac{h\nu_0 l_{\text{tot}}}{T_R^2 P_{\text{int}}}, \quad (6.26)$$

where  $h\nu_0$  is the photon energy,  $l_{\text{tot}}$  is the total power loss per cavity round trip,  $T_R$  is the cavity round-trip time, and  $P_{\text{int}}$  is the intracavity power. The FWHM linewidth of the empty laser cavity is

$$\Delta\nu_c = \frac{1}{2\pi} \frac{l_{\text{tot}}}{T_R}. \quad (6.27)$$

If the total power loss per cavity round trip is dominated by the transmission through the laser output coupler mirror, the output power is given by  $P = l_{\text{tot}}P_{\text{int}}$ . The resulting FWHM linewidth is

$$\Delta\nu_{\text{FWHM}} = \frac{\pi h\nu_0}{P} \Delta\nu_c^2. \quad (6.28)$$

This is equivalent<sup>3</sup> to the famous Schawlow-Townes formula that was originally derived by making an analogy with the linewidth of masers operating in the microwave range [184].

The other limit is  $f_c \rightarrow 0$ . In this case we get

$$\int_0^{f_c} \frac{\sin^2(\pi f\tau)}{f^2} df \approx \pi^2 \tau^2 f_c. \quad (6.29)$$

After inserting into Equation 6.23, we get

$$S_E^{\text{II}}(\nu - \nu_0) = \frac{E_0^2}{\sqrt{2\pi h_0 f_c}} e^{-\frac{(\nu - \nu_0)^2}{2h_0 f_c}}. \quad (6.30)$$

In this case the line shape is Gaussian with an FWHM linewidth of  $2\sqrt{2 \ln(2) h_0 f_c}$ .

Domenico *et al.* have numerically studied how the linewidth of the spectrum given by Equation 6.23 changes as a function of  $f_c$  for a fixed frequency noise level  $h_0$  [181]. Their result is that for  $f_c \ll h_0$  the line is Gaussian and the width increases with increasing  $f_c$ . For  $f_c \gg h_0$  the spectrum becomes Lorentzian and the linewidth stops to increase.

They were then able to generalize the result to arbitrary frequency noise spectra. It turns out that the frequency noise power spectral density can be separated into two regions. They are delimited by the point where  $S_\nu^{\text{I}}(f)$  crosses the so-called  $\beta$ -separation line  $8 \ln(2) f / \pi^2$  as shown in Figure 6.2. In the first region the frequency noise level is large compared to its Fourier frequency.<sup>4</sup> This corresponds to large phase excursions at low Fourier frequencies (slow phase/frequency noise) and leads to a Gaussian line shape. In the second region the opposite is the case. The frequency noise level is small compared to its Fourier frequency, corresponding to small phase excursions at high Fourier frequencies (fast phase/frequency noise). This part of the frequency noise power spectral density creates Lorentzian wings in the spectrum, but does not affect the FWHM linewidth. One consequence of this is that the linewidth alone is not always a good measure for the spectral purity of a laser.

<sup>3</sup>In the original Schawlow-Townes paper, the linewidths of the cavity and the emission are given as half width at half maximum. Furthermore, it was later found that the result is only valid for lasers operating below threshold and that the noise above threshold is smaller by a factor 2 [183].

<sup>4</sup>Note that frequency noise power spectral density has the unit  $\text{Hz}^2/\text{Hz}$  and can therefore be set in relation with a Fourier frequency in Hz.

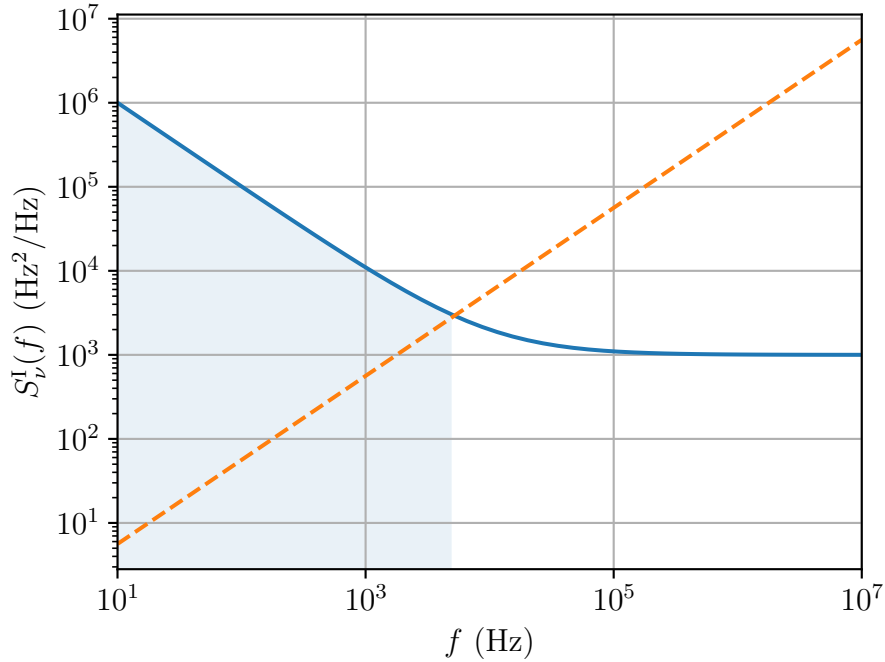


Figure 6.2: Illustration of the  $\beta$ -separation line concept [181]. The solid blue line shows an example for a frequency noise power spectral density of a laser. It consists of a component that scales with  $1/f$  and a frequency-independent component that dominates at high frequencies. The dashed orange line is the  $\beta$ -separation line  $8 \ln(2)f/\pi^2$ . Only the blue shaded part of the frequency noise power spectral density determines the laser linewidth. The higher frequency components lead only to small and fast phase excursions and contribute to the wings of the spectrum.

The FWHM linewidth is then given by [181]

$$\Delta\nu_{\text{FWHM}} = \sqrt{8 \ln(2)A}, \quad (6.31)$$

where

$$A = \int_{1/T_0}^{\infty} H[S_{\nu}^I(f) - 8 \ln(2)f/\pi^2] S_{\nu}^I(f) df \quad (6.32)$$

is the mean square integrated frequency noise in the Fourier frequency range where it exceeds the  $\beta$ -separation line (blue shaded area in Figure 6.2).  $H(x)$  is the Heaviside step function that is defined as

$$H(x) = \begin{cases} 1, & x \geq 0 \\ 0, & x < 0 \end{cases}. \quad (6.33)$$

$T_0$  is a characteristic measurement time that limits the minimum Fourier frequency that can be observed in an experiment. This could for example be the acquisition time of a spectrum analyzer measuring a beat note signal, or the pulse separation in a Ramsey-type spectroscopy experiment. At low Fourier frequencies, the frequency noise of oscillators often



scales as  $S_\nu^I(f) \propto 1/f$  (flicker frequency noise) or  $S_\nu^I(f) \propto 1/f^2$  (random walk frequency noise) [27, pp. 59–60]. In this case the integral in Equation 6.32 diverges for  $T_0 \rightarrow \infty$ , leading to an infinite linewidth. The underlying reason for this is that the frequency of a free-running oscillator can in principle drift by an arbitrary amount if one just waits long enough. Consequently, the observed oscillator linewidth depends on the application, and many possible definitions exist (see [185] for a detailed discussion of this issue). The  $\beta$ -separation line is one sensible definition that allows comparing different measurements. For large values of  $T_0$ , the linewidth scales as  $\Delta\nu_{\text{FWHM}} \propto \sqrt{\ln(T_0)}$  for  $1/f$  noise and as  $\Delta\nu_{\text{FWHM}} \propto \sqrt{T_0}$  for  $1/f^2$  noise [181]. Due to this relatively slow divergence, linewidth measurements are often not very sensitive to the measurement time.

With the  $\beta$ -separation line model, we can understand the beat note between the outputs of the two cavity-stabilized ECDLs shown in Figure 6.1. At low Fourier frequencies, the feedback loops stabilizing the lasers have very high gain and tightly lock the laser outputs to the cavity resonances. The low-frequency noise and hence the laser linewidths are therefore determined only by the stability of the reference cavities. In order to avoid oscillations, the gain of a feedback system has to drop below 0 dB before a phase delay of  $180^\circ$  is reached. This limits the achievable feedback bandwidth to a few hundred kHz for these particular laser systems. The high-frequency phase noise present in the output of the ECDLs can therefore only partially be suppressed. This leads to broad wings in the spectrum that form the noise pedestal. Even though the laser linewidths are only around 1 Hz, the pedestals extend over several MHz and contain around 2% of the total power.

### Phase noise measurement

We can now analyze how the power spectral density of fast phase noise influences the shape of the noise pedestal. As discussed above, slow phase noise contributes to the laser spectrum with a Gaussian line shape that rapidly falls off at Fourier frequencies above the linewidth. We introduce a cutoff Fourier frequency  $f_0$  that separates the narrow Gaussian carrier from the broad phase noise pedestal. The fast phase noise power spectral density is defined as [186]

$$S_{\phi, f_0}^I(f) = \begin{cases} 0, & 0 < f < f_0, \\ S_\phi^I(f), & f \geq f_0 \end{cases}. \quad (6.34)$$

We can approximate the spectrum of the pedestal, i.e. for  $|\nu - \nu_0| > f_0$ , by inserting Equation 6.34 into Equation 6.20:

$$\begin{aligned} S_E^{\text{II}}(\nu - \nu_0) &\approx E_0^2 \int_{-\infty}^{\infty} e^{-i2\pi(\nu - \nu_0)\tau} e^{-\int_{f_0}^{\infty} S_\phi^I(f)[1 - \cos(2\pi f\tau)]df} d\tau \\ &= E_0^2 \int_{-\infty}^{\infty} e^{-i2\pi(\nu - \nu_0)\tau} e^{-\phi_{\text{rms}}^2 + R_{\phi, f_0}(\tau)} d\tau, \end{aligned} \quad (6.35)$$

where

$$\phi_{\text{rms}} = \sqrt{\int_{f_0}^{\infty} S_\phi^I(f)df} \quad (6.36)$$

is the integrated fast phase noise, and

$$R_{\phi, f_0}(\tau) = \int_{f_0}^{\infty} S_{\phi}^I(f) \cos(2\pi f\tau) df \quad (6.37)$$

is the autocorrelation function of the fast phase noise. Note that  $R_{\phi, f_0}(\tau) \leq R_{\phi, f_0}(0) = \phi_{\text{rms}}^2$  since  $S_{\phi}^I(f)$  is a positive function.

For small integrated fast phase noise, i.e.  $\phi_{\text{rms}}^2 \ll 1$ ,  $R_{\phi, f_0}(\tau)$  therefore also has to be small. We can then expand the second exponential in the integrand in Equation 6.35 up to first order and get [27, p. 68]

$$\begin{aligned} S_E^{\text{II}}(\nu - \nu_0) &\approx E_0^2 \int_{-\infty}^{\infty} e^{-i2\pi(\nu - \nu_0)\tau} [1 - \phi_{\text{rms}}^2 + R_{\phi, f_0}(\tau)] d\tau \\ &= E_0^2 [(1 - \phi_{\text{rms}}^2) \delta(\nu - \nu_0) + S_{\phi, f_0}^{\text{II}}(\nu - \nu_0)], \end{aligned} \quad (6.38)$$

where we have used the integral representation of the Dirac delta distribution:

$$\delta(\nu - \nu_0) = \int_{-\infty}^{\infty} e^{-i2\pi(\nu - \nu_0)\tau} d\tau, \quad (6.39)$$

and have introduced in analogy with Equation 6.11 the power spectral density of fast phase noise:

$$S_{\phi, f_0}^{\text{II}}(f) = \int_{-\infty}^{\infty} R_{\phi, f_0}(\tau) e^{-i2\pi f\tau} d\tau. \quad (6.40)$$

The spectrum described by Equation 6.38 consists of a carrier surrounded by symmetric noise sidebands. Since the approximation only contains fast phase noise, the carrier is not resolved and shows up as an infinitely narrow peak at  $\nu = \nu_0$ . The sidebands are given by the two-sided fast phase noise power spectral density  $S_{\phi, f_0}^{\text{II}}(f)$  evaluated at  $f = \nu - \nu_0$ . This allows a direct measurement of this quantity using a spectrum analyzer. The power spectral density in the upper or lower noise sideband is measured and normalized to the carrier power. The result is called the *single sideband phase noise*<sup>5</sup>  $\mathcal{L}(f)$ . For historic reasons this quantity is commonly used to specify the spectral purity of oscillators. It is usually displayed on a logarithmic scale in dBc/Hz with a frequency axis relative to the carrier frequency. We can see from Equation 6.38 that in the low phase noise limit<sup>6</sup>

$$\mathcal{L}(f) = S_{\phi, f_0}^{\text{II}}(f) = \frac{1}{2} S_{\phi, f_0}^I(f). \quad (6.41)$$

<sup>5</sup>Note that the *single sideband* phase noise is equivalent to the *two-sided* fast phase noise power spectral density.

<sup>6</sup> $\mathcal{L}(f)$  is measured in dBc/Hz and  $S_{\phi, f_0}^{\text{II}}(f)$  in (rad)<sup>2</sup>/Hz. Since power ratios (measured in dBc) and phase angles (measured in rad) are both dimensionless, the conversion factor between these quantities in Equation 6.41 is unity.

### Frequency multiplication and carrier collapse

If the integrated fast phase noise is not small, we have to keep the higher-order terms in the second exponential in the integrand in Equation 6.35 and get

$$\begin{aligned} S_E^{\text{II}}(\nu - \nu_0) &\approx E_0^2 e^{-\phi_{\text{rms}}^2} \int_{-\infty}^{\infty} e^{-i2\pi(\nu - \nu_0)\tau} \left[ 1 + R_{\phi, f_0}(\tau) + \sum_{n=2}^{\infty} \frac{R_{\phi, f_0}(\tau)^n}{n!} \right] d\tau \\ &= E_0^2 e^{-\phi_{\text{rms}}^2} \left[ \delta(\nu - \nu_0) + S_{\phi, f_0}^{\text{II}}(\nu - \nu_0) + \int_{-\infty}^{\infty} e^{-i2\pi(\nu - \nu_0)\tau} \sum_{n=2}^{\infty} \frac{R_{\phi, f_0}(\tau)^n}{n!} d\tau \right]. \end{aligned} \quad (6.42)$$

Pure phase modulation leaves the total power of the signal unchanged [27, p. 28]. Hence, the relative power contained in the carrier is  $\exp(-\phi_{\text{rms}}^2)$ . With a good feedback loop, an integrated fast phase noise on the order of 100 mrad can be achieved even with a very simple cavity-stabilized ECDL [178]. Therefore, at the fundamental wavelength, the power lost from the carrier is typically a few percent at most. The situation changes when harmonics of the laser output are generated. Frequency multiplication increases the magnitude of the phase noise term  $\phi(t)$  by the multiplication factor [186]. Therefore, the integrated fast phase noise at the  $q$ th harmonic is given by  $q\phi_{\text{rms}}$ , and the power contained in the upconverted carrier is  $\exp(-q^2\phi_{\text{rms}}^2)$ . Once the argument of the exponential function surpasses a threshold of approximately  $(1 \text{ rad})^2$ , the carrier starts to collapse [186, 187]. We will excite the 1S-2S two-photon transition in  $\text{He}^+$  using the 17th harmonic of a frequency comb centered at 1033 nm. Intracavity HHG has been shown not to cause additional linewidth broadening beyond the unavoidable phase noise scaling [188]. In our application the two-photon absorption corresponds to another frequency doubling such that we are effectively generating the 34th harmonic of the fundamental light. Figure 6.3 shows how the power fraction remaining in the carrier depends on the integrated fast phase noise of the driving laser. Already at an integrated fast phase noise of 24 mrad, the available power drops to 50 %, putting a very stringent requirement on the spectral purity of the driving laser.

## 6.2 Cavity-stabilized continuous-wave laser

The small natural linewidth of the 1S-2S transition in  $\text{He}^+$  also mandates a driving laser for the HHG with a very narrow linewidth.

The slow phase noise of a free-running laser that determines the linewidth is usually dominated by technical noise created in the various components. Important contributions are for example pump intensity noise and mechanical vibrations that lead to fluctuations in the length of the laser resonator. On longer time scales, changes in temperature and air pressure lead to drifts of the output frequency. Passive optical resonators can reach much higher stabilities than laser cavities since they do not contain a pumped gain medium. Therefore, a standard method for constructing very stable lasers is to employ an external ultrastable Fabry-Pérot resonator as a frequency reference. An electronic feedback circuit is used to keep the laser output in resonance with the cavity.

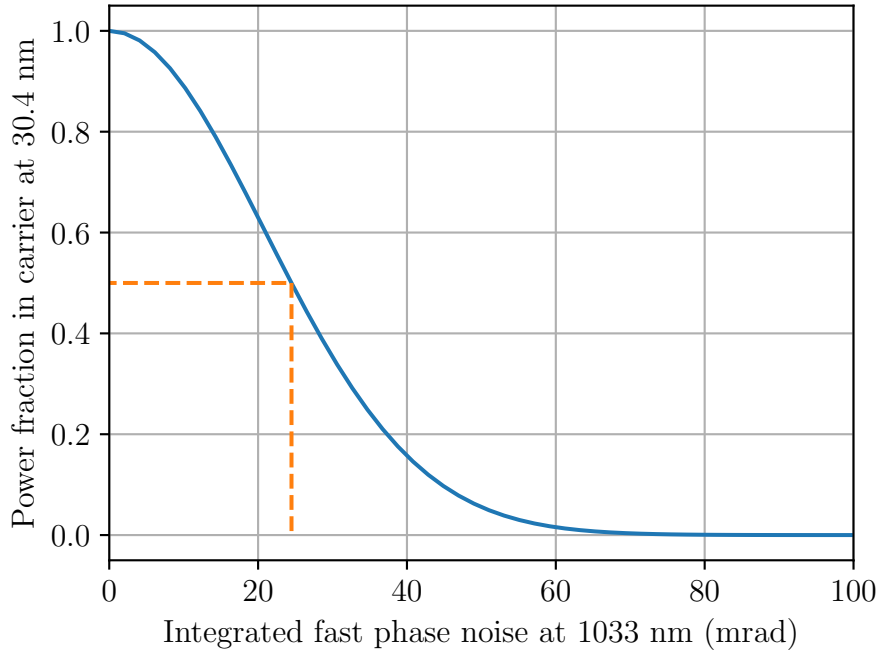


Figure 6.3: Carrier collapse when generating the 34th harmonic of a laser with phase noise. The blue solid line shows the power remaining in the carrier for a given amount of integrated fast phase noise in the driving laser. The dashed orange lines indicate the point where the carrier power has dropped by 50%.

While it is possible to directly stabilize a frequency comb to a reference cavity [189, 190], there are a number of practical limitations. For maximum coupling efficiency, all modes of the frequency comb have to be resonant at the same time. This means that the free spectral range of the cavity has to be an integer multiple of the comb repetition rate, leading to cavity lengths that are often impractical. If a shorter cavity is used, only a fraction of the comb modes can be simultaneously resonant. The other modes get reflected from the cavity input coupler and generate excess shot noise in the photodetector without contributing to the feedback error signal. Another challenge is that the coatings of the cavity mirrors can introduce higher-order dispersion. While the mode spacing of a frequency comb is perfectly regular, this is not the case for an optical resonator with group velocity dispersion. The resulting mode mismatch limits the usable bandwidth of the comb and can lead to asymmetries of the feedback error signal [189]. We therefore take the more common approach of using an additional continuous-wave (cw) laser to transfer the stability of the reference cavity to the frequency comb.

### 6.2.1 Interference-filter stabilized ECDL

ECDLs are ubiquitous in atomic physics experiments due to their simple construction and large range of available wavelengths. However, it was found that the high phase noise levels

of some ECDLs can lead to carrier collapse when a harmonic of the laser output is being generated [178]. The typical frequency noise spectrum of a diode laser has a similar shape as the example shown in Figure 6.2 [27, p. 67]. Below the corner frequency, technical noise dominates which typically follows a  $1/f$  scaling. Above the corner frequency, the noise spectrum is white. This is partially due to the quantum noise given in Equation 6.26. However, semiconductor lasers usually have a strong coupling between amplitude and phase fluctuations. This creates another noise contribution that is  $\alpha^2$  times the quantum noise, where  $\alpha$  is Henry's linewidth enhancement factor [182, 191]. Typical values of  $\alpha$  are in the range  $2 \dots 8$  [192]. The resulting white frequency noise component is<sup>7</sup>

$$S_{\nu}^I(f) = (1 + \alpha^2) \frac{1}{(2\pi)^2} \frac{h\nu_0 l_{\text{tot}}}{T_R^2 P_{\text{int}}}. \quad (6.43)$$

Since the frequency noise power spectral density scales with the inverse square of the laser cavity round-trip time  $T_R$ , increasing the laser cavity length is very effective at improving the noise performance [178]. The achievable intracavity power  $P_{\text{int}}$  is limited by the onset of optical damage to the diode output facet. Another factor is the round-trip loss  $l_{\text{tot}}$  which can be reduced by increasing the reflectivity of the output coupler. However, this comes at the cost of reduced output power.

A schematic of our laser is shown in Figure 6.4. It consists of an anti-reflection coated laser diode that is placed in a roughly 10 cm long external cavity.

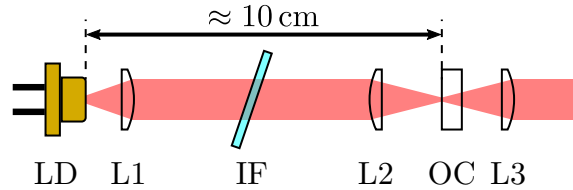


Figure 6.4: Interference-filter stabilized ECDL. LD, laser diode; L1, laser diode collimator ( $f = 4.5$  mm); IF, interference filter; L2: “cat’s eye” lens ( $f = 13.86$  mm); OC, output coupler ( $R = 85\%$ ); L3: output collimator ( $f = 13.86$  mm).

The cavity is formed by the back facet of the diode and a partially reflective mirror (output coupler). The laser diode output is collimated, and a second lens is used to focus the light onto the output coupler. This forms a “cat’s eye” retroreflector which significantly reduces the sensitivity against misalignment of the mirror [193, 194]. Single-mode operation is achieved by placing a narrow-band interference filter<sup>8</sup> in the laser cavity. The filter has a specified center wavelength of 1064 nm and an FWHM bandwidth of 0.5 nm. We tune the laser to the required wavelength of 1033 nm by tilting the filter. The output coupler has a relatively high reflectivity of 85% in order to minimize the white frequency noise.

<sup>7</sup>We limit our discussion to ECDLs with anti-reflection coated laser diodes where the reflection from the diode output facet can be neglected. See chapter 9.3.2 in [27] for a more general overview of diode laser configurations.

<sup>8</sup>Alluxa #4012.

This limits the typical output power to around 3 mW. Since this is not sufficient for our application, the output is subsequently amplified to around 30 mW in a small Yb-doped fiber amplifier. The temperature of the laser is actively stabilized with a Peltier element and a temperature sensor. In order to minimize drifts due to air pressure changes, it is surrounded by an airtight enclosure that is machined from an aluminum block. The ECDL and fiber amplifier are placed in a box made from sound-absorbing material to reduce the influence of acoustic noise.

### 6.2.2 Reference cavity and feedback system

Figure 6.5 shows a schematic of the cw laser stabilization setup. Part of the light is sent through a polarization maintaining single-mode fiber to the reference cavity assembly which is placed on an active vibration isolation table.<sup>9</sup> Like the ECDL, the assembly is placed in a sound-absorbing box for acoustic isolation.

#### Fiber-noise cancellation

Acoustic noise can induce significant fluctuations in the optical path length of a single-mode fiber which leads to phase noise on the transmitted light [195]. We therefore employ active fiber noise cancellation [196]. After the light has passed through the fiber, its frequency is shifted by  $f_{\text{AOM}}$  using an acousto-optic modulator (AOM) driven by a voltage-controlled oscillator (VCO). Part of the light is then retroreflected with a beam splitter and a mirror. After passing through the AOM and fiber again, it is overlapped with a reference beam that did not pass through the fiber. In our setup the reference beam is the Fresnel reflection from the fiber input facet which is cleaved at  $0^\circ$  [177]. The two beams create a beat note on a photodiode (PD1) at  $2f_{\text{AOM}}$ . This signal contains the phase fluctuations picked up by the light on its path through the fiber. It is mixed with an 80 MHz reference signal from an RF synthesizer in order to extract the phase difference. The phase locked loop is then closed via a loop filter that gives feedback to the tuning port of the VCO.

#### Reference cavity

An electro-optic modulator (EOM) is used to generate the sidebands required for locking the laser to the cavity using the Pound-Drever-Hall (PDH) technique [143]. The modulation frequency is 21.32 MHz, and the modulation index is  $\beta = 0.95$  which is close to the optimum value of  $\beta = 1.08$  [197]. The modulation index is measured by comparing the power transmitted through the cavity when locking to the modulation sidebands and when locking to the carrier. The cavity consists of a 77.5 mm long spacer made from ultra-low expansion (ULE) glass<sup>10</sup> and optically contacted dielectric mirrors with ULE substrates. A photon lifetime of  $\tau_c = 24.3 \mu\text{s}$  (relative drop of transmitted power to  $1/e$ ) corresponding to an

<sup>9</sup>Table Stable TS-150.

<sup>10</sup>Corning ULE.



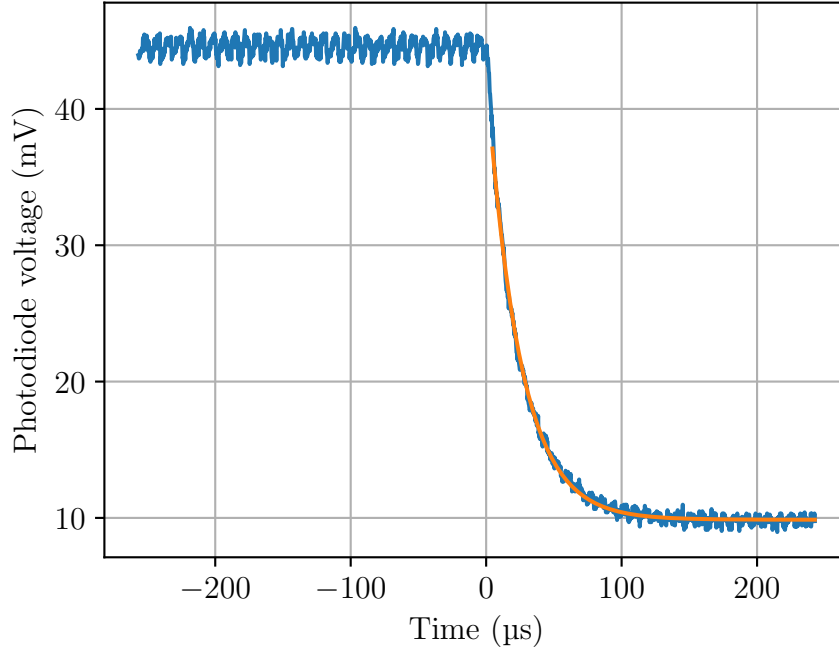


Figure 6.6: Ring-down measurement of the photon lifetime in the reference cavity. The blue trace shows the output voltage of the cavity transmission photodiode (PD4). The laser is initially locked to the cavity. At time  $t = 0$  the light is switched off using an AOM (fall time  $< 1 \mu\text{s}$ ). The orange line is an exponential fit to the experimental data. The measurement was repeated 10 times, resulting in an average photon lifetime of  $24.3 \mu\text{s}$ .

temperature setpoints. To allow the cavity to reach thermal equilibrium, we have waited for around one day after each setpoint change before recording the beat note frequency. Figure 6.7 shows the resulting data and a fit using Equation 6.44. We obtain  $T_c = 31.839^\circ\text{C}$  and  $A = 0.15 \text{ Hz/mK}^2$ . If we stabilize the temperature to within  $\pm 0.1 \text{ K}$  from  $T_c$ , the resulting residual temperature sensitivity is  $15 \text{ Hz/mK}$  at most.

The light reflected from the cavity is sent onto an InGaAs photodiode<sup>12</sup> (PD2) followed by a transimpedance amplifier with a gain of  $10 \text{ kV/A}$ . The signal is low-pass filtered at  $30 \text{ MHz}$  in order to suppress the influence of the second-order sidebands at twice the modulation frequency. After further amplification and demodulation in an RF mixer, the resulting PDH error signal is sent to a commercial loop filter<sup>13</sup> which gives feedback to the laser diode current of the ECDL. An  $f = 250 \text{ mm}$  lens is used for matching the laser beam to the cavity mode. We send about  $50 \mu\text{W}$  of light to the cavity, coupling in about  $60\%$  of the carrier power. This is measured by comparing the output voltage of PD2 when the laser is locked or unlocked. Even though the coatings of the cavity mirrors are just a few  $\mu\text{m}$  thick, their contribution to the overall thermal expansion is comparable to that of the

<sup>12</sup>Hamamatsu G8376-008A.

<sup>13</sup>Toptica FALC 110.



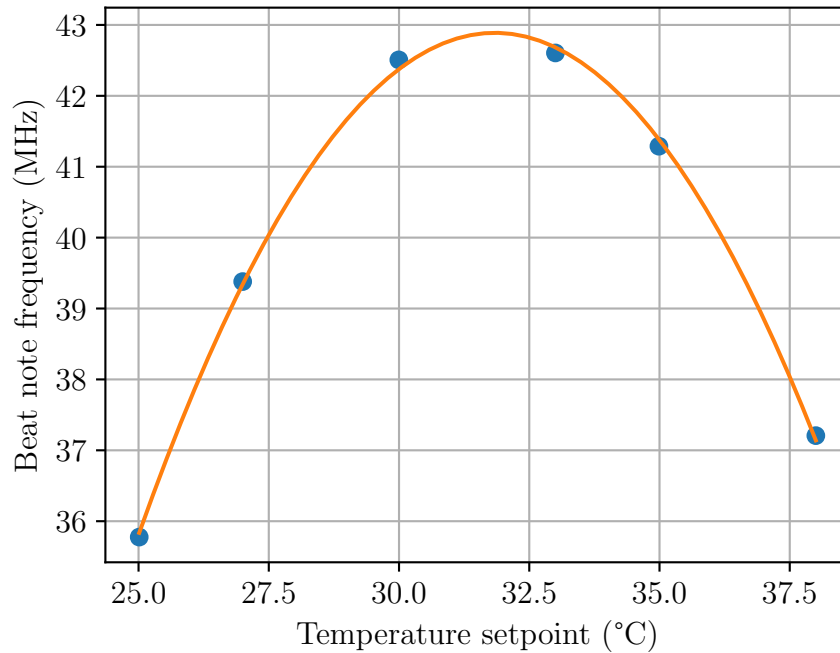


Figure 6.7: Temperature dependence of the cavity resonance frequency measured from a beat note with the output of a self-referenced frequency comb. The solid line is a fit of Equation 6.44.

ULE spacer held close to  $T_c$  [177]. Some of the power coupled into the cavity is dissipated in the coatings. This leads to localized heating and thermal expansion that quickly reacts to changing power levels. We have measured the frequency of the cavity-stabilized cw laser for different powers sent to the cavity and obtained a coefficient of  $-15\text{ Hz}/\mu\text{W}$ . In order to mitigate drifts, the power level going to the cavity is measured with an amplified photodiode<sup>14</sup> (PD3) and is stabilized by giving feedback to the AOM driving power. When the laser is locked to a resonance, a few  $\mu\text{W}$  are transmitted through the cavity. Half of the light is sent onto a camera in order to monitor the spatial mode inside the cavity. The other half is sent onto a photodiode (PD4) for monitoring the transmitted power.

### 6.2.3 Linewidth and stability

Part of the laser output is sent through a 100 m long polarization maintaining fiber to another lab which contains a commercial self-referenced frequency comb.<sup>15</sup> We use active fiber noise cancellation to compensate the phase fluctuations induced in the long fiber.

<sup>14</sup>Thorlabs PDA20CS2.

<sup>15</sup>Menlo Systems FC1500-250-ULN.

### Frequency comb stabilization

The frequency of the  $n$ th comb mode is (see section 3.1)

$$f_n = n f_{\text{rep}} + f_{\text{ceo}}, \quad (6.45)$$

where  $f_{\text{rep}}$  is the pulse repetition rate, and  $f_{\text{ceo}}$  is the carrier-envelope offset frequency. The frequency comb has two feedback systems. The first one uses actuators that are designed to mainly affect  $f_{\text{rep}}$ , while leaving  $f_{\text{ceo}}$  unchanged, and vice versa for the second one. The carrier-envelope offset frequency is measured with an  $f - 2f$  interferometer and is tightly locked to a 45 MHz reference derived from a hydrogen maser using the second feedback system. The first feedback system can be used in two different modes of operation that are sketched in Figure 6.8.

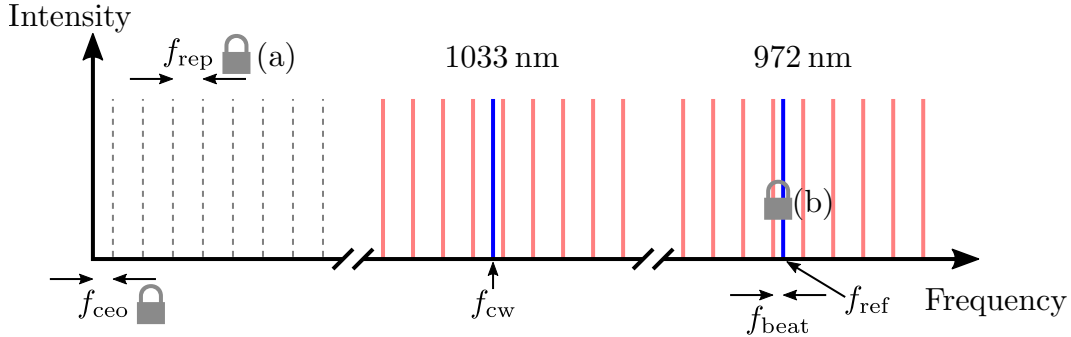


Figure 6.8: Illustration of frequency comb stabilization. The carrier-envelope offset frequency  $f_{\text{ceo}}$  is locked to a stable reference. The second degree of freedom can be fixed by stabilizing (a) the comb repetition rate  $f_{\text{rep}}$ , or (b) the beat note between a comb mode and the output of a stable laser at  $f_{\text{ref}}$ . The linewidth and stability of our cavity-stabilized cw laser can then be determined from the beat note with the stabilized frequency comb.

In the first mode (“RF lock”), the fourth harmonic of  $f_{\text{rep}}$  is locked to an RF reference close to 1 GHz that is also derived from the hydrogen maser. We can see from Equation 6.45 that the phase noise of the  $n$ th comb mode is  $n$  times the phase noise of  $f_{\text{rep}}$ . At 1033 nm, the mode number  $n$  is around one million. The feedback bandwidth is therefore limited to around 100 Hz to avoid catastrophic up-multiplication of the phase noise of the RF reference. The resulting linewidth of the comb modes is essentially that of the free-running laser, i.e. a few hundred kHz. This mode is used for measuring the frequency of various spectroscopy lasers relative to the hydrogen maser.

In the second mode (“optical lock”), a beat note between the output of an independent ultrastable reference laser at frequency  $f_{\text{ref}}$  and the closest comb mode is generated. The beat note frequency is

$$f_{\text{beat}} = n_{\text{ref}} f_{\text{rep}} + f_{\text{ceo}} - f_{\text{ref}}, \quad (6.46)$$

where  $n_{\text{ref}}$  is the number of the closest comb mode to the reference laser. The feedback system is then used to lock  $f_{\text{beat}}$  to an RF reference. We can see from Equation 6.46

that this indirectly stabilizes the repetition rate  $f_{\text{rep}}$ . The repetition rate is measured with a frequency counter that is referenced to the hydrogen maser. Since the beat note is generated between two similar optical frequencies, a tight phase lock can be employed without up-multiplying the RF phase noise. The resulting linewidths of the comb modes across the output spectrum are close to that of the reference laser. Therefore, this mode allows comparing the linewidths of lasers that are operating at different wavelengths. The lab with the frequency comb also contains a number of cavity-stabilized ECDLs used for hydrogen spectroscopy. We used two lasers operating at 972 nm (FP1 and FP2<sup>16</sup>) as references for stabilizing the frequency comb.

### Frequency stability

Figure 6.9 shows the stability of the beat note between the outputs of the cavity-stabilized cw laser and of the RF locked comb recorded over a continuous interval of four days.

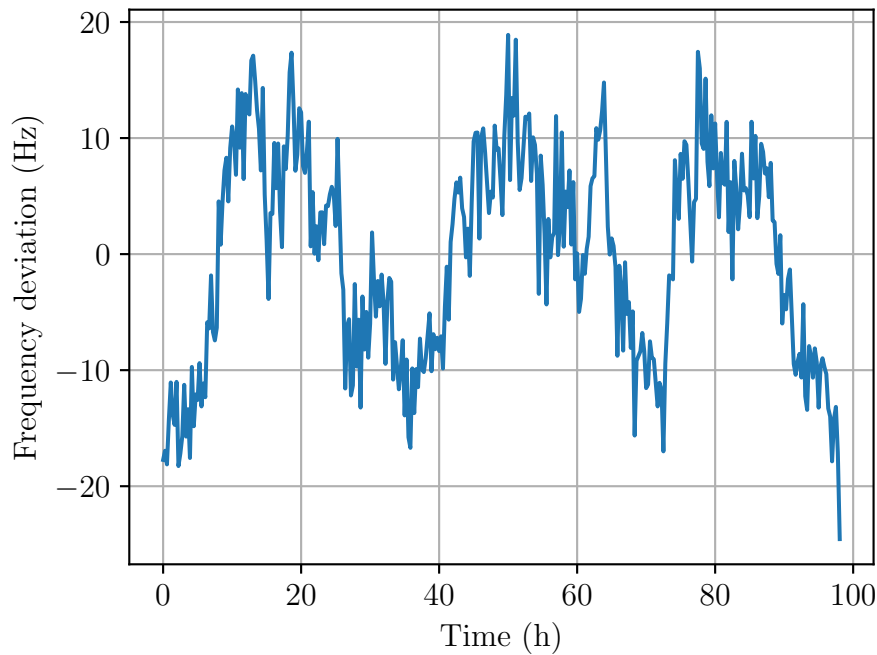


Figure 6.9: Frequency stability of the cavity-stabilized cw laser measured against the RF locked frequency comb. Counter data was recorded with 0.5 s gate time and the results were averaged over 1000 s intervals. A constant linear drift of 39 mHz/s was subtracted.

Aging of the cavity material leads to a constant frequency drift of 39 mHz/s that is subtracted from the data [177]. The data is averaged over 1000 s intervals in order to remove the contribution of frequency fluctuations of the hydrogen maser on shorter time scales. We can see that the frequency varies by around  $\pm 20$  Hz during the measurement

<sup>16</sup>These are further developed versions of the laser systems described in [177] and [178].

interval which is comparable to the performance of similar systems used in our group [177, 198].

### Line shape

Figure 6.10 shows beat notes between the outputs of our cavity-stabilized cw laser and of the frequency comb that was locked to either FP1 or FP2.

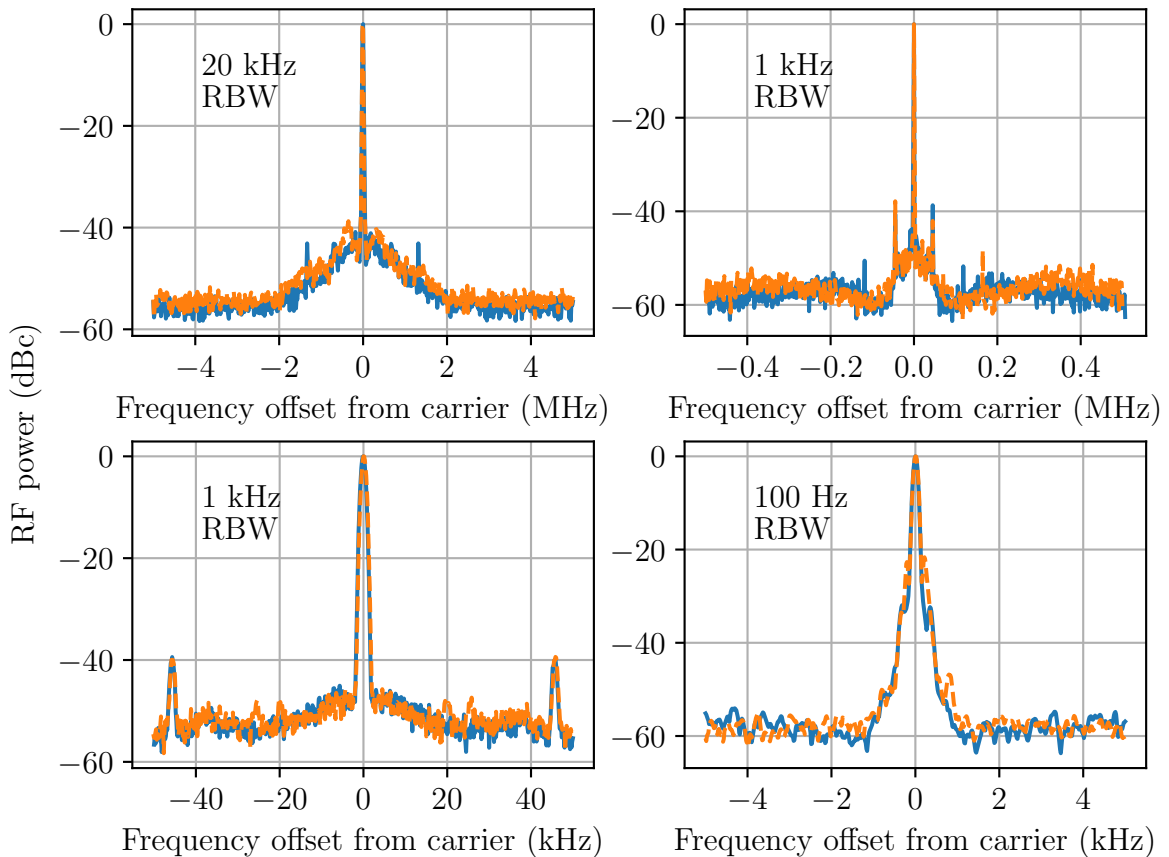


Figure 6.10: Beat notes between the outputs of the cavity-stabilized cw laser and of the optically locked frequency comb recorded with different frequency spans and resolution bandwidths (RBW). The solid blue traces are recorded with the comb locked to FP1 and the dashed orange traces with the comb locked to FP2. The beat note carrier frequencies are 55.4 MHz and 62.5 MHz for the comb locked to FP1 and FP2, respectively.

The narrow carrier and broadband noise can be clearly observed. We can also see some narrow spurious signals that show up at different frequency ranges. These can have various sources, for example the laser current drivers, PDH photodiodes, or loop filters. Some signals only show up when the comb is locked to either FP1 or FP2 which makes it possible to identify the laser responsible for them. For example, the spurs at 1.3 MHz

are due to FP1. Others are present in both cases and could therefore be caused by our laser or by the frequency comb itself. If a spur is entirely due to phase modulation, its power relative to the carrier power is given by  $J_1^2(\beta)/J_0^2(\beta)$  [27, pp. 25–30], where  $J_\alpha$  are the Bessel functions of the first kind, and  $\beta$  is the modulation index. The largest spurs visible in Figure 6.10 are at 46 kHz and have power levels of around 40 dB below the carrier, corresponding to  $\beta \approx 0.02$ . At the 34th harmonic this would result in a modulation index  $\beta \approx 0.68$ , and around 20% of the total power would be lost from the carrier. We later found out that they were caused by the PDH locking electronics of our laser and were able to mostly eliminate them (see Figure 6.14).

Figure 6.11 shows beat notes recorded with the highest resolution setting of our spectrum analyzer on a linear scale. The resulting FWHM linewidth of 1.2 Hz is comparable to the 1 Hz resolution bandwidth of the spectrum analyzer and represents an upper limit for the linewidth of the lasers.

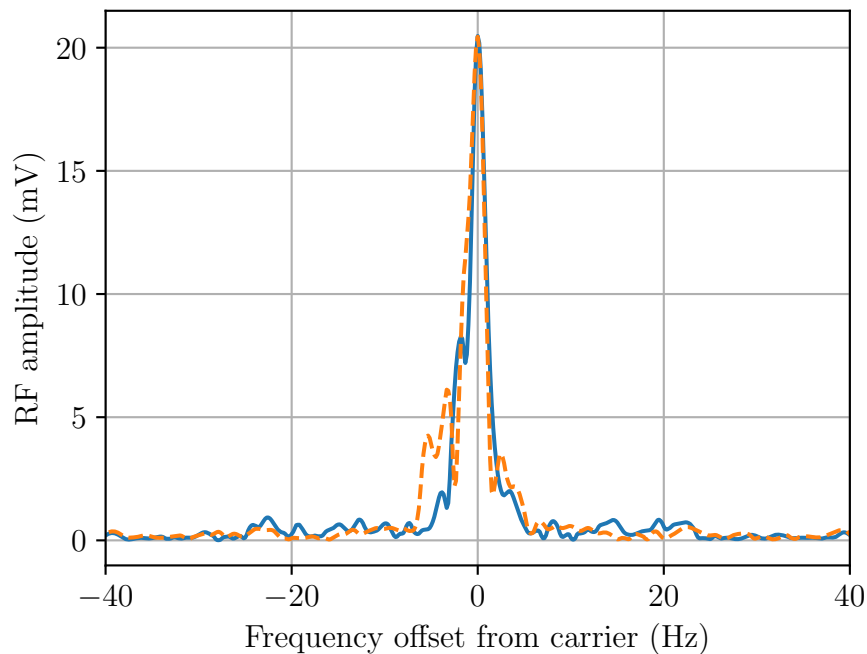


Figure 6.11: Beat notes between the outputs of the cavity-stabilized cw laser and of the optically locked frequency comb recorded with 1 Hz resolution bandwidth. The comb was locked to FP1 (solid blue trace) or FP2 (dashed orange trace). The  $-3$  dB linewidth of both traces is 1.2 Hz.

In order to test how the frequency comb itself affects the measured noise, we also recorded a direct beat note between the outputs of FP1 and FP2 and compared the result with beat notes between the outputs of one of the lasers and of the frequency comb which was optically locked to the other laser. Figure 6.12 shows the results. For Fourier frequencies up to a few tens of kHz, the spectra are almost identical, whereas for higher Fourier frequencies there is significantly more noise in the beat notes with the frequency comb

than in the beat note between the two cw lasers. We attribute this to the finite bandwidth of the comb feedback system which is around 1 MHz. At Fourier frequencies close to the feedback bandwidth, the feedback system can *increase* the noise of the system instead of decreasing it, leading to “servo bumps” in the noise spectrum. Due to these limitations we decided to investigate the fast phase noise of our laser system with a different method.

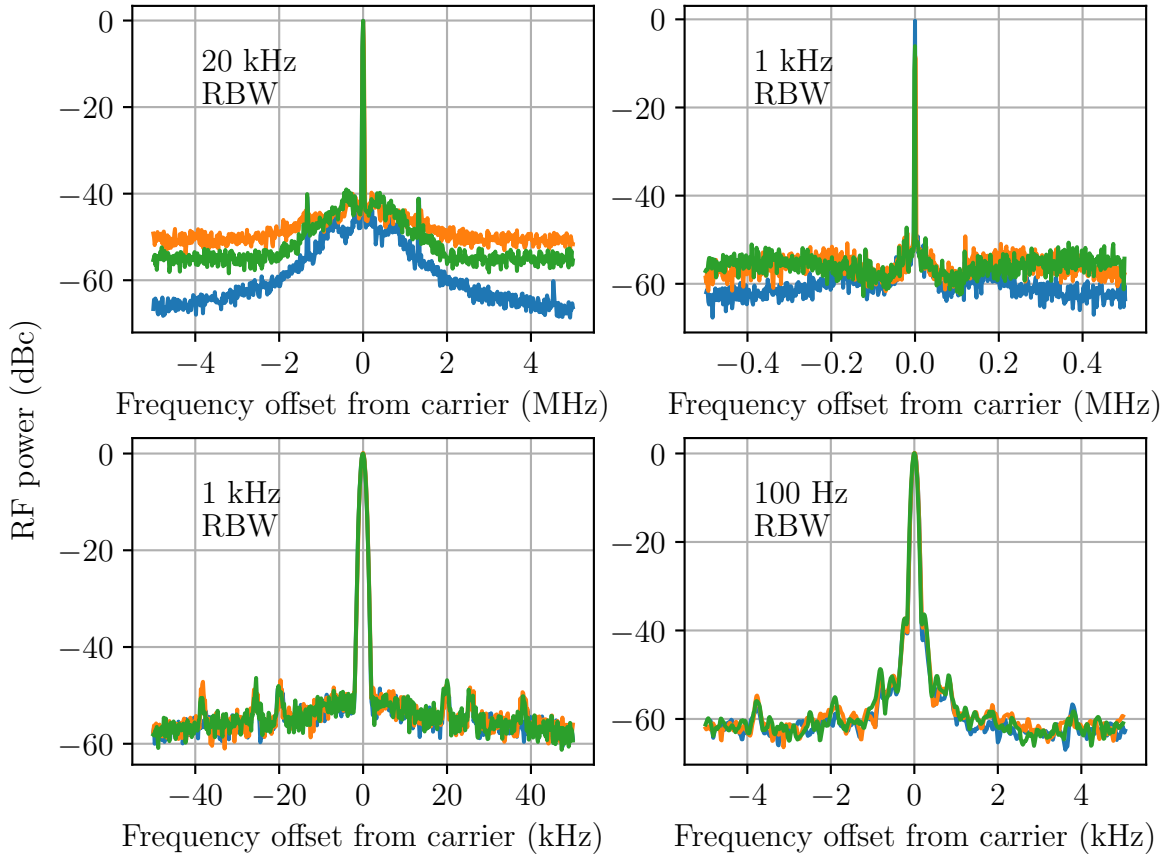


Figure 6.12: Beat notes between the outputs of FP1 and FP2 (blue traces), FP1 and the comb locked to FP2 (orange traces), and FP2 and the comb locked to FP1 (green traces). At low Fourier frequencies, the feedback loop stabilizing the frequency comb faithfully transfers the phase stability. At higher Fourier frequencies, the uncompensated noise of the frequency comb becomes significant.

### 6.2.4 Phase noise characterization

The standard method for a complete phase noise characterization of a laser system is to compare it with a second independent laser system with equal or better noise performance. Information about the phase noise spectrum can also be obtained using a delayed self-heterodyne interferometer with a fiber delay line [199]. Here, we show how the residual



The beat note is analyzed by an RF spectrum analyzer.<sup>17</sup> It is important to note that the envelope detection and logarithmic processing traditionally used in spectrum analyzers lead to systematic errors when measuring noise powers [203]. Many modern spectrum analyzers provide alternative detector options that avoid these issues. We measure the single sideband phase noise  $\mathcal{L}(f)$  using the integrated phase noise measurement function of our spectrum analyzer. In this mode the device automatically selects the correct detector, performs a logarithmic sweep of the frequency offset, and normalizes the measured traces according to the resolution bandwidth and carrier power.

The orange trace in Figure 6.14 shows the resulting phase noise spectrum for Fourier frequencies between 10 kHz and 10 MHz. In this frequency range the phase noise in the light transmitted through the cavity is suppressed by more than an order of magnitude and therefore does not affect the measurement. The phase noise of the laser reaches a maximum value of  $-98$  dBc/Hz at 30 kHz which we attribute to technical noise on the ECDL that is not completely suppressed by the feedback loop. The slight bump at 1.5 MHz is caused by the feedback loop whose phase margin reaches zero at this frequency. The phase noise of the reference oscillator inside the spectrum analyzer and of the signal generator that drives the frequency-shifting AOM (purple trace) contributes to the measured noise levels. It contains some spurious signals, but remains well below the phase noise of the laser in the entire Fourier frequency range. The photodetection noise (red trace) becomes comparable to the phase noise of the laser for Fourier frequencies above 3 MHz which sets the sensitivity limit in our particular setup.

The integrated phase noise starting from 10 MHz is plotted as a dashed orange line. It shows that most of the phase noise contribution comes from the Fourier frequency range between 2 MHz and a few hundred kHz where the limited gain of the feedback loop cannot fully suppress the intrinsic noise of the laser. The total integrated phase noise from 10 MHz to 10 kHz is  $\phi_{\text{rms}} = 10.2$  mrad. Based on our results we expect that if the stability of our laser can be faithfully transferred to the driving frequency comb of the HHG, 89% of the power will remain within 10 kHz around the carrier at the 34th harmonic (see Figure 6.3).

Another method for measuring the noise performance of a laser relative to its reference is to analyze the in-loop error signal of the lock. We use a wideband RF splitter<sup>18</sup> in order to send the same error signal to the loop filter and to a spectrum analyzer while maintaining impedance matching between the components. The spectrum analyzer measures the RF power  $p(f)$  of the signal on its input contained within the chosen resolution bandwidth at frequency  $f$ . The one-sided voltage power spectral density of the signal is obtained by normalizing to a 1 Hz bandwidth and multiplying with the system impedance:

$$S^1(f) = Z_0 p(f)/\text{RBW}, \quad (6.47)$$

where  $Z_0 = 50 \Omega$  is the system impedance, and RBW is the resolution bandwidth of the spectrum analyzer.

<sup>17</sup>Agilent E4440A.

<sup>18</sup>Mini-Circuits ZFRSC-2050+.



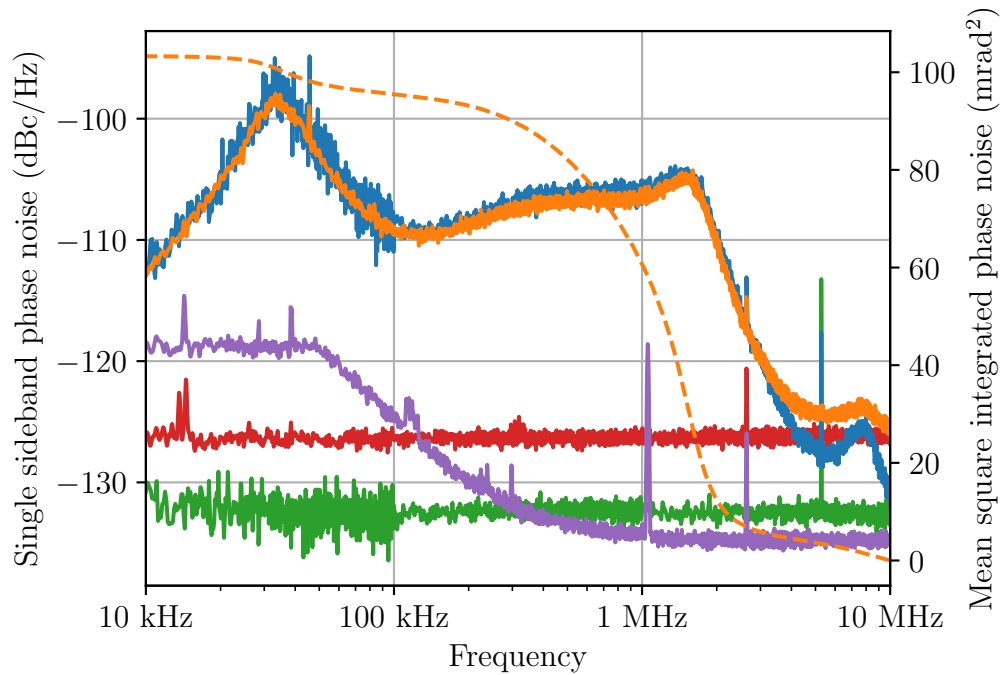


Figure 6.14: Single sideband phase noise  $\mathcal{L}(f)$  between the output of the cavity-stabilized cw laser and its reference cavity measured using the beat note with the cavity transmission (orange trace) and extracted from the in-loop error signal (blue trace). The noise floor originating from the beat note photodetection (red trace) is obtained by repeating the measurement with the cavity transmission light blocked. The phase noise of the reference oscillator inside the spectrum analyzer and of the signal generator that drives the frequency-shifting AOM is measured by directly connecting the signal generator to the spectrum analyzer (purple trace). The dashed orange curve shows the mean square integrated phase noise calculated from the beat note of the laser with the cavity transmission. An upper limit for the noise level of the PDH detection (green trace) is obtained by repeating the measurement with the feedback loop turned off and the laser detuned from the cavity resonance, such that the entire incident power is reflected onto the PDH photodiode. The spurious peak close to 5 MHz is an intermodulation product generated in the PDH detection.

In order to convert voltage fluctuations of the error signal to frequency fluctuations of the laser, the slope of the PDH error signal has to be determined. Since the free-running linewidth of our laser is much broader than the cavity line, we cannot directly observe the slope by sweeping the laser over the resonance. Instead, we lock the laser to the cavity and slowly modulate the setpoint of the loop filter at a frequency of about 100 Hz while recording the light intensity transmitted through the cavity. The drop in power transmitted through the cavity can be easily converted to a frequency offset using the known cavity linewidth [204]. In this way we measure a slope of the PDH error signal at DC of  $k_0 = 2.30 \times 10^{-4}$  V/Hz. At Fourier frequencies above the cavity linewidth, the field stored inside the cavity can no longer follow the fluctuations of the incident field. Therefore, the slope of the PDH discriminator has the frequency-dependent form [205, pp. 66–69]:

$$k(f) = \frac{k_0}{\sqrt{1 + 4 \left( \frac{f}{\Delta f_{\text{FWHM}}} \right)^2}}, \quad (6.48)$$

where  $f$  is the frequency of the signal, and  $\Delta f_{\text{FWHM}}$  is the FWHM linewidth of the cavity.

The phase noise of the laser can be obtained using the transfer function:

$$\mathcal{L}(f) = \frac{1}{2} S_{\phi}^{\text{I}}(f) = \frac{S_{\nu}^{\text{I}}(f)}{2f^2} = \frac{S^{\text{I}}(f)}{2f^2 k^2(f)}, \quad (6.49)$$

where  $S_{\nu}^{\text{I}}(f)$  and  $S_{\phi}^{\text{I}}(f)$  are the one-sided frequency and phase noise power spectral densities.

The result of the in-loop characterization is shown as the blue trace in Figure 6.14. It is in good agreement with the measurement using the cavity transmission. One complication when analyzing the in-loop error signal is that for sufficiently large gain the feedback loop can suppress the error below the error signal detection noise limit, thereby writing the noise onto the system output. In this case the analysis gives an underestimation of the system noise. In our measurement the detection noise limit (green trace) stays below the measured in-loop error signal in the analyzed Fourier frequency range which ensures that the feedback loop does not add significant noise from our detection setup to the laser system.

## 6.3 Stabilized driving laser system

Our HHG setup uses an Yb:KYW mode-locked oscillator as a seed laser. The laser is tightly locked to the cavity-stabilized cw laser which serves as a stable reference. Figure 6.15 shows an overview of the laser system. In the following the different components of the system will be explained.

### 6.3.1 Laser oscillator and amplifiers

The Yb:KYW oscillator was developed in our group and a more detailed description can be found in [206]. It emits 105 fs long pulses with a repetition rate of 40 MHz. The output

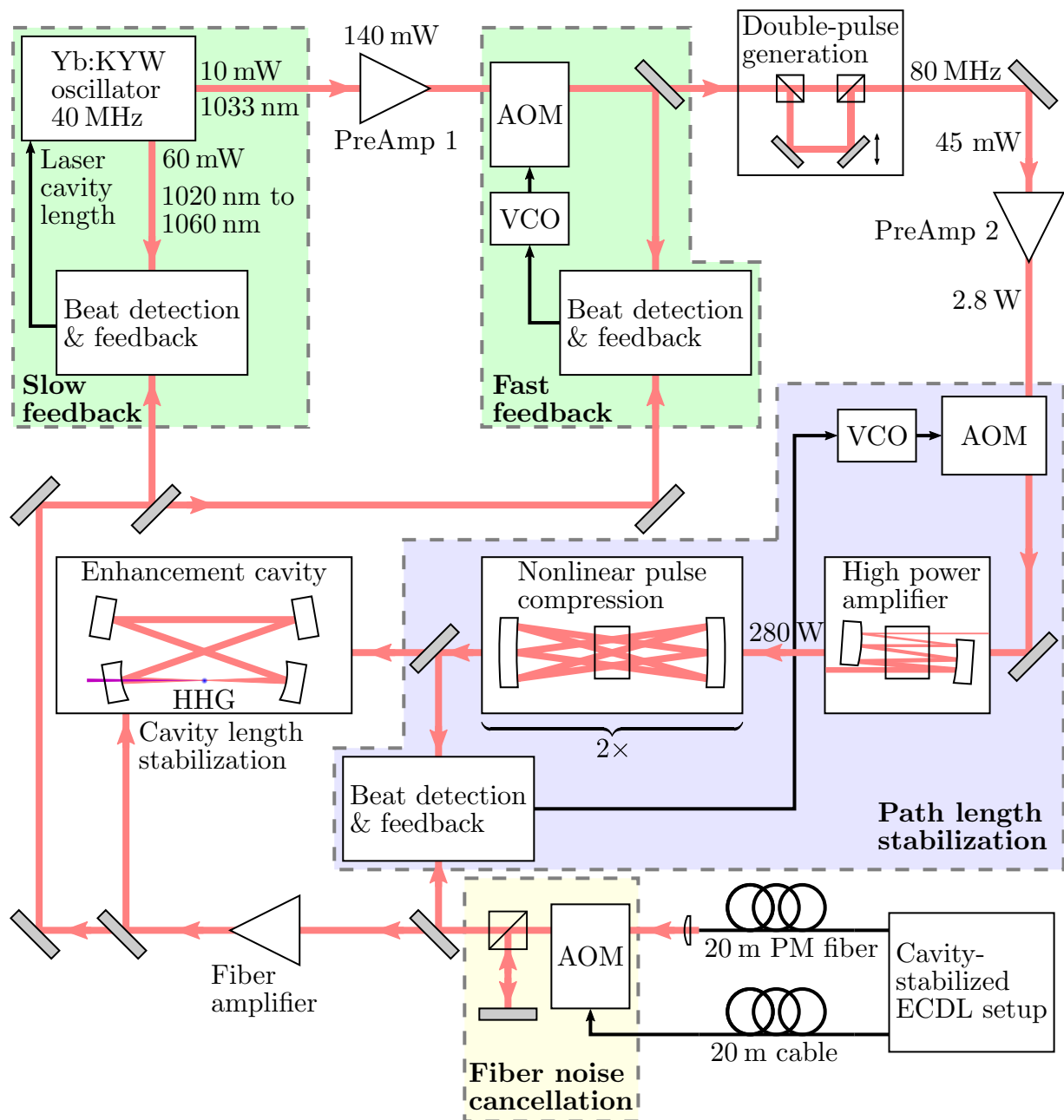


Figure 6.15: Overview of the laser setup for HHG. The output of the Yb:KYW seed laser is amplified in two preamplifiers and a power amplifier. The pulses are compressed in a pair of multi-pass cells before being sent into the enhancement cavity for HHG. The cavity-stabilized cw laser serves as the reference for stabilizing the driving laser frequency, the enhancement cavity length, and the optical path length in the setup. AOM, acousto-optic modulator; VCO, voltage-controlled oscillator; PM fiber, polarization maintaining fiber.

spectrum has a 10 nm FWHM bandwidth and is centered around 1030 nm. This overlaps with 17 times the wavelength of the  $\text{He}^+$  1S-2S two-photon transition. The average output power is 10 mW. The oscillator also has a secondary output with a total power of 60 mW that stems from the reflection from an intracavity filter that is used for shaping the emission spectrum. The spectrum of the secondary output is broad and spans from around 1020 nm to 1060 nm. This light can be used for measuring the carrier-envelope offset frequency in an  $f - 2f$  interferometer [206], and for generating a beat note with light from the cavity-stabilized cw laser. In this way the full power of the primary output remains available for the subsequent stages.

The HHG setup relies on a high power Yb:YAG Innoslab amplifier [33] which can produce an output power of up to 400 W. Since the Yb:KYW oscillator is not powerful enough to directly seed this amplifier, two diode-pumped Yb:LuAG preamplifiers are used to amplify the light first to around 140 mW and then to 2.8 W.

After the high power amplifier, the pulses are temporally compressed from a length of 800 fs to 60 fs in two consecutive compression units that are based on spectral broadening in multi-pass cells [207]. Finally, the light is coupled into an enhancement cavity in which HHG takes place.

### Double-pulse generation

As discussed in chapter 3, counter-propagating XUV frequency comb pulses have to meet at the position of the  $\text{He}^+$  ions for efficient Doppler-free two-photon excitation. This is achieved by back-reflecting the XUV beam (see subsection 4.4.2). However, at 40 MHz repetition rate, the pulse-to-pulse separation is 7.5 m. The back-reflection mirror would therefore have to be placed 3.75 m away from the ion trap, requiring an impractical size of the vacuum chambers. The distance could in principle be reduced by using a higher repetition rate. However, for constant average power this would reduce the pulse energy which has a strong influence on the efficiency of the HHG [208]. Another limiting factor in cavity-enhanced HHG is the accumulation of steady-state plasma in the laser focus which impedes phase matching and can destabilize the lock of the cavity length. This effect also becomes more significant with higher repetition rates [127].

Instead, in our setup a Mach-Zehnder interferometer is inserted into the frequency comb laser beam between the first and the second preamplifier. This turns the frequency comb pulses into pulse pairs that are spaced by the path length difference of 1 m. The double-pulse generation setup was constructed by V. Vaidyanathan and is described in detail in [209]. The pulse pairs travel together through the rest of the setup and are converted to the XUV in the enhancement cavity. The first and second pulse of each pulse pair are then made to collide at the position of the ions by putting the back-reflection mirror 50 cm behind the ion trap (see Figure 4.24). In this way the pulse energy is only halved, whereas increasing the repetition rate to 300 MHz, such that the spacing between *all* consecutive pulses is 1 m, would reduce the pulse energy by a factor of 7.5.

The mode structure of a frequency comb “survives” nonlinear processes, such as HHG, since in steady state each pulse experiences the same nonlinear effects. At first glance, it

might appear that this is no longer the case for our pulse pairs where the first pulse can experience a very different environment compared to the second one (for example due to plasma buildup in the enhancement cavity during the first pulse). However, the system is still in steady state such that *each first pulse* in the train of double pulses experiences the same nonlinearities as *each other first pulse*, and *each second pulse* experiences the same nonlinearities as *each other second pulse*. In other words, the output of the HHG setup contains the pulse trains of *two frequency combs* that share the same beam path and whose pulses are delayed by 1 m from each other. The back-reflection mirror “separates” the two frequency combs and makes them collide at the position of the ions. This also means that the mode spacing remains 40 MHz, even though pulses pass through the system at a rate of 80 MHz.

### 6.3.2 Low-noise beat detection

The ultimate performance limit of the frequency comb stabilization system is determined by how well we can detect the phase fluctuations between the frequency comb and the cavity-stabilized cw laser that serves as the reference. The phase is measured by generating a beat note between the cw laser and the closest mode of the frequency comb.

#### Beat detection setup

Figure 6.16 shows a schematic of the beat detection setup. Three identical setups are used in the stabilization system (see Figure 6.15).

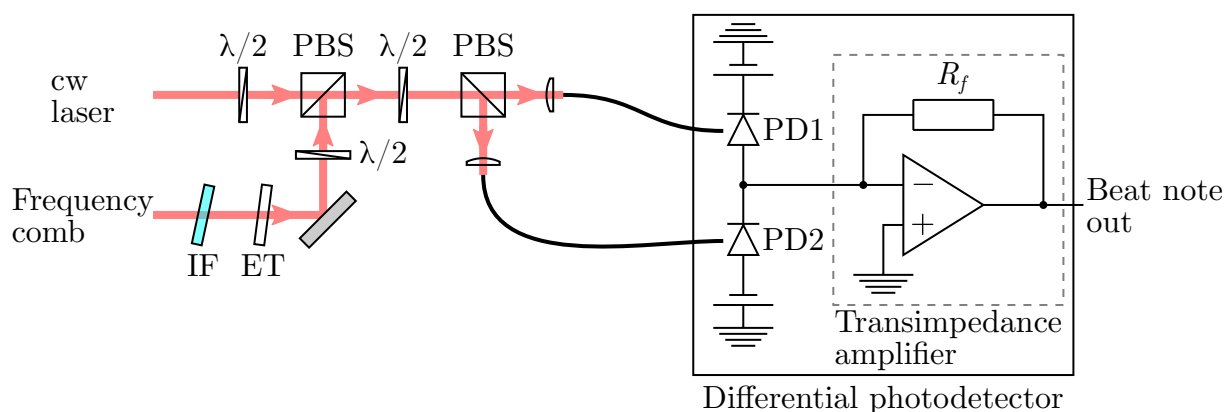


Figure 6.16: Beat detection setup. Single-mode fibers are used to guide the light to the differential photodetector. PBS, polarizing beam splitter; IF, interference filter; ET, etalon; PD, photodiode.

First, the light from the frequency comb is spectrally filtered to reduce the optical power at frequencies that do not contribute to the beat note. In this way the noise contributions from the frequency comb light are minimized. Furthermore, we found that the short optical pulses can saturate the photodiodes and subsequent amplifier at average power levels that

are far below the cw saturation power. Strong spectral filtering is therefore necessary such that the full available power of the frequency comb can be used. The first step is an interference filter<sup>19</sup> which has a specified FWHM bandwidth of 0.4 nm, corresponding to 112 GHz at 1033 nm. The light is then further filtered with an etalon<sup>20</sup> which consists of a 0.5 mm thick fused silica substrate and has a partially reflective coating ( $R = 90\%$ ) on both sides. This results in a free spectral range of 207 GHz and an FWHM linewidth of 6.9 GHz [137, pp. 155–156]. At a pulse repetition rate of 40 MHz, this corresponds to only around 170 comb modes passing through the filters.

The filtered frequency comb light is then overlapped with light from the cw laser on a polarizing beam splitter (PBS). A half-wave plate and another PBS are used to project the two laser beams onto common polarization axes. Both outputs of the PBS are then individually coupled into single-mode fibers which deliver the light to a pair of photodiodes that make up a differential photodetector. This arrangement is called a *balanced heterodyne detector* [202]. As we will show below, it can achieve a significantly higher signal-to-noise ratio compared to using a single photodetector

We begin our analysis by considering the signal and noise generated in a beat detection setup with a single photodetector.<sup>21</sup>

### Photodiode signal

In a photodiode, incident photons whose energy exceeds the band gap can excite electrons into the conduction band. The resulting output current is given by the rate of successfully detected photons times the elementary charge [210, p. 10]:

$$i_{\text{pd}} = \frac{\eta e}{h\nu_0} p_{\text{tot}}, \quad (6.50)$$

where  $\eta$  is the quantum efficiency of the photodiode,  $e$  is the elementary charge,  $h\nu_0$  is the photon energy, and  $p_{\text{tot}}$  is the total incident optical power.

In our beat detection setups, the laser beams are overlapped in single-mode optical fibers to ensure essentially perfect spatial mode matching. The electric fields therefore maximally interfere, and the total optical power at the detector is given by

$$p_{\text{tot}} = \left| \sqrt{p_{\text{cw}}} e^{i\omega_{\text{cw}}t} + \sum_n \sqrt{p_n} e^{i[\omega_n t + \Delta\varphi_n(t)]} \right|^2, \quad (6.51)$$

where  $p_{\text{cw}}$  and  $p_n$  are the power of the cw laser and of the  $n$ th comb mode, respectively,  $\omega_{\text{cw}}$  is the frequency of the cw laser,  $\omega_n = 2\pi(nf_{\text{rep}} + f_{\text{ceo}})$  is the frequency of the  $n$ th comb mode, and  $\Delta\varphi_n(t)$  are the phase fluctuations between the  $n$ th comb mode and the

<sup>19</sup>Layertec 157313.

<sup>20</sup>LightMachinery OP-6204-M.

<sup>21</sup>This corresponds to the setup from Figure 6.16 where one of the two photodiodes is taken out.

cw laser. Inserting Equation 6.51 into Equation 6.50 leads to

$$i_{\text{pd}} = \frac{\eta e}{h\nu_0} \left\{ p_{\text{cw}} + \sum_n p_n + 2 \sum_{n>m} \sqrt{p_n p_m} \cos[2\pi(n-m)f_{\text{rep}}t] + 2 \sum_n \sqrt{p_{\text{cw}} p_n} \cos[(\omega_n - \omega_{\text{cw}})t + \Delta\varphi_n(t)] \right\}. \quad (6.52)$$

The first and second term of Equation 6.52 give the DC photocurrent which is determined by the time-averaged total optical power that impinges on the photodiode:

$$i_{\text{dc}} = \frac{\eta e}{h\nu_0} (p_{\text{cw}} + p_{\text{comb}}), \quad (6.53)$$

where  $p_{\text{comb}} = \sum_n p_n$ .

As we will discuss below, the fluctuations of this current are an important noise source in any photodetector. The third term consists of frequency components at multiples of the comb repetition rate  $f_{\text{rep}}$ . This reflects the regular current bursts that are created by the frequency comb pulses striking the detector. The last term contains the beat notes between the cw laser and the comb modes. Electronic filters are used to select only the lowest frequency component. The signal current then is

$$i_{\text{sig}} = 2 \frac{\eta e}{h\nu_0} \sqrt{p_{\text{cw}} p_k} \cos[(\omega_k - \omega_{\text{cw}})t + \Delta\varphi_k(t)], \quad (6.54)$$

where the  $k$  is the index of the comb mode that is closest to the cw laser frequency. Since the power contained in a single comb mode is usually quite low, the signal current is often small compared to typical input noise levels of RF amplifiers or spectrum analyzers. A transimpedance amplifier is therefore used to convert the current signal into a voltage

$$U_{\text{sig}} = R_f i_{\text{sig}}, \quad (6.55)$$

where  $R_f$  is the gain of the amplifier which is measured in  $\Omega$ . A transimpedance amplifier can be constructed from a fast operational amplifier and a feedback resistor<sup>22</sup> as shown schematically in Figure 6.16. The level of the resulting signal is quantified by the average power it dissipates in a load that matches the characteristic impedance  $Z_0 = 50 \Omega$ :

$$p_{\text{sig}} = \frac{\langle U_{\text{sig}}^2 \rangle}{Z_0} = \frac{R_f^2}{Z_0} \langle i_{\text{sig}}^2 \rangle, \quad (6.56)$$

where  $\langle \rangle$  signifies temporal averaging. We insert Equation 6.54 and obtain

$$p_{\text{sig}} = 2 \frac{R_f^2}{Z_0} \left( \frac{\eta e}{h\nu_0} \right)^2 p_{\text{cw}} p_k. \quad (6.57)$$

<sup>22</sup>Transimpedance amplifiers are often constructed with a  $50 \Omega$  output impedance in order to match the characteristic impedance of standard coaxial cables. This forms a voltage divider with the  $50 \Omega$  input impedance of an RF amplifier or spectrum analyzer. The transimpedance gain is then equal to half the value of the feedback resistor.

### Detection noise

One consequence of the quantization of electric charge is that measuring a current is equivalent to counting the number of electrons per unit time. Since the arrival of the individual electrons is uncorrelated,<sup>23</sup> their number follows a Poisson distribution. The fluctuating electron number leads to a mean square noise current [210, pp. 12–13][211, p. 42]:

$$\langle i_{\text{sn}}^2 \rangle = 2ei_{\text{avg}}B, \quad (6.58)$$

where  $i_{\text{avg}}$  is the average current, and  $B$  is the detection bandwidth.<sup>24</sup> This contribution is called the *shot noise*. In the beat detection setup, the average current is given by Equation 6.53.<sup>25</sup> The transimpedance amplifier converts the shot noise current into a voltage such that the detected noise power is

$$p_{\text{sn}} = \frac{R_f^2}{Z_0} \langle i_{\text{sn}}^2 \rangle = 2 \frac{R_f^2}{Z_0} \frac{\eta e^2}{h\nu_0} (p_{\text{cw}} + p_{\text{comb}}) B. \quad (6.59)$$

In addition to the shot noise, technical fluctuations of the laser output power can lead to noise in the photocurrent. These fluctuations are often quantified as a *relative intensity noise* (RIN) spectrum which is defined as the normalized one-sided spectral density of the output power fluctuations  $\delta p$  [27, p. 56]:

$$\text{RIN}(f) = \frac{S_{\delta p}^1(f)}{p_{\text{out}}^2}, \quad (6.60)$$

where  $p_{\text{out}}$  is the mean output power of the laser. It is measured on a logarithmic scale in dBc/Hz. The resulting mean square intensity noise current is

$$\langle i_{\text{in}}^2 \rangle = \left( \frac{\eta e}{h\nu_0} \right)^2 [p_{\text{cw}}^2 \text{RIN}_{\text{cw}}(f) + p_{\text{comb}}^2 \text{RIN}_{\text{comb}}(f)] B, \quad (6.61)$$

where  $f$  is the Fourier frequency at which the noise is detected, and we assume that the RIN of the lasers does not change significantly within the detection bandwidth. The noise power is

$$p_{\text{in}} = \frac{R_f^2}{Z_0} \langle i_{\text{in}}^2 \rangle = \frac{R_f^2}{Z_0} \left( \frac{\eta e}{h\nu_0} \right)^2 [p_{\text{cw}}^2 \text{RIN}_{\text{cw}}(f) + p_{\text{comb}}^2 \text{RIN}_{\text{comb}}(f)] B. \quad (6.62)$$

Furthermore, any real photodetector produces technical noise at its output. A fundamental limit is set by thermal fluctuations of the charge carriers in the feedback resistor. These lead to a mean square noise current which is given by the Nyquist formula [211, p. 42]:

$$\langle i_{\text{ny}}^2 \rangle = \frac{4k_B T_R}{R_f} B, \quad (6.63)$$

<sup>23</sup>This is only strictly true if the light can be described as a coherent state, such as the output of a laser oscillator. The light emitted by “quantum light sources”, such as single atoms or light bulbs, can generate correlated (or anticorrelated) photoelectrons.

<sup>24</sup>If the signal is viewed on a spectrum analyzer, this is given by the selected resolution bandwidth.

<sup>25</sup>In principle the dark current of the photodiode also contributes to the shot noise. However, this contribution is negligible for detectors that operate in the near infrared.



where  $k_B$  is the Boltzmann constant, and  $T_R$  is the temperature of the resistor. The resulting noise power is

$$p_{\text{ny}} = \frac{R_f^2}{Z_0} \langle i_n^2 \rangle = \frac{4k_B T_R R_f}{Z_0} B. \quad (6.64)$$

Other technical noise sources include the input voltage and current noise of the operational amplifier. The total output noise of commercial amplified photodetectors, which includes the contribution of Nyquist noise, is often specified somewhat confusingly as a “minimum noise equivalent power” (NEP) which is measured in  $\text{W}/\sqrt{\text{Hz}}$ . This simply means that the detector produces an RF noise power<sup>26</sup>

$$p_{\text{det}} = \frac{R_f^2}{Z_0} \left( \frac{\eta_{\text{max}} e}{h\nu_{\text{max}}} \right)^2 \text{NEP}^2 B, \quad (6.65)$$

where  $\nu_{\text{max}}$  is the frequency where the quantum efficiency of the detector has its maximum value  $\eta_{\text{max}}$ .

The signal-to-noise ratio (SNR) is given by the ratio between the signal power and the sum of all noise powers:

$$\begin{aligned} \frac{S}{N} &= \frac{p_{\text{sig}}}{p_{\text{sn}} + p_{\text{in}} + p_{\text{det}}} \\ &= \frac{2 \left( \frac{\eta e}{h\nu_0} \right)^2 p_{\text{cw}} p_k}{\left\{ 2 \frac{\eta e^2}{h\nu_0} (p_{\text{cw}} + p_{\text{comb}}) + \left( \frac{\eta e}{h\nu_0} \right)^2 [p_{\text{cw}}^2 \text{RIN}_{\text{cw}}(f) + p_{\text{comb}}^2 \text{RIN}_{\text{comb}}(f)] + \left( \frac{\eta_{\text{max}} e}{h\nu_{\text{max}}} \right)^2 \text{NEP}^2 \right\} B}. \end{aligned} \quad (6.66)$$

The detection bandwidth  $B$  is assumed to be larger than the signal bandwidth, but smaller than the bandwidth of the various noise sources. The SNR is therefore inversely proportional to  $B$ . It takes its maximum value if the noise is dominated by the shot noise term due to the cw laser, i.e.

$$2 \frac{\eta e^2}{h\nu_0} p_{\text{cw}} \gg \left( \frac{\eta e}{h\nu_0} \right)^2 [p_{\text{cw}}^2 \text{RIN}_{\text{cw}}(f) + p_{\text{comb}}^2 \text{RIN}_{\text{comb}}(f)] + \left( \frac{\eta_{\text{max}} e}{h\nu_{\text{max}}} \right)^2 \text{NEP}^2, \quad (6.67)$$

and

$$p_{\text{cw}} \gg p_{\text{comb}}. \quad (6.68)$$

In this case, the detection is called *shot noise limited*,<sup>27</sup> and the SNR can be approximated by [213]

$$\left( \frac{S}{N} \right)_{\text{sn}} \approx \frac{\eta p_k}{h\nu_0 B}. \quad (6.69)$$

<sup>26</sup>The frequency dependence of the noise power spectral density is usually neglected here.

<sup>27</sup>This limit can in principle be exceeded by making use of multiple beat notes between the different modes of a frequency comb and a cw laser [212]. However, the technique adds experimental complexity and requires the use of very fast photodetectors.

Remarkably, the SNR only depends on the number of detected photons per time interval  $1/B$  from the comb mode that produces the beat signal with the cw laser. The design goal of the beat detection system is therefore to achieve shot noise limited detection while minimizing the amount of light that is lost from the frequency comb mode.

### Balanced heterodyne detection

Since the phase of an optical wave jumps by  $180^\circ$  upon reflection from an optically denser medium, the beat note signals generated in the two photodiodes of the differential photodetector are out of phase relative to each other. The photodiodes are arranged in series such that the difference of the two photocurrents enters the transimpedance amplifier. The resulting signal is therefore the sum of the beat note signals from the individual diodes, while common-mode signals, such as amplitude fluctuations of the laser light, are cancelled. The common-mode suppression of the balanced heterodyne detector can be optimized by adjusting the angle of the half-wave plate before the PBS [202]. The shot noise generated in the two photodiodes is uncorrelated and can therefore not be reduced by subtracting the currents [202]. Compared to using only one photodiode, the balanced heterodyne detector generates twice the shot noise power, while the signal power is quadrupled. If the detection is only limited by shot noise, it can therefore increase the SNR by up to a factor of 2 [9]. In practice, lasers often have technical amplitude noise far above the shot noise level such that the SNR gain can be much higher. Furthermore, the subtraction of the two photocurrents allows us to send more light onto the photodiodes before the transimpedance amplifier is saturated.

We use home-built differential photodetectors which contain two fiber-coupled InGaAs photodiodes<sup>28</sup> with a specified quantum efficiency of 76 % at 1033 nm. The transimpedance amplifier consists of a fast operational amplifier<sup>29</sup> and a  $12\text{ k}\Omega$  feedback resistor. The output is impedance matched to a coaxial cable using a  $50\ \Omega$  series resistor such that the transimpedance gain is  $6\text{ k}\Omega$ . We also tested two different commercial differential photodetectors with similar specifications<sup>30</sup> and achieved very similar performance.

### Beat note results

Figure 6.17 shows a beat note between light from the cw laser and one mode of the Yb:KYW oscillator (blue trace). The noise level due to amplitude noise of the cw laser light is measured by blocking the frequency comb light (orange trace). The noise due to the comb light alone is below the detector noise level (green trace). The resulting SNR is 60 dB in 100 kHz bandwidth. This corresponds to a phase noise detection limit of  $-110\text{ dBc/Hz}$  (see section 6.1.1). In total, 1.1 mW of cw laser light and  $26\ \mu\text{W}$  of frequency comb light are sent onto the detectors, corresponding to roughly 150 nW per mode. The shot noise limited SNR given by Equation 6.69 is then 68 dB in 100 kHz bandwidth. Our setup does

<sup>28</sup>Thorlabs FGA01FC.

<sup>29</sup>Texas Instruments OPA847.

<sup>30</sup>Wieserlabs WL-BPD220MA and Thorlabs PDB450C.

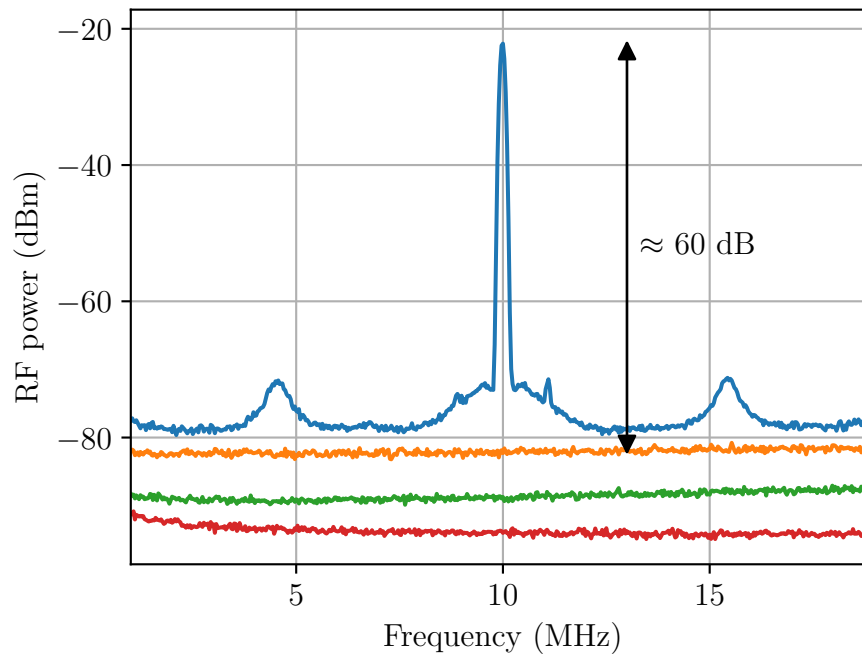


Figure 6.17: Beat note between light from the cw laser and one mode of the Yb:KYW oscillator generated by the beat detection setup (blue trace). The resolution bandwidth is 100 kHz. The orange trace is the noise floor due to the cw laser light. The green and red traces are the noise levels of the photodetector and the RF spectrum analyzer, respectively.

not quite reach this limit which indicates that the amplitude noise of the cw laser is not fully cancelled in the balanced heterodyne detection. Another explanation is that the actual comb mode power might be somewhat lower than our rough estimate. Nonetheless, the noise level stays below the beat note signal in the entire frequency range. The beat note contains prominent peaks at 5.5 MHz from the carrier. We attribute them to the Yb:KYW oscillator since they are not present in the cw laser spectrum (see subsection 6.2.4).

### 6.3.3 Frequency stabilization

Light from the cavity-stabilized cw laser setup is delivered from a neighboring lab to the driving laser system via a 20 m long polarization maintaining fiber. Optical path length fluctuations of the fiber are compensated using active fiber noise cancellation (see section 6.2.2). The light is used as a reference for stabilizing the driving laser frequency, the length of the enhancement cavity, and the optical beam path. The available power of around 5 mW is insufficient for these tasks such that an Yb-doped fiber amplifier is used to amplify it to 100 mW.

The basic concept for the stabilization is illustrated in Figure 6.18. Feedback is applied to the driving laser such that the  $k$ th comb mode is tightly phase locked to the cw laser.

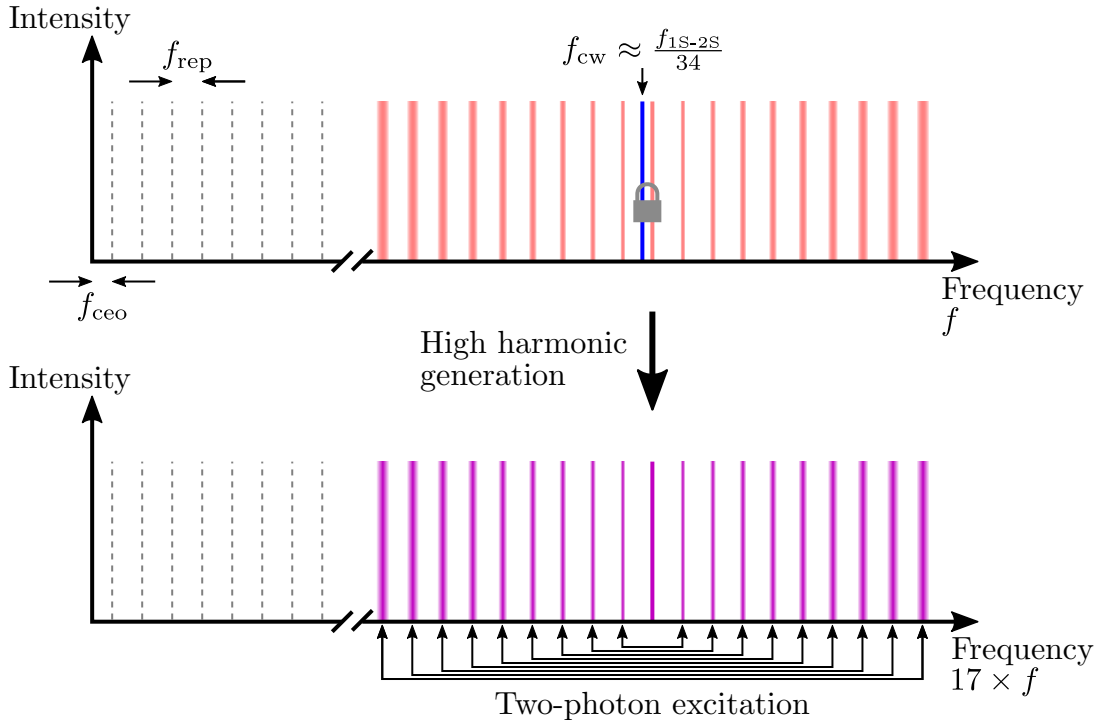


Figure 6.18: Illustration of the stabilization principle. One comb mode is tightly locked to the cavity-stabilized cw laser, making it the fixed point of the comb. According to the elastic tape model, the comb mode frequencies expand or contract symmetrically about the fixed point. The cw laser frequency  $f_{cw}$  is tuned close to the 34th sub-harmonic of the  $\text{He}^+$  1S-2S transition frequency  $f_{1S-2S}$ . The residual frequency fluctuations drop out in the two-photon excitation.

Its frequency is then given by

$$f_k = f_{cw} + f_{\text{beat}}, \quad (6.70)$$

where  $f_{cw}$  is the frequency of the cw laser, and  $f_{\text{beat}}$  is the frequency of the beat note which is determined by the feedback electronics. The frequencies are chosen such that

$$f_k = \frac{f_{1S-2S}}{34}, \quad (6.71)$$

where  $f_{1S-2S}$  is the  $\text{He}^+$  1S-2S transition frequency. The 17th harmonic of the frequency comb can therefore drive the transition. The frequency of the  $n$ th comb mode is

$$f_n = n f_{\text{rep}} + f_{\text{ceo}} = f_k + (n - k) f_{\text{rep}}, \quad (6.72)$$

where  $f_{\text{rep}}$  is the pulse repetition rate, and  $f_{\text{ceo}}$  is the carrier-envelope offset frequency. The two-photon transition is driven by mode pairs  $f_{k+m}$  and  $f_{k-m}$  whose photon energies add up to the transition energy (see subsection 3.2.1). The sum frequency can be expressed using Equation 6.72:

$$f_{k+m} + f_{k-m} = 2f_k. \quad (6.73)$$

This behavior can be understood using the elastic tape model of the frequency comb (see section 3.1). Even though the frequencies of the individual comb modes with mode numbers  $n \neq k$  are not actively stabilized, their fluctuations are symmetric with respect to the fixed point at frequency  $f_k$ . The fluctuations are then cancelled by the symmetry of the two-photon excitation. It is therefore not necessary to fully stabilize the frequency comb by giving feedback to the carrier-envelope offset frequency.

In order to ultimately determine the  $\text{He}^+$  1S-2S transition frequency, the frequency  $f_k$  has to be measured (see Equation 6.71). This can be done by measuring  $f_{\text{cw}}$  with a second frequency comb as described in subsection 6.2.3, and using Equation 6.70. Alternatively, the repetition rate  $f_{\text{rep}}$  and the carrier-envelope offset frequency  $f_{\text{ceo}}$  of the Yb:KYW oscillator can be measured with a photodiode and with a home-built  $f-2f$  interferometer [206], respectively. The frequency  $f_k$  can then be calculated using Equation 6.72.

A schematic of the frequency stabilization setup is shown in Figure 6.19. It consists of two consecutive stages with different feedback bandwidths.

### Slow feedback

The purpose of the first stage is to pre-stabilize the frequency of the comb mode. A beat note between the comb mode and the cw laser is created with the first beat detection setup. The secondary output from the Yb:KYW oscillator is used such that no power is lost from the main output. The signal is low-pass filtered to isolate a single beat note. A digital phase and frequency detector<sup>31</sup> (PFD) measures the phase difference between the beat note signal and a 10 MHz reference generated by an RF synthesizer. The PFD outputs a stream of pulses that are triggered by the zero crossings of the input signals. The digital logic is arranged such that the averaged output level is proportional to the phase difference between its input signals as long as the difference stays within  $\pm\pi$ . Once the phase difference exceeds this range, the device switches into a different mode where the averaged output level is proportional to the *frequency difference* between the input signals. This allows the feedback loop to reliably acquire the lock even if the beat frequency is far away from the reference frequency. The output of the PFD is low-pass filtered to “smooth out” the pulsed signal produced by the digital circuit. A home-built loop filter then gives feedback to the cavity length of the Yb:KYW oscillator using one of the end mirrors which is glued to a piezoelectric actuator. In this way a feedback bandwidth of a few kHz is reached. The actuator has only a relatively small range and cannot compensate larger drifts of the cavity length. The output of the loop filter is therefore used as the error signal for a second loop filter which controls a piezoelectric stage<sup>32</sup> that moves the other end mirror of the laser cavity. This stage has a very large range of 600  $\mu\text{m}$ , but the bandwidth is only a few Hz. In this way the piezoelectric actuator is always kept in the center of its travel range.

---

<sup>31</sup>onsemi MC100EP140.

<sup>32</sup>PI P-625.

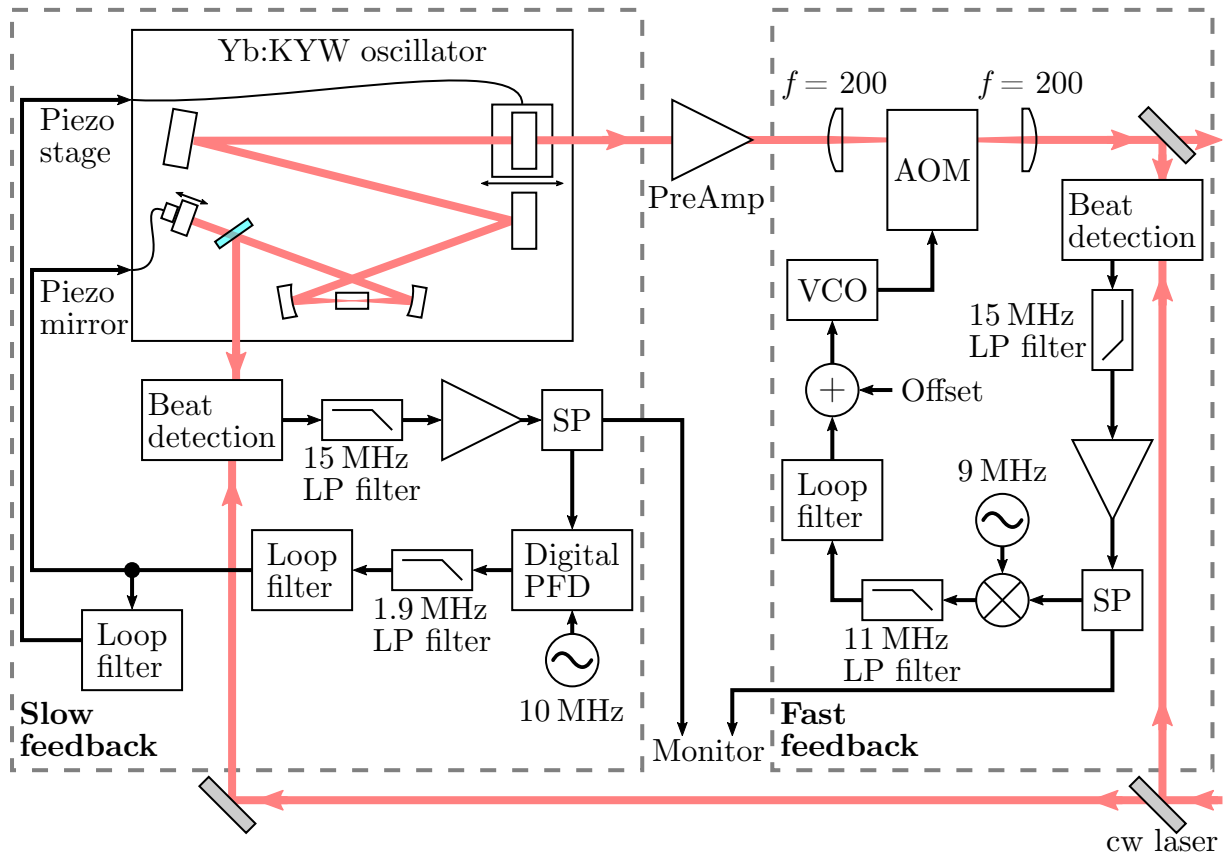


Figure 6.19: Driving laser frequency stabilization setup. This is a more detailed view of the two green boxes in Figure 6.15. The beam path inside the Yb:KYW oscillator is simplified and in reality contains more folding mirrors (see [206] for details). Two feedback loops are used to tightly lock one mode of the frequency comb to the cw laser. LP filter, low-pass filter; SP, RF splitter; PFD, phase-frequency detector; VCO, voltage-controlled oscillator; AOM, acousto-optic modulator. Focal lengths are given in mm.

### Fast feedback

While the slow feedback loop is able to keep the comb mode phase locked to the cw laser, the actuators are not fast enough to fully suppress the phase noise of the Yb:KYW oscillator (see the orange trace in Figure 6.21). A common technique for achieving higher feedback bandwidths in mode-locked oscillators is to modulate the pump power. However, the relatively long upper state lifetime of Yb:KYW limits the achievable bandwidth to a few tens of kHz [214]. A feedback bandwidth of 700 kHz has been achieved in a solid-state frequency comb by using an intra-cavity electro-optic modulator (EOM) [215]. However, adding an EOM to the laser cavity introduces additional dispersion and losses. The dispersion has to be compensated in order to achieve mode-locked operation, while the losses reduce the achievable output power [215]. We therefore decided to use an external acousto-optic modulator (AOM) as a fast actuator for adjusting the laser frequency [216].

The setup is shown schematically on the right of Figure 6.19. The output of the Yb:KYW oscillator is first amplified to around 100 mW. It then passes through the AOM<sup>33</sup> which is driven by a voltage-controlled oscillator<sup>34</sup> (VCO). The VCO was chosen for its relatively small tuning port capacitance of 82 pF which allows fast tuning of the output frequency. A beat note between one comb mode and the cw laser is then generated using a second beat detection setup. In this way a failure of the fast feedback loop does not affect the slow one. The beat note signal is isolated with a low-pass filter and is amplified. Acquiring the phase lock does not require a large phase range since the frequency is pre-stabilized by the slow feedback loop. An analog RF mixer is therefore used to detect the phase difference relative to a reference signal at 9 MHz. The feedback loop is closed by a fast analog loop filter<sup>35</sup> which acts on the tuning port of the VCO. One challenge is that the tuning range of the VCO is much larger than that of the AOM. Furthermore, the AOM is used in single-pass such that the angle of the output depends on the driving frequency. A failure of the feedback loop could therefore “turn off” the laser beam if the VCO frequency is changed too much. This might lead to damages in the laser amplifiers. The output range of the loop filter is therefore limited such that it can only change the VCO frequency by a few hundred kHz. The center frequency is adjusted by adding an offset voltage to the loop filter output using an operational amplifier.

The bandwidth of a feedback loop is ultimately limited by the total time delay of the signal propagating in the loop. An AOM consists of a transparent glass or crystal in which a travelling acoustic wave is generated by a piezoelectric transducer. The frequency of a laser beam passing through the material is shifted by the interaction with the periodic density modulation caused by the acoustic wave. The acoustic wave travels at the speed of sound in the AOM material which is around five orders of magnitude slower than the propagation of electrical signals in coaxial cables. Minimizing the distance between the laser beam and the AOM transducer is therefore crucial for achieving a large feedback

---

<sup>33</sup>AA MT110-B50A1-1064.

<sup>34</sup>Pasternack PE1V31008.

<sup>35</sup>Vescent Photonics D2-125 Laser Servo.

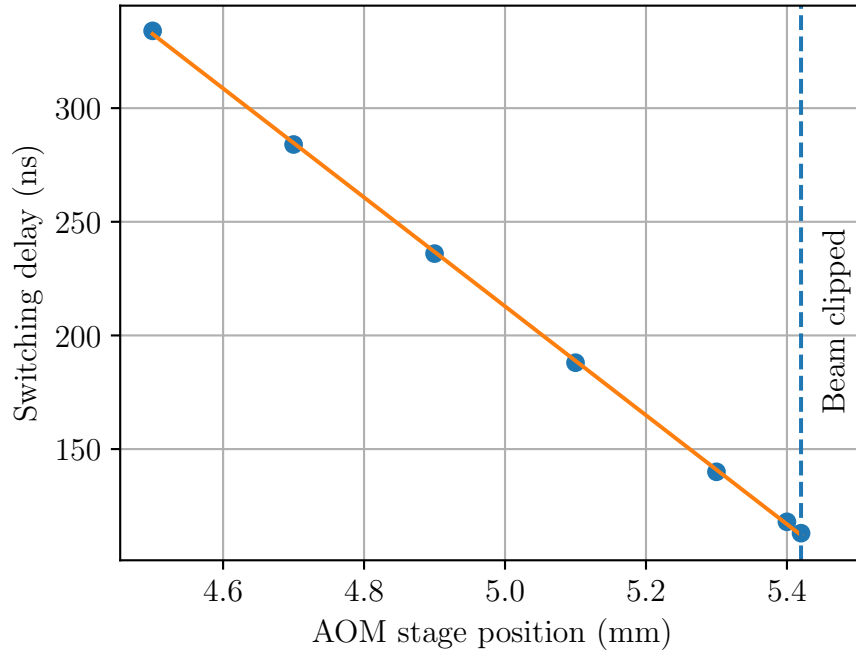


Figure 6.20: Measurement of the time delay in the AOM due to the finite speed of the acoustic wave (blue circles). The AOM drive signal was turned off with a fast RF switch, and the time delay until the diffracted power started dropping was measured with a fast photodiode. The orange line is a linear fit to the data which gives a speed of sound of 4.2 km/s, in agreement with the data sheet value for the  $\text{TeO}_2$  AOM crystal.

bandwidth.<sup>36</sup> The laser beam is loosely focused through the AOM with an  $f = 200$  mm lens to reduce the beam size. The AOM is placed on a linear stage such that the position perpendicular to the laser beam can be adjusted. As shown in Figure 6.20, a minimum delay of around 110 ns can be achieved before the beam is being clipped by the transducer. The resulting feedback bandwidth is around 600 kHz.

The residual in-loop phase noise achieved by the feedback systems is shown in Figure 6.21. The phase noise is extracted from the beat note signal using an RF spectrum analyzer<sup>37</sup> as described in subsection 6.2.4. The mean square integrated phase noise from 10 Hz to 10 MHz is  $1260 \text{ mrad}^2$ , corresponding to an rms phase noise of 35.5 mrad. Without further noise suppression, this level of phase noise would already lead to a drop of the carrier power at the 34th harmonic by a factor of four (see Figure 6.3). The dashed curve in Figure 6.21 shows that most of the phase noise is contributed by spectral components with Fourier frequencies above 1 MHz which is beyond the feedback bandwidth. In this frequency range the phase noise level is close to the noise floor such that an accurate measurement is difficult.

<sup>36</sup>In some AOMs this is only possible by modifying the casing.

<sup>37</sup>Agilent E4445A.



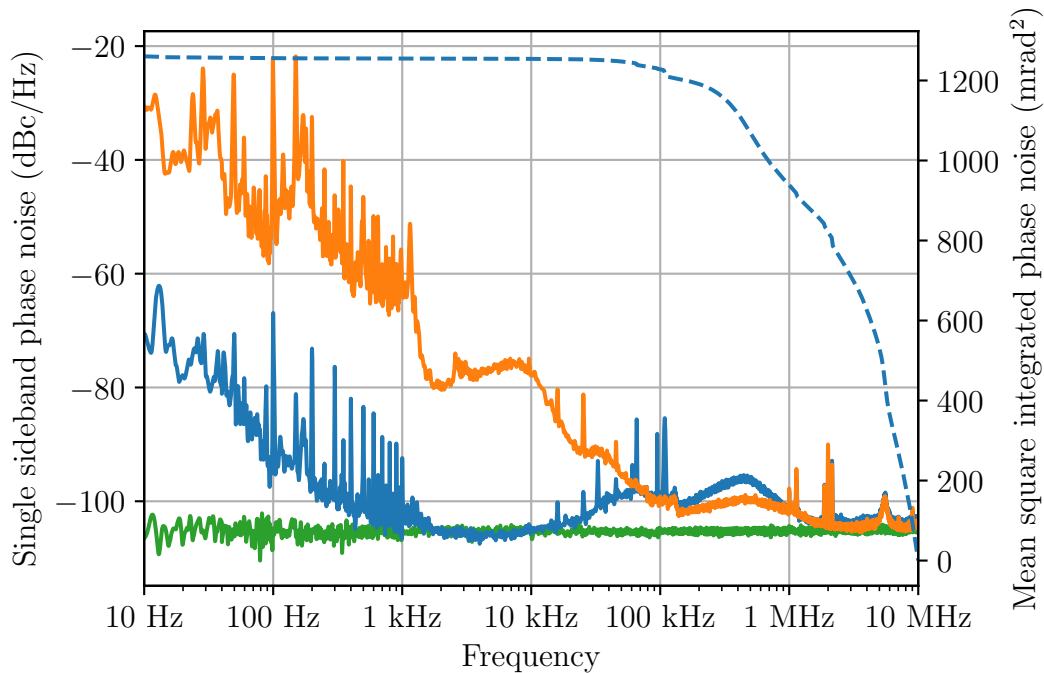


Figure 6.21: Single sideband phase noise of the beat note between the cw laser and one mode of the Yb:KYW oscillator. The signal is recorded at the output of the second beat detection setup which is also used for the fast feedback. The phase can be stabilized using the slow piezoelectric actuators only (orange trace), but much better noise suppression is achieved by adding the fast AOM feedback (blue trace). The detection noise floor is due to amplitude noise of the cw laser (green trace). The dashed blue curve shows the mean square integrated phase noise calculated from the blue trace.

### Phase noise filtering in the enhancement cavity

As shown in Figure 6.15, the HHG takes place in an enhancement cavity. While its main purpose is to increase the light intensity, the cavity also filters out phase noise that falls outside the linewidth of the resonances. The design of the cavity has not yet been finalized, but measurements on a preliminary version give a finesse of around 190. The free spectral range is 40 MHz to match the comb repetition rate. This results in an FWHM linewidth of 211 kHz. By averaging over fast phase fluctuations, the cavity acts as a low-pass filter with a slope of  $-20$  dB/decade for Fourier frequencies above the HWHM linewidth (see subsection 6.2.4). Figure 6.22 shows the expected filtering effect by the cavity. The mean square integrated phase noise of the signal from 10 Hz to 10 MHz is  $55.5 \text{ mrad}^2$ , corresponding to an rms phase noise of  $7.4 \text{ mrad}$ . This is well below the carrier collapse threshold for generating the 34th harmonic (see Figure 6.3).

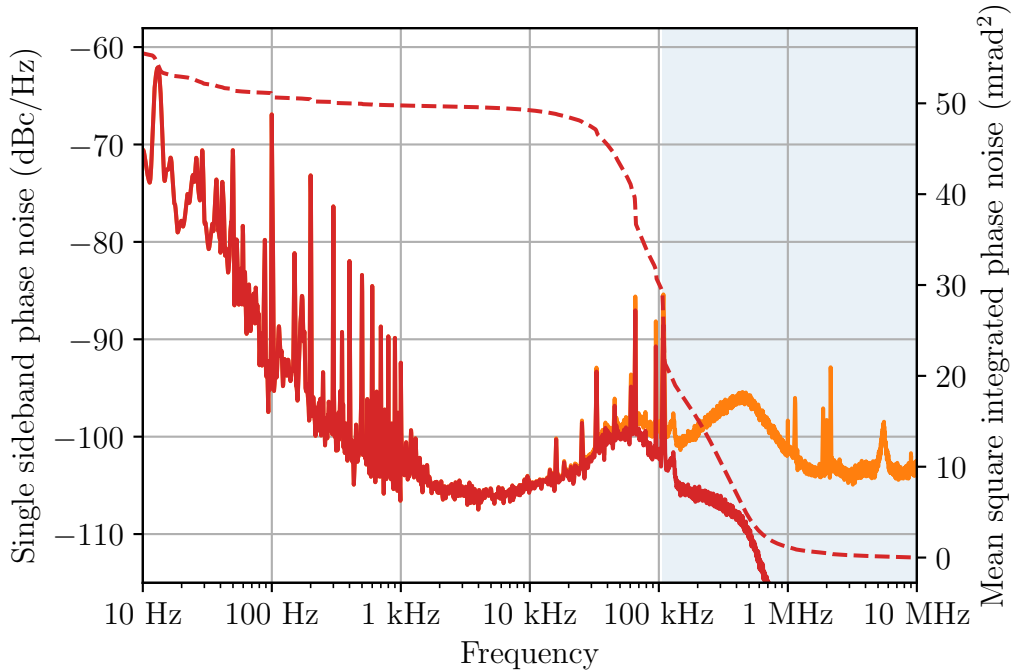


Figure 6.22: Expected phase noise filtering by the enhancement cavity. The orange trace is the measured phase noise as shown in Figure 6.21. The red trace shows the expected phase noise of the light circulating in an enhancement cavity with a 106 kHz HWHM linewidth. The frequency range above the HWHM linewidth is shown in light blue. The dashed red curve shows the mean square integrated phase noise calculated from the red trace.

### 6.3.4 Path length stabilization

The frequency stabilization setup tightly locks the phase of one frequency comb mode to that of the cavity-stabilized cw laser at the position of the second beat detection. However, the frequency comb laser beam then travels through several more components before being coupled into the enhancement cavity for HHG (see Figure 6.15). These components include the second preamplifier, the high power amplifier, and the multi-pass cells for nonlinear pulse compression. The high average power levels of up to 400 W lead to significant heating of the components and of the air in the beam path. An active beam pointing stabilization system<sup>38</sup> is used to compensate for the resulting thermal alignment drifts and fast pointing fluctuations. These thermal effects, as well as mechanical vibrations of the mirrors, also lead to fluctuations in the optical path length which introduce additional phase noise. Path length fluctuations have been observed to significantly broaden the linewidth of XUV frequency combs generated in similar setups [188].

We have therefore implemented an active path length stabilization system that is shown schematically in Figure 6.23. A small part of the frequency comb light is split off close

<sup>38</sup>TEM Messtechnik Aligna.

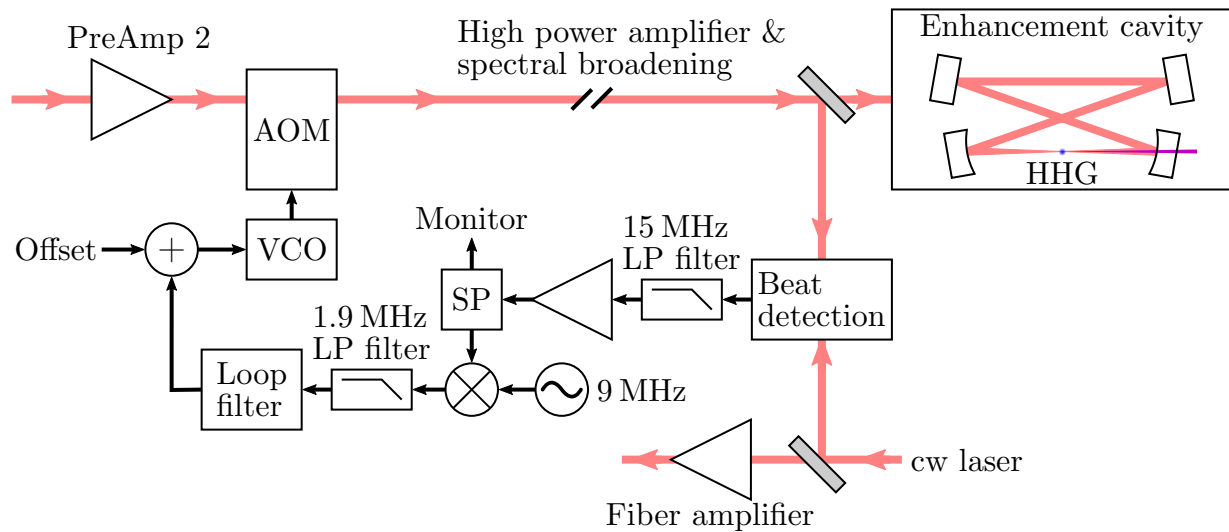


Figure 6.23: Path length stabilization setup. This is a more detailed view of the light blue box in Figure 6.15. The beat detection is placed close to the enhancement cavity such that most fluctuations can be compensated. LP filter, low-pass filter; SP, RF splitter; VCO, voltage-controlled oscillator; AOM, acousto-optic modulator.

to the enhancement cavity. A beat note is being generated with light from the cw laser. This light is taken from before the fiber amplifier in order to avoid potential phase noise contributions due to path length fluctuations in the gain fiber. A second AOM<sup>39</sup> is used as an actuator for giving feedback to the frequency of the comb modes. The AOM is placed behind the second preamplifier, but before the high power amplifier and pulse compression units. In this way the AOM only has to handle around 2.8 W of optical power, and the material dispersion is less critical. However, the light cannot be focused as tightly as in the frequency stabilization setup due to the higher intensity. This leads to a larger travel time of the acoustic wave in the AOM which limits the feedback bandwidth to 300 kHz. The feedback electronics are identical to those of the fast feedback (see section 6.3.3), except that a 1.9 MHz low-pass filter is used for the error signal. This reduces the amount of noise entering the loop filter, while the larger delay of the AOM makes the phase delay introduced by the filter unimportant.

Figure 6.24 shows the resulting in-loop phase noise measured at the output of the beat detection setup. Without stabilization a large amount of phase noise is visible in the frequency range up to a few kHz. The feedback loop manages to suppress most of these fluctuations such that a noise level close to the one shown in subsection 6.3.3 is achieved. After the high power amplifier and the spectral broadening, the frequency comb light contains much more power in the spectral region that matches the cw laser. The signal-to-noise ratio is therefore significantly higher than in the first two beat detection setups which results in a lower noise floor. The AOMs in the feedback systems are aligned

<sup>39</sup>Gooch & Housego 3110-197.

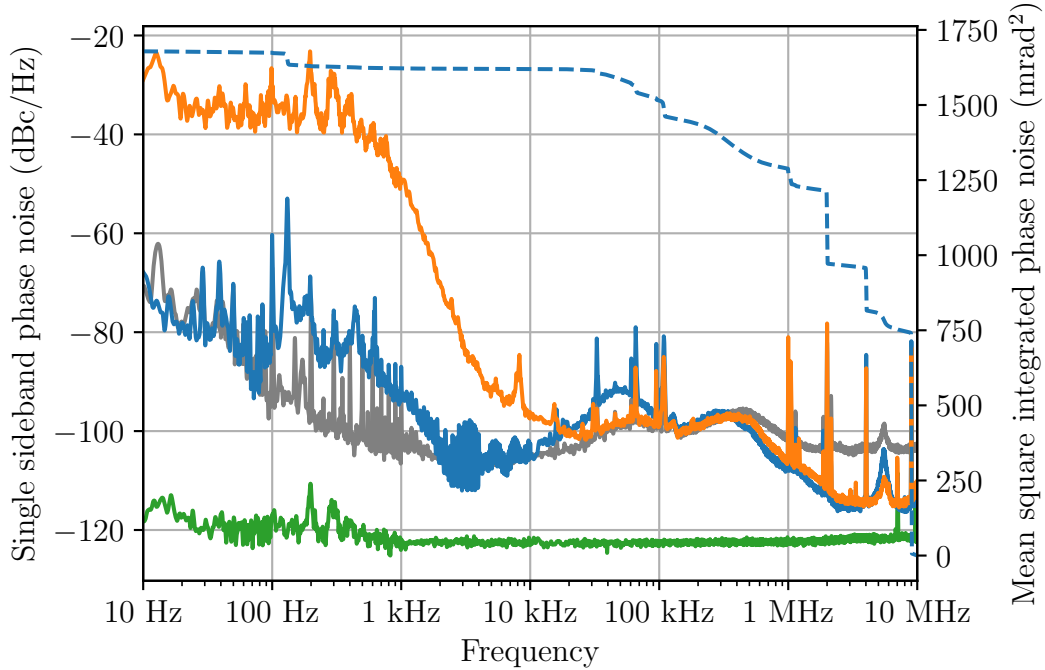


Figure 6.24: Single sideband phase noise measured in the path length stabilization setup. The orange trace is the phase noise without active stabilization and the blue trace with stabilization. For comparison, the in-loop phase noise between the cw laser and the Yb:KYW oscillator (blue trace in Figure 6.21) is shown in gray. The detection noise floor is due to the amplitude noise of the cw laser (green trace). The dashed blue curve shows the mean square integrated phase noise calculated from the blue trace.

such that most of the light is scattered into the +1st diffraction order. However, they also produce other diffraction orders, and a small amount of light from these orders leaks into the main beam. These components beat with the cw laser light and lead to the spurious signals visible in the phase noise plot in the MHz range. The beat note frequencies are chosen such that the spurs lie outside the feedback bandwidth and the linewidth of the enhancement cavity. They are therefore not expected to significantly influence the spectral purity of the generated XUV frequency comb. The integrated phase noise of the stabilized in-loop signal (blue trace) is 41 mrad. As described in section 6.3.3, the enhancement cavity is expected to filter out high-frequency components. After numerically filtering the signal with the theoretical noise transfer function of the cavity, a mean square integrated phase noise of 186 mrad<sup>2</sup> is reached which corresponds to an rms phase noise of 14 mrad. With this amount of phase noise at the fundamental wavelength, 80% of the power remain in the carrier at the 34th harmonic (see Figure 6.3).

# Chapter 7

## Conclusion and outlook

During this thesis work we have set up an ion trap and vacuum system in which spectroscopy of the 1S-2S transition in  $\text{He}^+$  can be performed. We have demonstrated that dark ions can be tracked in real time with single-particle resolution using the secular excitation method. This will be used as a sensitive and background-free detection scheme for locating the spectral line. A low-noise driving laser system was constructed which is expected to achieve a narrow linewidth even after frequency multiplication to the XUV. In parallel to the work presented here, an XUV frequency comb source based on cavity-enhanced high harmonic generation was set up in our group. Once this system achieves sufficient power at 60.8 nm, a search for the spectral line can be started.

An interesting intermediate step is to use a lower harmonic of the frequency comb to excite a two-photon transition in  $\text{Be}^+$ . This will be briefly sketched in the following.

### 7.1 Two-photon excitation of $\text{Be}^+$

Figure 7.1 shows the first few excited states of  $\text{Be}^+$ . The 3d level is located  $98\,055\text{ cm}^{-1}$  above the ground state [103]. The 2s-3d two-photon transition can therefore be driven by light at a wavelength of 204.0 nm. Due to the spectral broadening in the multi-pass cells (see Figure 6.15), the laser beam that drives our high harmonic generation has a strong spectral component at 1020 nm. We expect that with suitable spectral filtering, the system can be adapted such that the 5th harmonic of the laser beam matches the wavelength of the two-photon transition in  $\text{Be}^+$ .

The 3d state decays predominantly to the 2p state with a rate of  $\Gamma = 2\pi \times 176\text{ MHz}$  [217]. The resulting natural linewidth is much larger than the mode spacing given by the repetition rate of the frequency comb ( $f_{\text{rep}} = 40\text{ MHz}$ ) such that the comb structure of the excitation spectrum will not be resolved (see subsection 3.2.1). The excitation rate is therefore independent of the comb mode frequencies, and line broadening effects such as Doppler broadening are unimportant. Nonetheless, the excitation rate can be used as a signal for optimizing the alignment of the spectroscopy laser beam onto the ions.

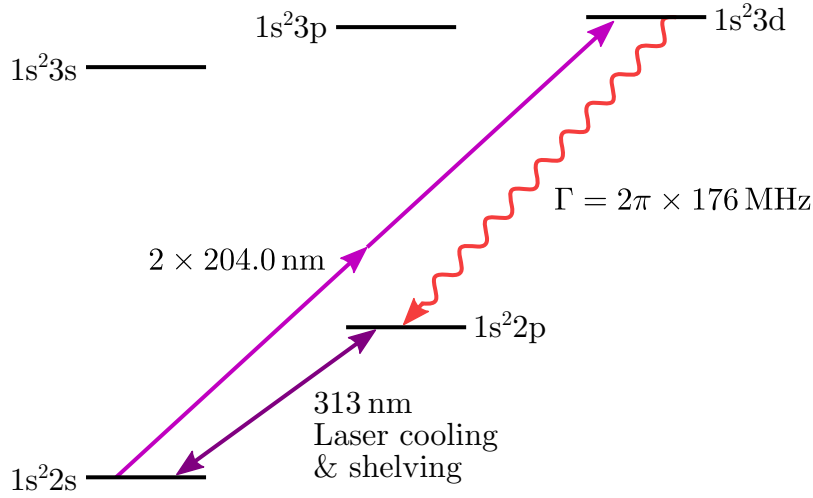


Figure 7.1: Simplified level scheme of Be<sup>+</sup>. With suitable spectral filtering, the 2s-3d two-photon transition can be excited using the 5th harmonic of the driving laser system of our high harmonic generation setup.

### Excitation dynamics

As described in section 3.4, we are going to excite the 1S-2S transition in He<sup>+</sup> with counter-propagating pulses which have to meet at the position of the ions. This pulse overlap can also be optimized using the two-photon excitation of Be<sup>+</sup>. In our setup the counter-propagating pulses are produced in a Mach-Zehnder interferometer in the driving laser system (see section 6.3.1). The position of the pulse collision volume can therefore be changed by adjusting the length of the interferometer which leaves the focus position and laser intensities unchanged.

Since the frequency comb structure is not resolved, the excitation dynamics can be described by considering the interaction between one Be<sup>+</sup> ion and a series of individual resonant laser pulses. For mathematical convenience we assume square pulses with a pulse duration  $\tau$ . During each pulse, the atom performs Rabi oscillations. Since typical pulse durations of a few ten fs are much shorter than the excited state lifetime  $\Gamma^{-1} = 0.90$  ns, the population decay during a pulse is negligible. The probability of having excited the ion after a pulse with intensity  $I$  is then given by [27, p. 137]

$$P_e = \sin^2\left(\frac{\Omega_{2p}\tau}{2}\right), \quad (7.1)$$

where  $\Omega_{2p} = 2(2\pi\beta_{ge})I$  is the two-photon Rabi frequency during the pulse with the two-photon matrix element  $\beta_{ge}$  [91] (see also chapter 3).

We assume that the transition is only weakly driven such that the Rabi angle  $\Omega_{2p}\tau$  is much smaller than unity. The excited state probability after the pulse can then be approximated by

$$P_e \approx \frac{\Omega_{2p}^2\tau^2}{4} = (2\pi\beta_{ge})^2 I^2 \tau^2. \quad (7.2)$$

During one pulse repetition time of the frequency comb ( $T = 1/f_{\text{rep}} = 25 \text{ ns}$ ), the ion interacts with the pulse pair and with its reflection as shown in Figure 7.2.

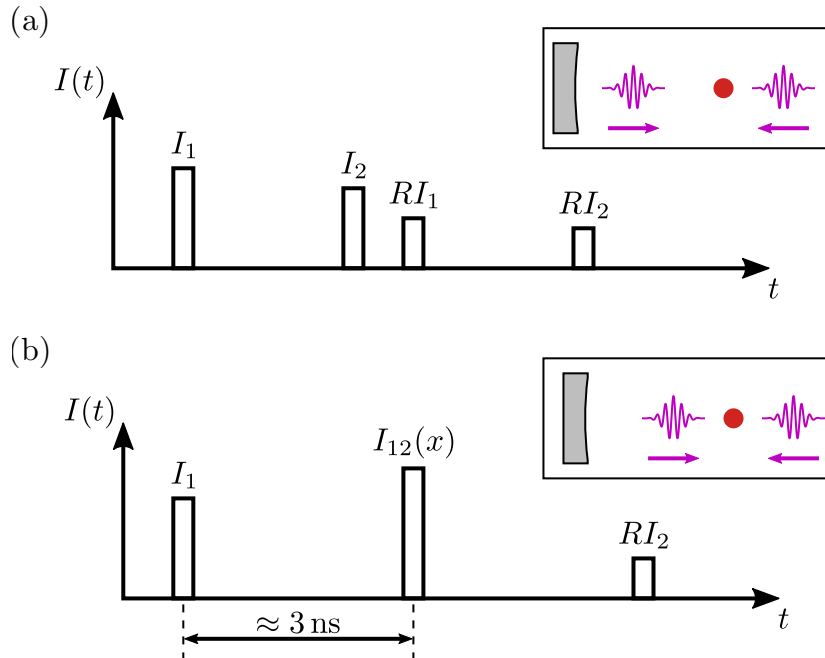


Figure 7.2: Schematic of pulse overlapping using two-photon excitation of a  $\text{Be}^+$  ion (red dot in the insets). The graphs show the pulse sequence at the ion position during one pulse repetition time of the frequency comb.  $I_1$  is the intensity of the first pulse,  $I_2$  is the intensity of the second pulse, and  $R$  is the reflectivity of the XUV mirror. (a) No pulse overlap. The ion “sees” four individual pulses. (b) The reflection of the first pulse is overlapped with the second pulse which leads to a standing wave with intensity  $I_{12}(x)$ , where  $x$  is the ion position. Due to the nonlinear behavior of the two-photon excitation, the excitation probability differs between the two cases.

We start with the case of non-overlapping pulses. In practice the delay line is first coarsely adjusted such that the pulse-to-pulse spacing matches the distance between the ion trap and the XUV mirror to within a few mm. The second pulse and the reflection of the first pulse then arrive at the ion position within a time interval that is much shorter than the excited state lifetime. The interaction with the two mutually coherent pulses leads to Ramsey fringes in the excitation probability if the phase delay between the pulses is scanned [218]. Since the pulses are counter-propagating, the phase delay also depends on the position of the ion. The spatial period of the Ramsey fringes is given by the transition wavelength<sup>1</sup> of 102 nm. The axial micromotion measured in our trap (see subsection 4.7.3) corresponds to a peak-to-peak excursion of around 90 nm such that the Ramsey fringes are “averaged out” by the ion motion. In the following we therefore assume that the ion interacts with all four pulses separately. The probability of having excited the ion after

<sup>1</sup>The two-photon excitation effectively doubles the carrier frequency of the excitation laser pulses.

the interaction is thus given by

$$\begin{aligned} P_e^{\text{n.o.}} &= (2\pi\beta_{ge})^2\tau^2(I_1^2 + I_2^2 + R^2I_1^2 + R^2I_2^2) \\ &= (2\pi\beta_{ge})^2\tau^2(1 + R^2)(I_1^2 + I_2^2), \end{aligned} \quad (7.3)$$

where  $I_1$  is the intensity of the first pulse,  $I_2$  is the intensity of the second pulse, and  $R$  is the reflectivity of the XUV mirror.

If the delay line is correctly adjusted, the reflection of the first pulse completely overlaps with the second pulse at the position of the ion (see Figure 7.2 (b)). The two pulses then form a standing wave with an intensity

$$I_{12}(x) = RI_1 + I_2 + 2\sqrt{RI_1I_2} \cos(2kx), \quad (7.4)$$

where  $k = 2\pi/204 \text{ nm}$  is the laser pulse wave number, and  $x$  is the position of the ion. Like the Ramsey fringes, the standing wave pattern is averaged out by the micromotion. For typical trap parameters the ion is only localized to within a few ten nm which is expected to further reduce the effective modulation depth of the standing wave. We estimate the excitation probability by taking the spatially averaged intensity:

$$I_{12} \approx \langle I_{12}(x) \rangle = RI_1 + I_2. \quad (7.5)$$

This is a conservative estimate since

$$\langle I_{12}(x) \rangle^2 = (RI_1 + I_2)^2 < (RI_1 + I_2)^2 + 2RI_1I_2 = \langle I_{12}(x)^2 \rangle. \quad (7.6)$$

The resulting excitation probability is

$$\begin{aligned} P_e^{\text{o.}} &= (2\pi\beta_{ge})^2\tau^2(I_1^2 + (RI_1 + I_2)^2 + R^2I_2^2) \\ &= (2\pi\beta_{ge})^2\tau^2(1 + R^2)(I_1^2 + I_2^2) \left( 1 + 2\frac{R}{1 + R^2} \frac{I_1I_2}{I_1^2 + I_2^2} \right). \end{aligned} \quad (7.7)$$

If the pulses are successfully overlapped at the ion position, the excitation rate will therefore increase by

$$\eta = \frac{P_e^{\text{o.}}}{P_e^{\text{n.o.}}} = 1 + 2\frac{R}{1 + R^2} \frac{I_1I_2}{I_1^2 + I_2^2}. \quad (7.8)$$

Our XUV mirrors have a reflectivity of  $R = 43\%$  at 204 nm. For equal pulse intensities ( $I_1 = I_2$ ), we obtain  $\eta = 1.36$ .

### Electron shelving detection

The excitation of  $\text{Be}^+$  ions to the 3d state can be detected with very high sensitivity using electron shelving. The  $\text{Be}^+$  ions are first brought into the  $2s \ ^2S_{1/2}(F = 2, m_F = \pm 2)$  stretched state using the  $\sigma^\pm$  polarized cooling laser and the repumper (see section 2.5). The cooling laser is then turned off, and the ions are illuminated with the 204 nm light. If the ions are successfully excited to the 3d state, they decay back to the ground state via the



2p state and can end up in the  $2s\ ^2S_{1/2}(F=1)$  hyperfine manifold. The cooling laser is then turned back on without the repumper. It is off-resonant from the  $2s\ ^2S_{1/2}(F=1) \rightarrow 2p\ ^2P_{3/2}$  transition by the ground state hyperfine splitting of 1.25 GHz. Successful excitation of the 2s-3d two-photon transition therefore manifests itself as a drop in the detected fluorescence intensity.

We have tested the detection scheme by driving transitions between the  $F=2$  and  $F=1$  ground state hyperfine manifolds using microwave radiation. A single  $\text{Be}^+$  ion was prepared in the  $(F=2, m_F=-2)$  state as described above. The ion was then either left in this state, or brought to the  $(F=1, m_F=-1)$  state by applying a  $\pi$ -pulse of microwave radiation that was resonant with the transition frequency between the two states (around 1.25 GHz). The state was then read out by applying the cooling laser without the repumper for 100  $\mu\text{s}$  and counting the number of fluorescence photons detected by one of the PMTs. The sequence was repeated 1000 times for each state which resulted in the photon count distributions shown in Figure 7.3 (left). By associating zero detected photons with the  $(F=1, m_F=-1)$  state, and one or more photons with the  $(F=2, m_F=-2)$  state, the state can be correctly identified in 94% of cases.

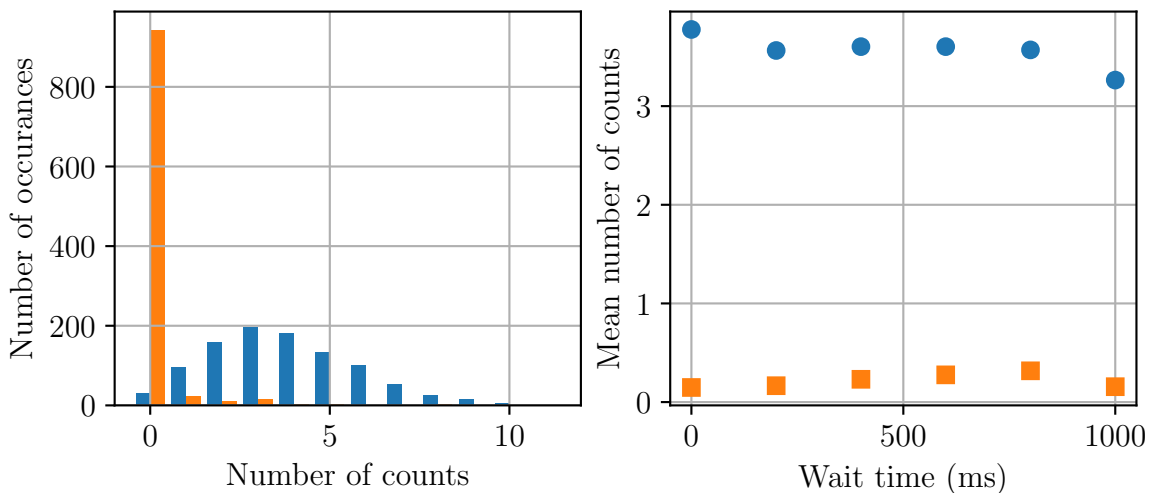


Figure 7.3: Detection of the hyperfine state of a single  $\text{Be}^+$  ion using electron shelving. The left plot shows histograms of detected photon counts when the ion was prepared in the  $(F=2, m_F=-2)$  state (blue), or in the  $(F=1, m_F=-1)$  state (orange). The right plot shows how the detected mean photon number depends on the wait time between state preparation and readout (same color code).

We then inserted a variable wait time between the state preparation and readout. This simulates the time during which the 204 nm light for the two-photon excitation will be applied. As shown in Figure 7.3 (right), the detected photon numbers change only slightly with different wait times. The probability of detecting the correct state remained above 91% in all cases.

### 5th harmonic generation in nonlinear crystals

In principle the XUV frequency comb source generates all odd harmonics of the infrared driving laser. If sufficient intensity is available after spectral filtering, it could therefore be used for exciting the 2s-3d transition in  $\text{Be}^+$ . However, a simpler and more efficient technique is to use nonlinear crystals for the frequency multiplication. This means that the enhancement resonator shown in Figure 6.15 is bypassed, and the light is sent into a separate frequency conversion unit instead. The generated 5th harmonic is then guided through a viewport into the high harmonic generation vacuum chamber. There, a mirror for 204 nm is inserted which sends the light along the beam line for the XUV frequency comb (see Figure 4.24).

A simplified scheme for a frequency conversion unit is shown in Figure 7.4. It is based on a design for generating the 5th harmonic of a mode-locked fiber laser at 1040 nm that was developed in the group of Y. Kobayashi at the University of Tokyo [219].

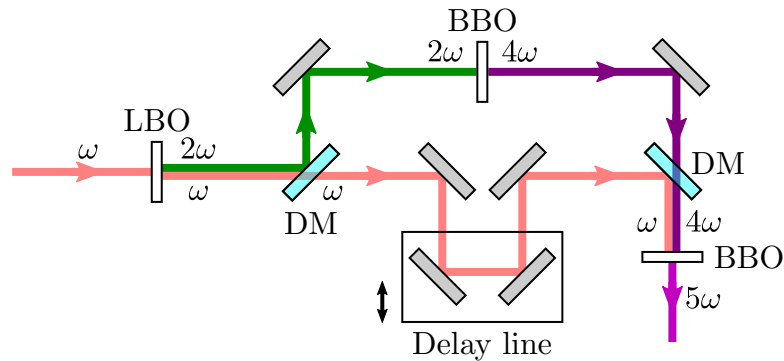


Figure 7.4: Simplified scheme for generating the 5th harmonic using nonlinear crystals. The fundamental light is frequency doubled twice in an LBO crystal and a BBO crystal. It is then overlapped with the residual light at the fundamental frequency in a second BBO crystal. Here, the 5th harmonic is generated as the sum frequency of the two inputs. The delay line is used to temporally overlap the pulses in the second BBO crystal. DM; dichroic mirror.

By adjusting the phase matching angles in the nonlinear crystals, the design can be adapted for operation at 1020 nm. First, the light is frequency doubled in a lithium borate (LBO) crystal. The fundamental is then separated from the second harmonic using a dichroic mirror. The second harmonic is then frequency doubled again in a  $\beta$ -barium borate (BBO) crystal. Finally, the fourth harmonic and the fundamental are overlapped in a second BBO crystal. There, the 5th harmonic is generated by sum frequency generation. In [219] the authors demonstrated an average output power of up to 0.3 mW. This power was limited by the available input power of 3 W, and none of the nonlinear processes were close to saturation.<sup>2</sup> The infrared frequency comb of our high harmonic generation setup has a similar pulse duration and repetition rate, but reaches average powers of more than

<sup>2</sup>A. Ozawa, private communication.

200 W. Even when taking into account losses due to spectral filtering, we expect that a similar setup should produce substantially more output power using our driving laser.



# Appendix A

## Objective design data

Table A.1: Parameters of the objective for horizontal imaging.

Surface	Radius of curvature (mm)	Distance to next surface (mm)	Material
Object		70.00	vacuum
1	$\infty$	6.35	fused silica
2	$\infty$	14.36	air
3	$\infty$	4.42	air
4	-193.40	6.60	fused silica
5	-63.00	1.24	air
6	$\infty$	6.60	fused silica
7	-92.00	1.42	air
8	183.00	6.50	fused silica
9	-183.00	16.69	air
10	-91.80	2.50	fused silica
11	$\infty$	780.10	air

Table A.2: Parameters of the objective for vertical imaging.

Surface	Radius of curvature (mm)	Distance to next surface (mm)	Material
Object		64.48	vacuum
1	$\infty$	9.50	fused silica
2	$\infty$	15.59	air
3	$\infty$	5.91	air
4	-193.40	6.60	fused silica
5	-63.00	1.63	air
6	$\infty$	6.60	fused silica
7	-92.00	1.72	air
8	183.00	6.50	fused silica
9	-183.00	17.53	air
10	-91.80	2.50	fused silica
11	$\infty$	803.28	air

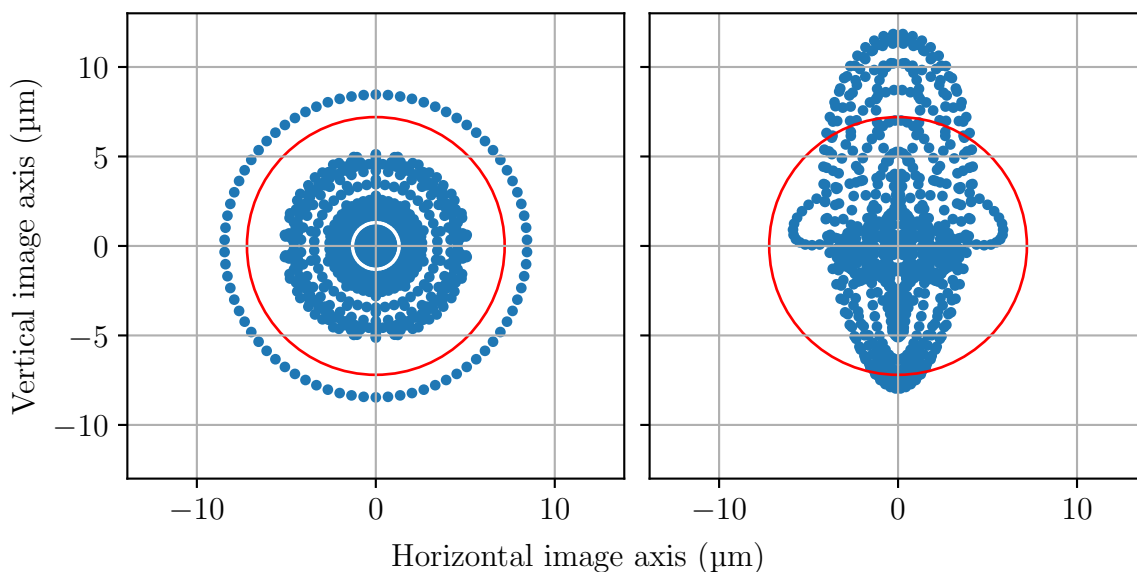


Figure A.1: Spot diagrams of the vertical objective simulated by the ray tracing software. The plots show how much rays originating from a single reference point in the object plane spread out in the image plane due to aberrations. In the left plot the reference point is on the axis of the objective, and in the right plot it is 0.5 mm from the axis. The red circles indicate the sizes of the Airy disks. This is a common measure for the spot size of a diffraction-limited imaging system [115].

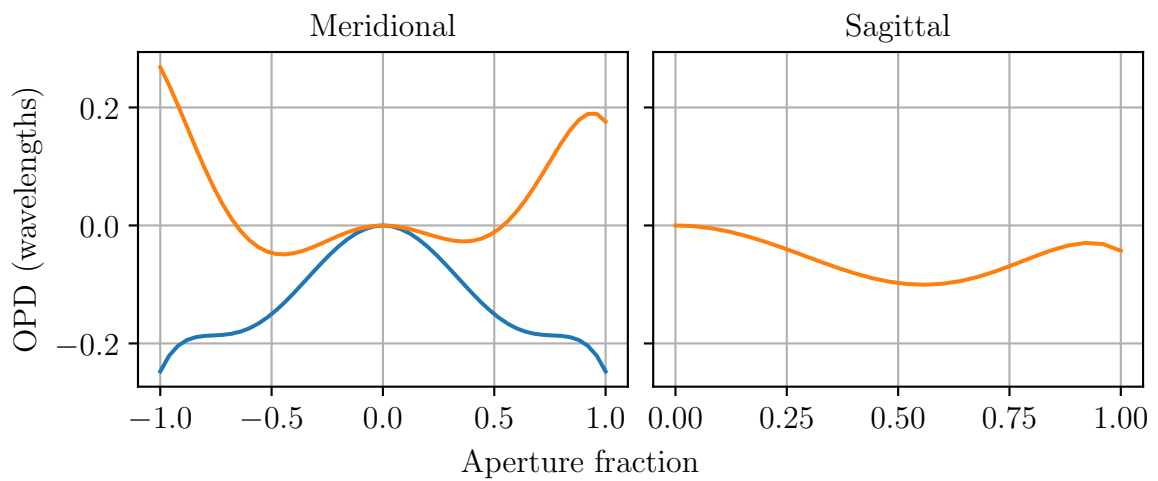


Figure A.2: Optical path difference (OPD) plots for the vertical objective. The path differences are measured relative to a reference ray that crosses the center of the input aperture of the imaging system. The rays originate on-axis (blue) and 0.5 mm off-axis (orange). The aperture fraction measures how far from the center the rays cross the input aperture. A value of 1 corresponds to marginal rays that hit the edge of the aperture.





# Appendix B

## Micromotion fluorescence fit function

In the rest frame of an ion that experiences micromotion, the cooling laser appears phase modulated at the trap frequency  $\Omega$  with a modulation index  $\beta$ . The electric field of the cooling laser is then given by

$$E(t) = \frac{E_0}{2} e^{i[\beta \cos(\Omega t) - \omega t]} + \text{c.c.}, \quad (\text{B.1})$$

where  $E_0$  and  $\omega$  are the electric field amplitude and frequency of the cooling laser, respectively. We assume that the ion is laser cooled on a cycling transition with circularly polarized light (see section 2.5). The electronic states of the ion can therefore be approximated by a two-level system with the ground state  $|g\rangle$  and the excited state  $|e\rangle$ . The cooling transition has the frequency  $\omega_0$  and the FWHM linewidth  $\Gamma$ .

The electronic state of the ion is described by the density matrix in the rotating frame (see for example Chapter 5 in [94]):

$$\rho = \begin{pmatrix} \rho_{gg} & \rho'_{ge} \\ \rho'_{eg} & \rho_{ee} \end{pmatrix}, \quad (\text{B.2})$$

where  $\rho_{gg}$  and  $\rho_{ee}$  are the populations of the ground state and excited state, respectively, and  $\rho'_{ge}$  and  $\rho'_{eg} = \rho_{ge}^*$  are the coherences in the rotating frame.

The coupled differential equations that describe the time evolution of  $\rho$  are called the *optical Bloch equations*. A derivation for the present system can be found in [113], so we here just write down the results:

$$\dot{\rho}_{gg} = -i \frac{\Omega_R}{2} (\rho'_{ge} e^{i\beta \cos(\Omega t)} - \rho'_{eg} e^{-i\beta \cos(\Omega t)}) + \Gamma \rho_{ee}, \quad (\text{B.3})$$

$$\dot{\rho}_{ee} = i \frac{\Omega_R}{2} (\rho'_{ge} e^{i\beta \cos(\Omega t)} - \rho'_{eg} e^{-i\beta \cos(\Omega t)}) - \Gamma \rho_{ee}, \quad (\text{B.4})$$

$$\dot{\rho}'_{ge} = -i \Delta \rho'_{ge} + i \frac{\Omega_R}{2} e^{-i\beta \cos(\Omega t)} (\rho_{ee} - \rho_{gg}) - \frac{\Gamma}{2} \rho'_{ge}, \quad (\text{B.5})$$

$$\dot{\rho}'_{eg} = i \Delta \rho'_{eg} - i \frac{\Omega_R}{2} e^{i\beta \cos(\Omega t)} (\rho_{ee} - \rho_{gg}) - \frac{\Gamma}{2} \rho'_{eg}, \quad (\text{B.6})$$

where  $\Omega_R = dE_0/\hbar$  is the Rabi frequency with the transition dipole matrix element  $d$ , and  $\Delta = \omega - \omega_0$  is the cooling laser detuning. In the experiment the saturation parameter  $s$  is measured which is related to the Rabi frequency by  $s = 2\Omega_R^2/\Gamma^2$ .

The time-dependent fluorescence rate detected by the PMT is given by

$$R(t) = \eta\Gamma\rho_{ee}(t + \varphi_0/\Omega), \quad (\text{B.7})$$

where  $\eta$  is the total photon detection efficiency, and  $\varphi_0 \in [0, 2\pi]$  accounts for the phase offset between the micromotion and the photon detection.

For a given set of parameters,  $\rho_{ee}(t)$  is calculated by numerically integrating Equations B.3-B.6. One typical example for the time evolution is shown in Figure B.1. After a short transient phase,  $\rho_{ee}(t)$  regularly fluctuates in sync with the trap RF cycles. We typically simulate the evolution for 20 RF cycles. The last two cycles of the result are used for evaluating Equation B.7. A least squares fitting algorithm is then used to find the parameters that best match the experimental data. The free parameters determined by the fit are  $\beta$ ,  $\eta$ , and  $\varphi_0$ , whereas  $\Delta$  and  $s$  were measured separately.

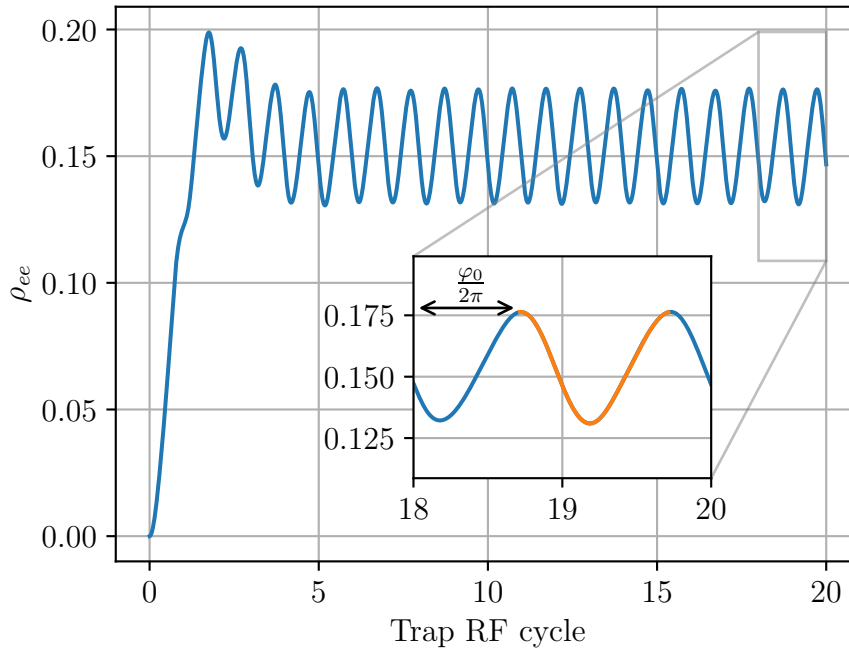


Figure B.1: Numerical solution of the optical Bloch equations for an ion experiencing micromotion. The parameters are  $\Omega = 2\pi \times 65$  MHz,  $s = 1.0$ ,  $\Gamma = 2\pi \times 18$  MHz,  $\Delta = -\Gamma/2$ , and  $\beta = 0.5$ . The inset (same axes) shows in orange the part of the solution that is used for fitting the experimental data.

# Bibliography

- [1] T. W. Hänsch, A. L. Schawlow, and G. W. Series, “The Spectrum of Atomic Hydrogen”, *Sci. Am.* **240**, 94 (1979).
- [2] N. Bohr, “On the Constitution of Atoms and Molecules”, *Phil. Mag.* **26**, 1 (1913).
- [3] E. Schrödinger, “Quantisierung als Eigenwertproblem”, *Ann. Phys.* **384**, 361 (1926).
- [4] A. A. Michelson and E. W. Morley, “On a Method of making the Wave-length of Sodium Light the actual and practical Standard of Length”, *Phil. Mag.* **24**, 463 (1887).
- [5] A. Sommerfeld, “Zur Quantentheorie der Spektrallinien”, *Ann. Phys.* **356**, 1 (1916).
- [6] E. Tiesinga, P. J. Mohr, D. B. Newell, and B. N. Taylor, “CODATA recommended values of the fundamental physical constants: 2018”, *Rev. Mod. Phys.* **93**, 025010 (2021).
- [7] W. E. Lamb and R. C. Retherford, “Fine Structure of the Hydrogen Atom by a Microwave Method”, *Phys. Rev.* **72**, 241 (1947).
- [8] H. A. Bethe, “The Electromagnetic Shift of Energy Levels”, *Phys. Rev.* **72**, 339 (1947).
- [9] Th. Udem, “Phasenkohärente optische Frequenzmessungen am Wasserstoffatom. Bestimmung der Rydberg-Konstanten und der 1S Lamb-Verschiebung”, PhD thesis (Ludwig-Maximilians-Universität München, Munich, Germany, 1997).
- [10] C. G. Parthey, A. Matveev, J. Alnis, B. Bernhardt, A. Beyer, R. Holzwarth, A. Maistrou, R. Pohl, K. Predehl, Th. Udem, T. Wilken, N. Kolachevsky, M. Abgrall, D. Rovera, C. Salomon, P. Laurent, and T. W. Hänsch, “Improved Measurement of the Hydrogen 1S-2S Transition Frequency”, *Phys. Rev. Lett.* **107**, 203001 (2011).
- [11] A. Matveev, C. G. Parthey, K. Predehl, J. Alnis, A. Beyer, R. Holzwarth, Th. Udem, T. Wilken, N. Kolachevsky, M. Abgrall, D. Rovera, C. Salomon, P. Laurent, G. Grosche, O. Terra, T. Legero, H. Schnatz, S. Weyers, B. Altschul, and T. W. Hänsch, “Precision Measurement of the Hydrogen 1S-2S Frequency via a 920-km Fiber Link”, *Phys. Rev. Lett.* **110**, 230801 (2013).
- [12] V. A. Yerokhin, K. Pachucki, and V. Patkóš, “Theory of the Lamb Shift in Hydrogen and Light Hydrogen-Like Ions”, *Ann. Phys.* **531**, 1800324 (2019).

- [13] A. Beyer, L. Maisenbacher, A. Matveev, R. Pohl, K. Khabarova, A. Grinin, T. Lamour, D. C. Yost, T. W. Hänsch, N. Kolachevsky, and Th. Udem, “The Rydberg constant and proton size from atomic hydrogen”, *Science* **358**, 79 (2017).
- [14] U. D. Jentschura, “Self-energy correction to the two-photon decay width in hydrogenlike atoms”, *Phys. Rev. A* **69**, 052118 (2004).
- [15] P. J. Mohr, D. B. Newell, and B. N. Taylor, “CODATA recommended values of the fundamental physical constants: 2014”, *Rev. Mod. Phys.* **88**, 035009 (2016).
- [16] A. Grinin, A. Matveev, D. C. Yost, L. Maisenbacher, V. Wirthl, R. Pohl, T. W. Hänsch, and Th. Udem, “Two-photon frequency comb spectroscopy of atomic hydrogen”, *Science* **370**, 1061 (2020).
- [17] H. Fleurbaey, S. Galtier, S. Thomas, M. Bonnaud, L. Julien, F. Biraben, F. Nez, M. Abgrall, and J. Guéna, “New Measurement of the 1S-3S Transition Frequency of Hydrogen: Contribution to the Proton Charge Radius Puzzle”, *Phys. Rev. Lett.* **120**, 183001 (2018).
- [18] N. Bezginov, T. Valdez, M. Horbatsch, A. Marsman, A. C. Vutha, and E. A. Hessels, “A measurement of the atomic hydrogen Lamb shift and the proton charge radius”, *Science* **365**, 1007 (2019).
- [19] A. D. Brandt, S. F. Cooper, C. Rasor, Z. Burkley, A. Matveev, and D. C. Yost, “Measurement of the  $2S_{1/2}$ - $8D_{5/2}$  Transition in Hydrogen”, *Phys. Rev. Lett.* **128**, 023001 (2022).
- [20] A. Antognini, F. Nez, K. Schuhmann, F. D. Amaro, F. Biraben, J. M. R. Cardoso, D. S. Covita, A. Dax, S. Dhawan, M. Diepold, L. M. P. Fernandes, A. Giesen, A. L. Gouvea, T. Graf, T. W. Hänsch, P. Indelicato, L. Julien, C.-Y. Kao, P. Knowles, F. Kottmann, E.-O. L. Bigot, Y.-W. Liu, J. A. M. Lopes, L. Ludhova, C. M. B. Monteiro, F. Mulhauser, T. Nebel, P. Rabinowitz, J. M. F. dos Santos, L. A. Schaller, C. Schwob, D. Taqqu, J. F. C. A. Veloso, J. Vogelsang, and R. Pohl, “Proton Structure from the Measurement of  $2S$ - $2P$  Transition Frequencies of Muonic Hydrogen”, *Science* **339**, 417 (2013).
- [21] R. Pohl, A. Antognini, F. Nez, F. D. Amaro, F. Biraben, J. M. R. Cardoso, D. S. Covita, A. Dax, S. Dhawan, L. M. P. Fernandes, A. Giesen, T. Graf, T. W. Hänsch, P. Indelicato, L. Julien, C.-Y. Kao, P. Knowles, E.-O. L. Bigot, Y.-W. Liu, J. A. M. Lopes, L. Ludhova, C. M. B. Monteiro, F. Mulhauser, T. Nebel, P. Rabinowitz, J. M. F. dos Santos, L. A. Schaller, K. Schuhmann, C. Schwob, D. Taqqu, J. F. C. A. Veloso, and F. Kottmann, “The size of the proton”, *Nature* **466**, 213 (2010).
- [22] M. Ahmadi, B. X. R. Alves, C. J. Baker, W. Bertsche, E. Butler, A. Capra, C. Carruth, C. L. Cesar, M. Charlton, S. Cohen, R. Collister, S. Eriksson, A. Evans, N. Evetts, J. Fajans, T. Friesen, M. C. Fujiwara, D. R. Gill, A. Gutierrez, J. S. Hangst, W. N. Hardy, M. E. Hayden, C. A. Isaac, A. Ishida, M. A. Johnson, S. A. Jones, S. Jonsell, L. Kurchaninov, N. Madsen, M. Mathers, D. Maxwell, J. T. K. McKenna, S. Menary, J. M. Michan, T. Momose, J. J. Munich, P. Nolan, K. Olchanski, A.

- Olin, P. Pusa, C. Ø. Rasmussen, F. Robicheaux, R. L. Sacramento, M. Sameed, E. Sarid, D. M. Silveira, S. Stracka, G. Stutter, C. So, T. D. Tharp, J. E. Thompson, R. I. Thompson, D. P. van der Werf, and J. S. Wurtele, “Observation of the 1S-2S transition in trapped antihydrogen”, *Nature* **541**, 506 (2017).
- [23] M. Ahmadi, B. X. R. Alves, C. J. Baker, W. Bertsche, A. Capra, C. Carruth, C. L. Cesar, M. Charlton, S. Cohen, R. Collister, S. Eriksson, A. Evans, N. Evetts, J. Fajans, T. Friesen, M. C. Fujiwara, D. R. Gill, J. S. Hangst, W. N. Hardy, M. E. Hayden, C. A. Isaac, M. A. Johnson, J. M. Jones, S. A. Jones, S. Jonsell, A. Khramov, P. Knapp, L. Kurchaninov, N. Madsen, D. Maxwell, J. T. K. McKenna, S. Menary, T. Momose, J. J. Munich, K. Olchanski, A. Olin, P. Pusa, C. Ø. Rasmussen, F. Robicheaux, R. L. Sacramento, M. Sameed, E. Sarid, D. M. Silveira, G. Stutter, C. So, T. D. Tharp, R. I. Thompson, D. P. van der Werf, and J. S. Wurtele, “Characterization of the 1S-2S transition in antihydrogen”, *Nature* **557**, 71 (2018).
- [24] Th. Udem, A. Huber, B. Gross, J. Reichert, M. Prevedelli, M. Weitz, and T. W. Hänsch, “Phase-Coherent Measurement of the Hydrogen 1S-2S Transition Frequency with an Optical Frequency Interval Divider Chain”, *Phys. Rev. Lett.* **79**, 2646 (1997).
- [25] T. W. Hänsch, “Nobel Lecture: Passion for precision”, *Rev. Mod. Phys.* **78**, 1297 (2006).
- [26] J. L. Hall, “Nobel Lecture: Defining and measuring optical frequencies”, *Rev. Mod. Phys.* **78**, 1279 (2006).
- [27] F. Riehle, *Frequency Standards: Basics and Applications* (Wiley-VCH, Weinheim, 2004), ISBN: 978-3-527-40230-4.
- [28] W. L. Wiese and J. R. Fuhr, “Accurate Atomic Transition Probabilities for Hydrogen, Helium, and Lithium”, *J. Phys. Chem. Ref. Data* **38**, 565 (2009).
- [29] J. J. Krauth, K. Schuhmann, M. A. Ahmed, F. D. Amaro, P. Amaro, F. Biraben, T.-L. Chen, D. S. Covita, A. J. Dax, M. Diepold, L. M. P. Fernandes, B. Franke, S. Galtier, A. L. Gouvea, J. Götzfried, T. Graf, T. W. Hänsch, J. Hartmann, M. Hildebrandt, P. Indelicato, L. Julien, K. Kirch, A. Knecht, Y.-W. Liu, J. Machado, C. M. B. Monteiro, F. Mulhauser, B. Naar, T. Nebel, F. Nez, J. M. F. dos Santos, J. P. Santos, C. I. Szabo, D. Taqqu, J. F. C. A. Veloso, J. Vogelsang, A. Voss, B. Weichelt, R. Pohl, A. Antognini, and F. Kottmann, “Measuring the  $\alpha$ -particle charge radius with muonic helium-4 ions”, *Nature* **589**, 527 (2021).
- [30] J. G. Eden, “High-order harmonic generation and other intense optical field-matter interactions: review of recent experimental and theoretical advances”, *Prog. Quantum. Electron.* **28**, 197 (2004).
- [31] Y. V. Baklanov and V. P. Chebotayev, “Narrow resonances of two-photon absorption of super-narrow pulses in a gas”, *Appl. Phys.* **12**, 97 (1977).
- [32] I. Pupeza, C. Zhang, M. Högner, and J. Ye, “Extreme-ultraviolet frequency combs for precision metrology and attosecond science”, *Nat. Photonics* **15**, 175 (2021).

- [33] P. Russbueldt, T. Mans, G. Rotarius, J. Weitenberg, H. D. Hoffmann, and R. Poprawe, “400 W Yb:YAG Innoslab fs-amplifier”, *Opt. Express* **17**, 12230 (2009).
- [34] N. Huntemann, C. Sanner, B. Lipphardt, C. Tamm, and E. Peik, “Single-Ion Atomic Clock with  $3 \times 10^{-18}$  Systematic Uncertainty”, *Phys. Rev. Lett.* **116**, 063001 (2016).
- [35] W. F. McGrew, X. Zhang, R. J. Fasano, S. A. Schäffer, K. Beloy, D. Nicolodi, R. C. Brown, N. Hinkley, G. Milani, M. Schioppo, T. H. Yoon, and A. D. Ludlow, “Atomic clock performance enabling geodesy below the centimetre level”, *Nature* **564**, 87 (2018).
- [36] T. Bothwell, D. Kedar, E. Oelker, J. M. Robinson, S. L. Bromley, W. L. Tew, J. Ye, and C. J. Kennedy, “JILA SrI optical lattice clock with uncertainty of  $2.0 \times 10^{-18}$ ”, *Metrologia* **56**, 065004 (2019).
- [37] S. M. Brewer, J.-S. Chen, A. M. Hankin, E. R. Clements, C. W. Chou, D. J. Wineland, D. B. Hume, and D. R. Leibbrandt, “ $^{27}\text{Al}^+$  Quantum-Logic Clock with a Systematic Uncertainty below  $10^{-18}$ ”, *Phys. Rev. Lett.* **123**, 033201 (2019).
- [38] M. H. Anderson, J. R. Ensher, M. R. Matthews, C. E. Wieman, and E. A. Cornell, “Observation of Bose-Einstein Condensation in a Dilute Atomic Vapor”, *Science* **269**, 198 (1995).
- [39] K. B. Davis, M.-O. Mewes, M. R. Andrews, N. J. van Druten, D. S. Durfee, D. M. Kurn, and W. Ketterle, “Bose-Einstein Condensation in a Gas of Sodium Atoms”, *Phys. Rev. Lett.* **75**, 3969 (1995).
- [40] K. Blaum, “High-accuracy mass spectrometry with stored ions”, *Phys. Rep.* **425**, 1 (2006).
- [41] E. G. Myers, “High-Precision Atomic Mass Measurements for Fundamental Constants”, *Atoms* **7**, 37 (2019).
- [42] D. Hanneke, S. Fogwell, and G. Gabrielse, “New Measurement of the Electron Magnetic Moment and the Fine Structure Constant”, *Phys. Rev. Lett.* **100**, 120801 (2008).
- [43] W. Paul and H. Steinwedel, “Ein neues Massenspektrometer ohne Magnetfeld”, *Z. Naturforsch. A* **8**, 448 (1953).
- [44] W. Paul, O. Osberghaus, and E. Fischer, *Ein Ionenkäfig*, Vol. 415, Forschungsberichte des Wirtschafts- und Verkehrsministeriums Nordrhein-Westfalen (1958), ISBN: 978-3-663-04689-9.
- [45] D. Leibfried, R. Blatt, C. Monroe, and D. Wineland, “Quantum dynamics of single trapped ions”, *Rev. Mod. Phys.* **75**, 281 (2003).
- [46] N. W. McLachlan, *Theory and Application of Mathieu Functions* (Oxford University Press, 1947).
- [47] F. G. Major, V. N. Gheorghie, and G. Werth, *Charged Particle Traps: Physics and Techniques of Charged Particle Field Confinement*, Springer Series on Atomic, Optical, and Plasma Physics 37 (Springer, Berlin, 2005), ISBN: 978-3-540-26576-4.

- [48] D. J. Berkeland, J. D. Miller, J. C. Bergquist, W. M. Itano, and D. J. Wineland, “Minimization of ion micromotion in a Paul trap”, *J. Appl. Phys.* **83**, 5025 (1998).
- [49] R. G. DeVoe, J. Hoffnagle, and R. G. Brewer, “Role of laser damping in trapped ion crystals”, *Phys. Rev. A* **39**, 4362 (1989).
- [50] J. D. Prestage, G. J. Dick, and L. Maleki, “New ion trap for frequency standard applications”, *J. Appl. Phys.* **66**, 1013 (1989).
- [51] M. G. Raizen, J. M. Gilligan, J. C. Bergquist, W. M. Itano, and D. J. Wineland, “Ionic crystals in a linear Paul trap”, *Phys. Rev. A* **45**, 6493 (1992).
- [52] S. Seidelin, J. Chiaverini, R. Reichle, J. J. Bollinger, D. Leibfried, J. Britton, J. H. Wesenberg, R. B. Blakestad, R. J. Epstein, D. B. Hume, W. M. Itano, J. D. Jost, C. Langer, R. Ozeri, N. Shiga, and D. J. Wineland, “Microfabricated Surface-Electrode Ion Trap for Scalable Quantum Information Processing”, *Phys. Rev. Lett.* **96**, 253003 (2006).
- [53] W. Paul, H. P. Reinhard, and U. von Zahn, “Das elektrische Massenfilter als Massenspektrometer und Isotopentrenner”, *Z. Phys.* **152**, 143 (1958).
- [54] D. R. Denison, “Operating Parameters of a Quadrupole in a Grounded Cylindrical Housing”, *J. Vac. Sci. Technol.* **8**, 266 (1971).
- [55] H. G. Dehmelt, “Radiofrequency Spectroscopy of Stored Ions I: Storage”, in *Advances in Atomic and Molecular Physics*, Vol. 3, edited by D. R. Bates and I. Estermann (Academic Press, New York, 1968), pp. 53–72.
- [56] O. D. Kellogg, *Foundations of Potential Theory* (Springer, Berlin, 1967), ISBN: 978-3-642-86748-4.
- [57] D. J. Wineland, J. J. Bollinger, W. M. Itano, and J. D. Prestage, “Angular momentum of trapped atomic particles”, *J. Opt. Soc. Am. B* **2**, 1721 (1985).
- [58] D. H. E. Dubin, “Theory of structural phase transitions in a trapped Coulomb crystal”, *Phys. Rev. Lett.* **71**, 2753 (1993).
- [59] P. Lebedew, “Untersuchungen über die Druckkräfte des Lichtes”, *Ann. Phys.* **311**, 433 (1901).
- [60] H. J. Metcalf and P. van der Straten, *Laser Cooling and Trapping* (Springer, New York, 1999), ISBN: 978-1-4612-1470-0.
- [61] T. W. Hänsch and A. L. Schawlow, “Cooling of gases by laser radiation”, *Opt. Commun.* **13**, 68 (1975).
- [62] D. Wineland and H. Dehmelt, “Proposed  $10^{14}\Delta\nu < \nu$  Laser Fluorescence Spectroscopy on  $\text{Tl}^+$  Mono-Ion Oscillator III.”, *Bull. Am. Phys. Soc.* **20**, 637 (1975).
- [63] D. H. E. Dubin and T. M. O’Neil, “Trapped nonneutral plasmas, liquids, and crystals (the thermal equilibrium states)”, *Rev. Mod. Phys.* **71**, 87 (1999).
- [64] J. P. Schiffer, “Melting of Crystalline Confined Plasmas”, *Phys. Rev. Lett.* **88**, 205003 (2002).

- [65] C. B. Zhang, D. Offenberg, B. Roth, M. A. Wilson, and S. Schiller, “Molecular-dynamics simulations of cold single-species and multispecies ion ensembles in a linear Paul trap”, *Phys. Rev. A* **76**, 012719 (2007).
- [66] B. Roth and S. Schiller, *Sympathetically cooled molecular ions: from principles to first applications*, (2008) arXiv:0812.1154 [quant-ph].
- [67] M. R. Tarbutt, “Laser cooling of molecules”, *Contemp. Phys.* **59**, 356 (2018).
- [68] P. Micke, T. Leopold, S. A. King, E. Benkler, L. J. Spieß, L. Schmöger, M. Schwarz, J. R. Crespo López-Urrutia, and P. O. Schmidt, “Coherent laser spectroscopy of highly charged ions using quantum logic”, *Nature* **578**, 60 (2020).
- [69] B. Roth, P. Blythe, H. Wenz, H. Daerr, and S. Schiller, “Ion-neutral chemical reactions between ultracold localized ions and neutral molecules with single-particle resolution”, *Phys. Rev. A* **73**, 042712 (2006).
- [70] W. Nörtershäuser, C. Geppert, A. Krieger, K. Pachucki, M. Puchalski, K. Blaum, M. L. Bissell, N. Frömmgen, M. Hammen, M. Kowalska, J. Krämer, K. Kreim, R. Neugart, G. Neyens, R. Sánchez, and D. T. Yordanov, “Precision Test of Many-Body QED in the  $\text{Be}^+$  2p Fine Structure Doublet Using Short-Lived Isotopes”, *Phys. Rev. Lett.* **115**, 033002 (2015).
- [71] T. Andersen, K. A. Jessen, and G. Sørensen, “Mean-Life Measurements of Excited Electronic States in Neutral and Ionic Species of Beryllium and Boron”, *Phys. Rev.* **188**, 76 (1969).
- [72] J. Bromander, “Lifetimes and Oscillator Strengths in Spectra of Be, B and C”, *Phys. Scr.* **4**, 61 (1971).
- [73] I. Bergström, J. Bromander, R. Buchta, L. Lundin, and I. Martinson, “Mean lives of excited terms in Be I, Be II, B I, B II, C II and C III”, *Phys. Lett. A* **28**, 721 (1969).
- [74] Z.-C. Yan, M. Tambasco, and G. W. F. Drake, “Energies and oscillator strengths for lithiumlike ions”, *Phys. Rev. A* **57**, 1652 (1998).
- [75] M. Auzinsh, D. Budker, and S. M. Rochester, *Optically Polarized Atoms: Understanding Light-Atom Interactions* (Oxford University Press, Oxford, 2010), ISBN: 978-0-19-956512-2.
- [76] D. J. Wineland, J. J. Bollinger, and W. M. Itano, “Laser-Fluorescence Mass Spectroscopy”, *Phys. Rev. Lett.* **50**, 628 (1983).
- [77] N. Shiga, W. M. Itano, and J. J. Bollinger, “Diamagnetic correction to the  $^9\text{Be}^+$  ground-state hyperfine constant”, *Phys. Rev. A* **84**, 012510 (2011).
- [78] M. Puchalski and K. Pachucki, “Fine and hyperfine splitting of the 2P state in Li and  $\text{Be}^+$ ”, *Phys. Rev. A* **79**, 032510 (2009).
- [79] Th. Udem, “Die Messung der Frequenz von Licht mit modengekoppelten Lasern”, Habilitationsschrift (Ludwig-Maximilians-Universität München, Munich, Germany, 2002).



- [80] Th. Udem, R. Holzwarth, and T. W. Hänsch, “Optical frequency metrology”, *Nature* **416**, 233 (2002).
- [81] S. A. Diddams, K. Vahala, and Th. Udem, “Optical frequency combs: Coherently uniting the electromagnetic spectrum”, *Science* **369**, eaay3676 (2020).
- [82] H. Telle, B. Lipphardt, and J. Stenger, “Kerr-lens, mode-locked lasers as transfer oscillators for optical frequency measurements”, *Appl. Phys. B* **74**, 1 (2002).
- [83] E. Benkler, H. R. Telle, A. Zach, and F. Tauser, “Circumvention of noise contributions in fiber laser based frequency combs”, *Opt. Express* **13**, 5662 (2005).
- [84] L. A. M. Johnson, P. Gill, and H. S. Margolis, “Evaluating the performance of the NPL femtosecond frequency combs: agreement at the  $10^{-21}$  level”, *Metrologia* **52**, 62 (2015).
- [85] E. Benkler, B. Lipphardt, T. Puppe, R. Wilk, F. Rohde, and U. Sterr, “End-to-end topology for fiber comb based optical frequency transfer at the  $10^{-21}$  level”, *Opt. Express* **27**, 36886 (2019).
- [86] M. Giunta, W. Hänsel, M. Fischer, M. Lezius, Th. Udem, and R. Holzwarth, “Real-time phase tracking for wide-band optical frequency measurements at the 20th decimal place”, *Nat. Photonics* **14**, 44 (2020).
- [87] W. C. Swann, J. J. McFerran, I. Coddington, N. R. Newbury, I. Hartl, M. E. Fer-  
mann, P. S. Westbrook, J. W. Nicholson, K. S. Feder, C. Langrock, and M. M. Fejer,  
“Fiber-laser frequency combs with subhertz relative linewidths”, *Opt. Lett.* **31**, 3046  
(2006).
- [88] M. J. Martin, S. M. Foreman, T. R. Schibli, and J. Ye, “Testing ultrafast mode-  
locking at microhertz relative optical linewidth”, *Opt. Express* **17**, 558 (2009).
- [89] Q. Quraishi, S. A. Diddams, and L. Hollberg, “Optical phase-noise dynamics of  
Titanium:sapphire optical frequency combs”, *Opt. Commun.* **320**, 84 (2014).
- [90] M. Göppert-Mayer, “Über Elementarakte mit zwei Quantensprüngen”, *Ann. Phys.*  
**401**, 273 (1931).
- [91] M. Haas, U. D. Jentschura, C. H. Keitel, N. Kolachevsky, M. Herrmann, P. Fendel,  
M. Fischer, Th. Udem, R. Holzwarth, T. W. Hänsch, M. O. Scully, and G. S. Agar-  
wal, “Two-photon excitation dynamics in bound two-body Coulomb systems includ-  
ing ac Stark shift and ionization”, *Phys. Rev. A* **73**, 052501 (2006).
- [92] J. J. Sakurai, *Modern Quantum Mechanics*, edited by S. F. Tuan, Rev. ed. (Addison-  
Wesley Pub. Co, Reading, 1994), ISBN: 978-0-201-53929-5.
- [93] V. Paulisch, H. Rui, H. K. Ng, and B.-G. Englert, “Beyond adiabatic elimination:  
A hierarchy of approximations for multi-photon processes”, *Eur. Phys. J. Plus* **129**,  
12 (2014).
- [94] D. A. Steck, *Quantum and Atom Optics*, revision 0.12.6, available online at <http://steck.us/teaching> (2019).

- [95] M. Herrmann, M. Haas, U. D. Jentschura, F. Kottmann, D. Leibfried, G. Saathoff, C. Gohle, A. Ozawa, V. Batteiger, S. Knünz, N. Kolachevsky, H. A. Schüssler, T. W. Hänsch, and Th. Udem, “Feasibility of coherent xuv spectroscopy on the 1S-2S transition in singly ionized helium”, *Phys. Rev. A* **79**, 052505 (2009).
- [96] P. Fendel, “Präzisionsspektroskopie an Wasserstoff und Deuterium”, PhD thesis (Ludwig-Maximilians-Universität München, Munich, Germany, 2005).
- [97] D. J. Wineland and W. M. Itano, “Laser cooling of atoms”, *Phys. Rev. A* **20**, 1521 (1979).
- [98] G. Morigi and H. Walther, “Two-species Coulomb chains for quantum information”, *Eur. Phys. J. D* **13**, 261 (2001).
- [99] D. F. V. James, “Quantum dynamics of cold trapped ions with application to quantum computation”, *Appl. Phys. B* **66**, 181 (1998).
- [100] D. J. Wineland, C. Monroe, W. M. Itano, D. Leibfried, B. E. King, and D. M. Meekhof, “Experimental Issues in Coherent Quantum-State Manipulation of Trapped Atomic Ions”, *J. Res. Natl. Inst. Stand. Technol.* **103**, 259 (1998).
- [101] H. Goldstein, C. P. Poole, and J. L. Safko, *Classical mechanics*, 3rd ed. (Pearson Education, Harlow, 2014), ISBN: 978-1-292-02655-8.
- [102] E. Jannitti, M. Mazzoni, P. Nicolosi, G. Tondello, and W. Yongchang, “Photoabsorption spectrum of  $\text{Be}^+$ ”, *J. Opt. Soc. Am. B* **2**, 1078 (1985).
- [103] A. E. Kramida, “Critical Compilation of Wavelengths and Energy Levels of Singly Ionized Beryllium (Be II)”, *Phys. Scr.* **72**, 309 (2005).
- [104] J. J. Krauth, L. S. Dreissen, C. Roth, E. L. Gründeman, M. Collombon, M. Favier, and K. S. E. Eikema, “Paving the way for fundamental physics tests with singly ionized helium”, in *Proceedings of International Conference on Precision Physics and Fundamental Physical Constants - PoS(FFK2019)*, Vol. 353 (2020), p. 049.
- [105] J. B. Wübbena, S. Amairi, O. Mandel, and P. O. Schmidt, “Sympathetic cooling of mixed-species two-ion crystals for precision spectroscopy”, *Phys. Rev. A* **85**, 043412 (2012).
- [106] S. Alighanbari, M. G. Hansen, V. I. Korobov, and S. Schiller, “Rotational spectroscopy of cold and trapped molecular ions in the Lamb-Dicke regime”, *Nat. Phys.* **14**, 555 (2018).
- [107] H. J. Lipkin, *Quantum Mechanics: New Approaches to Selected Topics* (North-Holland, Amsterdam, 1973), ISBN: 0-7204-0258-1.
- [108] Y. Wan, F. Gebert, J. B. Wübbena, N. Scharnhorst, S. Amairi, I. D. Leroux, B. Hemmerling, N. Lörch, K. Hammerer, and P. O. Schmidt, “Precision spectroscopy by photon-recoil signal amplification”, *Nat. Commun.* **5**, 3096 (2014).
- [109] J. H. Moore, C. C. Davis, M. A. Coplan, and S. C. Greer, *Building scientific apparatus*, 4th ed (Cambridge University Press, Cambridge, 2009), ISBN: 978-0-511-60979-4.

- [110] W. W. Macalpine and R. O. Schildknecht, “Coaxial Resonators with Helical Inner Conductor”, *Proc. Inst. Electr. Eng.* **47**, 2099 (1959).
- [111] J. D. Siverns, L. R. Simkins, S. Weidt, and W. K. Hensinger, “On the application of radio frequency voltages to ion traps via helical resonators”, *Appl. Phys. B* **107**, 921 (2012).
- [112] K. Deng, Y. L. Sun, W. H. Yuan, Z. T. Xu, J. Zhang, Z. H. Lu, and J. Luo, “A modified model of helical resonator with predictable loaded resonant frequency and Q-factor”, *Rev. Sci. Instrum.* **85**, 104706 (2014).
- [113] F. Schmid, “Development and Characterization of a Beryllium Ion Trap”, MA thesis (Technische Universität München, Munich, Germany, 2016).
- [114] S. Panja, S. De, S. Yadav, and A. Sen Gupta, “Note: Measuring capacitance and inductance of a helical resonator and improving its quality factor by mutual inductance alteration”, *Rev. Sci. Instrum.* **86**, 056104 (2015).
- [115] H. Gross, *Fundamentals of Technical Optics*, edited by H. Gross, Vol. 1, Handbook of Optical Systems (Wiley-VCH, Weinheim, 2005), ISBN: 978-3-527-40377-6.
- [116] W. Alt, “An objective lens for efficient fluorescence detection of single atoms”, *Optik* **113**, 142 (2002).
- [117] L. M. Bennie, P. T. Starkey, M. Jasperse, C. J. Billington, R. P. Anderson, and L. D. Turner, “A versatile high resolution objective for imaging quantum gases”, *Opt. Express* **21**, 9011 (2013).
- [118] H. Gross, H. Zügge, M. Peschka, and F. Blechinger, *Aberration Theory and Correction of Optical Systems*, edited by H. Gross, Vol. 3, Handbook of Optical Systems (Wiley-VCH, Weinheim, 2007), ISBN: 978-3-527-40379-0.
- [119] A. C. Wilson, C. Ospelkaus, A. P. VanDevender, J. A. Mlynek, K. R. Brown, D. Leibfried, and D. J. Wineland, “A 750-mW, continuous-wave, solid-state laser source at 313 nm for cooling and manipulating trapped  $^9\text{Be}^+$  ions”, *Appl. Phys. B* **105**, 741 (2011).
- [120] V. Batteiger, “Experiments with dipole-allowed transitions in trapped ions”, PhD thesis (Ludwig-Maximilians-Universität München, Munich, Germany, 2011).
- [121] T. W. Hänsch and B. Couillaud, “Laser frequency stabilization by polarization spectroscopy of a reflecting reference cavity”, *Opt. Commun.* **35**, 441 (1980).
- [122] J. Hall, M. Long-Sheng, and G. Kramer, “Principles of Optical Phase-Locking: Application to Internal Mirror He-Ne Lasers Phase-Locked via Fast Control of the Discharge Current”, *IEEE J. Quantum Electron.* **23**, 427 (1987).
- [123] M. Prevedelli, T. Freearde, and T. W. Hänsch, “Phase locking of grating-tuned diode lasers”, *Appl. Phys. B* **60**, S241 (1995).
- [124] E. A. Donley, T. P. Heavner, F. Levi, M. O. Tataw, and S. R. Jefferts, “Double-pass acousto-optic modulator system”, *Rev. Sci. Instrum.* **76**, 063112 (2005).

- [125] Y. Colombe, D. H. Slichter, A. C. Wilson, D. Leibfried, and D. J. Wineland, “Single-mode optical fiber for high-power, low-loss UV transmission”, *Opt. Express* **22**, 19783 (2014).
- [126] C. D. Marciniak, H. B. Ball, A. T.-H. Hung, and M. J. Biercuk, “Towards fully commercial, UV-compatible fiber patch cords”, *Opt. Express* **25**, 15643 (2017).
- [127] G. Porat, C. M. Heyl, S. B. Schoun, C. Benko, N. Dörre, K. L. Corwin, and J. Ye, “Phase-matched extreme-ultraviolet frequency-comb generation”, *Nat. Photonics* **12**, 387 (2018).
- [128] O. Pronin, V. Pervak, E. Fill, J. Rauschenberger, F. Krausz, and A. Apolonski, “Ultrabroadband efficient intracavity XUV output coupler”, *Opt. Express* **19**, 10232 (2011).
- [129] S. Bourdeauducq, whitequark, R. Jördens, Y. Sionneau, enjoy-digital, cjbe, D. Nadlinger, hartyp, JBoulder, D. Slichter, Drew, mntng, r-srinivas, apatura-iris, S. Mackenzie, Z. Smith, P. K. M. Weber, kemstevens, F. Held, and D. Leibbrandt, *ARTIQ, A leading-edge control system for quantum information experiments*, 2018, <https://zenodo.org/record/591804>.
- [130] J. R. Rumble, ed., *CRC Handbook of Chemistry and Physics*, 102nd Edition (Internet Version 2021) (CRC Press/Taylor & Francis, Boca Raton, 2021).
- [131] J. Robin, “Laser Cooling of Beryllium Ions in a Segmented Linear RF Trap”, MA thesis (Ludwig-Maximilians-Universität München, Munich, Germany, 2012).
- [132] E. C. Cook, A. D. Vira, C. Patterson, E. Livernois, and W. D. Williams, “Testing Quantum Electrodynamics in the Lowest Singlet State of Neutral Beryllium-9”, *Phys. Rev. Lett.* **121**, 053001 (2018).
- [133] R. Schnabel and M. Kock, “ $f$ -value measurement of the Be I resonance line using a nonlinear time-resolved laser-induced-fluorescence technique”, *Phys. Rev. A* **61**, 062506 (2000).
- [134] R. Beigang, D. Schmidt, and P. J. West, “Laser Spectroscopy of High Rydberg States of Light Alkaline-Earth Elements: Be and Mg”, *J. Phys. Colloques* **44**, C7-229 (1983).
- [135] L. Ricci, M. Weidemüller, T. Esslinger, A. Hemmerich, C. Zimmermann, V. Vuletic, W. König, and T. W. Hänsch, “A compact grating-stabilized diode laser system for atomic physics”, *Opt. Commun.* **117**, 541 (1995).
- [136] T. Nishikawa, A. Ozawa, Y. Nishida, M. Asobe, F.-L. Hong, and T. W. Hänsch, “Efficient 494 mW sum-frequency generation of sodium resonance radiation at 589 nm by using a periodically poled Zn:LiNbO<sub>3</sub> ridge waveguide”, *Opt. Express* **17**, 17792 (2009).
- [137] W. Demtröder, *Laser Spectroscopy 1*, 5th ed. (Springer, Berlin, 2014), ISBN: 978-3-642-53859-9.

- [138] G. D. Boyd and D. A. Kleinman, “Parametric Interaction of Focused Gaussian Light Beams”, *J. Appl. Phys.* **39**, 3597 (1968).
- [139] T. Freearge, J. Coutts, J. Walz, D. Leibfried, and T. W. Hänsch, “General analysis of type I second-harmonic generation with elliptical Gaussian beams”, *J. Opt. Soc. Am. B* **14**, 2010 (1997).
- [140] T. Freearge and C. Zimmermann, “On the design of enhancement cavities for second harmonic generation”, *Opt. Commun.* **199**, 435 (2001).
- [141] H.-Y. Lo, J. Alonso, D. Kienzler, B. C. Keitch, L. E. de Clercq, V. Negnevitsky, and J. P. Home, “All-solid-state continuous-wave laser systems for ionization, cooling and quantum state manipulation of beryllium ions”, *Appl. Phys. B* **114**, 17 (2013).
- [142] E. S. Polzik and H. J. Kimble, “Frequency doubling with  $\text{KNbO}_3$  in an external cavity”, *Opt. Lett.* **16**, 1400 (1991).
- [143] R. W. P. Drever, J. L. Hall, F. V. Kowalski, J. Hough, G. M. Ford, A. J. Munley, and H. Ward, “Laser Phase and Frequency Stabilization Using an Optical Resonator”, *Appl. Phys. B* **31**, 97 (1983).
- [144] D. R. Leibbrandt and J. Heidecker, “An open source digital servo for atomic, molecular, and optical physics experiments”, *Rev. Sci. Instrum.* **86**, 123115 (2015).
- [145] S. van der Walt, J. L. Schönberger, J. Nunez-Iglesias, F. Boulogne, J. D. Warner, N. Yager, E. Gouillart, and T. Yu, “scikit-image: image processing in Python”, *PeerJ* **2**, e453 (2014).
- [146] G. W. Zack, W. E. Rogers, and S. A. Latt, “Automatic measurement of sister chromatid exchange frequency”, *J. Histochem. Cytochem.* **25**, 741 (1977).
- [147] C. Steger, M. Ulrich, and C. Wiedemann, eds., *Machine vision algorithms and applications*, 2nd ed. (Wiley-VCH, Weinheim, 2018), ISBN: 978-3-527-41365-2.
- [148] G. Herzberg, “Ionization potentials and Lamb shifts of the ground states of  $^4\text{He}$  and  $^3\text{He}$ ”, *Proc. R. Soc. Lond.* **248**, 309 (1958).
- [149] B.-m. Ann, “Investigation of Beryllium and Magnesium mixed ion crystal toward Helium<sup>+</sup> 1S-2S spectroscopy.”, MA thesis (Ludwig-Maximilians-Universität München, Munich, Germany, 2016).
- [150] J. Keller, H. L. Partner, T. Burgermeister, and T. E. Mehlstäubler, “Precise determination of micromotion for trapped-ion optical clocks”, *J. Appl. Phys.* **118**, 104501 (2015).
- [151] A. van Wijngaarden, F. Holuj, and G. W. F. Drake, “Lamb shift in  $\text{He}^+$ : Resolution of a discrepancy between theory and experiment”, *Phys. Rev. A* **63**, 012505 (2000).
- [152] J. Keller, D. Kalincev, T. Burgermeister, A. P. Kulosa, A. Didier, T. Nordmann, J. Kiethe, and T. E. Mehlstäubler, “Probing Time Dilation in Coulomb Crystals in a High-Precision Ion Trap”, *Phys. Rev. Appl.* **11**, 011002 (2019).

- [153] F. Schmid, J. Weitenberg, J. Moreno, T. W. Hänsch, Th. Udem, and A. Ozawa, “Number-resolved detection of dark ions in Coulomb crystals”, *Phys. Rev. A* **106**, L041101 (2022).
- [154] C. Schneider, S. J. Schowalter, K. Chen, S. T. Sullivan, and E. R. Hudson, “Laser-Cooling-Assisted Mass Spectrometry”, *Phys. Rev. Appl.* **2**, 034013 (2014).
- [155] K. A. E. Meyer, L. L. Pollum, L. S. Petralia, A. Tauschinsky, C. J. Rennick, T. P. Softley, and B. R. Heazlewood, “Ejection of Coulomb Crystals from a Linear Paul Ion Trap for Ion-Molecule Reaction Studies”, *J. Phys. Chem. A* **119**, 12449 (2015).
- [156] D. Rösch, H. Gao, A. Kilaj, and S. Willitsch, “Design and characterization of a linear quadrupole ion trap for high-resolution Coulomb-crystal time-of-flight mass spectrometry”, *EPJ Tech. Instrum.* **3**, 5 (2016).
- [157] P. C. Schmid, J. Greenberg, M. I. Miller, K. Loeffler, and H. J. Lewandowski, “An ion trap time-of-flight mass spectrometer with high mass resolution for cold trapped ion experiments”, *Rev. Sci. Instrum.* **88**, 123107 (2017).
- [158] P. Blythe, B. Roth, U. Fröhlich, H. Wenz, and S. Schiller, “Production of Ultracold Trapped Molecular Hydrogen Ions”, *Phys. Rev. Lett.* **95**, 183002 (2005).
- [159] M. Germann, X. Tong, and S. Willitsch, “Observation of electric-dipole-forbidden infrared transitions in cold molecular ions”, *Nat. Phys.* **10**, 820 (2014).
- [160] K. Okada, M. Ichikawa, M. Wada, and H. A. Schuessler, “Quasiequilibrium Characterization of Mixed-Ion Coulomb Crystals”, *Phys. Rev. Appl.* **4**, 054009 (2015).
- [161] B. Roth, P. Blythe, and S. Schiller, “Motional resonance coupling in cold multispecies Coulomb crystals”, *Phys. Rev. A* **75**, 023402 (2007).
- [162] B.-m. Ann, F. Schmid, J. Krause, T. W. Hänsch, Th. Udem, and A. Ozawa, “Motional resonances of three-dimensional dual-species Coulomb crystals”, *J. Phys. B: At. Mol. Opt. Phys.* **52**, 035002 (2019).
- [163] T. Baba and I. Waki, “Chemical reaction of sympathetically laser-cooled molecular ions”, *J. Chem. Phys.* **116**, 1858 (2002).
- [164] J. Biesheuvel, J.-P. Karr, L. Hilico, K. S. E. Eikema, W. Ubachs, and J. C. J. Koelemeij, “High-precision spectroscopy of the HD<sup>+</sup> molecule at the 1-p.p.b. level”, *Appl. Phys. B* **123**, 23 (2016).
- [165] M. Herrmann, V. Batteiger, S. Knünz, G. Saathoff, Th. Udem, and T. W. Hänsch, “Frequency Metrology on Single Trapped Ions in the Weak Binding Limit: The  $3s_{1/2} - 3p_{3/2}$  Transition in  $^{24}\text{Mg}^+$ ”, *Phys. Rev. Lett.* **102**, 013006 (2009).
- [166] S. Alighanbari, G. S. Giri, F. L. Constantin, V. I. Korobov, and S. Schiller, “Precise test of quantum electrodynamics and determination of fundamental constants with HD<sup>+</sup> ions”, *Nature* **581**, 152 (2020).

- [167] S. Patra, M. Germann, J.-P. Karr, M. Haidar, L. Hilico, V. I. Korobov, F. M. J. Cozijn, K. S. E. Eikema, W. Ubachs, and J. C. J. Koelemeij, “Proton-electron mass ratio from laser spectroscopy of  $\text{HD}^+$  at the part-per-trillion level”, *Science* **369**, 1238 (2020).
- [168] J. Schmidt, T. Louvradoux, J. Heinrich, N. Sillitoe, M. Simpson, J.-P. Karr, and L. Hilico, “Trapping, Cooling, and Photodissociation Analysis of State-Selected  $\text{H}_2^+$  Ions Produced by (3+1) Multiphoton Ionization”, *Phys. Rev. Appl.* **14**, 024053 (2020).
- [169] L. Ratschbacher, C. Zipkes, C. Sias, and M. Köhl, “Controlling chemical reactions of a single particle”, *Nat. Phys.* **8**, 649 (2012).
- [170] M. T. Bowers, D. D. Elleman, and J. King, “Analysis of the Ion–Molecule Reactions in Gaseous  $\text{H}_2$ ,  $\text{D}_2$ , and  $\text{HD}$  by Ion Cyclotron Resonance Techniques”, *J. Chem. Phys.* **50**, 4787 (1969).
- [171] J. K. Kim and W. T. Huntress, “Ion cyclotron resonance studies on the reaction of  $\text{H}_2^+$  and  $\text{D}_2^+$  ions with various simple molecules and hydrocarbons”, *J. Chem. Phys.* **62**, 2820 (1975).
- [172] J. A. Burt, J. L. Dunn, M. J. McEwan, M. M. Sutton, A. E. Roche, and H. I. Schiff, “Some Ion-Molecule Reactions of  $\text{H}_3^+$  and the Proton Affinity of  $\text{H}_2$ ”, *J. Chem. Phys.* **52**, 6062 (1970).
- [173] A. P. Thompson, H. M. Aktulga, R. Berger, D. S. Bolintineanu, W. M. Brown, P. S. Crozier, P. J. in 't Veld, A. Kohlmeyer, S. G. Moore, T. D. Nguyen, R. Shan, M. J. Stevens, J. Tranchida, C. Trott, and S. J. Plimpton, “LAMMPS - a flexible simulation tool for particle-based materials modeling at the atomic, meso, and continuum scales”, *Comput. Phys. Commun.* **271**, 108171 (2022).
- [174] E. Bentine, C. J. Foot, and D. Trypogeorgos, “(py)LIon: A package for simulating trapped ion trajectories”, *Comput. Phys. Commun.* **253**, 107187 (2020).
- [175] V. L. Ryjkov, X. Zhao, and H. A. Schuessler, “Simulations of the rf heating rates in a linear quadrupole ion trap”, *Phys. Rev. A* **71**, 033414 (2005).
- [176] F. Schmid, J. Weitenberg, T. W. Hänsch, Th. Udem, and A. Ozawa, “Simple phase noise measurement scheme for cavity-stabilized laser systems”, *Opt. Lett.* **44**, 2709 (2019).
- [177] J. Alnis, A. Matveev, N. Kolachevsky, Th. Udem, and T. W. Hänsch, “Subhertz linewidth diode lasers by stabilization to vibrationally and thermally compensated ultralow-expansion glass Fabry-Pérot cavities”, *Phys. Rev. A* **77**, 053809 (2008).
- [178] N. Kolachevsky, J. Alnis, C. G. Parthey, A. Matveev, R. Landig, and T. W. Hänsch, “Low phase noise diode laser oscillator for 1S-2S spectroscopy in atomic hydrogen”, *Opt. Lett.* **36**, 4299 (2011).

- [179] M. Zhu and J. L. Hall, “Stabilization of optical phase/frequency of a laser system: application to a commercial dye laser with an external stabilizer”, *J. Opt. Soc. Am. B* **10**, 802 (1993).
- [180] D. S. Elliott, R. Roy, and S. J. Smith, “Extracavity laser band-shape and bandwidth modification”, *Phys. Rev. A* **26**, 12 (1982).
- [181] G. D. Domenico, S. Schilt, and P. Thomann, “Simple approach to the relation between laser frequency noise and laser line shape”, *Appl. Opt.* **49**, 4801 (2010).
- [182] R. Paschotta, H. R. Telle, and U. Keller, “Noise of Solid-State Lasers”, in *Solid-State Lasers and Applications*, edited by A. Sennaroglu, Optical Science and Engineering 119 (CRC Press, Boca Raton, 2007), pp. 473–523, ISBN: 978-0-8493-3589-1.
- [183] C. Henry, “Phase Noise in Semiconductor Lasers”, *J. Light. Technol.* **4**, 298 (1986).
- [184] A. L. Schawlow and C. H. Townes, “Infrared and Optical Masers”, *Phys. Rev.* **112**, 1940 (1958).
- [185] D. G. Matei, T. Legero, S. Häfner, C. Grebing, R. Weyrich, W. Zhang, L. Sonderhouse, J. M. Robinson, J. Ye, F. Riehle, and U. Sterr, “1.5  $\mu\text{m}$  Lasers with Sub-10 mHz Linewidth”, *Phys. Rev. Lett.* **118**, 263202 (2017).
- [186] F. L. Walls and A. Demarchi, “RF Spectrum of a Signal after Frequency Multiplication; Measurement and Comparison with a Simple Calculation”, *IEEE Trans. Instrum. Meas.* **24**, 210 (1975).
- [187] H. R. Telle, “Absolute Measurement of Optical Frequencies”, in *Frequency Control of Semiconductor Lasers*, edited by M. Ohtsu (Wiley, New York, 1996), pp. 137–172, ISBN: 0-471-01341-2.
- [188] C. Benko, T. K. Allison, A. Cingöz, L. Hua, F. Labaye, D. C. Yost, and J. Ye, “Extreme ultraviolet radiation with coherence time greater than 1 s”, *Nat. Photonics* **8**, 530 (2014).
- [189] R. Jason Jones, J.-C. Diels, J. Jasapara, and W. Rudolph, “Stabilization of the frequency, phase, and repetition rate of an ultra-short pulse train to a Fabry–Perot reference cavity”, *Opt. Commun.* **175**, 409 (2000).
- [190] R. Jason Jones, I. Thomann, and J. Ye, “Precision stabilization of femtosecond lasers to high-finesse optical cavities”, *Phys. Rev. A* **69**, 051803(R) (2004).
- [191] C. Henry, “Theory of the linewidth of semiconductor lasers”, *IEEE J. Quantum Electron.* **18**, 259 (1982).
- [192] M. Osinski and J. Buus, “Linewidth Broadening Factor in Semiconductor Lasers-An Overview”, *IEEE J. Quantum Electron.* **23**, 9 (1987).
- [193] P. Zorabedian and W. R. Trutna, “Interference-filter-tuned, alignment-stabilized, semiconductor external-cavity laser”, *Opt. Lett.* **13**, 826 (1988).



- [194] X. Baillard, A. Gauguier, S. Bize, P. Lemonde, Ph. Laurent, A. Clairon, and P. Rosenbusch, “Interference-filter-stabilized external-cavity diode lasers”, *Opt. Commun.* **266**, 609 (2006).
- [195] Y. Pang, J. J. Hamilton, and J.-P. Richard, “Frequency noise induced by fiber perturbations in a fiber-linked stabilized laser”, *Appl. Opt.* **31**, 7532 (1992).
- [196] L.-S. Ma, P. Jungner, J. Ye, and J. L. Hall, “Delivering the same optical frequency at two places: accurate cancellation of phase noise introduced by an optical fiber or other time-varying path”, *Opt. Lett.* **19**, 1777 (1994).
- [197] E. D. Black, “An introduction to Pound–Drever–Hall laser frequency stabilization”, *Am. J. Phys.* **69**, 79 (2001).
- [198] K. Predehl, “A 920 km Optical Fiber Link for Frequency Metrology at the 19th Decimal Place”, PhD thesis (Ludwig-Maximilians-Universität München, Munich, Germany, 2012).
- [199] H. Tsuchida, “Laser frequency modulation noise measurement by recirculating delayed self-heterodyne method”, *Opt. Lett.* **36**, 681 (2011).
- [200] J. Hald and V. Ruseva, “Efficient suppression of diode-laser phase noise by optical filtering”, *J. Opt. Soc. Am. B* **22**, 2338 (2005).
- [201] T. Nazarova, C. Lisdat, F. Riehle, and U. Sterr, “Low-frequency-noise diode laser for atom interferometry”, *J. Opt. Soc. Am. B* **25**, 1632 (2008).
- [202] H. R. Carleton and W. T. Maloney, “A Balanced Optical Heterodyne Detector”, *Appl. Opt.* **7**, 1241 (1968).
- [203] *Spectrum and Signal Analyzer Measurements and Noise*, Application Note (Keysight Technologies, 2017).
- [204] D. Gatti, R. Gotti, T. Sala, N. Coluccelli, M. Belmonte, M. Prevedelli, P. Laporta, and M. Marangoni, “Wide-bandwidth Pound-Drever-Hall locking through a single-sideband modulator”, *Opt. Lett.* **40**, 5176 (2015).
- [205] W. Nagourney, *Quantum Electronics for Atomic Physics and Telecommunication*, Second Edition (Oxford University Press, 2014), ISBN: 978-0-19-966548-8.
- [206] J. Moreno, “Stabilization of the carrier-envelope offset frequency of an Yb:KYW femtosecond laser for the generation of an XUV comb for He<sup>+</sup> spectroscopy”, MA thesis (University of Jyväskylä, Jyväskylä, Finland, 2021).
- [207] J. Weitenberg, A. Vernaleken, J. Schulte, A. Ozawa, T. Sartorius, V. Pervak, H.-D. Hoffmann, Th. Udem, P. Russbüldt, and T. W. Hänsch, “Multi-pass-cell-based nonlinear pulse compression to 115 fs at 7.5 J pulse energy and 300 W average power”, *Opt. Express* **25**, 20502 (2017).
- [208] A. Ozawa, J. Rauschenberger, C. Gohle, M. Herrmann, D. R. Walker, V. Pervak, A. Fernandez, R. Graf, A. Apolonski, R. Holzwarth, F. Krausz, T. W. Hänsch, and Th. Udem, “High Harmonic Frequency Combs for High Resolution Spectroscopy”, *Phys. Rev. Lett.* **100**, 253901 (2008).

- [209] V. V. S. Vaidyanathan, “Double Pulse Generation for He<sup>+</sup> Spectroscopy and Characterisation of Deformation of Laser Mirror Mounted on Piezoelectric Transducer”, MA thesis (Technische Universität München, Munich, Germany, 2021).
- [210] R. H. Kingston, *Detection of Optical and Infrared Radiation*, Springer Series in Optical Sciences 10 (Springer, Berlin, 1979), ISBN: 978-3-540-35948-7.
- [211] V. V. Protopopov, *Laser Heterodyning*, Springer Series in Optical Sciences 149 (Springer, Berlin, 2009), ISBN: 978-3-642-02338-5.
- [212] J.-D. Deschênes and J. Genest, “Heterodyne beats between a continuous-wave laser and a frequency comb beyond the shot-noise limit of a single comb mode”, *Phys. Rev. A* **87**, 023802 (2013).
- [213] J. Reichert, R. Holzwarth, Th. Udem, and T. W. Hänsch, “Measuring the frequency of light with mode-locked lasers”, *Opt. Commun.* **172**, 59 (1999).
- [214] S. A. Meyer, T. M. Fortier, S. Lecomte, and S. A. Diddams, “A frequency-stabilized Yb:KYW femtosecond laser frequency comb and its application to low-phase-noise microwave generation”, *Appl. Phys. B* **112**, 565 (2013).
- [215] N. Torcheboeuf, G. Buchs, S. Kundermann, E. Portuondo-Campa, J. Bennès, and S. Lecomte, “Repetition rate stabilization of an optical frequency comb based on solid-state laser technology with an intra-cavity electro-optic modulator”, *Opt. Express* **25**, 2215 (2017).
- [216] J. L. Hall and T. W. Hänsch, “External dye-laser frequency stabilizer”, *Opt. Lett.* **9**, 502 (1984).
- [217] C. Froese Fischer, M. Saporov, G. Gaigalas, and M. Godefroid, “BREIT-PAULI ENERGIES, TRANSITION PROBABILITIES, AND LIFETIMES FOR 2s, 2p, 3s, 3p, 3d, 4s <sup>2</sup>L LEVELS OF THE LITHIUM SEQUENCE, Z = 3-8”, *At. Data Nucl. Data Tables* **70**, 119 (1998).
- [218] J. Morgenweg and K. S. E. Eikema, “Ramsey-comb spectroscopy: Theory and signal analysis”, *Phys. Rev. A* **89**, 052510 (2014).
- [219] Y. Ishida, T. Otsu, A. Ozawa, K. Yaji, S. Tani, S. Shin, and Y. Kobayashi, “High repetition pump-and-probe photoemission spectroscopy based on a compact fiber laser system”, *Rev. Sci. Instrum.* **87**, 123902 (2016).

# Acknowledgements

Science is a team effort, and this dissertation would not have been possible without the contributions of many people that I would like to acknowledge here.

First of all, I want to thank Prof. Theodor Hänsch for providing the excellent research environment in the laser spectroscopy division at MPQ. His philosophy of “curiosity driven research” permeates the group and has allowed me to explore a wide range of technologies and scientific questions during my thesis work.

Thomas Udem gave me the opportunity to work on this project and agreed to supervise my thesis. I learned a lot from his uncompromising desire to get to the ground of things and greatly enjoyed the countless discussions about all kinds of science and non-science topics.

It is hard to overstate how much I learned from Akira Ozawa during my time at MPQ. I always enjoyed discussing the details of the experiment and spending many hours in the lab together to build it.

Johannes Weitenberg set up the HHG enhancement cavity for the He<sup>+</sup> spectroscopy. Not only his encyclopedic knowledge about lasers and optics, but also his great sense of humor made it a pleasure to share the lab with him! Recently our newest team member Jorge Moreno took on the challenge to continue with the project, and he already made great progress in getting the system ready for routine operation.

A special thanks goes to the team members of the two hydrogen experiments who never hesitated to help with experimental or theoretical problems: Lothar Maisenbacher, Vitaly Wirthl, Alexey Grinin, Arthur Matveev, and Derya Taray.

I further want to thank Savely Karshenboim, Randolph Pohl, Michele Giunta, Omer Amit, Julian Krauth, Anna Sótér, Gulnara Vishnyakova, Masaki Hori, and all the other current and former members of the Hänsch group that made my PhD such an enjoyable experience. In particular the yearly group retreats at Schloss Ringberg were always a great source of inspiration and a lot of fun!

Without our group technicians Wolfgang Simon and Charly Linner, the lab would be still as empty as it was the day we started the project. Many thanks not only for your skillful work, but also for your cheerful attitude towards solving difficult experimental issues!

Helmut Brückner’s custom-built electronics switch, measure, and regulate countless signals to make the experiment “tick”. I particularly enjoyed developing the digital feedback controller together!

I would also like to thank the other students and the coordinators of the IMPRS-APS graduate school for the many great events! Sharing ideas and experiences with students from different fields has been invaluable.

Many thanks go to Ingrid Hermann, Marianne Kargl, and Gabriele Gschwendtner for taking care of all organisational issues.

I also want to thank Ticijana Ban and her group at the Institute of Physics in Zagreb for their hospitality during my research visit and for showing me that working with atoms can also be fun if they are not charged.

Finally, I want to thank my parents Angelika and Ralf, and my sister Carolin for their continuous support.